



National Library  
of Canada

Acquisitions and  
Bibliographic Services Branch

395 Wellington Street  
Ottawa, Ontario  
K1A 0N4

Bibliothèque nationale  
du Canada

Direction des acquisitions et  
des services bibliographiques

395, rue Wellington  
Ottawa (Ontario)  
K1A 0N4

*Your file - Votre référence*

*Our file - Notre référence*

## NOTICE

The quality of this microform is heavily dependent upon the quality of the original thesis submitted for microfilming. Every effort has been made to ensure the highest quality of reproduction possible.

If pages are missing, contact the university which granted the degree.

Some pages may have indistinct print especially if the original pages were typed with a poor typewriter ribbon or if the university sent us an inferior photocopy.

Reproduction in full or in part of this microform is governed by the Canadian Copyright Act, R.S.C. 1970, c. C-30, and subsequent amendments.

## AVIS

La qualité de cette microforme dépend grandement de la qualité de la thèse soumise au microfilmage. Nous avons tout fait pour assurer une qualité supérieure de reproduction.

S'il manque des pages, veuillez communiquer avec l'université qui a conféré le grade.

La qualité d'impression de certaines pages peut laisser à désirer, surtout si les pages originales ont été dactylographiées à l'aide d'un ruban usé ou si l'université nous a fait parvenir une photocopie de qualité inférieure.

La reproduction, même partielle, de cette microforme est soumise à la Loi canadienne sur le droit d'auteur, SRC 1970, c. C-30, et ses amendements subséquents.

Canada

**CRYSTALLIZATION AND DISSOLUTION STUDIES OF  
IRON INTERMETALLICS IN Al-Si ALLOYS**

**ANANTHA NARAYANAN LAKSHMANAN**

A thesis Submitted to the Faculty of Graduate Studies  
and Research in Partial Fulfillment of the requirement for the  
Degree of Doctor of Philosophy

Department of Mining and Metallurgical Engineering  
McGill University  
Montreal, Quebec, Canada

©

February, 1994



National Library  
of Canada

Bibliothèque nationale  
du Canada

Acquisitions and  
Bibliographic Services Branch

Direction des acquisitions et  
des services bibliographiques

395 Wellington Street  
Ottawa, Ontario  
K1A 0N4

395, rue Wellington  
Ottawa (Ontario)  
K1A 0N4

*Your file* *Votre référence*

*Our file* *Notre référence*

**The author has granted an irrevocable non-exclusive licence allowing the National Library of Canada to reproduce, loan, distribute or sell copies of his/her thesis by any means and in any form or format, making this thesis available to interested persons.**

**L'auteur a accordé une licence irrévocable et non exclusive permettant à la Bibliothèque nationale du Canada de reproduire, prêter, distribuer ou vendre des copies de sa thèse de quelque manière et sous quelque forme que ce soit pour mettre des exemplaires de cette thèse à la disposition des personnes intéressées.**

**The author retains ownership of the copyright in his/her thesis. Neither the thesis nor substantial extracts from it may be printed or otherwise reproduced without his/her permission.**

**L'auteur conserve la propriété du droit d'auteur qui protège sa thèse. Ni la thèse ni des extraits substantiels de celle-ci ne doivent être imprimés ou autrement reproduits sans son autorisation.**

ISBN 0-315-94660-1

**Canada**

*Dedicated to my late father*

## ABSTRACT

The crystallization behaviour of iron intermetallics during solidification and the dissolution behaviour of iron intermetallics during heat treatment and their subsequent effect on mechanical properties have been studied.

Addition of iron decreases DAS and affects eutectic silicon particle size as nucleation and growth of silicon crystals takes place on the  $\beta$ -AlFeSi platelets, thus minimizing isothermal dendrite arm coarsening at the eutectic temperature. Increase of iron also increases the size and volume percent of the iron bearing intermetallics.

In the absence of manganese, the iron intermetallics crystallize in the  $\beta$ -phase, at all cooling rates ranging from 0.1 to 20 °C/s when cast from a normal casting temperature of 750 °C. In the presence of manganese, the iron intermetallic crystallizes in  $\alpha$ -phase at low cooling rates and in both the  $\alpha$ - and  $\beta$ -phases at high cooling rates. This reverse crystallization behaviour is explained based on the segregation effect displayed by the phase diagram.

When the melt is superheated to a high temperature (about 200 to 300 degrees above the liquidus temperature), the iron intermetallic crystallizes in the  $\alpha$ -phase at high cooling rates. This behaviour is attributed to the fact that  $\gamma$ -alumina which forms at low melt temperatures ( $\leq 750$  °C) acts as a nucleus for crystallization of  $\beta$ -phase. When the melt is superheated to a high temperature ( $\geq 850$  °C), the  $\gamma$ -alumina transforms to  $\alpha$ -alumina. The  $\alpha$ -alumina is found to be a poor nucleus for the  $\beta$ -phase crystallization, and as a result the  $\alpha$ -phase forms. The importance of nucleation and growth undercooling for the crystallization of iron intermetallics is highlighted.

Investigation of the dissolution behaviour of the iron intermetallics on non-

equilibrium heat treatment indicates that the  $\beta$ -phase platelets dissolve slowly through concurrent fragmentation and then dissolution at the plate tips. Addition of manganese hinders the dissolution of iron intermetallics. The amount of liquid phase formed during non-equilibrium heat treatment increases dramatically once a critical temperature is exceeded. This critical temperature is estimated to be 520 and 515 °C for samples initially solidified at 10 and 15 °C/s respectively.

The 0.15 % Fe alloy exhibits the highest tensile strength and percent elongation compared to 1.0 % Fe and 1.0 % Fe + 0.5 % Mn alloys under as-cast and equilibrium heat treated conditions. However, under non-equilibrium heat treatment conditions, ie., 30 degrees above the T4 equilibrium solution temperature, the strength properties of 1.0 % Fe alloy exceed, or at least equal, that of the equilibrium heat treated 0.15 % Fe alloy.

An attempt is made to correlate the iron intermetallics present in the microstructure and mechanical properties with the associated fracture mode in this alloy.

## RÉSUMÉ

Le comportement de cristallisation des intermétalliques de fer, leur comportement de dissolution pendant le traitement thermique et leur effet subséquent sur les propriétés mécaniques ont été étudiés.

L'addition de fer diminue le DAS et affecte la taille des particules de silicium eutectique puisque la germination et la croissance des cristaux de silicium se fait sur les plaques de  $\beta$ -AlFeSi, minimisant ainsi le grossissement du bras de dendrite isotherme à la température eutectique. Une augmentation en fer augmente la taille et le pourcentage en volume des intermétalliques contenant du fer.

En l'absence de manganèse, les intermétalliques de fer cristallisent dans la phase  $\beta$ , à toutes les vitesses de refroidissement allant de 0.1 à 20 °C/s avec une température de coulée normale de 750 °C. En présence de manganèse, l'intermétallique de fer cristallise dans la phase  $\alpha$  pour les vitesses de refroidissement élevées. Le comportement de cristallisation contraire est expliqué sur la base de l'effet de ségrégation présenté par le diagramme de phase.

Quand la coulée est surchauffée à une température élevée (environ 200 à 300 degrés au-dessus de la température de liquidus), l'intermétallique de fer cristallise dans la phase  $\alpha$  pour des vitesses de refroidissement élevées. Ce comportement est attribué au fait que l'alumine  $\gamma$  qui se forme à des températures de coulée basses ( $< 750^{\circ}\text{C}$ ), se comporte comme un germe pour la cristallisation de la phase  $\beta$ . Quand la coulée est surchauffée à une température élevée ( $> 850^{\circ}\text{C}$ ), l'alumine  $\gamma$  se transforme en alumine  $\alpha$ . L'alumine  $\alpha$  a été trouvé être un germe faible pour la cristallisation de la phase  $\beta$ , d'où la formation de la phase  $\alpha$ . L'importance de la surfusion de germination et de croissance pour la cristallisation des intermétalliques de fer est soulignée.

L'étude du comportement de dissolution des intermétalliques de fer sur le

traitement thermique hors équilibre indique que les plaques de la phase  $\beta$  se dissolvent lentement par la fragmentation concourante et ensuite par la dissolution des extrémités des plaques. L'addition de manganèse empêche la dissolution des intermétalliques de fer. La quantité de phase liquide formée pendant le traitement thermique hors équilibre augmente énormément lorsqu'une température critique est dépassée. Cette température critique est estimée à 520 et 515 °C respectivement pour des échantillons solidifiés initialement à 10 et 15 °C/s.

Pour les conditions brut de coulée et traité thermiquement à l'équilibre, l'alliage contenant 0.15 % de fer présente la résistance à la traction et l'allongement à la rupture les plus élevés comparativement aux alliages contenant 1.0 % Fe ou 1.0 % Fe + 0.5 % Mn. Cependant sous des conditions de traitement thermique hors équilibre, c.a.d 30 degrés au-dessus de la température de mise en solution à l'équilibre, les propriétés de résistance de l'alliage avec 0.15 % Fe sont supérieures ou tout au moins égales à celles de l'alliage avec 0.15 % Fe et traité thermiquement à l'équilibre.

Une tentative a été faite pour relier les intermétalliques de fer présents dans la microstructure et les propriétés mécaniques avec le mode de fracture associé dans cet alliage.

## ACKNOWLEDGEMENTS

The author would like to express his sincere gratitude to Prof. J.E. Gruzleski, Dept. of Mining and Metallurgical Engineering, McGill University and Prof. F.H. Samuel, Dept. of Applied Sciences, UQAC, for their support and guidance throughout this work.

The author is grateful to the staff members of the Dept. of Applied Sciences, UQAC and Dept. of Mining and Metallurgical Eng., McGill University, for their help in the production of castings and metallography samples.

The author would like to thank his several colleagues and friends like Hasim Mulazimoglu, Florence Paray, Saeed Shabestari, Daryoush Emadi, Pravansu Mohanty, Wittaya La-Orchan and Gail Stephen for their selfless help and creating enjoyable working atmosphere.

The author gratefully acknowledges the financial support provided by the ALCAN-NSERC Aluminum Industrial Chair, the Fondation Sagamie de l'Université du Québec à Chicoutimi and the Natural Sciences and Engineering Research Council of Canada.

The author wishes to express his sincere thanks to Prof. & Mrs. Seshadri for their hospitality, care and support during the course of his stay in Montreal. Thanks are extended to Dr. Gowri Subramanyam for her invaluable discussion and help during the progress of this research work and completion of the thesis.

Finally, the author would like to record his deep gratitude to the members of his family in India for their perennial love, encouragement and emotional support during the period of this research work.

## TABLE OF CONTENTS

<b>ABSTRACT</b> .....	i
<b>RÉSUMÉ</b> .....	iii
<b>ACKNOWLEDGEMENTS</b> .....	v
<b>TABLE OF CONTENTS</b> .....	vi
<b>LIST OF FIGURES</b> .....	x
<b>LIST OF TABLES</b> .....	xviii
<b>CHAPTER 1 : INTRODUCTION</b> .....	1
ALUMINUM CASTING ALLOYS .....	1
ALUMINUM-SILICON CASTING ALLOYS .....	1
EFFECT OF IMPURITIES/ALLOYING ELEMENTS .....	2
Al-Si-Cu-Mg ALLOYS .....	5
319 ALUMINUM ALLOY .....	6
OBJECTIVES OF THE PRESENT WORK .....	8
<b>CHAPTER 2 : LITERATURE REVIEW</b> .....	12
INTRODUCTION .....	12
IRON IN ALUMINUM-SILICON ALLOYS .....	12
EQUILIBRIUM Al-Fe-Si SYSTEM .....	12
NON-EQUILIBRIUM Al-Fe-Si SYSTEM .....	16
GROWTH OF IRON INTERMETALLICS .....	21
EFFECT OF IRON ON THE MECHANICAL PROPERTIES .....	23
NEUTRALIZATION OF IRON .....	25
RAPID SOLIDIFICATION .....	25
MANGANESE ADDITION .....	25
SLUDGING .....	30
MELT SUPERHEAT .....	31
STRONTIUM ADDITION .....	32
HEAT TREATMENT .....	34

PRECIPITATION HARDENING .....	34
SOLUTION HEAT TREATMENT .....	35
MICROSTRUCTURE MODIFICATION .....	36
SILICON PARTICLES .....	36
Al-Fe-Si INTERMETALLIC PARTICLES .....	38
<b>CHAPTER 3 : EXPERIMENTAL PROCEDURE .....</b>	<b>40</b>
CHEMICAL COMPOSITION .....	40
MICROSTRUCTURAL STUDIES .....	41
CRYSTALLIZATION STUDIES .....	45
DISSOLUTION STUDIES .....	49
MECHANICAL PROPERTIES .....	51
<b>CHAPTER 4 : MICROSTRUCTURAL STUDIES .....</b>	<b>54</b>
INTRODUCTION .....	54
GRAIN SIZE .....	55
DENDRITE ARM SPACING .....	60
EUTECTIC SILICON STRUCTURE .....	63
IRON INTERMETALLICS .....	71
EFFECT OF COOLING RATE .....	71
HARDNESS .....	74
FLUIDITY .....	74
POROSITY .....	79
MANGANESE .....	79
SUMMARY .....	81
<b>CHAPTER 5 : CRYSTALLIZATION BEHAVIOUR OF IRON</b>	
INTERMETALLICS .....	83
INTRODUCTION .....	83
EFFECT OF COOLING RATE .....	84
IN ABSENCE OF MANGANESE .....	85
IN PRESENCE OF MANGANESE .....	87

EFFECT OF MELT SUPERHEAT . . . . .	94
UNDERCOOLING . . . . .	98
LENGTH OF THE $\beta$ -PHASE PLATELETS . . . . .	99
EFFECT OF MAGNESIUM . . . . .	108
TGA AND XRD ANALYSIS . . . . .	08
NUCLEATION EFFECTS . . . . .	118
MECHANISM . . . . .	123
SUMMARY . . . . .	123
<b>CHAPTER 6 : DISSOLUTION BEHAVIOUR OF IRON INTERMETALLICS . . . .</b>	<b>125</b>
INTRODUCTION . . . . .	125
NON-EQUILIBRIUM HEAT TREATMENT . . . . .	126
MICROSTRUCTURE . . . . .	127
EFFECT OF SOLUTION TEMPERATURE . . . . .	127
IN THE ABSENCE OF MANGANESE . . . . .	129
IN THE PRESENCE OF MANGANESE . . . . .	135
EFFECT OF COOLING RATE . . . . .	141
EFFECT OF SOLUTION TIME . . . . .	148
PARTIAL MELTING . . . . .	148
DISSOLUTION MECHANISM . . . . .	155
BASIS OF DISSOLUTION . . . . .	155
NATURE OF DISSOLUTION . . . . .	155
DRIVING FORCE . . . . .	156
IN PRESENCE OF MANGANESE . . . . .	159
SUMMARY . . . . .	160
<b>CHAPTER 7 : EFFECT OF IRON INTERMETALLICS ON TENSILE</b>	
<b>PROPERTIES . . . . .</b>	<b>162</b>
INTRODUCTION . . . . .	162
TENSILE PROPERTIES . . . . .	164
AS-CAST . . . . .	164
EQUILIBRIUM HEAT TREATMENT . . . . .	165

NON-EQUILIBRIUM HEAT TREATMENT . . . . .	166
FURTHER SCOPE OF NON-EQUILIBRIUM HEAT TREATMENT . . . . .	172
FRACTURE MECHANISMS . . . . .	178
SUMMARY . . . . .	178
<b>CHAPTER 8 : CONCLUSIONS AND FUTURE WORK . . . . .</b>	<b>182</b>
CONCLUSIONS . . . . .	182
FROM THE CRYSTALLIZATION STUDIES . . . . .	182
FROM DISSOLUTION STUDIES . . . . .	184
FROM MECHANICAL PROPERTY STUDIES . . . . .	185
SUGGESTIONS FOR FUTURE WORK . . . . .	186
<b>STATEMENT OF ORIGINALITY . . . . .</b>	<b>188</b>
<b>REFERENCES . . . . .</b>	<b>190</b>

## LIST OF FIGURES

Fig. 1.1 : Part of the equilibrium Al-Si phase diagram showing composition ranges of various alloy types [2]. . . . .	3
Fig. 2.1 : The equilibrium diagram of Al-Fe-Si system after Munson [13]. . . . .	13
Fig. 2.2 : The microstructure of Al-Fe-Si alloy showing the $\alpha$ -phase. . . . .	15
Fig. 2.3 : The microstructure of Al-Fe-Si alloy showing the $\beta$ -phase. . . . .	16
Fig. 2.4 : The particle diagram for strip cast sheets (cooling rate = 10 °C/s) [17]. . . . .	18
Fig. 2.5 : Suggested "metastable" AlFeSi liquidus surfaces [18]. . . . .	18
Fig. 2.6 : The compositional limits of the phases, according to [17]. . . . .	18
Fig. 2.7 : The growth mode of (a) Al <sub>3</sub> Fe and (b) $\beta$ -AlFeSi phases [25]. . . . .	22
Fig. 2.8 : Fatigue strength evaluated from step tests as a function of iron content at room temperature [34]. . . . .	24
Fig. 2.9 : Fraction of failure at different origins (percentage of total number of samples broken during fatigue testing) [34]. . . . .	24
Fig. 2.10 : Dependence of the percentage of m-phase particle vs. iron concentration [41]. . . . .	27
Fig. 2.11 : Dependence of the $\beta$ -phase appearance vs. silicon concentration [41]. . . . .	27
Fig. 2.12 : Maximum observed length of $\beta$ -plates vs. DAS for AlSi7Mg0.3 containing various amounts of iron [42]. . . . .	28
Fig. 2.13 : Effects of Fe and Mn contents on tensile strength of Al-9.2Si-4Cu-0.5Mg alloy [44]. . . . .	28
Fig. 2.14 : The simplified phase diagrams of Al-Fe-Si system at constant Mn levels of (a) = 0 , (b) = 0.1 , (c) = 0.2 and	

(d) = 0.3 % Mn [45]. . . . .	30
Fig. 2.15 : Effects of superheating temperature and iron content on crystallized structure of iron compounds in (a) Al-6%Si-Fe alloy and (b) Al-11%Si-Fe alloy [47]. . . . .	33
Fig. 2.16 : Effect of magnesium content on crystallized structure of iron compounds in Al-6%Si-Mg-0.4%Fe alloy castings [47]. . . . .	33
Fig. 2.17 : Effect of solidification time on crystallized structure of AlFeSi compounds in Al-7%Si-0.3%Mg-0.4%Fe alloy [47]. . . . .	33
Fig. 2.18 : Portion of aluminum-copper binary phase diagram. Temperature ranges for annealing, precipitation heat treating, and solution heat treating are indicated [50]. . . . .	35
Fig. 2.19 : Effect of solution treatment on the unmodified microstructure. . . . .	37
Fig. 2.20 : Schematic characterization of the three stages of spheroidization and coarsening of the eutectic silicon phase [57]. . . . .	39
Fig. 3.1 : Schematic showing cross-section of alumina, graphite and metallic molds used in the present study. Specimens for microstructural observations were cut and polished along the plane indicated A-A. . . . .	42
Fig. 3.2 : A characteristic cooling showing thermal analysis parameters. . .	44
Fig. 3.3 : Schematic of a casting by the metallic step mold. Specimens for microstructural observations were cut from the regions marked A and B. . . . .	47
Fig. 3.4 : Photographs of a typical sample, (a) before and (b) after utilizing the special features in image analysis. Several phases are identified by different colors. . . . .	52
Fig. 3.5 : Schematic of a broken test bar showing the location of samples	

for fracture and metallographic analysis. . . . .	53
Fig. 4.1 : Effect of cooling rate on the liquidus undercooling recalescence temperature, $\Delta T_{UR}$ , for (a) 0.15 % and (b) 1.0 % iron alloys. . . . .	56
Fig. 4.2 : Effect of cooling rate on the liquidus undercooling arrest time, $t_3$ , for (a) 0.15 % and (b) 1.0 % iron alloy. . . . .	57
Fig. 4.3 : Plot of grain size versus cooling rate. . . . .	58
Fig. 4.4 : Micrographs showing grain size for (a) 0.15 % and (b) 1.0 % iron alloy for the same cooling rate (9 °C/s). . . . .	59
Fig. 4.5 : Effect of Ti on the grain size. . . . .	61
Fig. 4.6 : Thermal analysis curve in the liquidus region for the 0.15 and 1.0 % iron alloy at the same cooling rate (5 °C/s). . . . .	61
Fig. 4.7 : Plot of DAS versus cooling rate. . . . .	62
Fig. 4.8 : Micrograph showing nucleation and growth of silicon crystals on the AlFeSi needles (Cooling rate = 0.3 °C/s). . . . .	64
Fig. 4.9 : Thermal analysis curve showing eutectic region for the 0.15 and 1.0 % iron alloy at same cooling rate (1.2 °C/s). . . . .	65
Fig. 4.10 : Photomicrographs of samples quenched at (i) point A (beginning of eutectic), (ii) point B (end of eutectic in 1.0 % iron alloy) as indicated in Fig. 4.9, and (iii) air cooled. . . . .	66
Fig. 4.11 : Effect of cooling rate on the silicon morphology. . . . .	70
Fig. 4.12 : Effect of cooling rate on the eutectic nucleation temperature. . . . .	70
Fig. 4.13 : Micrographs of silicon structure for 0.15 % iron and 1.0 % iron alloys at cooling rates of (a) 20 °C/s and (b) 0.2 °C/s. . . . .	72
Fig. 4.14 : Thermal analysis and differentiated thermal analysis curves of 0.15 % iron alloy ; (b) micrograph. (Cooling rate = 5 °C/s). . . . .	75
Fig. 4.15 : Thermal analysis and differentiated thermal analysis curves of 1.0 % iron alloy ; (b) micrograph. (Cooling rate = 5 °C/s). . . . .	76

Fig. 4.16 : Plot of hardness versus cooling rate. . . . .	77
Fig. 4.17 : Effect of melt temperature and iron content on the fluidity. . . . .	78
Fig. 4.18 : Nucleation of micro-pores on the $\beta$ -AlFeSi platelets. . . . .	80
Fig. 5.1 : The cooling curve of 319 alloy (0.3 % Mg). Cooling rate = 2.5 °C/s. . . . .	86
Fig. 5.2 : Plots of average maximum length of $\beta$ -phase platelets and $\beta$ - phase eutectic temperature versus cooling rate. . . . .	88
Fig. 5.3 : Micrograph showing crystallization of the iron compounds under different cooling rates : (a) 0.1 °C/s, (b) 10 °C/s and (c) 20 °C/s in high magnesium alloy having an Fe:Mn ratio of 1.5. . . . .	90
Fig. 5.4 : The segregation effect displayed by Fe and Mn during solidification. . . . .	93
Fig. 5.5 : Microstructure of $\alpha$ -phase obtained by (a) adding manganese and (b) superheating the melt to 850 °C. . . . .	95
Fig. 5.6 : Micrographs of the alloy containing 1.0 % Fe and 0.003 % Mg : (a) superheated to 750 °C and (b) superheated to 850 °C prior to casting (Cooling rate = 10 °C/s). . . . .	97
Fig. 5.7 : Cooling curves of high magnesium alloy (0.3 % Mg) superheated to 750, 850 and 900 °C prior to casting. (Cooling rate = 10 °C/s). . . . .	100
Fig. 5.8 : Cooling curves of low magnesium alloy (0.003 % Mg) superheated to 750, 850 and 900 °C prior to casting. (Cooling rate = 10 °C/s). . . . .	101
Fig. 5.9 : The first derivative on the cooling curves of low Mg alloy, superheated to (a) 750 °C and (b) 850 °C. Note that the Al <sub>3</sub> FeSi peak disappears if the melt is superheated to 850 °C. . . . .	102
Fig. 5.10 : Photomicrographs of the high magnesium alloy sample showing	

: top section of the casting (marked A in Fig. 3.3), melt superheated to (a) 750 °C and (b) 850 °C ; and bottom section of the casting (marked B in Fig. 3.3), melt superheated to (c) 750 °C and (d) 850 °C. . . . . 103

Fig. 5.11 : Plot of average maximum length of  $\beta$ -phase platelets versus cooling rate for the high magnesium alloys superheated to different temperatures. . . . . 104

Fig. 5.12 : Plot of average maximum length of  $\beta$ -phase platelets versus cooling rate for the low magnesium alloys superheated to different temperatures. . . . . 105

Fig. 5.13(a) : TGA curve of low magnesium alloy containing 0.6 % Fe, heated up to 1000 °C under atmospheric conditions, for the first cycle of heating and cooling. (heating rate : 5 °C/min and cooling rate : 25 °C/min). . . . . 110

Fig. 5.13(b) : TGA curve of low magnesium alloy containing 0.6 % Fe, heated up to 1000 °C under atmospheric conditions, for the second cycle of heating and cooling. (heating rate : 5 °C/min and cooling rate : 25 °C/min). . . . . 111

Fig. 5.13(c) : TGA curve of low magnesium alloy containing 1.0 % Fe, heated up to 1000 °C under atmospheric conditions, for the first cycle of heating and cooling. (heating rate : 5 °C/min and cooling rate : 25 °C/min). . . . . 112

Fig. 5.13(d) : TGA curve of low magnesium alloy containing 1.0 % Fe, heated up to 1000 °C under atmospheric conditions, for the second cycle of heating and cooling. (heating rate : 5 °C/min and cooling rate : 25 °C/min). . . . . 113

Fig. 5.14(a) : TGA curve of low magnesium alloy containing 1.0 % Fe,

heated up to 1000 °C under argon atmosphere condition, for the first cycle of heating and cooling. (heating rate : 5 °C/min and cooling rate : 25 °C/min). . . . .	114
Fig. 5.14(b) : TGA curve of low magnesium alloy containing 1.0 % Fe, heated up to 1000 °C under argon atmosphere condition, for the second cycle of heating and cooling. (heating rate : 5 °C/min and cooling rate : 25 °C/min). . . . .	115
Fig. 5.15 : Photomicrograph showing nucleation of the $\beta$ -AlFeSi platelets on the oxide stringers (dark chains). . . . .	120
Fig. 5.16 : X-ray mapping of Al, O, and Fe regions. (b) corresponds to enlarged view at the region indicated by box and arrow in (a). . . .	121
Fig. 5.17 : Nucleation of the $\beta$ -AlFeSi needles on the $\gamma$ -Alumina (light grey spherical particle), at an angle of 70° (approx.) to the tangent of intersection with the particle. . . . .	122
Fig. 6.1 : Solution temperature ranges used for the equilibrium and non-equilibrium heat treatment. . . . .	128
Fig. 6.2 : Photomicrographs of the manganese-free alloy samples at three different solution temperatures of (a) 485 °C, (b) 515 °C and (c) 535 °C. (Cooling rate = 10 °C/s). . . . .	130
Fig. 6.3 : Image analysis results of manganese-free alloy samples solidified at 10 °C/s. . . . .	133
Fig. 6.4 : Photomicrographs of the manganese containing alloy samples at three different solution temperatures of (a) 485 °C , (b) 515 °C and (c) 535 °C (Cooling rate = 10 °C/s). . . . .	136
Fig. 6.5 : Photomicrograph of the $\alpha$ -phase structure in a manganese containing alloy sample solution treated at 535 °C (Cooling rate = 10 °C/s). . . . .	138

Fig. 6.6 : Image analysis results of manganese containing alloy samples solidified at 10 °C/s. . . . .	139
Fig. 6.7 : Bar chart showing the dissolution of iron intermetallics in manganese containing alloys as a function of solution temperature. . . . .	140
Fig. 6.8 : Photomicrographs showing the dissolution of iron intermetallics in (a) manganese-free and (b) manganese containing alloy samples initially solidified at 15 °C/s and solution treated at 515 °C. . . . .	142
Fig. 6.9 : Image analysis results of manganese-free alloy samples solidified at 15 °C/s. . . . .	143
Fig. 6.10 : Re-precipitation of iron intermetallics from melted zone in manganese-free alloys (Cooling rate = 15 °C/s) . . . . .	145
Fig. 6.11 : Image analysis results of manganese containing alloy samples solidified at 15 °C/s. . . . .	146
Fig. 6.12 : Re-precipitation of iron intermetallics from melted zone in manganese containing alloys (Cooling rate = 15 °C/s). . . . .	147
Fig. 6.13 : Image analysis results plotted as a function of solution time for the samples solution treated at 515 °C. . . . .	149
Fig. 6.14 : Fraction solid versus temperature of a B319.1 alloy [77]. . . . .	151
Fig. 6.15 : Grain boundary melting. . . . .	152
Fig. 6.16 : Interdendritic melting. . . . .	152
Fig. 6.17 : Shrinkage porosity developed due to sudden quenching of liquid phase. . . . .	153
Fig. 6.18 : X-ray mapping of Fe, Si and Cu fields in the microstructure containing fragmented and partly dissolved $\beta$ -phase particles. . . . .	157
Fig. 6.19 : Schematic illustration of the mechanism of the $\beta$ -phase fragmentation and dissolution. . . . .	158
Fig. 7.1 : Effect of non-equilibrium heat treatment on tensile strength of the	

alloy. . . . .	168
Fig. 7.2 : Effect of non-equilibrium heat treatment on yield strength of the alloy. . . . .	169
Fig. 7.3 : Effect of non-equilibrium heat treatment on percent elongation of the alloy. . . . .	170
Fig. 7.4 : (a) As-cast and (b) solution treated at 535 °C, microstructure of low magnesium alloys (0.003 % Mg) (Cooling rate = 20 °C/s). . .	175
Fig. 7.5 : Plot of tensile strength vs. solution time, as a function of solution temperature, for low magnesium (0.001 %) alloys [88]. . . . .	176
Fig. 7.6 : Plot of yield strength vs. solution time, as a function of solution temperature, for low magnesium (0.001 %) alloys [88]. . . . .	176
Fig. 7.7 : Plot of percent elongation vs. solution time, as a function of solution temperature, for low magnesium (0.001 %) alloys [88]. . .	177
Fig. 7.8 : SEM picture showing crack propagation along the boundary between the $\beta$ -phase platelets and aluminum matrix. . . . .	179
Fig. 7.9 : SEM picture showing crack propagation through the $\alpha$ -phase. .	179
Fig. 7.10 : Optical photograph showing fracture along the boundary between the $\beta$ -phase and aluminum matrix. . . . .	180
Fig. 7.11 : Optical photograph showing fracture through the $\alpha$ -phase colony. . . . .	180

## LIST OF TABLES

Table. 1.1 : Chemical composition limits of 319 group of alloys. . . . .	6
Table. 1.2 : Typical mechanical properties of 319 alloy. . . . .	8
Table. 2.1 : List of structures of the intermetallic phases. . . . .	19
Table. 3.1 : Chemical composition of 319 aluminum alloy. . . . .	40
Table. 5.1 : EPMA results (wt%) of iron compounds in Al-Si-Fe-Mn alloys. . . . .	89
Table. 5.2 : The silicon eutectic temperatures of low and high magnesium alloys for different Fe/Mn ratios. . . . .	92
Table. 5.3 : Average maximum length of $\beta$ -phase platelets for low and high magnesium alloys at two different Mn levels. . . . .	94
Table. 5.4 : EPMA results (wt%) of iron containing compounds in Al-Si-Fe alloys superheated to high temperature. . . . .	98
Table. 5.5 : The silicon eutectic and $\beta$ -phase start temperature as a function of melt superheating temperature. . . . .	107
Table. 5.6 : The reaction onset and peak temperatures obtained from TGA charts. . . . .	116
Table. 6.1: Fraction solid (fs) as a function of temperature at two different cooling rates [77]. . . . .	154
Table. 7.1 : As-cast tensile properties of alloy samples solidified at two different cooling rates of 10 and 15 °C/s. . . . .	164
Table. 7.2 : Tensile properties of equilibrium heat treated alloy samples initially solidified at two different cooling rates of 10 and 15 °C/s. . . . .	166
Table. 7.3 : Summary of tensile properties of as-cast, equilibrium and non- equilibrium heat treated samples. . . . .	173

# CHAPTER 1

## INTRODUCTION

### 1.1 : ALUMINUM CASTING ALLOYS :

Aluminum and its alloys possess unique characteristics -- low melting point combined with good casting characteristics, light weight, high reflectivity, superior corrosion resistance and easy workability -- which put them in an enviable position among the non-ferrous light alloys. Aluminum alloys are formed by various processes : casting, forging, rolling and extrusion. Among the various forming processes metal casting offers an economical and simple route to the production of one or several parts of the same alloy weighing from a few grams to several hundred tons. A wide variety of components, simple to complex, can be produced by selecting proper casting processes. The choice of casting process itself depends on the size, quantity and properties of the final castings. The three main casting processes that are commercially used for the production of aluminum alloys are : (i) sand, (ii) permanent mold (iii) die casting. The mechanical properties, surface quality, dimensional tolerance, uniformity of the casting and cost all depend on the specific casting process.

### 1.2 : ALUMINUM-SILICON CASTING ALLOYS

Aluminum-silicon alloys are among the most important cast alloys. Silicon imparts fluidity, wear resistance, low specific gravity, high thermal conductivity, low thermal expansion coefficient and good retention of physical and mechanical properties at elevated temperatures.

A major portion of the Al-Si alloys is utilized by the automobile industries where there has been a continuing demand for greater fuel efficiency and higher performance materials. Higher fuel efficiency can be achieved by reducing the

weight of the vehicles. The components which have the most weight saving potential are engine and drive train components, like cylinder heads, engine blocks and gear-box housings. The traditional material that has been used for these parts is cast iron which is three times heavier than aluminum-silicon alloys. Since Al-Si alloys possess the same properties as cast iron for the particular parts, the current trend has been to replace cast iron with Al-Si alloys. A recent survey [1] shows that when a cast iron engine block is replaced by an Al-Si casting a direct weight saving of about 50 % with indirect weight reductions of an additional 25 % can be achieved.

The Al-Si binary system (Fig. 1.1) [2] exhibits a simple phase diagram with a single eutectic point at 577 °C and 12.6 wt% Si. Aluminum-silicon alloys can be broadly classified into three categories, based on their silicon content. The alloys which contain 2-9 wt% Si are classified as hypoeutectic alloys, 10-13 wt% Si are classified as eutectic alloys and 14-25 wt % are classified as hypereutectic alloys. Although aluminum-silicon alloys having different silicon contents ranging from hypo to hyper-eutectic alloys are used, 7 percent and 13 percent aluminum-silicon alloys are among the most popular. The characteristic feature of these alloys is that they consist of a primary phase, aluminum or silicon, and a eutectic mixture of these two elements.

### **1.3 : EFFECT OF IMPURITIES/ALLOYING ELEMENTS**

To aluminum-silicon alloys, various alloying elements such as Cu, Mg, Zn, Mn, Fe, Ni, Cr, Co, Ti etc, are added to improve certain desirable mechanical properties and/or to suppress the effect of some undesirable impurity elements. Impurities and alloying elements, in general, partly go into solution in the matrix and partly form intermetallic particles during the solidification process.

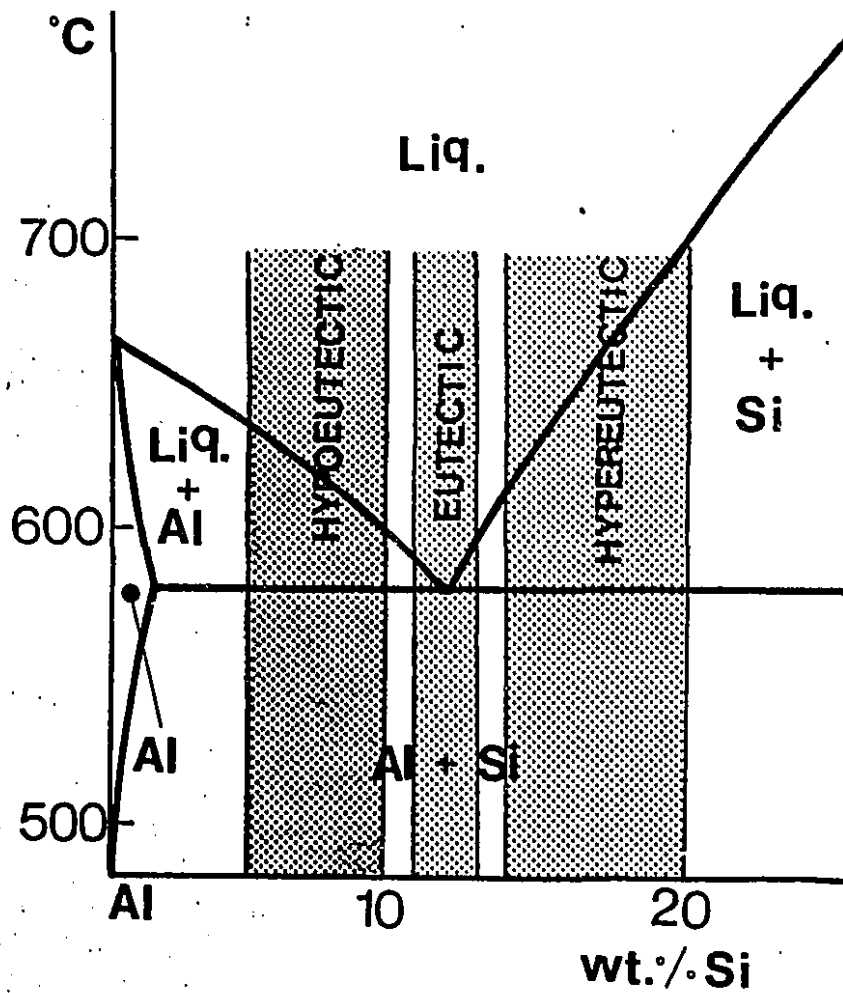


Fig. 1.1 : Part of the equilibrium Al-Si phase diagram showing composition ranges of various alloy types [2].

**1.3.1 : COPPER :**

Alloyed with aluminum, copper adds strength, hardness and improved machinability up to approximately 12 % Cu. Above this level, the aluminum base alloy (Al-Cu) is too brittle for engineering purposes. Under equilibrium conditions up to 5.65 % Cu is soluble in aluminum at the binary (Al-Cu) solidus temperature (548 °C). This solid solubility decreases to less than 0.1 % at room temperature, and it is this decreasing solid solubility which accounts for the excellent response of Al-Cu alloys to heat treatment and precipitation or age hardening. Artificial aging (usually after solution heat treatment), produces finely dispersed  $\text{CuAl}_2$  precipitates. The addition of copper increases the strength and fatigue resistance without loss of castability [3].

**1.3.2 : MAGNESIUM :**

Magnesium in Al-Si alloys acts as a powerful hardening element. It, particularly after heat treatment, increases the strength substantially, but at the expense of ductility.  $\text{Mg}_2\text{Si}$  precipitates out from the alloy solid solution during the aging treatment following quenching of the alloy. Its influence on the properties of the alloy is the same as that of copper ; it increases strength, elastic properties and hardness, but reduces ductility [4][5].

**1.3.3 : IRON :**

Iron is a natural impurity in most aluminum ore bodies (bauxite). Common sources of iron pick-up in foundry processing are from melting equipment like holding furnace pots, ladles and other melt mixing tools and from remelted scrap castings. Iron readily dissolves in liquid aluminum, and the rate increases with increasing melt temperature and decreases with increasing iron content in the aluminum bath. One of the reasons why high iron alloys are preferred in the die-casting industry is to prevent dissolution of iron from the dies and suppress the tendency to welding (soldering) to steel dies [6]. Iron is the most deleterious

impurity element in cast aluminum alloys because it forms large needles and platelets of an iron-aluminum-silicon complex which rapidly reduce the alloy's ductility.

#### **1.3.4 : MANGANESE :**

Manganese is normally added in small quantities to neutralize the detrimental effect of iron. The addition of manganese converts, partly or fully, the crystallization of needle-like AlFeSi phase to the less harmful Chinese script form, depending on the cooling rate and/or Fe:Mn ratio [7].

#### **1.3.5 : ZINC :**

Zinc content up to 3 percent has no effect upon the properties [8] except for a slight change in density. Depending upon market conditions, the higher zinc content generally lowers the cost of the alloy.

#### **1.3.6 : NICKEL :**

Nickel in aluminum alloys forms Al<sub>3</sub>Ni intermetallic compounds and increases tensile strength, yield strength, proportional limit and reduces elongation and impact strength slightly. It is usually added to Al-Si alloys to improve elevated temperature properties for use in the range of 250 °C to 375 °C [9].

#### **1.3.7 : TRACE ELEMENTS :**

Other elements such as sodium, strontium, antimony, beryllium, titanium, boron etc, may be added in very low amounts (ppm level) to improve silicon structure [10] during solidification and to refine the grain size [11].

### **1.4 : Al-Si-Cu-Mg ALLOYS :**

Among aluminum-silicon alloys, the most important group is the one which contains copper and/or magnesium (3XX series). The special advantages of these alloys are the excellent casting characteristics, weldability, pressure tightness and corrosion resistance.

Small amounts of **copper** (< 5 %) are added to these alloys (380, 383, 384 etc) to improve strength, machinability and thermal conductivity ; however, ductility and corrosion resistance decrease appreciably. In certain Al-Si alloys (356, 357), small amounts of **magnesium** (<0.6 %) are added to improve heat treatment properties of the alloy. A uniform distribution of magnesium silicide ( $Mg_2Si$ ) can be obtained through a solution heat treatment, quenching and aging procedure. Various heat treatment procedures will provide a wide range of mechanical and physical properties. The Al-Si alloys which contain **both** copper and magnesium (319, 355, 332, 390) provide greater response to heat treatment than either element alone. Thus great improvements in strength properties are obtained at the cost of ductility and corrosion resistance.

### 1.5 : 319 ALUMINUM ALLOY

319 alloys, as mentioned above, contain both copper and magnesium as the hardening elements. This is a popular alloy type with good castability and good mechanical properties. Since the aim of the present work (which will be discussed in the following sections) is to study the influence of iron in aluminum-silicon alloys, a 319 type of alloy was chosen because it contains 1.2 % iron (max). Its

Table. 1.1 : Chemical composition limits of 319 group of alloys.

AA No Alloy	Elements (wt %)						
	Si	Fe	Cu	Mn	Mg	Ni	Zn
319.1	5.5-6.5	0.8	3.0-4.0	0.5	0.10	0.35	1.0
A319.1	5.5-6.5	0.8	3.0-4.0	0.5	0.10	0.35	3.0
B319.1	5.5-6.5	0.9	3.0-4.0	0.8	0.15-0.50	0.50	1.0

physical and mechanical properties are listed below [12] :

**COMPOSITION** : The chemical composition specification limits for the 319 group of alloys are presented in Table. 1.1.

**PHYSICAL CONSTANTS :**

Density, kg/m <sup>3</sup> .....	2790
Liquidus temperature, °C .....	605
Solidus temperature, °C .....	515
Coeff. of thermal expansion $\mu\text{m}/\text{m.K}$ .....	23.0
Specific heat, J/kg.K .....	963
Latent heat of fusion, kJ/kg .....	389
Thermal conductivity W/m.K .....	109
Electrical conductivity %IACS .....	27
Electrical resistivity, sand, n $\Omega$ .....	63.9

**CASTABILITY :**

319 alloys have very good resistance to hot cracking, very good fluidity and pressure tightness. The solidification shrinkage tendency is also very good. The melting temperature range is 675 - 815 °C and the casting temperature is 675 - 790 °C. For remelting of these alloys, a gaseous type flux such as nitrogen or chlorine, or a solid aluminum chloride base flux is used.

**HEAT TREATMENT :**

Sand cast alloys are given either T5 or T6 temper treatment and permanent mold cast alloys are usually given T6 temper treatment.

Solution temperature : 500 to 505 °C ; hold for 12 h (sand), 8 h (permanent mold) ; quench in water at 65 to 100 °C.

Aging temperature : 150 to 155 °C ; hold for 2 to 5 h ; furnace cool to room temperature.

**FABRICATION** : Both sand castings and permanent mold castings are used.

**TYPICAL MECHANICAL PROPERTIES :**

Table. 1.2 : Typical mechanical properties of 319 alloy.

Property	Sand cast		Permanent mold cast	
	As-cast	T6	As-cast	T6
Tensile strength, MPa	185	250	235	280
Yield strength, MPa	125	165	130	185
Elongation, % (a)	2.0	2.0	2.5	3.0
Hardness, HB (b)	70	80	85	95
Shear strength, MPa	150	200	165	185
Fatigue strength, MPa (c)	70	75	70	...
Comp. yield strength, MPa	130	170	130	...

(a) In 50 mm or 2 in, (b) 500 kg load ; 10 mm ball, (c) At  $5 \times 10^8$  cycles.

**APPLICATIONS :**

Aluminum 319.0 alloy is used for piano plates and frames, crankcases, housings, typewriter frames, engine parts, water-cooled cylinder heads, oil tanks, oil pans, rear-axle housings, castings requiring leak tightness and other general purpose uses.

**1.6 : OBJECTIVES OF THE PRESENT WORK**

As discussed in earlier sections, iron is the major impurity element normally present in aluminum-silicon alloys. Its level is usually restricted to below 0.15 % Fe, in commercial casting alloys such as 356, 357, 358 and 359. However,

increased activity in the recycling of spent automobiles, in order to cut down the alloy production cost, causes iron levels to soar as high as 1.5 % to 2.0 %. Unlike magnesium and other elements, iron cannot be readily removed from molten aluminum by conventional foundry treatments.

It is well known that iron is a deleterious element and cause inferior mechanical properties. This is attributed to the crystallization of an Al-Fe-Si intermetallic compound in needle-like form ( $\beta$ -phase), whose length and volume fraction increase with increase in iron. Therefore, high iron alloys ( $> 0.7$  % Fe) are considered inferior and are used mainly for parts that are subjected to low stress levels. In order to widen the scope of application of these alloys, it is essential to study the influence of iron on microstructure and mechanical properties and to develop efficient techniques to neutralize the negative effect of iron.

The conventional method of minimizing the detrimental effect of iron is by the addition of a neutralizer, such as manganese or chromium. The addition of manganese or other neutralizer converts, partly or fully, the crystallization of the intermetallic compound in needle-like form ( $\beta$ -phase) to the less harmful Chinese script form ( $\alpha$ -phase). This conversion phenomenon is also reported to occur during rapid quenching or melt superheating to high temperature followed by casting under non-equilibrium cooling conditions. The exact mechanisms for the crystallization of the  $\alpha$ -phase rather than the  $\beta$ -phase during Mn addition, rapid quenching or melt superheating are not clear. Also, no completely satisfactory explanations for the nucleation and growth conditions of these intermetallic phases have been advanced.

Current heat treatment techniques in Al-Si-Cu-Mg alloys to achieve optimum mechanical properties are limited to (i) precipitation strengthening due to the presence of copper and magnesium compounds and (ii) spheroidization of silicon particles. The iron intermetallic compounds once formed during

solidification, do not dissolve during the heat treatment process. They are stable and insoluble under the conventional (equilibrium) heat treating cycle of solution and precipitation treatment. Clearly, some means to dissolve these particles and thereby improve the mechanical properties would be advantageous.

In the present work the 319 type of alloy is chosen for study due to its popularity among aluminum-silicon alloys which contain high levels of iron (1.2 % max). Also, it is in high demand in the automotive industry which is the largest consumer of cast aluminum-silicon alloys.

The main goal of the present study is to (i) understand the complete **crystallization (nucleation and growth) behaviour** of iron compounds on solidification, as a function of manganese content, melt superheating temperature and cooling rate, and (ii) develop **new (non-equilibrium) heat treatment techniques** to dissolve the harmful iron intermetallics in the matrix, thereby improving the mechanical properties. Emphasis will be placed on understanding the mechanisms behind the crystallization and dissolution behaviour of iron compounds. The final objective of this present work is to correlate the microstructure obtained by the above mentioned techniques with the mechanical properties, so that its importance can be demonstrated.

In order to fulfill the broad objectives of the present work, the study is divided into four different phases as follows :

Phase I : To study the influence of iron on the microstructural features of grain size, DAS, silicon structure, and size and shape of the iron intermetallics as a function of cooling rate, and to compare these with the thermal analysis parameters.

Phase II : To study the crystallization behaviour of iron containing compounds on manganese addition and melt superheating, as a function of cooling rate. The mechanisms behind the crystallization of  $\alpha$ -phase rather than  $\beta$ -phase on

melt superheating are to be thoroughly investigated.

Phase III : To study the dissolution behaviour of iron compounds on non-equilibrium heat treatment for alloys with and without manganese. Their kinetics of dissolution and their mechanisms are also to be studied.

Phase IV : The influence of the shape and size of the iron compounds on the tensile properties of as-cast and heat treated samples are to be studied, and their fracture mechanisms investigated by SEM.

# CHAPTER 2

## LITERATURE REVIEW

### 2.1 : INTRODUCTION :

Iron is the most deleterious impurity element in cast aluminum alloys because it forms large needles and platelets of an iron-aluminum-silicon complex which cause inferior mechanical properties. The amount of iron allowed by ANSI/ASTM specifications, in aluminum casting alloys, is relatively low, particularly for sand casting alloys. Specifications normally permit considerably more iron to be present in alloys for pressure die castings and permanent mold castings because the cooling rate is rapid and the constituent size is small. The higher iron content also reduces the solution potential for the iron components of the casting machine and mold.

In order to combat the negative effects of iron in aluminum-silicon alloys, it is important to :

- (i) know the effect of iron content on the microstructure and mechanical properties of aluminum-silicon casting alloys,
- (ii) understand various neutralization techniques and their mechanisms
- (iii) explore new ways of dissolving the harmful iron intermetallics through heat treatment.

A literature review on these topics is dealt with in the following three sections.

### 2.2 : IRON IN ALUMINUM-SILICON ALLOYS

#### 2.2.1 : EQUILIBRIUM Al-Fe-Si SYSTEM

Fig. 2.1 represents the equilibrium diagram of the Al-Fe-Si system for the range of silicon 0-12, iron 0-6 percent (after Munson [13]). These ternary

Fig. 2.1 : The equilibrium diagram of Al-Fe-Si system after Munson [13].

elements produce five primary phase fields, namely : aluminum,  $\text{FeAl}_3$ ,  $\alpha(\text{AlFeSi})$ ,  $\beta(\text{AlFeSi})$ , and silicon. The primary aluminum field ABCDEF is bounded by eutectic valleys associated with the separation of binary complexes of aluminum with  $\text{FeAl}_3$  (BC),  $\alpha(\text{AlFeSi})$  (CD),  $\beta(\text{AlFeSi})$  (DE), and silicon (FE). The last two meet at the ternary eutectic point E.  $\text{FeAl}_3$  is primary in the concentration region BCHG, and it reacts peritectically with the liquid along CH to give the ternary phase  $\alpha(\text{AlFeSi})$ . In the concentration region CDIKH the constituent  $\alpha(\text{AlFeSi})$  is primary. It reacts peritectically along DI to give  $\beta(\text{AlFeSi})$ . This phase is primary in the concentration region DEJK. All of these peritectic reactions do not proceed to completion during solidification with the result that, crystals of  $\text{FeAl}_3$  are often found wholly or partially surrounded by a

sheath of  $\alpha(\text{AlFeSi})$  and later by  $\beta(\text{AlFeSi})$ . However, during annealing, both the  $\text{FeAl}_3$  and  $\alpha(\text{AlFeSi})$  tend to convert to  $\beta(\text{AlFeSi})$ .

The binary  $\text{FeAl}_3$  compound appears in alloys containing silicon contents less than 0.5 % (approx.). This phase has a monoclinic structure [14] with lattice parameters of  $a = 15.49 \text{ \AA}$ ,  $b = 8.08 \text{ \AA}$ ,  $c = 12.47 \text{ \AA}$ , and  $\beta = 107^\circ$ . Its chemical composition corresponds to 37.40 % Fe and 0.13 % Si, with a formula approximating to  $\text{FeAl}_{3.35}$ . This phase crystallizes in the form of long prisms or needles. The crystals of  $\text{FeAl}_3$  form pseudo-tetragonal blades (plate-like morphology) in which the dominating faces belong to the  $\{100\}$  group. However, for high silicon contents ( $>0.5 \%$ ),  $\text{Al}_3\text{Fe}$  does not form and is not considered in the present study.

According to Phragmén [15], ternary  $\alpha\text{-AlFeSi}$  phase has a cubic symmetry ( $a_1 = 12.523 \text{ \AA}$ ) with a chemical composition of 31.9 % iron, 5.57 % silicon and 62.4 % aluminum. A formula approximating to this composition is  $\text{Al}_{12}\text{Fe}_3\text{Si}$ . The phase particles are light grey in color when observed under an optical microscope. As a eutectic with solid aluminum, the  $\alpha$ -phase crystals are constrained to interdendritic areas due to the difference in growth kinetics between these two phases leading to crystallization in a dendritic morphology generally described as Chinese script. The microstructure of the  $\alpha$ -phase is shown in Fig. 2.2.

For alloys containing high levels of silicon ( $> 1\%$ ) the iron compound crystallizes as primary  $\beta\text{-AlFeSi}$  phase. The chemical composition of  $\beta\text{-AlFeSi}$  phase is 27.4 % iron, 13.6 % silicon and 58.2 % aluminum [15] and corresponds closely to the formula  $\text{Al}_5\text{FeSi}$ . It has a monoclinic crystal structure with unit-cell dimensions  $a_1 = a_2 = 6.11$ ,  $a_3 = 41.4 \text{ \AA}$  and  $\alpha_2 = 91^\circ$ . The crystals of  $\alpha\text{-AlFeSi}$  form pseudo-tetragonal blades (plate-like morphology) in which the dominating faces belong to the  $\{001\}$  group. The crystals form twin lamellae, the

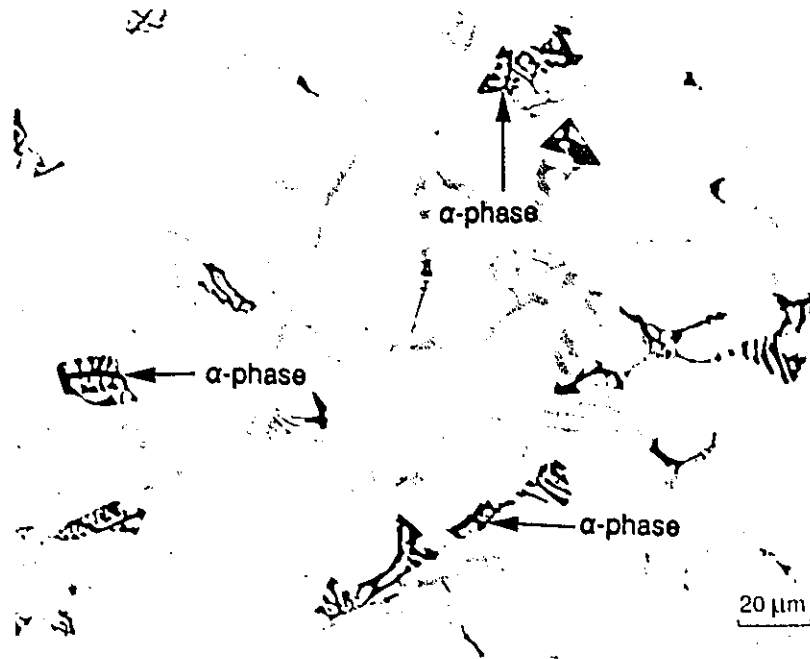


Fig. 2.2 : The microstructure of Al-Fe-Si alloy showing the  $\alpha$ -phase.

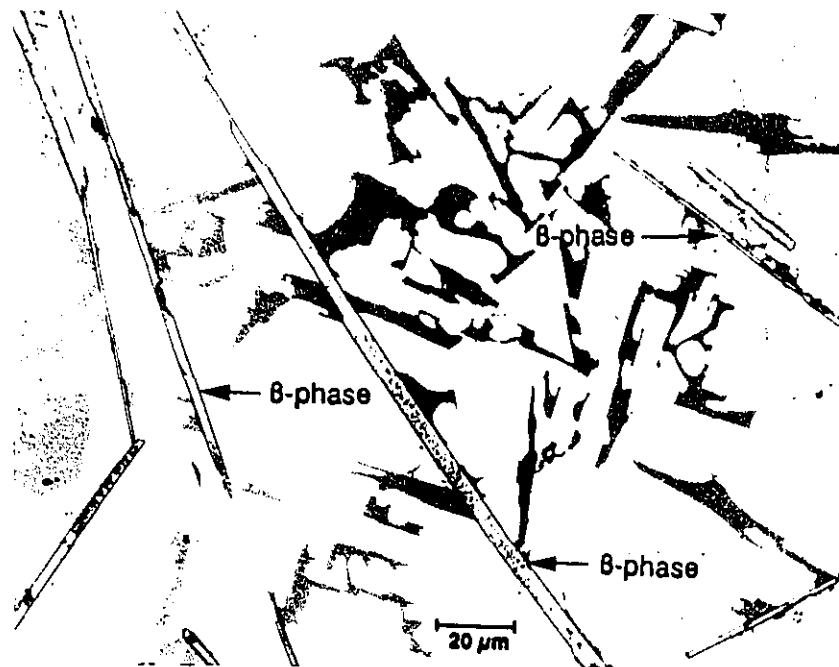


Fig. 2.3 : The microstructure of Al-Fe-Si alloy showing the  $\beta$ -phase.

twinning planes belonging to the  $\{011\}$  group. The crystals appear as needle-like shape (in cross section) and are yellowish grey color when observed under the optical microscope. The microstructure of the primary  $\beta$ -phase is shown in Fig. 2.3.

### 2.2.2 : NON-EQUILIBRIUM Al-Fe-Si SYSTEM :

As described in the previous section, iron and silicon combine with aluminum and form a series of intermetallic compounds. However, the distribution of Fe and Si in the as-cast material strongly depends on the cooling rate during solidification, because solubility of these elements varies with cooling rate. For example, in rapidly solidified castings (splat quenching), several wt % of Fe and Si can be retained in solid solution [16]. However, commercial casting techniques -- sand and permanent mold casting -- produce materials in which the major part of Fe and to a certain degree Si are present as intermetallic compounds formed on the grain boundaries and between the dendrite arms.

With the wide differences in cooling conditions that prevail in industrial casting processes, ranging from 0.5 to 10 K/s, the information contained in phase diagrams may not necessarily be applicable to the casting process. Phase diagrams have been constructed from data obtained from experiments in which mixtures of two or three very pure elements have been given time to reach equilibrium at a given temperature. However industrial alloys, which may contain many more elements are cooled to room temperature as fast as economically possible.

Also, in order to apply the Al-Fe-Si phase diagram to the industrial casting of these alloys, one has to assume a certain temperature at which the approach to equilibrium is best. This temperature may be chosen as the solidus temperature, room temperature, or some intermediate temperature, and it is possible to obtain different results with different assumptions.

Further complications which arise from industrial alloys is that certain minor alloying/impurity elements present in the alloy may stabilize phases other than those indicated in the phase diagram. This, coupled with rapid cooling favours the formation of metastable phases not predicted by the phase diagram. In addition, the local cooling rate varies from the surface to the centre of the actual castings. Accordingly, different Al-Fe-Si phases may form throughout the casting and gradients in the phase distribution may be introduced.

As equilibrium phase diagrams do not contain information about metastable phases, Dons [17] constructed a "particle diagram" based on her experimental results and literature data, as shown in Fig. 2.4. This diagram gives a rough estimate of the particles which may form under high cooling rates, 10 °C/s, but this diagram is greatly affected by the concentration of minor alloying/impurity elements and the local cooling rate. Langsrud [18] from his experimental findings, suggested a metastable phase diagram valid for "high" (~10 °C/s), "intermediate" (~3 °C/s) and "low" (~1 °C/s) cooling rates as reproduced in Fig. 2.5. The list of intermetallic phases observed in industrial cast Al-Si alloys and their structures and lattice parameters are summarized in Table. 2.1, with their compositional limits plotted in Fig. 2.6.

#### Binary Al-Fe Phases :

The only binary Al-Fe phase that is reported as an equilibrium phase is FeAl<sub>3</sub>. According to Miki et al [19], the formation of FeAl<sub>3</sub> during casting requires a cooling rate below 1 °C/s. Hollingsworth et al [20] reported a metastable phase which was ascribed a chemical formula FeAl<sub>6</sub> due to its close relationship to MnAl<sub>6</sub>. FeAl<sub>6</sub> is reported to form at cooling rates in the region of 1 to 10 °C/s [19]. Another metastable phase which forms at cooling rates exceeding 10 °C/s is termed as FeAl<sub>m</sub> [19]. The value of m is approximately 4.4.

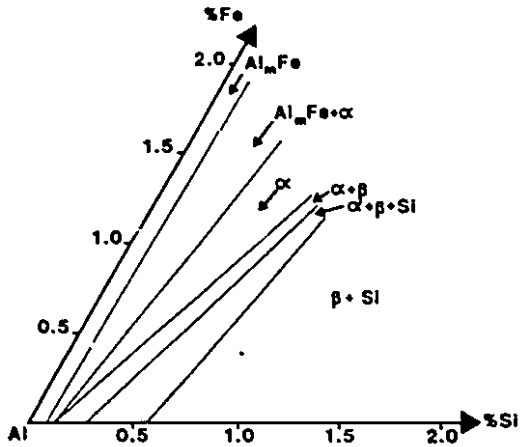


Fig. 2.4 : The particle diagram for strip cast sheets (cooling rate = 10 °C/s) [17].

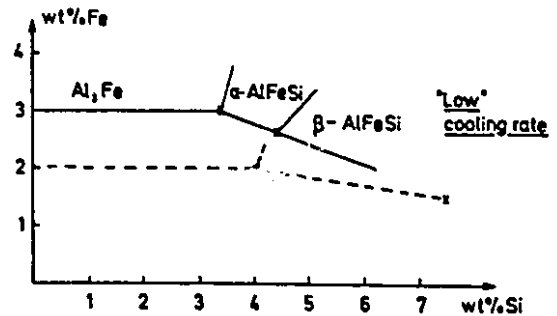
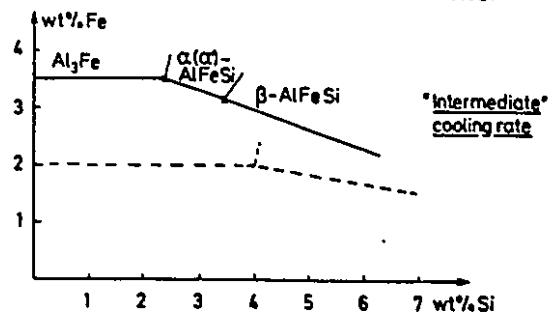
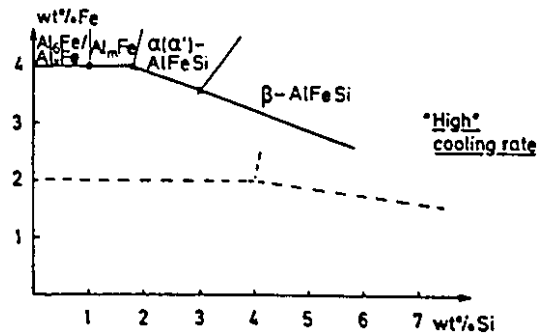


Fig. 2.5 : Suggested "metastable" AlFeSi liquidus surfaces [18].

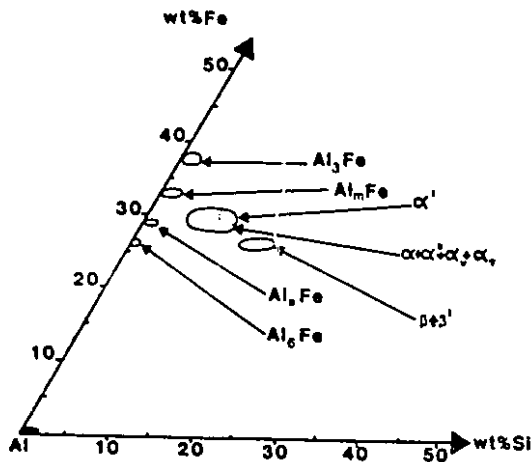


Fig. 2.6 : The compositional limits of the phases, according to [17].

Table. 2.1 : List of structures of the intermetallic phases.

Name	Crystal Structure	a (Å)	b (Å)	c (Å)	$\beta$ (°)
Al <sub>3</sub> Fe	monoclinic	15.49	8.08	12.47	107.5
Al <sub>m</sub> Fe	bct	8.84	-	21.6	-
Al <sub>x</sub> Fe	monoclinic	21.6	9.3	9.05	94
Al <sub>6</sub> Fe	C-cent. ortho.	6.49	7.44	8.79	-
$\alpha$	bcc	12.56	-	-	-
$\alpha'$	hexagonal	12.3	-	26.2	-
$\alpha''$	tetragonal	12.6	-	37.0	-
$\alpha_V$	monoclinic	8.47	6.35	6.10	93.4
$\alpha_T$	monoclinic	28.1	30.8	20.8	97.74
$\beta$	monoclinic	6.12	6.12	41.5	91
$\beta'$	monoclinic	8.9	4.9	41.6	92

One more metastable binary Al-Fe phase with highly irregular diffraction patterns was reported by Westengen [21]. This was termed as FeAl<sub>x</sub>, where X is close to 5.8. However, during annealing treatment at 590 °C, some of these metastable binary Al-Fe phases tend to transform into more stable phases.

#### Ternary Al-Fe-Si Phases :

Dons [17] in her work sorted out the different  $\alpha$ -phases (ie., phases with compositions in the range Al<sub>12-15</sub>Fe<sub>3</sub>Si<sub>1-2</sub>) according to the rate of cooling and heat

treatment. They are :

Heat treatment :  $\alpha$ ,  $\alpha'$ ,  $\alpha''$ ,  $\alpha_T$

DC cast inner zone :  $\alpha$ ,  $\alpha_V$ ,  $\alpha_T$

DC cast outer zone :  $\alpha$ ,  $\alpha''$

Strip cast :  $\alpha$

The **cubic  $\alpha$ -phase** is not regarded as a stable phase in the pure ternary Al-Fe-Si system, but can be stabilized by transition elements like Mn and Cr which are present in small amounts in commercial alloys [13]. The  $\alpha$ -phase is a less ordered phase than  $\alpha'$ , and must be expected to be favoured by rapid cooling. At intermediate rates of cooling, or after heat treatments, it may develop one of the superstructures  $\alpha''$  or  $\alpha_T$ .

The **hexagonal  $\alpha'$ -AlFeSi phase** is regarded as the equilibrium form of  $\alpha$  in the absence of transition elements other than Fe [13]. This phase is generally observed in heat treated material and is difficult to nucleate [17]. According to Sun and Mondolfo [22], this phase may also form in the pure AlFeSi system after extremely slow cooling.

In certain alloys, a **tetragonal  $\alpha''$ -AlFeSi phase** has been reported [21]. This structure is closely related to that of the cubic  $\alpha$ . Two axes are identical and the third is multiplied by a factor close to 3. This means that 3 unit cells of the cubic  $\alpha$  constitute one unit cell of the  $\alpha''$ .

**$\alpha_V$ -AlFeSi** is a new name for a phase structurally related to the  $Al_9Fe_2$  phase reported by Simensen and Vellasamy [23]. The a-axis is 2.6 % shorter and the c-axis is 3.6 % shorter than in  $Al_9Fe_2$ . The composition also differs from that of  $Al_9Fe_2$  phase. The  $Al_9Fe_2$  phase contains less than 2 % Si, while Si contents ranging from 4.5 to 10.5 % were reported by Dons [24]. This composition falls within the  $\alpha$ - $\alpha'$  range, so it was named  $\alpha_V$ , after Vellasamy.

Dons [24] in her work, identified a new AlFeSi phase, with a similar

composition to that of the  $\alpha$ -phase, but with larger variations. This phase showed a similar diffraction pattern to that of  $\alpha$ -AlFeSi, except that a few extra spots were observed. Therefore, she called this phase as  $\alpha_T$ -AlFeSi, as a working name.

In high silicon alloys ( $> 1\%$ ), **monoclinic  $\beta$ -AlFeSi phase** is observed. In low silicon alloys, the  **$\beta'$ -AlFeSi phase** is observed which shows some resemblance to the well known  $\beta$ -AlFeSi phase [21], but with lattice parameters that are slightly different (see Table. 2.1). In addition, the Fe/Si peak ratio is higher than 2, whereas the regular  $\beta$ -phase shows a ratio close to unity.

### 2.2.3 : GROWTH OF IRON INTERMETALLICS :

Eutectic growth can be divided into two types : (i) normal or continuous growth and (ii) lateral or faceted growth. In the case of normal growth, the crystal grows by the random attachment of atoms to the solid-liquid interface. These crystals grow in irregular, curved fashion conforming to the complicated shape of the interdendritic space during solidification. During crystallization atoms can add on to the solidified part when they arrive at the interface. In this case there is a "**rough**" interface between the solid and liquid. This type of growth occurs at high driving forces of solidification, i.e., at high undercoolings  $\Delta T$ . The form of crystals in this case is controlled by the temperature gradient and by the diffusion of atoms in the liquid.

In the case of lateral growth, the interface is considered atomically planar and the transition zone is theoretically reduced to one interatomic distance. The crystals of this type are bounded by slowly growing planes of low indices. These surfaces are relatively "**smooth**" on the atomic scale, and atoms from the liquid find only a few possibilities to join the interface. Growth is therefore restricted and slow. This type of growth occurs at low driving forces or slow solidification, i.e., low degrees of undercooling  $\Delta T$ . However, this growth mode can be increased by

certain irregularities or steps such as twin planes or screw dislocations.

The observed morphologies of the eutectic compounds of  $\text{Al}_3\text{Fe}$ ,  $\text{Al}_6\text{Fe}$ ,  $\text{Al}_m\text{Fe}$ ,  $\beta\text{-AlFeSi}$  and  $\alpha\text{-AlFeSi}$  suggest that the  $\text{Al}_6\text{Fe}$ ,  $\text{Al}_m\text{Fe}$  and  $\alpha\text{-AlFeSi}$  phases belong to the former group, i.e., normal or continuous growth group while the  $\text{Al}_3\text{Fe}$  and  $\beta\text{-AlFeSi}$  phases belong to the latter group, i.e., lateral or faceted crystal growth. According to Iglessis et al [25], at low cooling rates, the undercooling developed is very small, leading to the lateral growth mechanism aided by the formation of twin planes in the  $\text{Al}_3\text{Fe}$  and  $\beta$ -phase. Thus the twin planes constituting the solid-liquid interface form a step couple with a fixed angle, on which each step acts as a nucleus for atomic plane formation on the opposite face. Fig. 2.7 shows a possible arrangement of planes in the  $\text{Al}_3\text{Fe}$  and  $\beta$ -phases. The growth along the twin plane direction is not limited by the nucleation as long as the undercooling is less than a certain value,  $\Delta T_c$ . On the other hand, at high cooling rates, the undercooling developed is large, thus the rigid growth of the  $\text{Al}_3\text{Fe}$  and  $\beta$ -phase is replaced by the less rigid growth of the  $\text{Al}_6\text{Fe}$ ,  $\text{Al}_m\text{Fe}$  and  $\alpha\text{-AlFeSi}$  phases, which have no preferential growth directions.

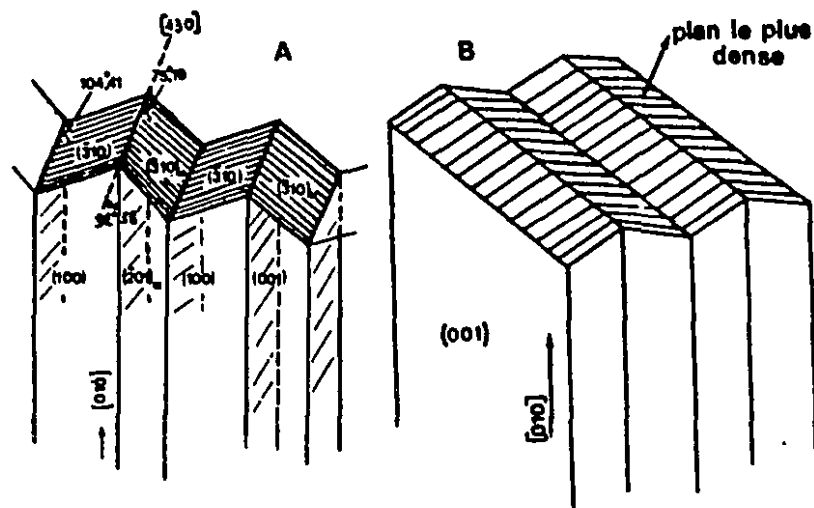


Fig. 2.7 : The growth mode of (a)  $\text{Al}_3\text{Fe}$  and (b)  $\beta\text{-AlFeSi}$  phases [25].

#### 2.2.4 : EFFECT OF IRON ON THE MECHANICAL PROPERTIES :

Literature dealing with the effect of iron on the mechanical properties of Al-Si alloys is abundant, thus showing the importance of this element in Al alloys. Couture [26] in his review reported that the addition of iron to aluminum-silicon alloys is detrimental to the mechanical properties. Vorobev et al [27] claim that, even small Fe additions to Al-Si alloys seriously diminish tensile strength and elongation. This is due to the formation of the brittle intermetallic compound,  $\text{Al}_5\text{FeSi}$ , ( $\beta$ -phase) at cooling rates normally employed in permanent and sand mold castings. This compound tends to form thin plates (that appear as needles in cross section), which are very hard and brittle and have a relatively low bond strength with the matrix [28]. As the iron content of the alloy increases, the number of  $\text{Al}_5\text{FeSi}$  crystals does not increase appreciably, but their size does. Thus, when the iron content is above 0.7 %, the  $\text{Al}_5\text{FeSi}$  compound tends to crystallize in extremely large crystals, i.e., in primary crystal form [29]. In general, the length of the  $\text{Al}_5\text{FeSi}$  crystals increases with increasing iron content and decreasing cooling rate [30][31].

According to Bonsack [32] any amount of Fe over 0.5 % will be present as Al-Fe silicide in large needles which, up to about 0.8 % Fe, increases strength and hardness but slightly reduces ductility. Above 0.8 % Fe, both strength and elongation deteriorate rapidly, and there is a deleterious effect on machinability. Hajas [33] claims that  $\text{Al}_5\text{FeSi}$  ( $\beta$ -phase) crystals are formed in the Al-10Si-Mg alloy and that this causes stress cracking and void formation in castings. Iron contents, up to 0.2 %, improve the tensile strength while high Fe contents reduce the tensile strength and elongation and increase the hardness.

Bischofberger et al [34] studied the high cycle fatigue behaviour at room temperature, 150 °C and 250 °C, of cast aluminum-silicon alloys of type GK-AlSi12CuMgNi as a function of iron content. Fig. 2.8 shows the influence of iron

content on the mean fatigue strength at room temperature as reported by [34]. Although a large scattering exists in the data, a significant reduction of fatigue strength takes place at the highest iron level (1.5 wt%). By means of scanning electron fractography, they plotted the fraction of failure at different origins (identifying where the crack had started) as shown in Fig. 2.9. They have also explained the mechanism of crack initiation at low and high temperatures in the final castings.

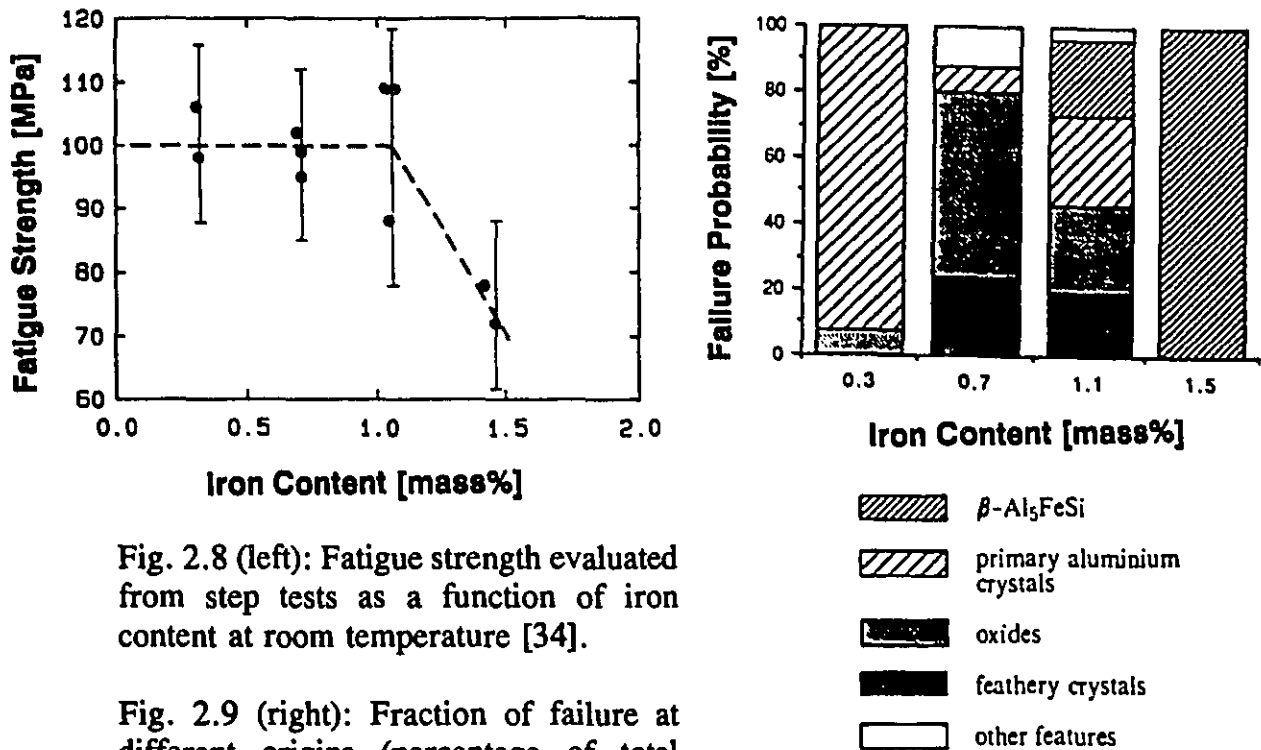


Fig. 2.8 (left): Fatigue strength evaluated from step tests as a function of iron content at room temperature [34].

Fig. 2.9 (right): Fraction of failure at different origins (percentage of total number of samples broken during fatigue testing) [34].

According to Mascré [35], the  $\beta$ -phase has a detrimental influence on the properties only when it is in the primary state. When it is part of a eutectic, its effect may be negligible or even beneficial. Grand [36] and Mascré [35] mention that slow cooling increases the size of the Al-Si-Fe particles if enough Fe

is present, and such particles may form early in the solidification process. They tend to prevent the flow of liquid metal through the feeding channels and may therefore cause unsoundness.

### **2.3 : NEUTRALIZATION OF IRON**

The detrimental effect of iron can be overcome/minimized by any one of the following techniques :

- (i) rapid solidification**
- (ii) addition of manganese**
- (iii) melt superheating and**
- (iv) strontium addition,**

All of these techniques convert the crystallization of the needle-like  $\beta$ -AlFeSi phase to the less harmful Chinese script form,  $\alpha$ -AlFeSi. Each one of these methods described below has its own advantages and limitations.

#### **2.3.1 : RAPID SOLIDIFICATION :**

The rapid solidification technique involves solidifying the melt at a very high cooling rate. By this means, the iron compound tends to crystallize as  $\alpha$ -AlFeSi phase rather than  $\beta$ -AlFeSi phase. According to Iglessis et al [37], this conversion from  $\beta$  to  $\alpha$ -phase is possible only at low levels of iron and silicon. In their later paper [25], they proposed a theoretical model for the growth process of  $\text{Al}_3\text{Fe}$ , metastable- $\alpha$  and  $\beta$  phases and a possible explanation for the observed transition from  $\text{Al}_3\text{Fe} \rightarrow \alpha$ -phase and  $\beta$ -phase  $\rightarrow \alpha$ -phase at high cooling rates, as explained in section 2.2.3.

#### **2.3.2 : MANGANESE ADDITION :**

The most common addition to neutralize the effects of iron is manganese,

although other metals have also been used, but with less success [26,89]. According to Moldolfo [28], manganese is the best all round addition for iron correction, compared to chromium, cobalt, molybdenum and nickel. The literature on the "neutralization" of iron by adding Mn to Al-Si alloys is quite abundant.

The ANSI/ASTM specification [38] says that if the Fe content exceeds 0.45 %, "it is desirable to have Mn present in an amount equal to one half of the Fe." Colwell and Kissling [39] say that Mn, in the Mn:Fe ratio of 1:2 breaks down the long needles of AlFeSi phase and thus helps both the mechanical properties and castability. Mascré [35] studied the Al-13Si alloy at varying contents of Fe and Mn up to 1.2 % and 1.3 % respectively, using test bars cast in sand and in permanent molds. He presented contour diagrams and, from these, arrived at the general "neutralization" formula for sand mold and permanent mold castings as :  $Mn \% = 2(Fe \% - 0.5)$ .

Iron and manganese form a quaternary intermetallic phase with the main components of Al-Si alloys. This phase crystallizes in three distinctly different morphologies [40]:

- (i) as needles or in fact thin platelets ( $\beta$ -phase), which cause deterioration of the mechanical properties,
- (ii) as Chinese script ( $\alpha$ -phase) which has a less significant influence on the tensile properties,
- (iii) as polyhedral crystals (primary  $\alpha$ -phase), which form under high Mn/Fe ratio and low cooling rate.

The crystallization and volume fractions of these three different morphologies depend on the Fe:Mn ratio, the cooling rate and the melt holding temperature. Dons [24] investigated  $\alpha$ -Al(Mn,Fe,Cr)Si particles under a TEM equipped with a quantitative EDX system. She found that the primary  $\alpha$ -Al(Mn,Fe,Cr)Si particles (sludge) are BCC and contain more Fe than Mn or Cr.

However, the secondary  $\alpha$ -Al(Mn,Fe,Cr) particles contain more Mn or Cr than Fe, and show simple cubic structure ( $h+k+l = 2n+1$ ) with an abundance of anti-phase domains.

Yeneva et al [41] have studied the appearance of iron intermetallic phases in Al-Si cast alloys at different Fe and Mn concentrations. They showed that for a given concentration of Mn, the percentage of needle-like phase rapidly increases with increasing iron concentration as shown in Fig. 2.10. At 0.9 wt% Fe nearly all iron containing precipitates are needle-like causing a decrease in the fatigue strength. Fig. 2.11 shows the decreasing percentage of needle-like compound in Al-Si alloys with lower Si-content.

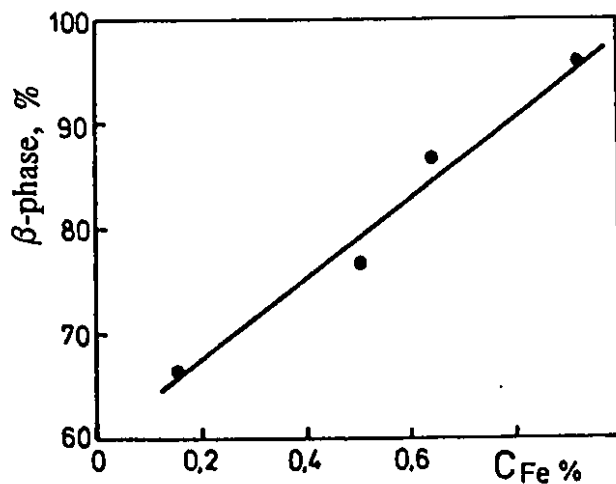


Fig. 2.10 : Dependence of the percentage of  $\beta$ -phase particle vs. iron concentration [41].

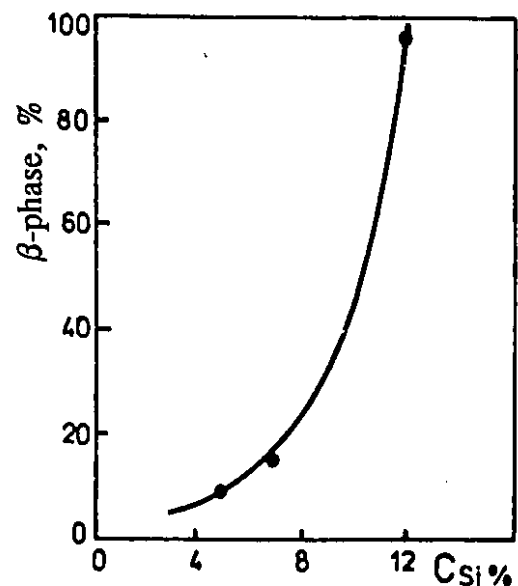


Fig. 2.11 : Dependence of the  $\beta$ -phase appearance vs. silicon concentration [41].

Evensen et al [42] have studied the influence of iron on the microstructure in AlSi7Mg0.3 alloys, by varying the iron contents from 0.15 to

0.8 % and casting in a wedge shaped mold. According to them, the morphology of Chinese script phase ( $\alpha$ -phase) shows little dependence on solidification rate, but the volume fraction decreases with increasing cooling rate and approaches zero at the lowest solidification rates. However, the size and volume fraction of  $\beta$ -plates increases with increasing iron content and decreasing solidification rate. The distribution of the maximum plate length versus dendrite arm spacing at different iron contents is shown in Fig. 2.12. The reason for the marked change in slope is unknown. Similarly, Gustafsson et al [31] have made size measurements on  $\alpha$ - and  $\beta$ -phases on 356 alloy samples with and without Cr. They plotted the length measurements of  $\beta$ -phase and arm length measurements of  $\alpha$ -phase versus DAS for 356 alloy, and this is in good agreement with the results of Evensen et al [42].

Tagami and Hashiura [43] studied the influence of Fe and Fe+Mn contents on the fracture toughness of as cast and aged alloys by a double torsion bending test. The fracture toughness of as cast and aged alloys is unsusceptible, or shows a marginal increase, to Fe concentrations less than 0.57 wt%. When the

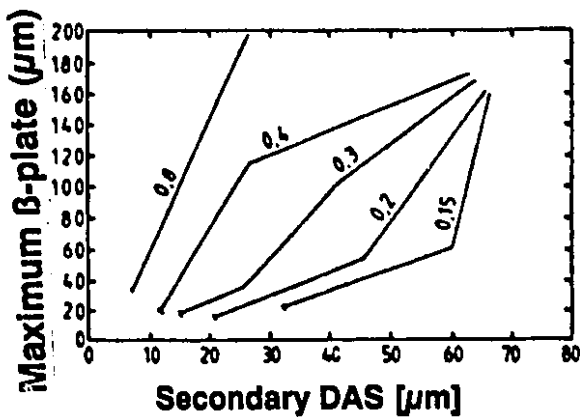


Fig. 2.12 : Maximum observed length of  $\beta$ -plates vs. DAS for AlSi7Mg0.3 containing various amounts of iron [42].

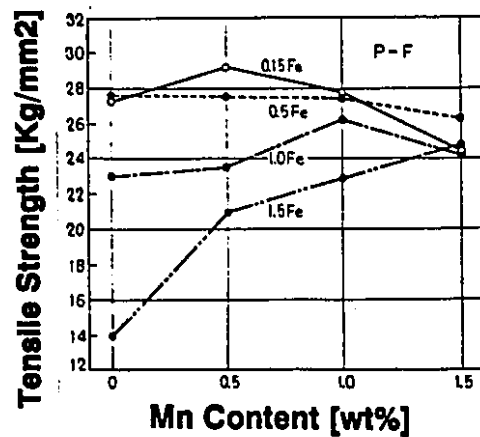


Fig. 2.13 : Effects of Fe and Mn contents on tensile strength of Al-9.2Si-4Cu-0.5Mg alloy [44].

Fe content is increased to 1 wt%, the fracture toughness is lowered by about 20 %. However, fracture toughness and percent elongation increase with increasing Mn concentration. The work of Komiyama et al [44] shows (Fig. 2.13) that Mn content has a strong influence on tensile strength only when the iron contents are high ( $> 1.0$  %). However, they caution that when the Mn/Fe ratio exceeds a certain limit, it has a harmful effect due to the formation of primary  $\alpha$ -phase. This effect on the tensile strength is seen from Fig. 2.13.

Iwahori et al [30] in their work on feedability of AC2B (Al-Si-Cu) alloy, stated that the shrinkage porosity is encouraged with an increase in iron content, and this is due to the crystallization of needle-like iron compound at an early stage of solidification. When Mn is added to these alloys, the morphology of the iron compound changes to Chinese script, and the occurrence of shrinkage porosity is inhibited by the improved feedability of the alloys, which are now able to better compensate for solidification shrinkage.

The simplified phase diagrams of the Al-Si-Fe system at constant Mn levels [45] are shown in Fig. 2.14 where it can be seen that, increasing addition of manganese expands the  $\alpha$ -phase region, and thus crystallization of  $\alpha$ -phase is possible even at high levels of iron. The morphology and chemical composition of this phase is very similar to the  $\alpha$ -phase obtained in alloys without manganese, except some solubility of manganese is observed in the former case. The chemical formula for this phase can be represented approximately by  $Al_{15}(Fe,Mn)_3Si_2$  although this phase can dissolve a fairly good amount of copper, chromium, nickel, etc., if they are present as alloying elements. These alloying elements replace part of the iron and thus the overall chemical composition of this phase remains almost the same. Unlike the  $\alpha$ -phase, the  $\beta$ -phase does not dissolve manganese or other alloying elements. The major disadvantage of this method of neutralization is that manganese coupled with chromium and nickel can cause

serious "sludging" problems as discussed in the following sub-section.

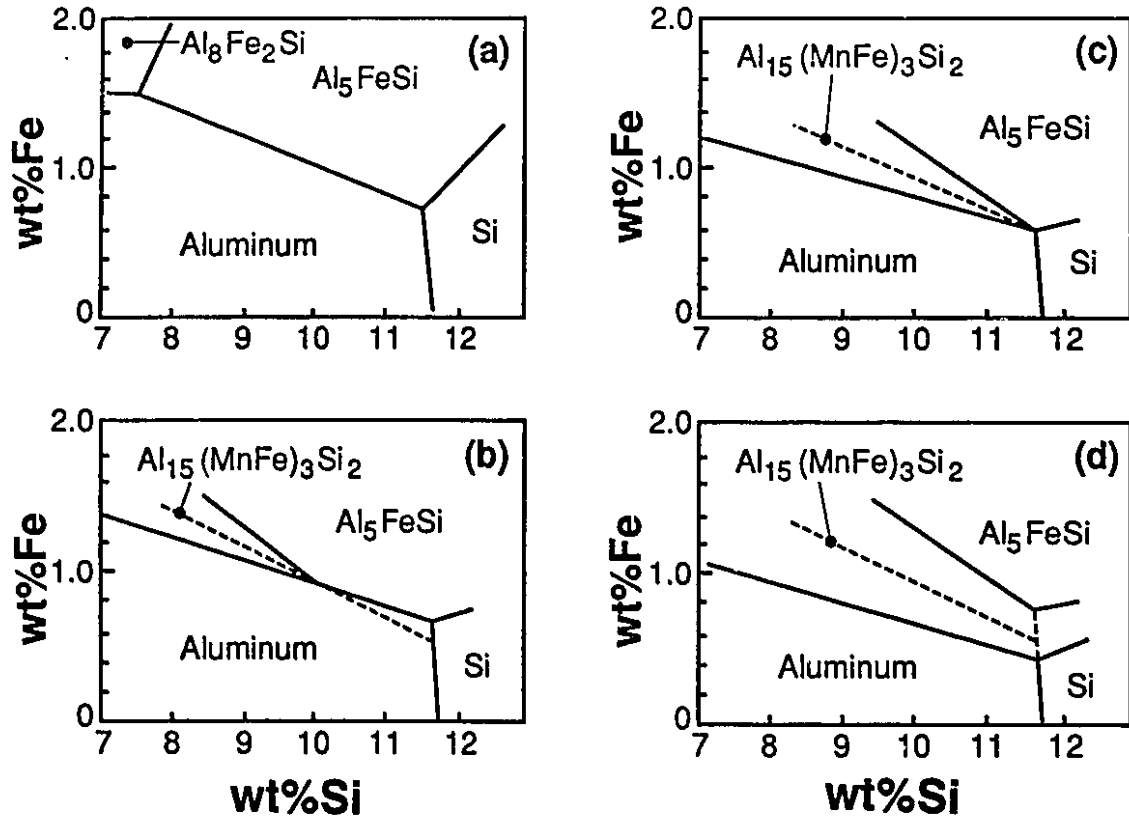


Fig. 2.14 : The simplified phase diagrams of Al-Fe-Si system at constant Mn levels of (a) = 0 , (b) = 0.1 , (c) = 0.2 and (d) = 0.3 % Mn [45].

### 2.3.2.1 : SLUDGING :

For the binary Al-Mn system at the solidus temperature (658 °C) manganese is soluble in pure aluminum up to about 1.8 %. This solid solubility decreases to less than 0.3 % at room temperature. Small amounts of manganese (usually Mn:Fe = 1:2) play a positive role in combining with iron to form the Chinese script structure instead of a plate-like structure ; however, when present at higher ratios of Mn/Fe and/or in the presence of chromium, a complex multicomponent sludge is produced. This sludge consists of intermetallic compounds which are hard, and

thus affect the mechanical properties of the castings. While the compounds also contain aluminum and silicon as well as Fe-Mn-Cr, they have a higher specific gravity than their parent alloy and settle to the bottom of the melt. Once formed they are nearly impossible to re-dissolve due to their high melting points.

The tendency to form sludge is temperature dependent in combination with the concentrations of iron, manganese and chromium. The higher the holding or casting temperature, the greater the amount of these impurities that can be tolerated without forming sludge. As a result, pressure die casters frequently experience sludging due to their nominal casting temperature of approximately 650 °C. Sand and permanent mold working temperatures are generally well above this so that sludging is seldom experienced.

An empirical formula, called "**sludge factor**" is suggested [7] for these alloys to serve as a guide, but not as a guarantee, to avoid sludging. This factor is obtained by merely adding the percentages of Fe-Mn-Cr in the following ratio:

$$\text{Sludge Factor} = \% \text{ Fe} + 2 \times \% \text{ Mn} + 3 \times \% \text{ Cr}$$

A sludge factor of 1.8 will normally not result in sludge formation if a casting temperature for die casting alloys of 650 °C or more is maintained. However, if the holding temperature is below this range, a sludge factor of 1.4 or less may be required.

### 2.3.3 : MELT SUPERHEAT :

According to Barlock and Moldolfo [46], superheating favours coupled eutectics rather than divorced leading to crystallization of  $(\text{FeMn})\text{Al}_6$  or  $(\text{FeMn})_3\text{Si}_2\text{Al}_{15}$  phases in Al-Fe-Mg-Mn-Si alloys. Recently, Awano and Shimizu [47], demonstrated a novel method of neutralizing the effect of iron without any addition of elements like Mn or Cr by superheating the melt to high temperatures before pouring. In this way, while cooling, the  $\text{AlFeSi}$  compound has been found

to crystallize in the Chinese script rather than needle-like morphology, under non-equilibrium cooling conditions (ie., high cooling rates). Based on their quenching experiments, they found that the iron compound in needle-like form ( $\beta$ -phase) crystallizes just after the beginning of the silicon eutectic reaction, but the Chinese script compound ( $\alpha$ -phase) crystallizes just after the end of the silicon eutectic reaction. This confirms that the Chinese script form crystallizes instead of the needle-like compound with enrichment of iron in the residual liquid as solidification progresses.

They also studied the relationship between melt superheating temperature and shape of the iron compound upon crystallization, as well as the effects of iron, silicon and magnesium content and solidification time. The influence of these parameters on microstructure is plotted in Figs. 2.15 - 2.17. Their results highlight the importance of low iron, silicon and magnesium content as well as high cooling rate in order to achieve complete crystallization of iron compounds in  $\alpha$ -AlFeSi form, but they neither explain the reasons behind this, nor the mechanism for the change in crystallization behaviour of the iron compound on melt superheating.

#### **2.3.4 : STRONTIUM ADDITION :**

For the past several years, strontium has been used as an additive to Al-Si casting alloys to modify the shape of the eutectic silicon phase. It has been recently discovered [48][49] that strontium alters the acicular AlFeSi intermetallic ( $\beta$ -phase) particles found in commercial 6XXX series alloys to the Chinese script form ( $\alpha$ -phase). This suggests that Sr can be used as an iron neutralizer and as an alternative to Mn or Cr in wrought alloys. Mulazimoglu et al [49] claim that only 0.015 wt % of Sr is required to neutralize 0.5 wt % Fe, which is quite low compared to the levels of Mn or Cr (>0.1 wt %).

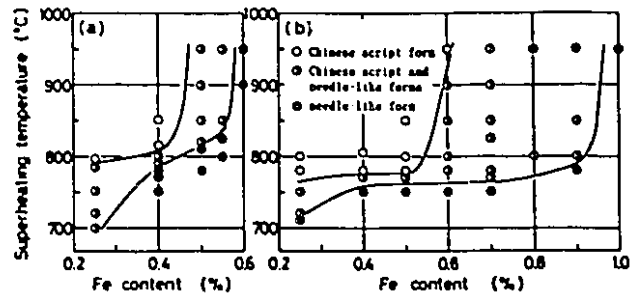


Fig. 2.15 : Effects of superheating temperature and iron content on crystallized structure of iron compounds in (a) Al-6%Si-Fe alloy and (b) Al-11%Si-Fe alloy [47].

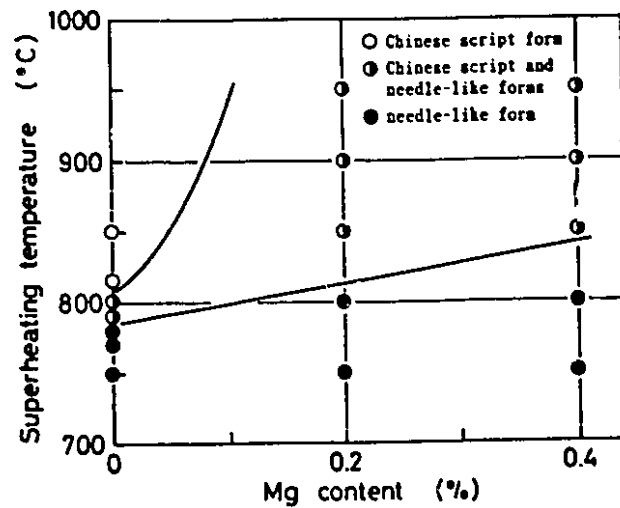


Fig. 2.16 : Effect of magnesium content on crystallized structure of iron compounds in Al-6%Si-Mg-0.4%Fe alloy castings [47].

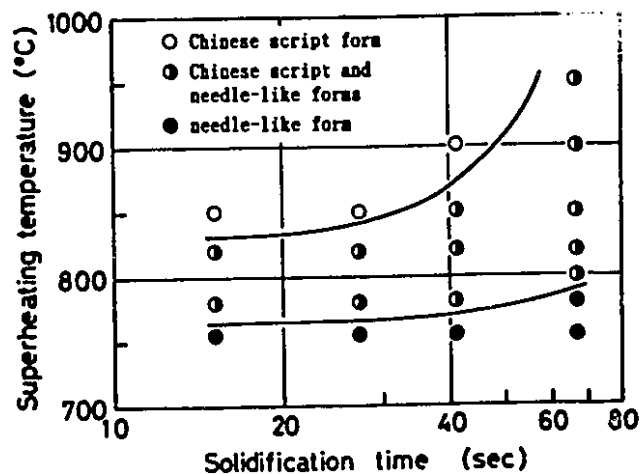


Fig. 2.17 : Effect of solidification time on crystallized structure of AlFeSi compounds in Al-7%Si-0.3%Mg-0.4%Fe alloy [47].

## 2.4 : HEAT TREATMENT :

Heat treatment in cast aluminum alloys refers to any of the heating and cooling operations that are performed for the purpose of increasing strength and hardness of the alloy through precipitation hardening and/or microstructure modification.

### 2.4.1 : PRECIPITATION HARDENING :

The main feature of a precipitation hardening alloy system is its increasing solid solubility with increasing temperature. This can be observed from the phase diagram, shown for the Al-Cu system in Fig. 2.18. Although this condition is met by most of the binary aluminum alloy systems, many exhibit very little precipitation hardening, and these alloys are not suitable for heat treatment [50]. For example, the alloys of the binary aluminum-silicon and aluminum-manganese systems are relatively insensitive to precipitation hardening treatments. The major aluminum alloy systems which exhibit precipitation hardening include:

- \* Aluminum-copper systems due to precipitation of  $\text{CuAl}_2$
- \* Aluminum-copper-magnesium systems (magnesium intensifies precipitation)
- \* Aluminum-magnesium-silicon systems due to precipitation of  $\text{Mg}_2\text{Si}$
- \* Aluminum-silicon-copper-magnesium systems (319 alloy) exhibit pronounced response due to the cumulative effect of  $\text{CuAl}_2$  and  $\text{Mg}_2\text{Si}$  precipitation.

The steps involved in the precipitation hardening heat treatments are : (i) solution heat treatment which involves dissolution of soluble phases ; (ii) quenching which produces supersaturation of second phase constituents ; and (iii) age hardening which involves precipitation of solute atoms either at room temperature (natural aging) or elevated temperature (artificial aging).

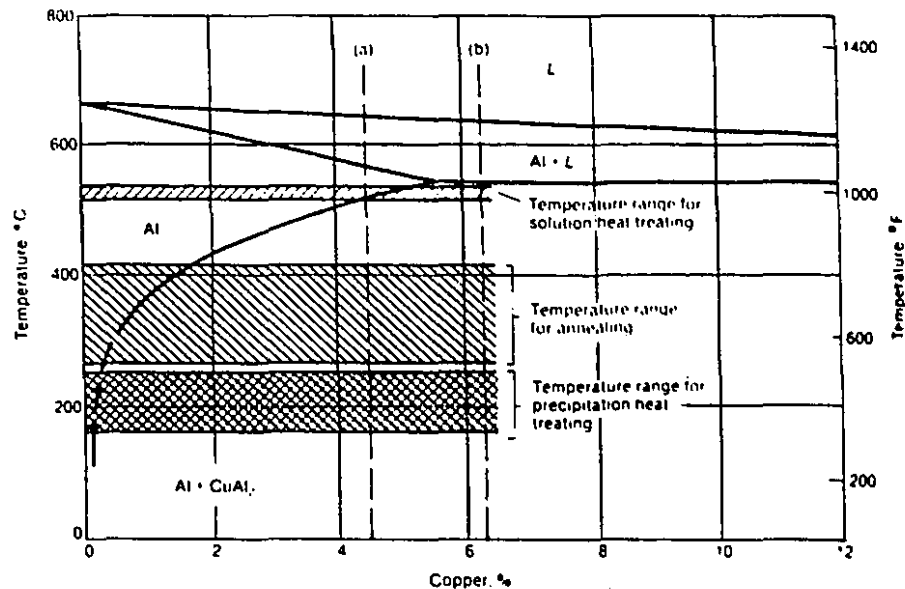


Fig. 2.18 : Portion of aluminum-copper binary phase diagram. Temperature ranges for annealing, precipitation heat treatment, and solution heat treatment are indicated [50].

#### 2.4.2 : SOLUTION HEAT TREATMENT :

The main objective of the solution heat treatment is to take the maximum practical amount of the soluble hardening elements in the alloy into solid solution. The process consists of soaking the alloy at a temperature sufficiently high and for a long enough time to achieve a nearly homogeneous solid solution. Nominal commercial solution heat treatment temperature and time are determined by the composition limits of the alloy with an allowance for furnace temperature fluctuations [51].

(i) **Overheating :** During solution treatment, care must be exercised to avoid exceeding the lowest eutectic melting temperature. If appreciable eutectic melting occurs, the properties such as tensile strength, ductility and fracture toughness decrease sharply [52]. Evidence of grain-boundary melting that occurs above the eutectic melting temperature of the alloy, is not usually detectable by either visual examination or non destructive testing.

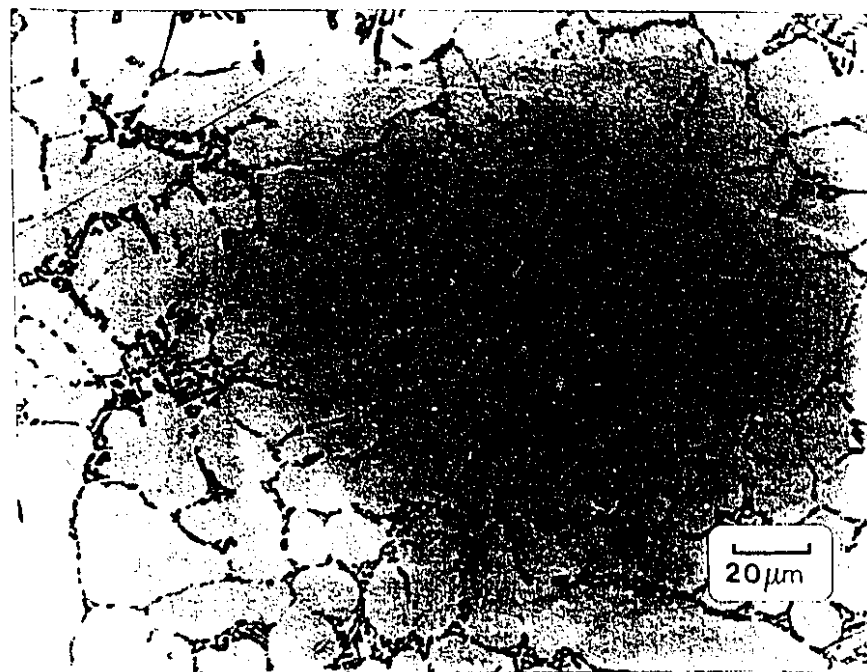
(ii) **Non-Equilibrium Melting** : When high heating rates are employed, the phenomenon of non-equilibrium melting occurs. When the heating rate is slow, the second phase particles begin to dissolve, and if heating is slow enough, all of these particles are dissolved when temperatures above the solvus are reached. However, when the heating rate is high, much of the second phase remains undissolved. If a material with this microstructure is heated at or above the eutectic temperature, melting will begin at the interface between the second phase particle and the matrix. With sufficient time above the eutectic temperature, this metastable liquid will dissolve to form a solid solution. This may also lead to formation of a void at the interface due to condensation of hydrogen gas. If the product is quenched before the liquid has time to equilibrate, it will solidify and form fine eutectic rosettes. Nonequilibrium melting should not be confused with true equilibrium melting, which usually involves grain boundary melting [53].

(iii) **Underheating** : When the temperatures attained by the parts or pieces being heat treated are appreciably below the normal range, solution is incomplete, and strength lower than normal values will result.

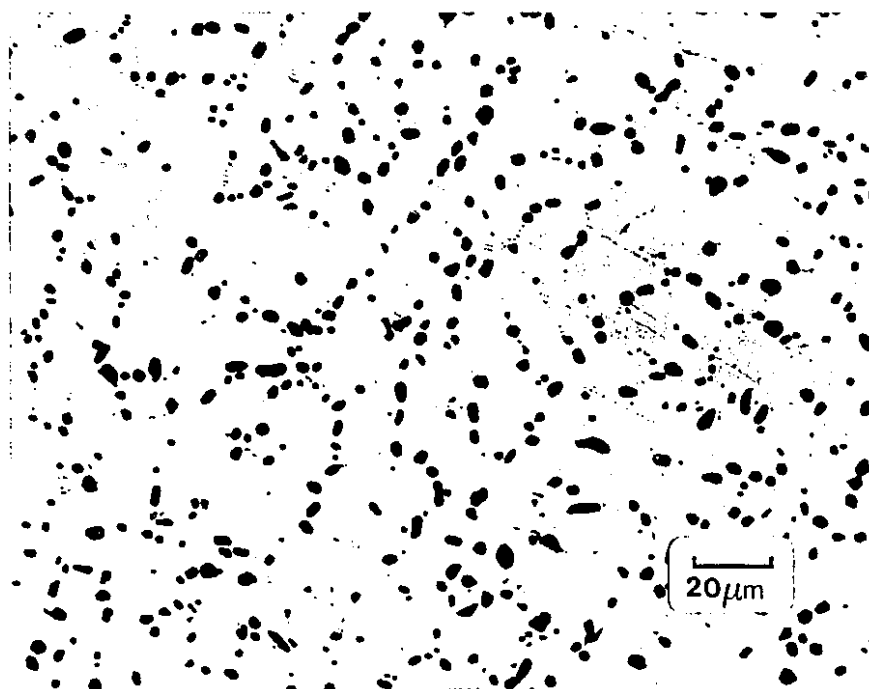
### **2.4.3 : MICROSTRUCTURE MODIFICATION :**

#### **2.4.3.1 : SILICON PARTICLES :**

During solution treatment of Al-Si alloys, the second phase silicon particles undergo morphological changes : **breaking-up, spherodization and coarsening**. The effect of solution treatment on the unmodified microstructure is presented in Figs. 2.19 (a) and (b) for the 356 alloy. In unmodified alloys the eutectic silicon forms a network of interconnected irregular flakes. During heat treatment these transform, initially, into isolated flakes, then into particles [54]. Adam and Jenkinson [55] found that during heat treatment the silicon fibres developed



(a) As-cast



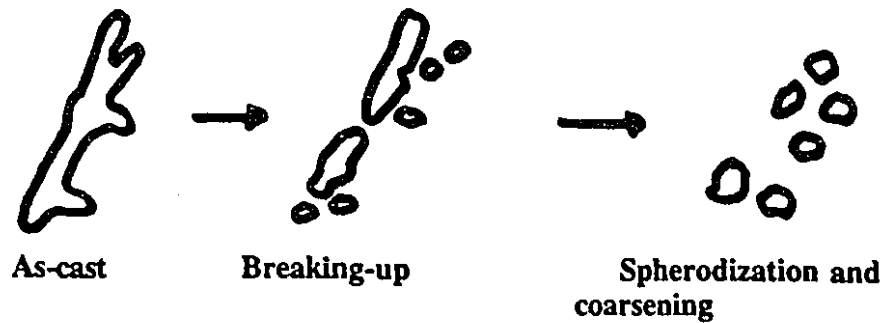
(b) 8 hours

Fig. 2.19 : Effect of solution treatment on the unmodified microstructure.

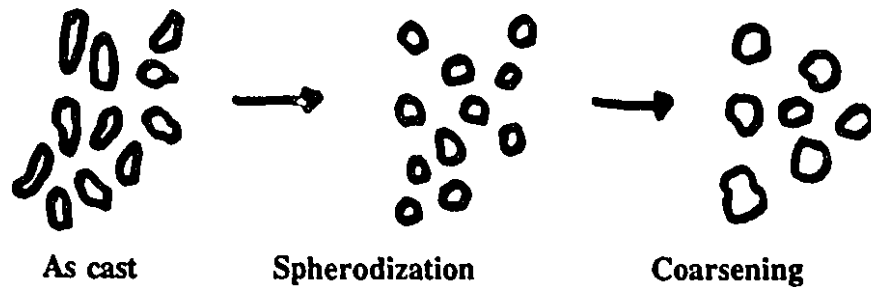
periodic variations in thickness which led to the breakdown of the fibres into particles. According to Shivkumar et al [56] and Paray [57], during the initial stages of solution treatment, the silicon particles undergo necking and are separated into segments which retain their original morphology. This process is strongly affected by the morphology of the Si flake. The smaller the length of the flake of the discontinuous phase, the greater the granulation rate. Any process that promotes eutectic Si branching (modification, higher cooling rate which results in a finer structure) will be able to speed up the progress of separation and the spherodization. The spherodization and coarsening of eutectic Si can occur concurrently during the second stage. The driving force for spherodization processes is the reduction in interfacial energy, i.e., the system tries to reduce the excess surface to the minimum possible. Modification facilitates the fragmentation by promoting the eutectic Si branching, and therefore the rate of spherodization is much more rapid in modified alloys than in unmodified alloys. The schematic representation of the granulation or spherodization process of silicon through heat treatment [57] is shown in Fig. 2.20.

#### 2.4.3.2 : Al-Fe-Si INTERMETALLIC PARTICLES :

Griger et al [58] observed that the metastable  $\alpha_C$ -AlFeSi phase which forms in 1XXX series alloys, transforms to  $Al_3Fe$  phase during heat treatment between 450 and 575 °C for prolonged times. The complete transformation of  $\alpha_C$ -AlFeSi  $\rightarrow$   $Al_3Fe$  phase occurs only after heat treatment for one week at 575 °C or 10 min at 630 °C. The  $\alpha_C$ -AlFeSi phases first coagulate and then dissolve gradually into the matrix. At the same time, nuclei of  $Al_3Fe$  appear and grow as acicular crystals to develop further to crystals of irregular shape. According to these authors [58], the  $\beta$ -AlFeSi phase which forms in the cast alloys with higher Si-content does not transform into another phase, but its morphology is changed



(a) unmodified silicon



(b) modified silicon

Fig. 2.20 : Schematic characterization of the three stages of spheroidization and coarsening of the eutectic silicon phase [57].

slightly. However, when the samples are heat treated at 620 °C, some curved  $\beta$ -AlFeSi plates dissolve while others become well developed crystals. By further increasing the heat treatment temperature, even up to partial melting of the alloy, the  $\beta$ -AlFeSi phase proves to be stable.

With the addition of a small amounts of Mn or Cr, the  $\alpha$ -AlFeSi phase becomes more stable. Therefore, as reported by Gustafsson et al [31] and others, no changes are noted in size, number or morphology of the  $\alpha$ - and  $\beta$ -phases during T6 heat treatment for alloys containing small amounts of Mn or Cr.

# CHAPTER 3

## EXPERIMENTAL PROCEDURE

### 3.1 : CHEMICAL COMPOSITION :

The chemical analysis of the 319 aluminum alloy ingots used in the present work is given in Table 3.1 along with the aluminum association (AA) standard composition. In order to study the effect of iron and manganese on the morphology of iron intermetallics formed on solidification, the iron and manganese contents were restricted to a very low level in the base alloy, and the desired amount of these elements was added to the melt to make up the final composition. This was achieved by the addition of a suitable amount of Al-25%Fe and Al-50%Mn master alloy.

Table 3.1 : Chemical composition of 319 aluminum alloy.

Alloy Composition	Elements (wt%)						
	Si	Cu	Mg	Fe	Mn	Zn	Ni
AA-Standard	6.0	3.5	0.3	1.2	0.8	1.0	0.5
High Mg Alloy	6.23	3.2	0.31	0.15	0.028	0.004	0.002
Low Mg Alloy	5.97	3.0	0.003	0.12	0.022	0.006	0.001

Since the present work covers a broad spectrum, several experimental procedures were used. The experimental methodology work is presented for each of the phases of work (as described in section 1.6) in the following sections.

### 3.2 : MICROSTRUCTURAL STUDIES :

The influence of iron on the microstructure of 319 alloy was examined by thermal analysis and metallography. For this, the allowable extreme levels of iron in the 319 - high Mg alloy were used. These were (i) 0.15 % Fe, as present in the base alloy, and (ii) 1.0 % Fe. The amount of Mn was intentionally kept at a low level to minimize its influence on the crystallization of iron compounds. To study the effect of grain refiner and eutectic modifier, 0.08 % Ti was added as Al-5Ti-1B master alloy and 0.026 % Sr was added as Al-10Sr master alloy. These levels of Ti and Sr were chosen in accordance with the suggested values reported in the literature for 319 aluminum alloys [11][59][60]. For each casting, samples for chemical analysis were taken and the compositions of the various alloying elements analysed.

Melting was done in an electrical resistance furnace and maintained at  $750\text{ }^{\circ}\text{C} \pm 5\text{ }^{\circ}\text{C}$ . Prior to pouring, the melt surface was thoroughly skimmed. In order to achieve different cooling rates ranging from  $0.2\text{ }^{\circ}\text{C/s}$  to  $25\text{ }^{\circ}\text{C/s}$ , alumina, graphite and metallic molds preheated to different temperatures were used. The approximate dimensions of the castings obtained using these molds are indicated in Fig. 3.1. Cooling rates of  $25\text{ }^{\circ}\text{C/s}$  and above were achieved by circulation of water through the spiral copper tube which was attached to the outer jacket of the metallic mold. The melt pouring temperature was kept constant at a temperature of  $740\text{ }^{\circ}\text{C} \pm 5\text{ }^{\circ}\text{C}$ .

Conventional thermal analysis was performed on all samples using high-sensitivity thermocouples 0.3 mm diameter, and data were acquired by a high-speed data acquisition system linked to a computer. In order to measure various thermal analysis parameters and the crystallization temperature of the Al-Fe-Si intermetallic compound in needle-like form accurately, differentiated thermal analysis was performed on specific samples. There is considerable variation in the

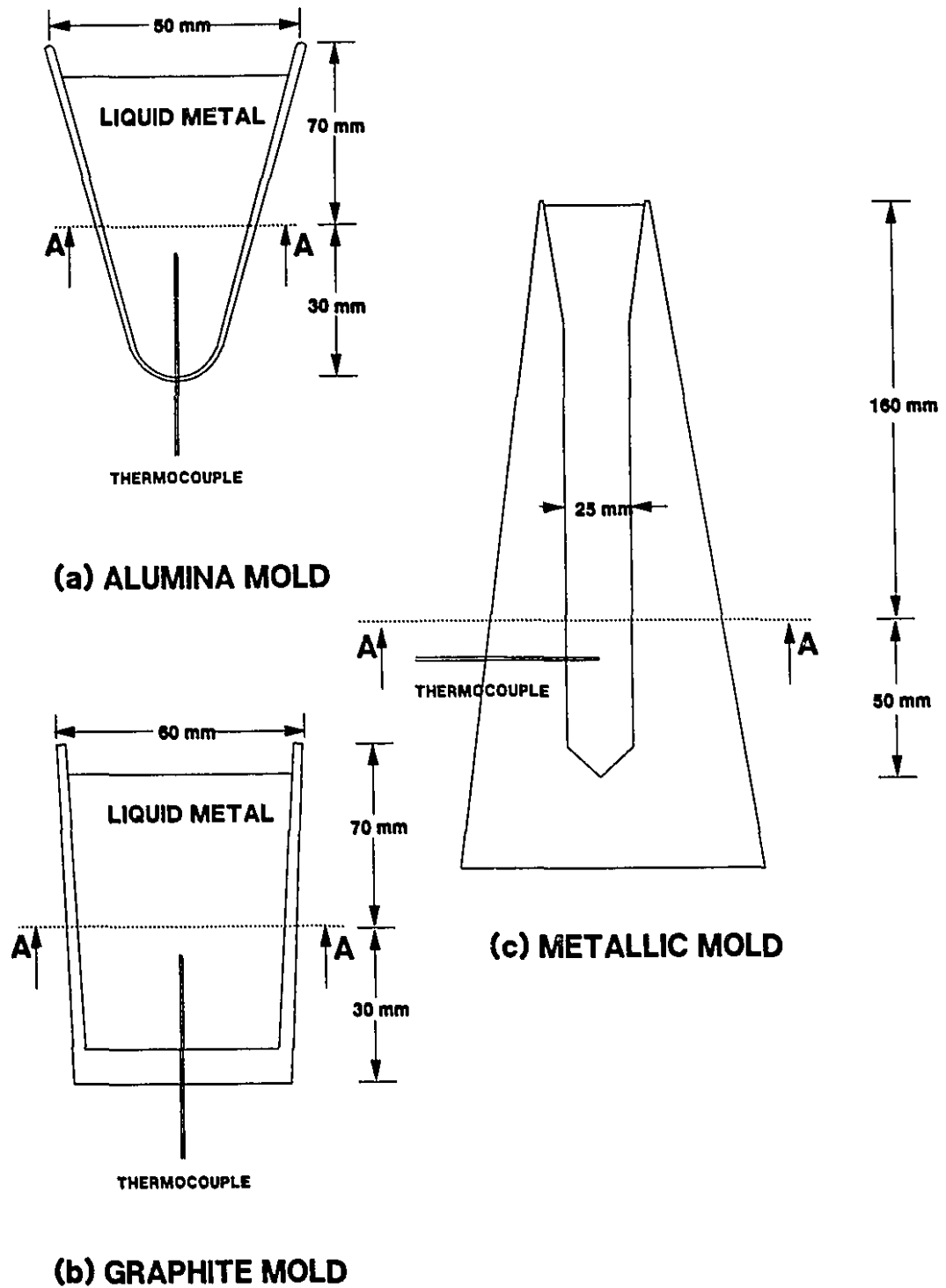


Fig. 3.1 : Schematic showing cross-section of alumina, graphite and metallic molds used in the present study. Specimens for microstructural observations were cut and polished along the plane indicated A-A.

literature concerning the definitions of thermal analysis parameters. Therefore, the definitions set by the AFS thermal analysis committee [61] are followed in the present work. The method of calculation of cooling rate and local solidification time adopted here is as follows and is illustrated in Fig. 3.2.

- \* Cooling Rate (C.R) : is calculated by taking the average slope of the approximate straight line portion of the cooling curve in the temperature interval (590 - 560 °C).
- \* Total Solidification Time ( $t_f$ ) : is defined as the time interval between solidification start time and copper eutectic finish time (500 °C).
- \* Liquidus Temperature ( $T_L$ ) : Temperature corresponding to the liquidus maximum undercooling temperature.
- \* Liquidus Undercooling Recalescence Temperature ( $\Delta T_{UR}$ ) : The sum of the undercooling temperature interval and the recalescence temperature interval.
- \* Undercooling Arrest Time ( $t_3$ ) : The time interval between the time that the sample reaches the maximum undercooling temperature and the time that the sample reaches the maximum recalescence temperature.
- \* Eutectic Nucleation Temperature ( $T_{EN}$ ) : is the minimum temperature to which the melt cools before eutectic solidification begins.

Metallographic analysis was carried out on the samples, which were cut near the tip of the thermocouple. The samples were polished up to 0.05  $\mu$  alumina and observed under a NEOPHOT microscope. In order to reveal dendrites and grain boundaries clearly, 0.5 %HF and Poulton's reagent ( 12 mL HCl (conc), 6 mL HNO<sub>3</sub> (conc), 1mL HF (48 %), 1 mL H<sub>2</sub>O) were used respectively. The dendrite arm spacings and grain sizes were measured using a LECO 2001 image analyzer. Ten field measurements were taken each from the edge and center of the sample and the values were averaged.

In order to elucidate the mechanism of dendrite arm coarsening in low iron

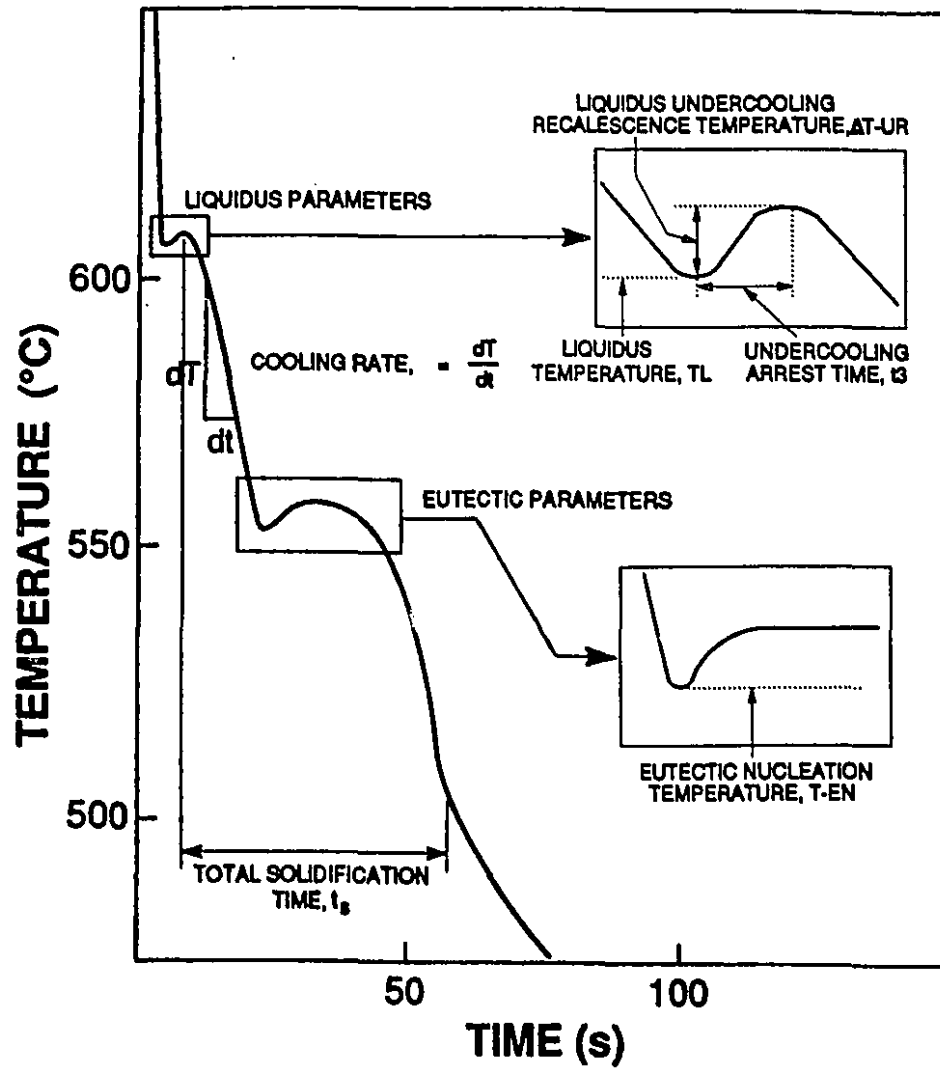


Fig. 3.2 : A characteristic cooling curve showing thermal analysis parameters.

alloys, both 0.15 and 1.0 % Fe alloy samples were machined to cylindrical dimensions of 1 inch diameter and 2 inch length, and remelted in a separately sealed quartz tube. Two pairs of samples containing 0.15 and 1.0 % Fe alloy were quenched together in water ; one at a temperature just before the start and another just after the silicon eutectic reaction. In addition one pair of samples was cooled to room temperature under the same cooling conditions. In order to know the exact temperature at the time of quenching, high sensitivity thermocouples were inserted through the quartz tube and cooling curves were monitored on-line while quenching. The samples were cut and polished near the thermocouple tip and the DAS were measured.

Hardness measurements were done on all the samples by means of a standard Brinell hardness tester using a 500 kg load. For each sample, ten measurements were done and the average value was calculated. Fluidity of the melts containing 0.15 and 1.0 % Fe alloy was measured using a Ragone vacuum fluidity tester at different melt temperatures ranging from 650 to 850 °C. For this, one end of a hollow pyrex tube of 3 mm dia (ID) was dipped one inch beneath the melt surface and the length of the metal raised at 200 mm Hg was used as an arbitrary scale to measure fluidity. The same procedure was adopted in all cases in order to maintain reproducibility of results. For each melt chemistry/temperature, three such tests were done and the average value calculated.

To study the influence of manganese on the crystallization of iron intermetallics, 0.5 % Mn was introduced to a melt containing 1.0 % Fe alloy (Fe:Mn = 2:1), by the addition of Al-50%Mn master alloy.

### **3.3 : CRYSTALLIZATION STUDIES :**

The crystallization behaviour of iron intermetallics under different melting

and casting conditions such as manganese addition, melt superheating and rapid cooling was studied as described below.

The effect of melt superheat on the crystallization behaviour of the iron containing compounds was investigated by heating the melt to different temperatures, viz., 750 °C, 850 °C and 900 °C and holding for approximately 30 minutes. Since the melt holding time is reported to be not important for the crystallization of iron intermetallics [47], it was not varied in the experiments. In each case, the melt was furnace cooled to 750 °C before pouring, and the final pouring temperature was always maintained at 750 °C. To minimize an excessive gas and oxide content resulting from the high superheating temperatures, the melt was thoroughly skimmed and degassed with pre-dried argon gas before pouring. In order to avoid the interference of grain refiner (Ti-B) and eutectic modifier (Sr) on the crystallization behaviour of iron intermetallics, they were not added to the melt. For each casting, samples for chemical analysis were taken and the compositions of various alloying elements analysed.

Experiments were carried out at both very low (0.003 % Mg) and high (0.3 % Mg) magnesium concentrations. This was done in order to ascertain why it is difficult to crystallize the iron compound in the  $\alpha$ -phase form even at a high superheating temperature of 900 °C in high magnesium alloys, and to study the influence of magnesium on the crystallization behaviour of these compounds.

To study the influence of manganese, this element was added to a melt containing 1.0 % Fe. Two different Fe/Mn ratios were used : 1.5 and 3.0, keeping the Fe level constant at 1.0 wt%. In all cases, Mn was added only after the complete dissolution of iron in the melt.

To obtain various solidification rates, casting was done in a metallic step mold having sections with different thicknesses (see Fig. 3.3), with the mold maintained at room temperature or preheated to 300 °C. Thermal analysis was

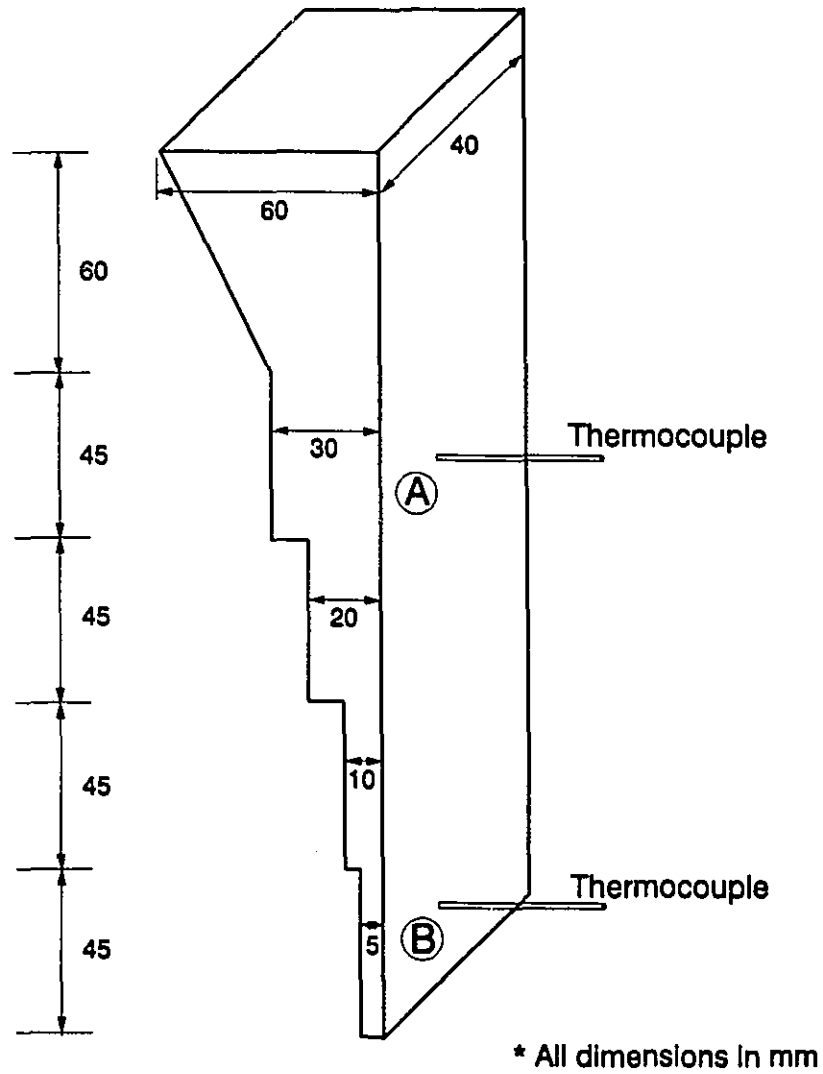


Fig. 3.3 : Schematic of a casting by the metallic step mold. Specimens for microstructural observations were cut from the regions marked A and B.

performed in the step mold by attaching high sensitivity thermocouples (0.3 mm diameter) at the top and bottom sections of the mold, and the data was acquired using a high speed data acquisition system (LABTECH NOTEBOOK) linked to a computer. The cooling rate was calculated as the average slope of the approximately linear portion of the cooling curve, between the liquidus and the silicon eutectic temperature as described previously. In order to estimate the exact crystallization temperature of the iron compound in the  $\beta$ -phase, differentiated thermal analysis was performed on the cooling curves.

Metallographic samples were cut from positions near the tip of the thermocouples in order to correlate the thermal analysis parameters with the microscopic observations. Due to many technical difficulties involved in differentiating the color contrast (grey level) between the iron compounds and other intermetallic compounds using image analysis, the exact volume fractions of the  $\alpha$ - and  $\beta$ -phases were not measured. However, it is usual practice to measure the average or maximum length of the  $\beta$ -phase platelets [31][42], which in turn can be directly related to the volume fraction [62]. This length was measured using an image analysis system (LECO 2001), and the average of the ten highest readings among 50 or more measurements was reported as the *average maximum length of  $\beta$ -phase platelet*. Sufficient length measurements were done for each sample in order to make sure that there was only 10 % or less deviation in the average of ten highest readings.

Electron Probe Micro Analysis (EPMA) at current and voltage levels of 100  $\mu$ A and 15 KV respectively was used for the chemical analysis of the different phases, and the average of ten readings is reported for each phase. For the element analysis, ZAF correction was made with reference to the standard pure element.

A few specific samples were subjected to thermogravimetric analysis (SETARAM - TAG24) under air and argon atmosphere to explore the mechanism

behind the crystallization of the  $\alpha$ , rather than  $\beta$ -phase, on melt superheating. These samples, each weighing about 60 mg, were heated to 750 °C and 1000 °C at a heating rate of 5 °C/min and then cooled at a rate of 25 °C/min. The analysis was performed for two subsequent cycles of heating and cooling on the same sample.

The surface oxides of the superheated melt were carefully skimmed and analyzed using XRD (REGAKU) at 150  $\mu$ A and 50 KV to identify the nature of oxides formed at different melt superheat temperatures.

In order to study the nucleation of iron compounds on oxides which are usually present in the melt, a few selected samples were observed under SEM (JEOL 840) linked to EDS. X-ray mapping was performed using an ultra-thin window in order to map-out the oxygen rich areas. Also,  $\gamma$ - and  $\alpha$ -alumina particles, 5  $\mu$ m and 100  $\mu$ m size respectively, were individually added to the melts using a fluidized particle injection technique [63], and the nucleation of iron compounds on these externally added oxide particles was studied.

### **3.4 : DISSOLUTION STUDIES :**

The dissolution behaviour of iron containing compounds during non-equilibrium heat treatment (solution treatment at a temperature above the final eutectic temperature, in this case, 500 °C), was studied for the alloys (high Mg) containing 0.15 % Fe, 1.0 % Fe and 1.0 % Fe + 0.5 % Mn. For this purpose standard test bars of two inch gage length were cast in a Stahl mold. To study the influence of size of the iron intermetallics in the original cast samples on the dissolution behaviour of these compounds, each of the alloys was cast in a Stahl mold which was pre-heated to either 450 °C or 200 °C.

Of the 30 test bars obtained for each alloy chemistry, half were retained for the study of dissolution kinetics of iron compounds and the other half for

performing tensile tests. For the dissolution studies, samples of approximately 10 mm width were cut from the gage length portion of the test bar. Thus five samples for heat treatment were obtained from each of the bars used for the dissolution studies. Ample specimens were therefore available for heat treatment, and since the gage length portion was used, a subsequent heat treatment could be carried out on the full (not cut) bars retained for mechanical testing with confidence that the microstructure of these bars after heat treatment would be the same as that observed in the small sample used for the dissolution study.

The heat treatment cycle followed was identical to the T6 temper treatment guidelines set by the Aluminum Association (AA standard) [12], except that the solution temperatures and times were varied. The heat treatment conditions were as follows :

- (a) solution treatment at 495 °C - 535 °C in steps of 10 degrees with solution time ranging from one hour to one week
- (b) water quench at 70 °C
- (c) artificial aging at 150 °C for 5 hours
- (d) air cooling.

In order to avoid localized melting and shape distortions, the maximum solution treatment temperature was always restricted to a few degrees (5 °C approx.) below the silicon eutectic temperature. However, as will be discussed in a later chapter the eutectic temperature strongly depends upon the solidification conditions employed. Therefore, thermal analysis was used to evaluate the eutectic temperatures under various cooling conditions. This was achieved by inserting high sensitivity thermocouples at the gage length portion of the Stahl mold and recording cooling curve data for all alloy chemistry/mold temperature conditions.

The dissolution kinetics of the iron intermetallics was computed based on the volume fraction and average length as measured by the LECO 2005 image

analysis. For this average over 50 fields were calculated. In order to differentiate the color contrast (grey level) between the iron intermetallics and other phases present in the structure, certain manual features such as BOOLEAN FUNCTIONS, COPY, FILL AND KILL, available in the image analysis routine were used. Fig. 3.4 shows photographs of a typical sample, before and after the utilization of such features.

The diffusion of elemental iron, manganese and silicon in the iron intermetallics during non-equilibrium heat treatment was studied by X-ray mapping. The dimensional stability of these alloys under non-equilibrium heat treating conditions was investigated by subjecting certain samples to dimensional and density change measurements. In order to facilitate easy and accurate measurements and to prevent a coating of oxide layer at heat treating temperatures, the samples were machined to cylindrical dimensions of 13 mm X 13 mm (dia) and sealed in a quartz tube under argon. On quenching, the quartz tube was crushed under water, as quickly as possible.

### **3.5 : MECHANICAL PROPERTIES :**

The tensile properties were evaluated on the as-cast and heat treated test-bars using a standard Instron testing machine. The three test bars were pulled for each alloying and solution treatment conditions at a stroke rate of 4.2  $\mu\text{m/s}$  and the average value was calculated. Solution temperatures and times were selected based on the results obtained in dissolution studies as described in previous section 3.4. The properties were correlated with dissolution of intermetallics and generation of liquid phases during heat treatment, so that optimum solution conditions could be determined.

For an interpretation of mechanical properties based on the microstructure, the test bars were cut and polished near the fracture surface as shown in Fig. 3.5

and examined with both an optical and scanning electron (JEOL 840) microscope. The fracture surfaces were also viewed under SEM to determine the role of iron intermetallics on the fracture mode.

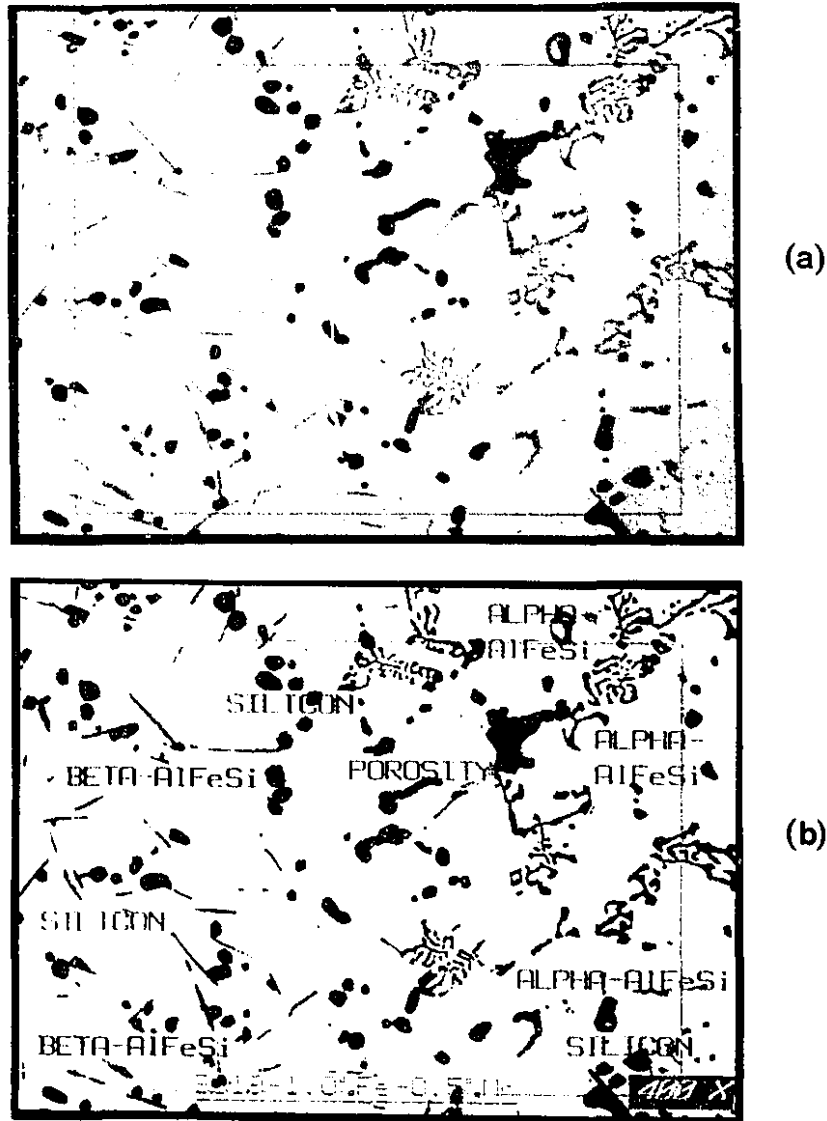


Fig. 3.4 : Photographs of a typical sample, (a) before and (b) after utilizing the special features in image analysis. Several phases are identified by different colors.

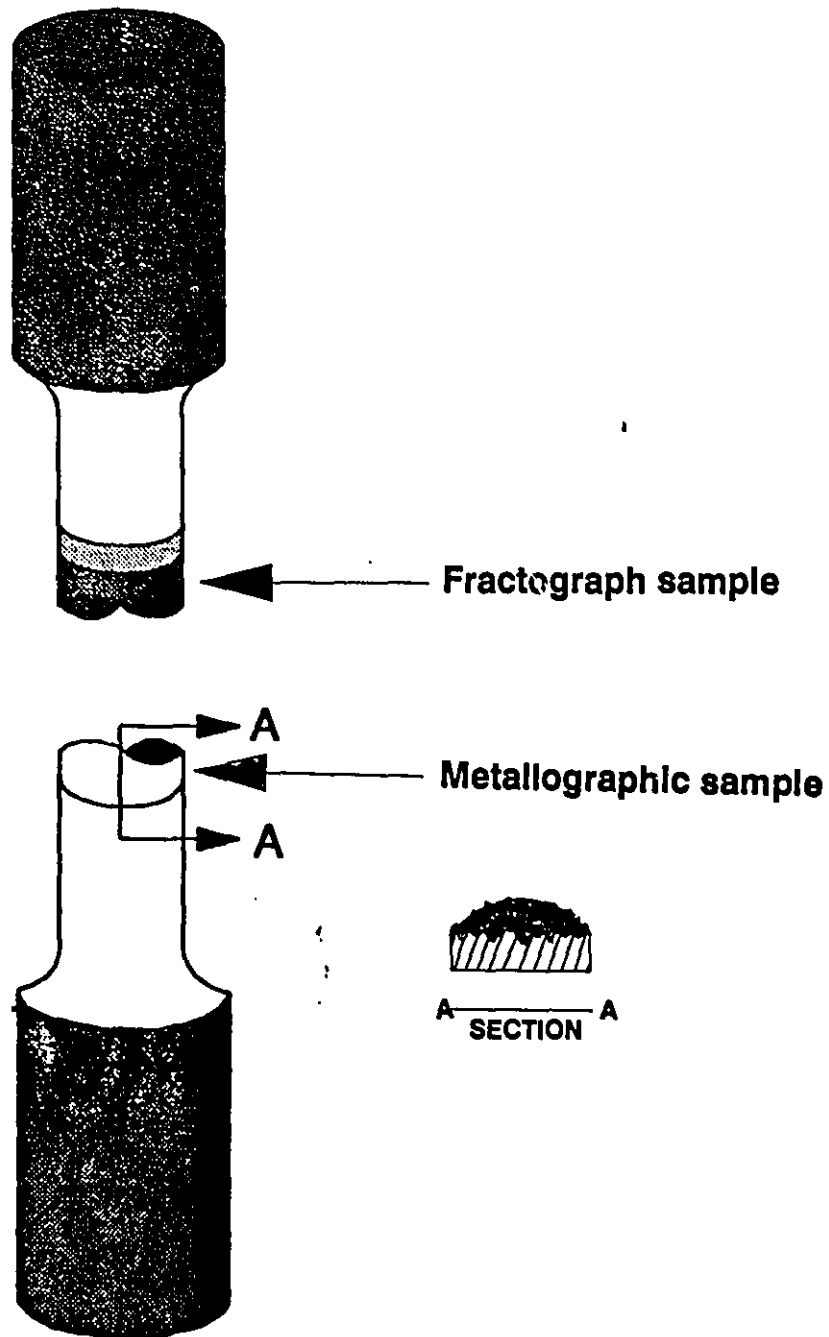


Fig. 3.5 : Schematic of a broken test bar showing the location of samples for fracture and metallographic analysis.

# CHAPTER 4

## MICROSTRUCTURAL STUDIES

### 4.1 : INTRODUCTION :

It is well known that the mechanical properties of any cast alloy depend on the casting quality and the microstructural features. In cast Al-Si alloys, melt treatments such as grain refinement and modification and the cooling conditions should be optimized in order to achieve suitable properties for the application and service conditions desired.

The mechanical properties of 319 aluminum alloy depend greatly on microstructural features such as grain size, cell size, eutectic silicon structure [64], and shape and size of iron intermetallics [26][65]. The three major molten metal processing techniques conventionally adopted in order to achieve the proper microstructure and so to provide the required mechanical and physical properties are grain refinement, modification, and iron neutralization. Although the optimum amounts of grain refiner, eutectic modifier and iron neutralizer to achieve good mechanical properties are reasonably well established for aluminum-silicon alloys, the effectiveness of these melt additions as a function of iron content are not well known. Moreover, in the literature, these melt additions are usually specified for sand casting conditions. Therefore, it is of interest to study the effect of iron on the various molten metal processing techniques such as grain refinement, modification and iron neutralization as a function of cooling rate.

In the present work, the effect of increased iron content from 0.15 % to 1.0 % on the grain size, cell size, eutectic silicon structure and morphology of iron intermetallics was studied as a function of cooling rate by means of thermal analysis and metallography. Also studied were the influence of grain refiner and eutectic modifier on these microstructural features as was the influence of

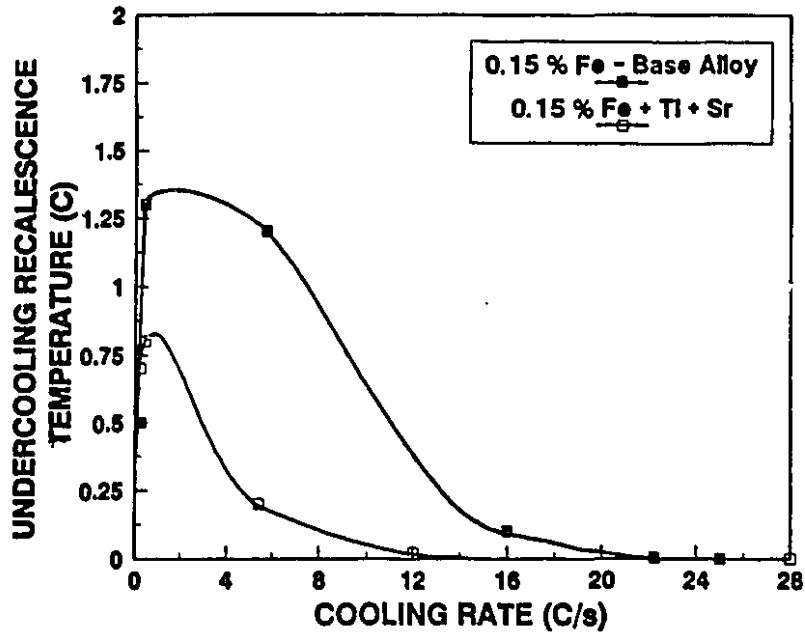
manganese on the crystallization of iron intermetallics.

#### 4.2 : GRAIN SIZE :

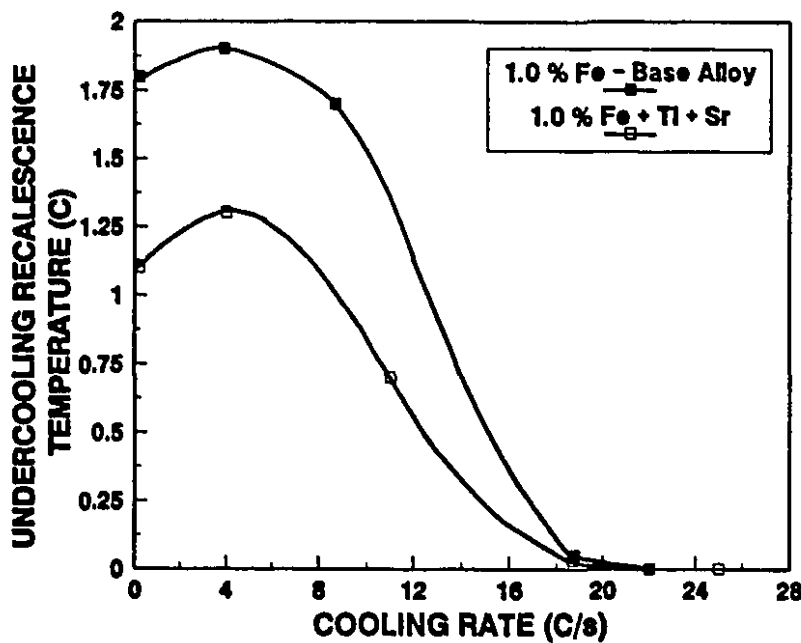
The addition of iron from 0.15 % to 1.0 % decreases the liquidus temperature by about 3-4 °C. However, the liquidus temperature does not show any variation with cooling rate. The values of undercooling recalescence temperature and undercooling arrest time ( $t_3$ ) versus cooling rate are plotted in Figs. 4.1-4.2. As expected, for the addition of 0.07 % Ti, the curve falls below that of the non-grain refined alloy. The shape of the curve agrees very well with plots drawn as a function of grain refiner [66].

The grain size variation with cooling rate exhibits an exponential relationship suggesting that only marginal grain refinement takes place at higher cooling rate. However, in logarithmic scale, the plot of grain size versus cooling rate (Fig. 4.3) shows a linear dependence for all the alloys considered. The standard deviation of grain size measurements varies from sample to sample depending on its grain size. Highest deviation of  $\pm 12$  % for fine grains (200  $\mu\text{m}$  approx.) and lowest deviation of  $\pm 4$  % for coarse grains (3000  $\mu\text{m}$  approx.) is observed. An interesting phenomenon observed with the addition of iron is that it coarsens the grain size at all cooling rates, but the effect is more pronounced at low rates. For the same level of grain refiner addition, 1.0 % Fe alloys show very little grain refinement as compared to 0.15 % Fe alloys, but, in general, grain refiner efficiency improves with cooling rate for both contents of iron. In Fig. 4.4, the micrographs of grain structure are shown for both 0.15 and 1.0 % Fe alloy for the same cooling condition. Similar observations have been quoted in the Japanese literature [67] for Al-Si-Mg-Zn alloys.

To study the effect of increased addition of Ti on the grain refinement behaviour of 0.15 and 1.0 % Fe alloys, 0.15 and 0.30 % Ti were tried and the

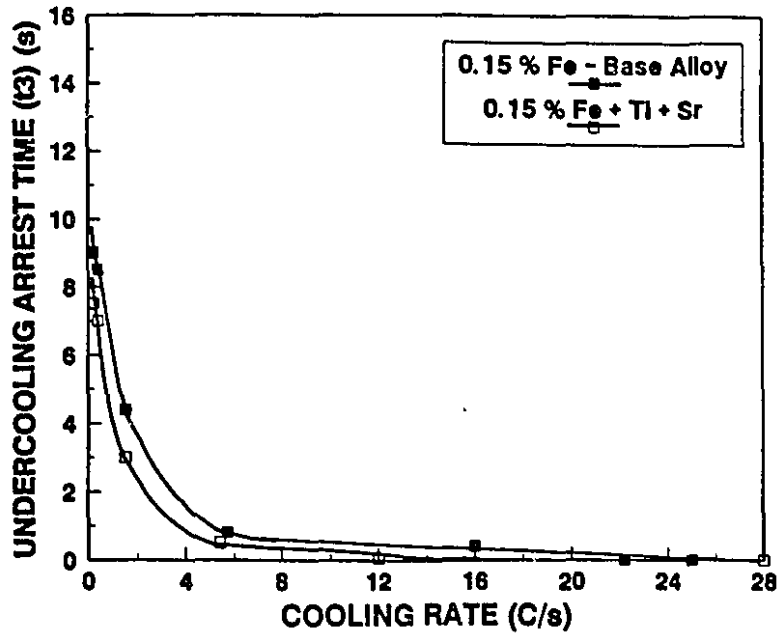


(a)

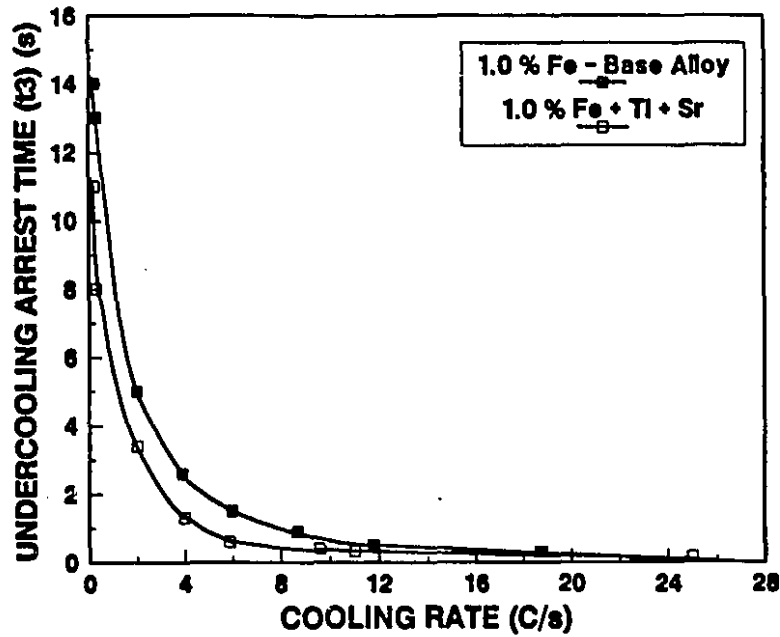


(b)

Fig. 4.1 : Effect of cooling rate on the liquidus undercooling recalescence temperature,  $\Delta T_{UR}$ , for (a) 0.15 % and (b) 1.0 % iron alloys.



(a)



(b)

Fig. 4.2 : Effect of cooling rate on the liquidus undercooling arrest time,  $t_3$ , for (a) 0.15 % and (b) 1.0 % iron alloy.

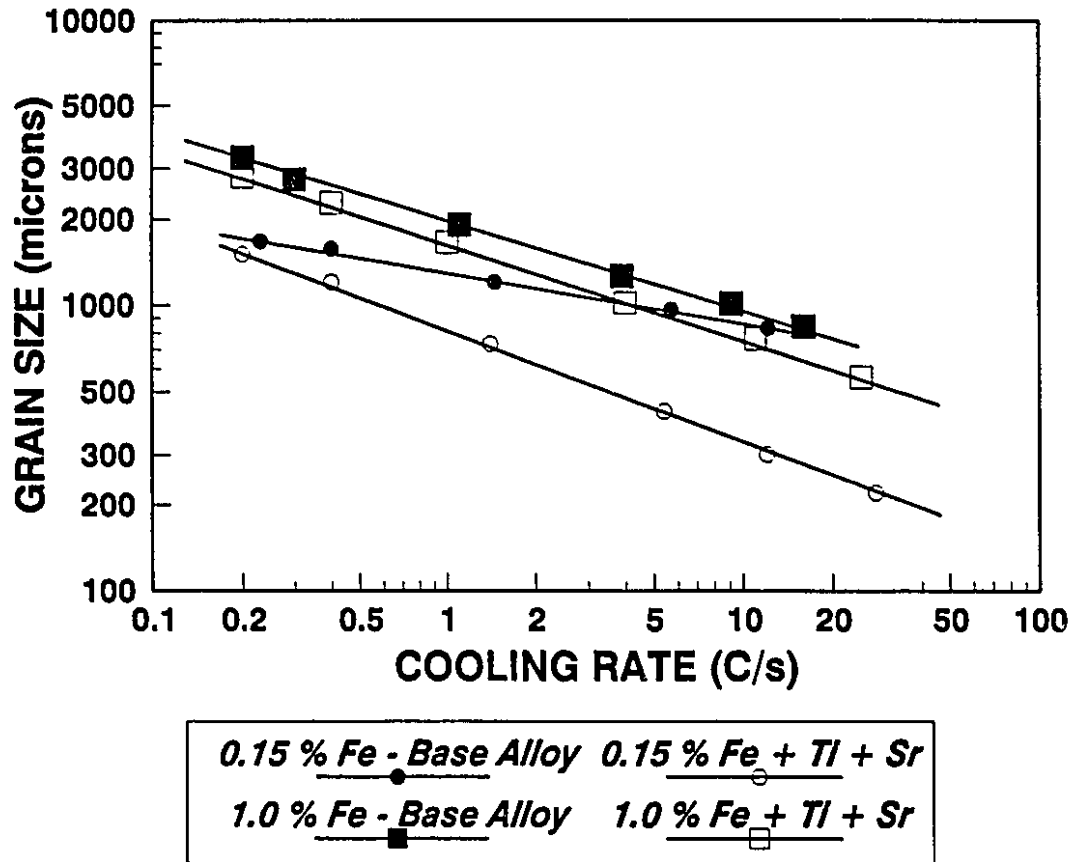


Fig. 4.3 : Plot of grain size versus cooling rate.

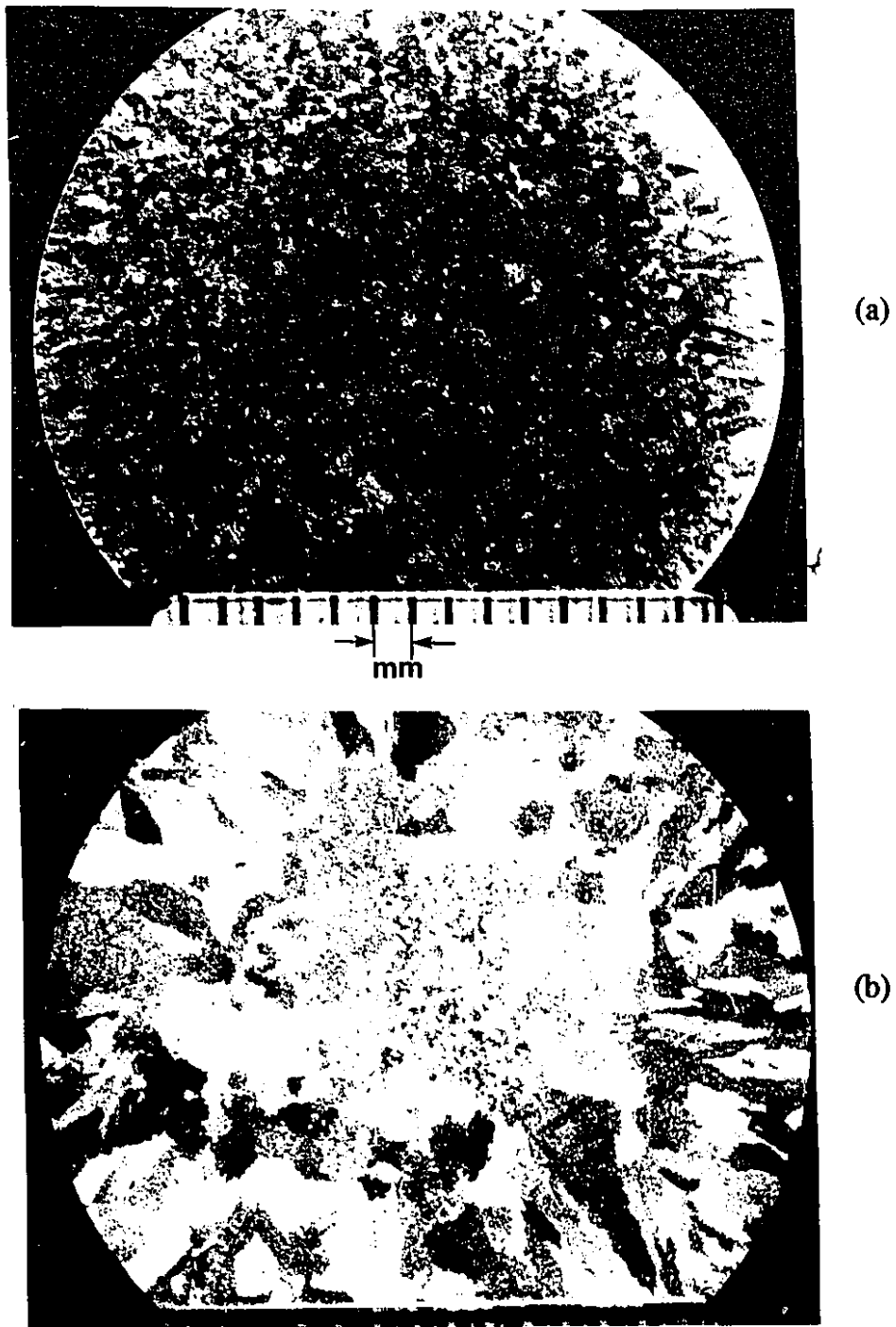


Fig. 4.4 : Micrographs showing grain size for (a) 0.15 % and (b) 1.0 % iron alloy for the same cooling rate ( $9\text{ }^{\circ}\text{C/s}$ ).

results are plotted in Fig. 4.5. The curves are in good agreement with reported results on Al-Si alloys [11]. It can be seen from Fig. 4.5 that, for a given cooling rate, 1.0 % Fe alloy requires more Ti to achieve the same grain size as 0.15 % Fe alloy. The possible reason for this grain coarsening may be due to decreased nucleation potential and/or growth enhancement on addition of iron. This is evident in Figs. 4.1-4.2 where it is seen that the undercooling temperature and arrest time increase with iron content. Typical cooling curves in the liquidus region for 0.15 and 1.0 % Fe alloys are also shown in Fig. 4.6 for comparison.

### 4.3 : DENDRITE ARM SPACING :

Both the grain size and DAS are dependent on the cooling rate, but the grain size can be refined independently by the addition of grain refiners. The effect of cooling rate (C.R) on the dendrite arm spacing is shown in Fig. 4.7. This is in general agreement with the relationship :

$$\text{DAS} = A (M \times \text{C.R}^{-m})$$

where A = constant ; M = coarsening parameter ; m = exponent.

The addition of iron decreases DAS, and this is more pronounced at the low cooling rates. The observed standard deviation with DAS measurements was found to vary between 5-7 %. As can be seen from Fig. 4.7, the addition of iron to the alloy does not affect the slope of the line. The calculated value of m is 0.312, which is in general agreement with results reported (m = 0.3) for other Al-Si alloys [68].

The reason for the higher value of DAS in alloys containing 0.15 % iron is due to the coarsening of dendrites at the silicon eutectic temperature. With the increase in iron content and decrease in cooling rate, the size and volume fraction of AlFeSi needles increases. Since these needles form at a higher temperature, i.e., above the silicon eutectic temperature, they act as nucleation sites for silicon

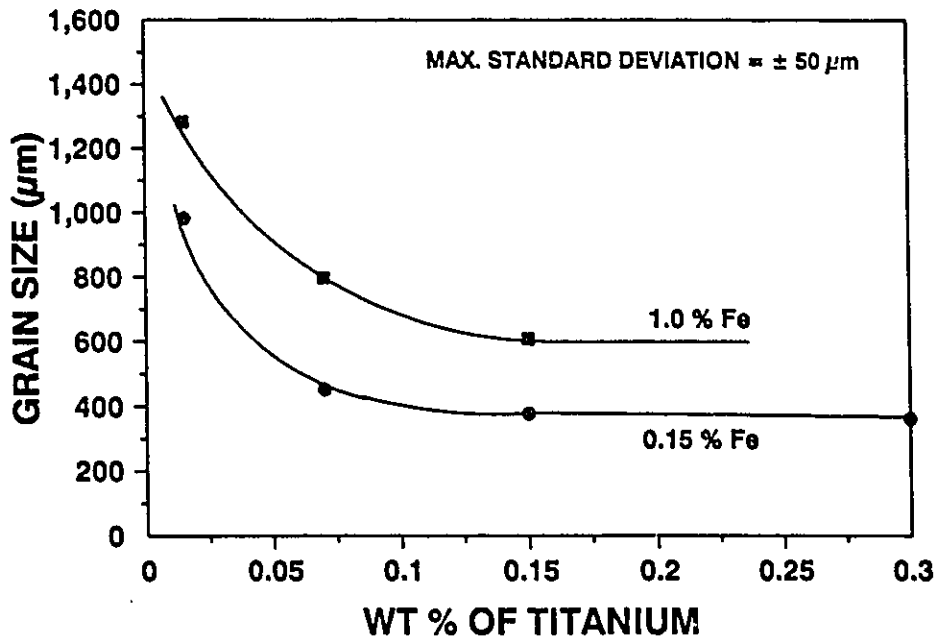


Fig. 4.5 : Effect of Ti on the grain size.

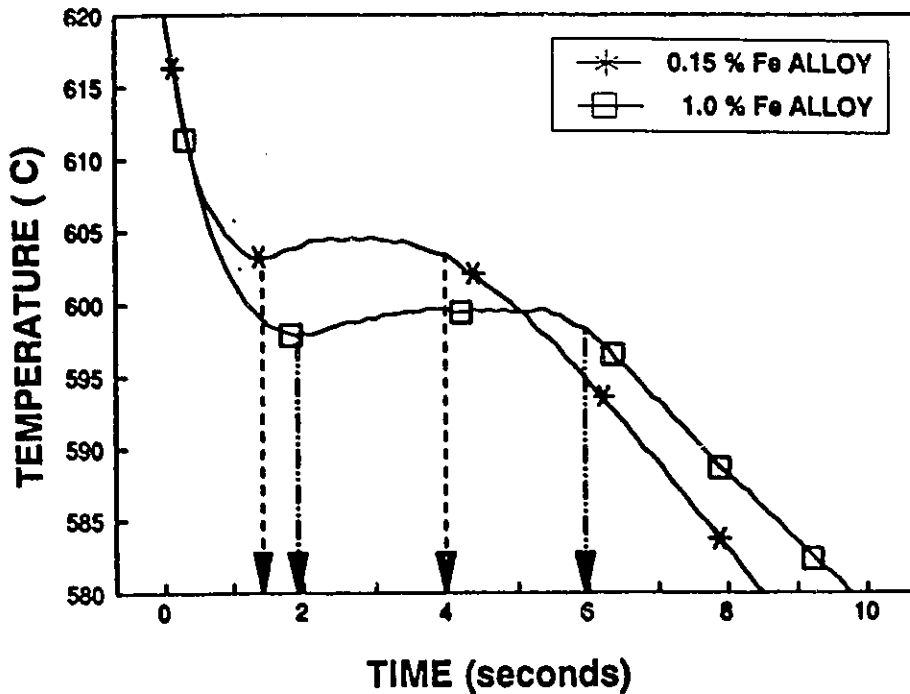


Fig. 4.6 : Thermal analysis curve in the liquidus region for the 0.15 and 1.0 % iron alloy at the same cooling rate (5 °C/s).

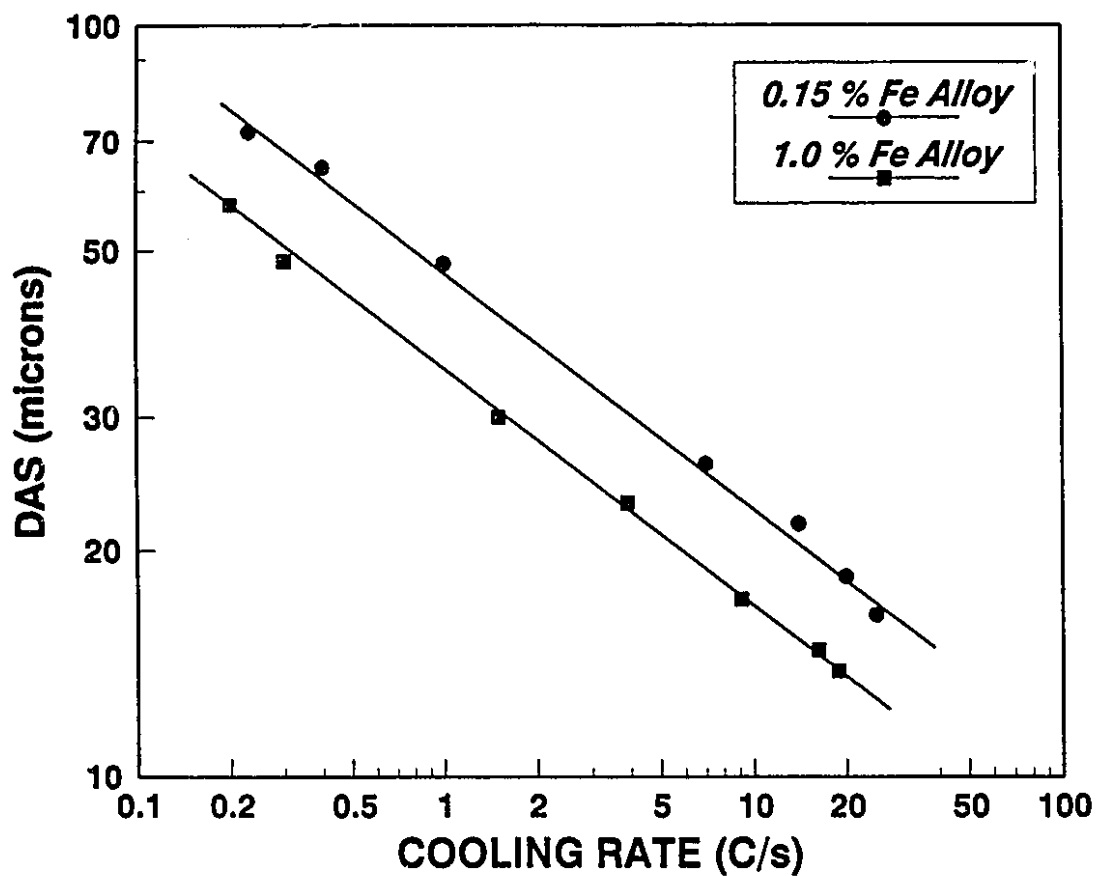


Fig. 4.7 : Plot of DAS versus cooling rate.

growth. This is clearly shown in Fig. 4.8, where the silicon crystals are seen to nucleate on the AlFeSi needles and grow as bulky crystals. Thus in 1.0 % iron alloys, less time is needed for the completion of the silicon eutectic reaction and isothermal dendrite arm coarsening is limited in these alloys. In the case of 0.15 % iron alloys a longer silicon eutectic time is needed due to low volume percent of AlFeSi needle-like phase and thus dendrites coarsen isothermally. This effect is evident on the thermal analysis curve, Fig. 4.9, which shows the eutectic arrest time for the two iron alloys at the same cooling conditions.

The fundamental mechanism which operates in the formation of a dendrite structure is one of "coarsening" which occurs steadily throughout solidification. Dendrite arm spacing is also influenced by the concentration of alloying elements, dendrite growth velocity, temperature gradient [69], and isothermal coarsening temperature [70] all of which have an additional influence on the coarsening process. In order to study the influence of iron intermetallics on dendrite coarsening both 0.15 and 1.0 % Fe samples were quenched just before and after the silicon eutectic reaction.

The samples quenched just before and after the silicon eutectic reaction corresponding to 1.0 % iron alloy show the same DAS for both the iron contents (0.15 % and 1.0 % Fe) of alloy, while samples air cooled to room temperature show a difference in DAS between the 0.15 and the 1.0 % iron alloys. Photomicrographs of samples quenched at different solidification intervals as indicated in Fig. 4.9, are presented in Fig. 4.10. These clearly show that dendrite refinement on addition of iron is due to isothermal dendrite coarsening at the silicon eutectic temperature and not due to nucleation or undercooling phenomena.

#### **4.4 : EUTECTIC SILICON STRUCTURE :**

The variables that determine the microstructure of eutectic silicon particles

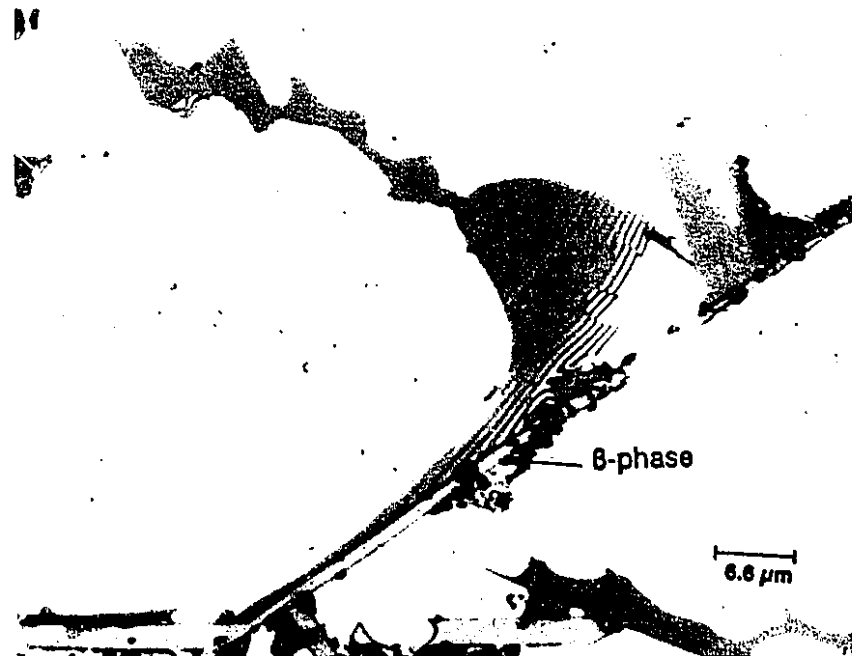


Fig. 4.8 : Micrograph showing nucleation and growth of silicon crystals on the  $\text{AlFeSi}$  needles (Cooling rate =  $0.3 \text{ }^\circ\text{C/s}$  ; Mag = 1500 X).

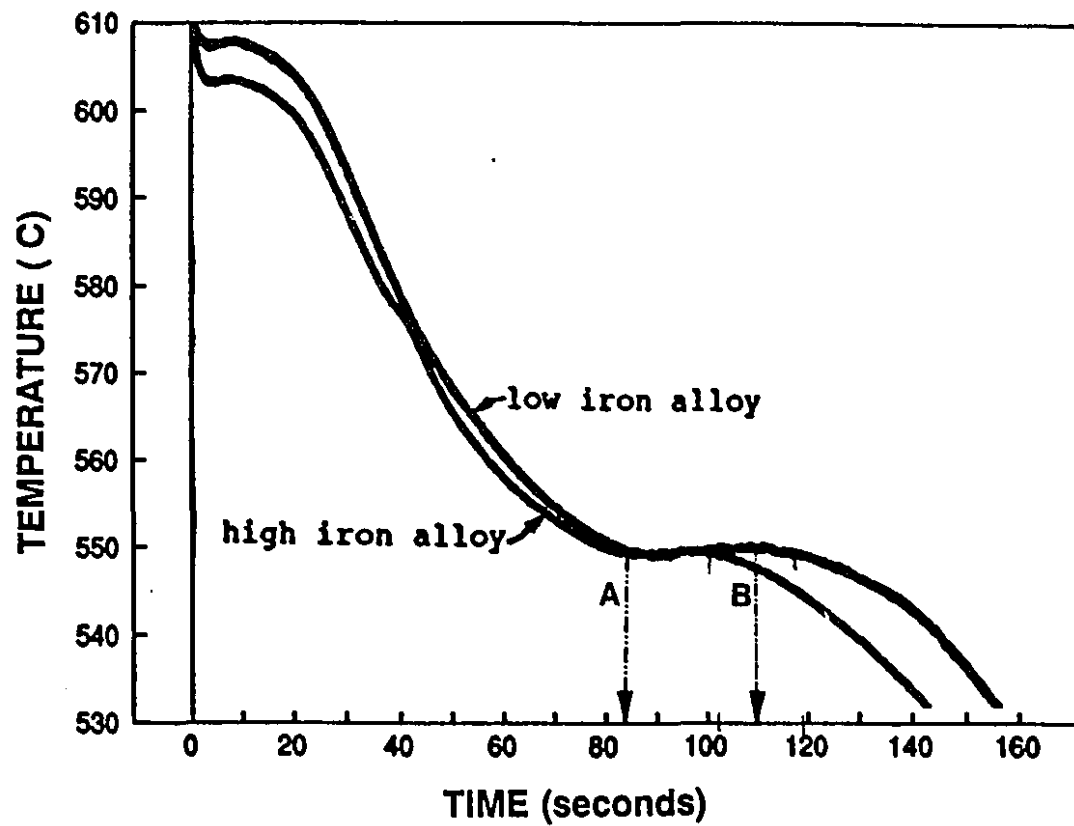
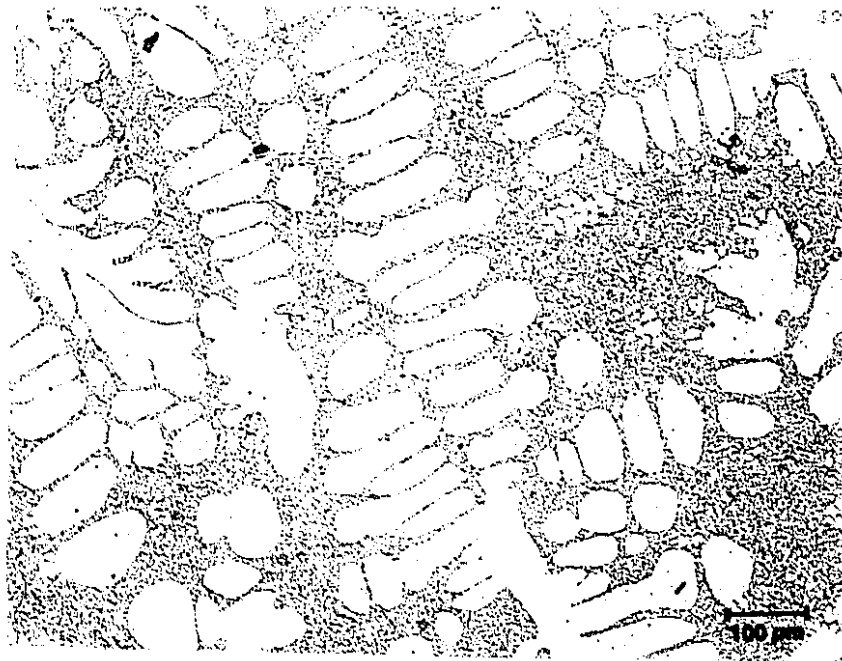
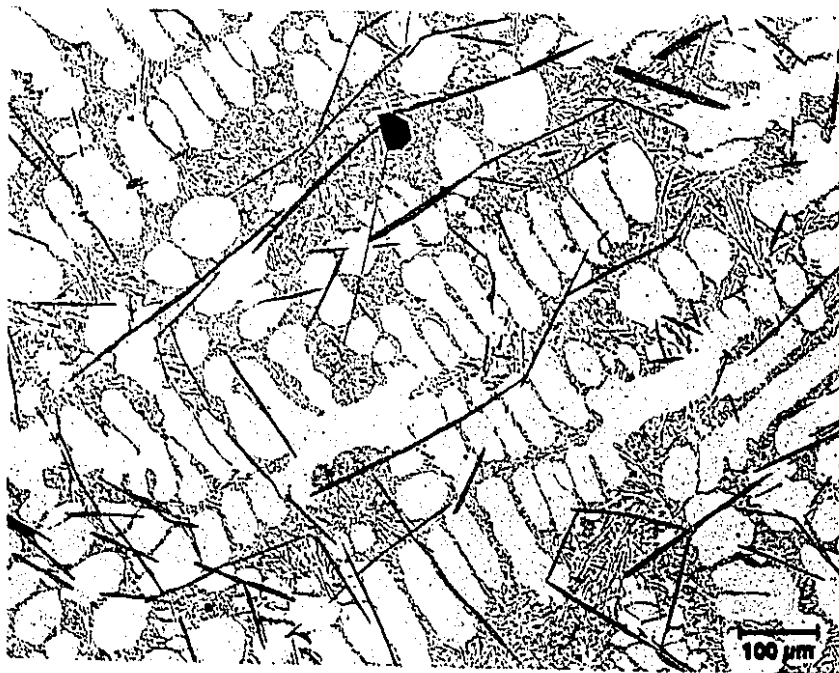


Fig. 4.9 : Thermal analysis curve showing eutectic region for the 0.15 and 1.0 % iron alloy at same cooling rate (1.2 °C/s).



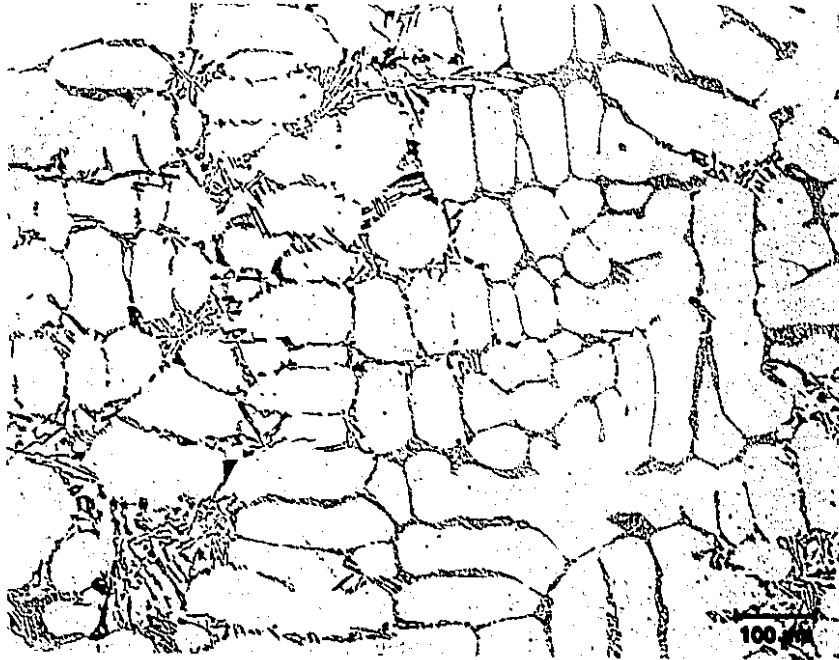
(a) 0.15 % iron alloy ; DAS = 37  $\mu\text{m}$ .



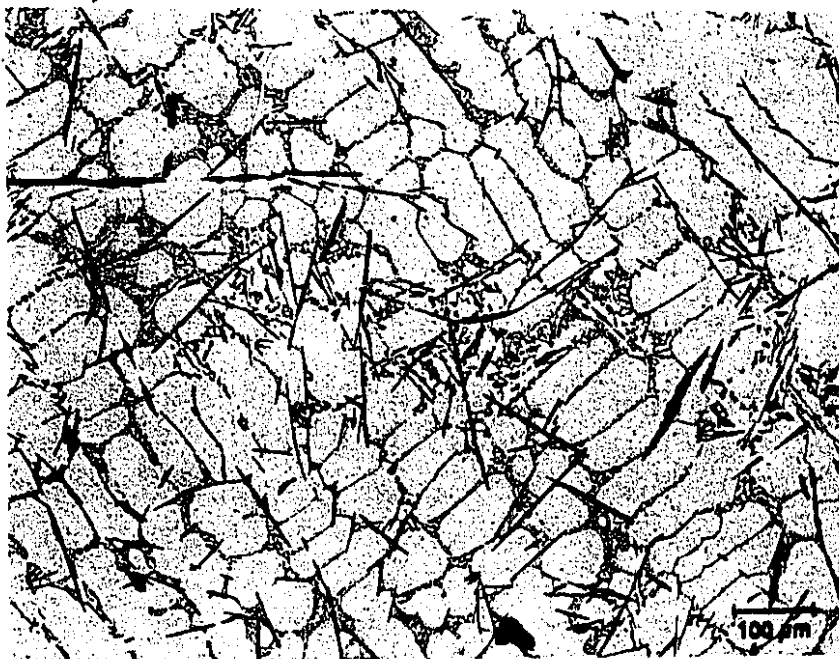
(b) 1.0 % iron alloy ; DAS = 35  $\mu\text{m}$ .

(i) Quenched at point A in Fig. 4.9.

Fig. 4.10 : Photomicrographs of samples quenched at (i) point A (beginning of eutectic), (ii) point B (end of eutectic in 1.0 % iron alloy) as indicated in Fig. 4.9, and (iii) air cooled.

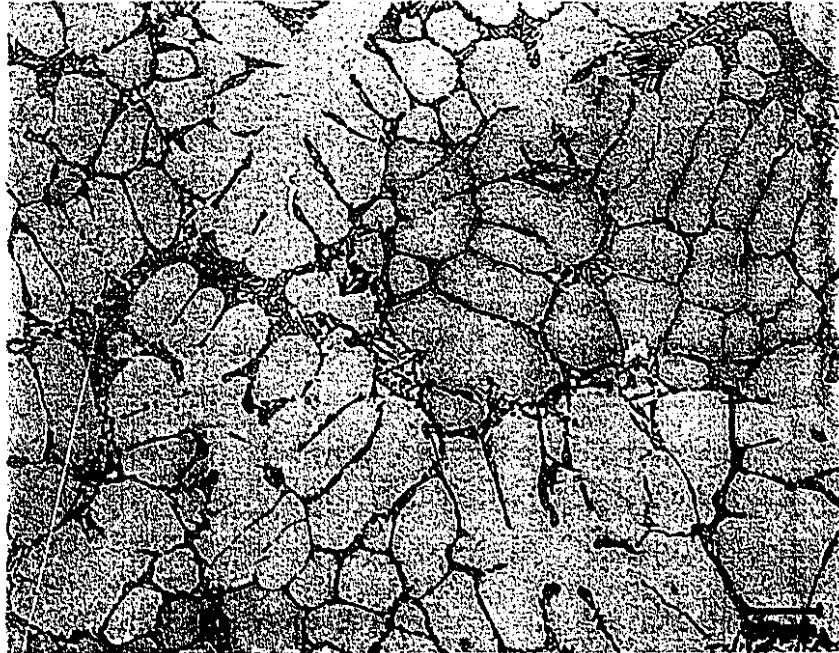


(a) 0.15 % iron alloy ; DAS = 52  $\mu\text{m}$ .

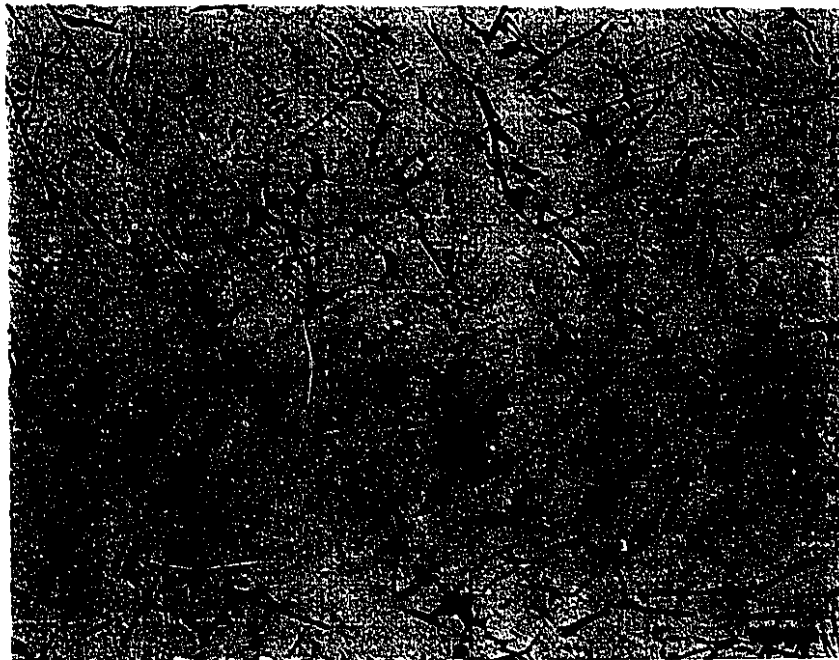


(b) 1.0 % iron alloy ; DAS = 48  $\mu\text{m}$ .

(ii) Quenched at point B in Fig. 4.9.



(a) 0.15 % iron alloy ; DAS = 61  $\mu\text{m}$ .



(b) 1.0 % iron alloy ; DAS = 49  $\mu\text{m}$ .

(iii) Air cooled to room temperature.

[71][72] are : (i) type of modifier used, (ii) amount of modifier used, (iii) impurities such as phosphorous present in the melt, (iv) silicon content of the alloy, and (v) freezing rate. These five variables interact in a highly complex manner.

Of the above mentioned five variables, studies on the effect of impurities on the microstructure of silicon particles require special attention. It is well known that phosphorus in the melt combines with aluminum to form AlP [71], which is a strong nucleant for the crystallization of silicon. Although AlP acts as a primary nucleant for the crystallization of silicon particles, the role of secondary nuclei such as intermetallic compounds which form prior to the silicon eutectic or oxide inclusions, may be important especially when present in a high volume percent. In the present work, the influence of iron intermetallics on the microstructure of eutectic silicon particles was studied. For quantification purposes, the silicon morphology rating procedure suggested by Apelian et al [73] was adopted.

In Fig. 4.11, the rating level is plotted against cooling rate for both Sr containing and Sr-free alloys, and the effect of iron from 0.15 to 1.0 % is presented. Since this rating procedure [73] involves judgement by eye, a significant error is involved in these measurements. A maximum error committed in these calculations is estimated to be  $\pm 0.1$ . At higher cooling rates ( $> 20$  °C/s), silicon is fine due to the chilling effect, and the rating is greater than 4 irrespective of the iron content. In the unmodified alloy, ie., without any Sr addition, the silicon structure remains partially modified/unmodified at cooling rates below 15 °C/s and 20 °C/s for the 0.15 % and 1.0 % iron alloys, respectively. Silicon modification improves however especially at low cooling rates with the addition of 0.026 % Sr.

Quench modification is evident from the plot of eutectic nucleation temperature versus cooling rate, as shown in Fig. 4.12. For the change in cooling rate from 0.2 °C/s to 25 °C/s, the eutectic nucleation temperature drops by more

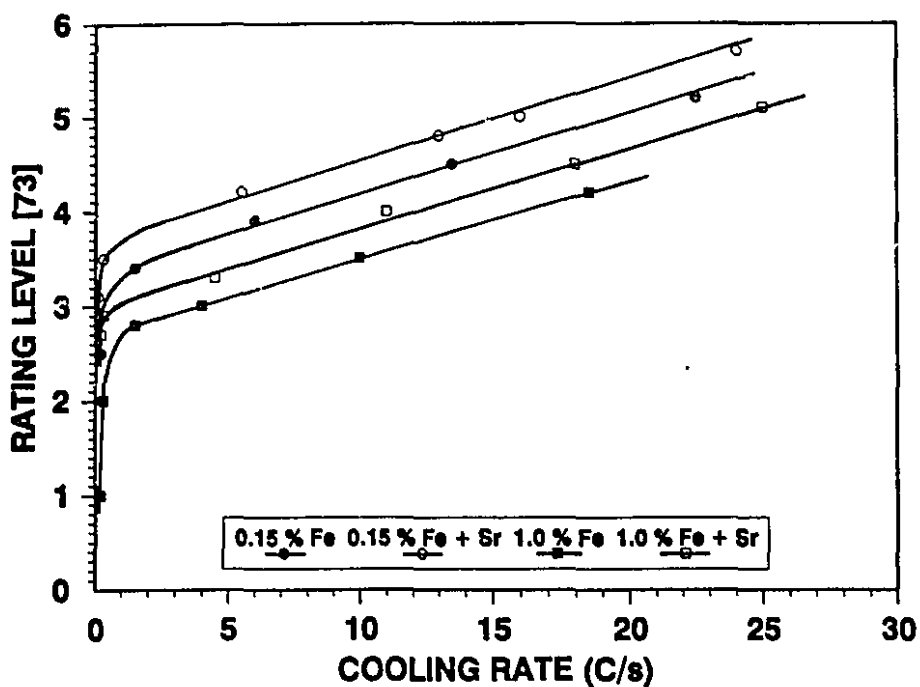


Fig. 4.11 : Effect of cooling rate on the silicon morphology.

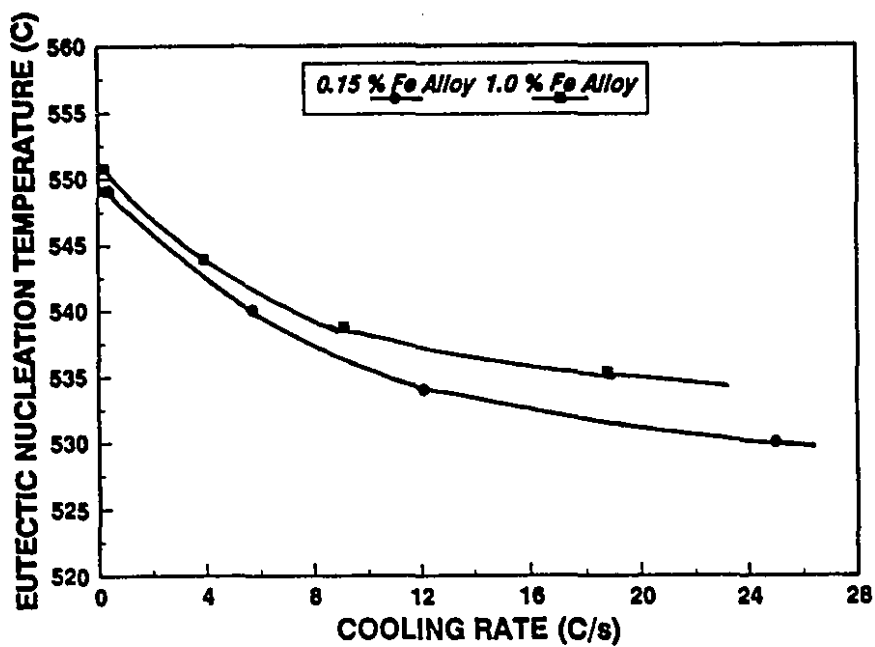


Fig. 4.12 : Effect of cooling rate on the eutectic nucleation temperature.

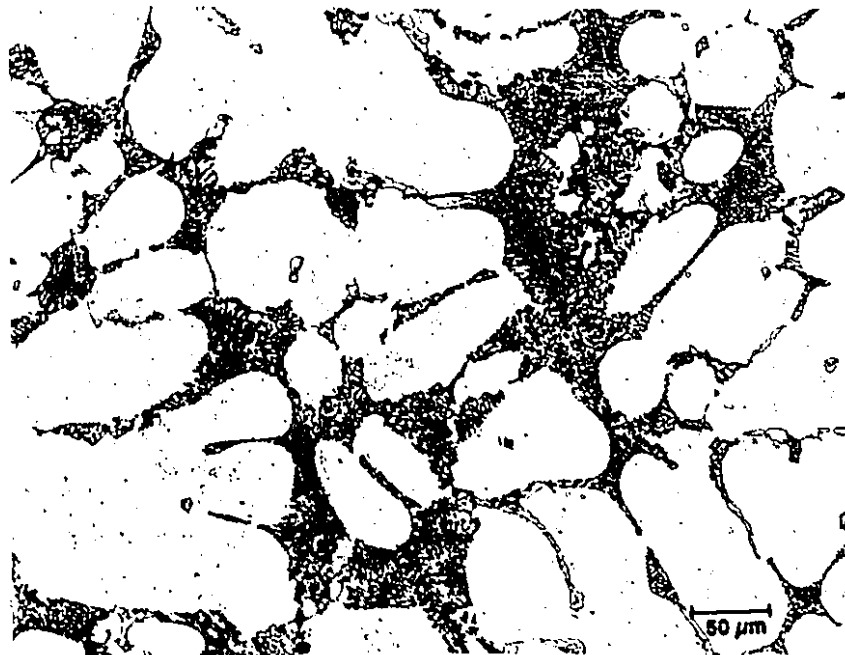
than 20 °C and 15 °C for the 0.15 and 1.0 % iron alloys, respectively. Although this drop in eutectic nucleation temperature with increase in cooling rate is not reported in the literature, several published studies [74] indicate that, the chemical modification process decreases the eutectic nucleation temperature by approximately 10 °C. This suggests that, modification in general is associated with a decrease in eutectic nucleation temperature irrespective of the type of process used, and this parameter can be used as a tool to assess the degree of modification.

From Fig. 4.11, it can be observed that the addition of iron affects eutectic silicon structure, and the effect is more pronounced at cooling rates below 0.3 °C/s. The reason for this is due to the nucleation and growth of silicon crystals on the AlFeSi needles (see Fig. 4.8). At low cooling rates silicon crystals nucleate and grow on secondary nucleation sites such as iron intermetallics. The length and volume fraction of AlFeSi needles also increase with decrease in cooling rate. Therefore, at low cooling rates, these needles offer a large number of nucleation sites for silicon crystals to grow. This is clearly shown in the micrographs, Fig. 4.13, for both 0.15 and 1.0 % iron alloy at the extreme cooling rates of 20 and 0.2 °C/s. Even with the addition of 0.026 % Sr, which is supposedly high enough for complete modification of Al-Si alloys, there exists a strong tendency for the silicon crystals to nucleate and grow on the AlFeSi needles. Thus, for the same cooling conditions, a higher level of iron in the alloy requires more modifier compared to lower iron concentrations for good modified silicon structure.

## **4.5 : IRON INTERMETALLICS :**

### **4.5.1 : EFFECT OF COOLING RATE :**

In the absence of Mn, the iron intermetallics crystallize primarily as AlFeSi



0.15 % iron alloy



1.0 % iron alloy

(a) 20 °C/s

Fig. 4.13 : Micrographs of silicon structure for 0.15 % iron and 1.0 % iron alloys at cooling rates of (a) 20 °C/s and (b) 0.2 °C/s.



0.15 % iron alloy



1.0 % iron alloy

(b) 0.2 °C/s

compounds in the needle-like form, called  $\beta$ -phase as shown in Fig. 2.3. The length of the  $\beta$ -phase needles increases with increase in iron content and decrease in cooling rate. Thermal analysis shows a small arrest corresponding to the crystallization of primary  $\beta$ -phase needles, between the liquidus and the silicon eutectic temperature. The temperature of crystallization of the  $\beta$ -phase can be very accurately determined by means of differentiated thermal analysis, as shown in Figs. 4.14 and 4.15. Unless the AlFeSi needles crystallize in primary form (large needles), their formation cannot be detected by thermal analysis as shown in Fig. 4.14 due to insufficient latent heat evolution to cause a marked change on the cooling curves. Note that in Figs. 4.14 and 4.15, the dotted line corresponds to the "zero" of the first derivative.

#### **4.5.2 : HARDNESS :**

As expected, hardness increases with cooling rate for 0.15 and 1.0 % iron alloys and shows a linear variation as seen in Fig. 4.16. For an increase in iron content from 0.15 to 1.0 %, hardness increases approximately by 10 and 20 HB at cooling rates of 0.2 and 20 °C/s respectively. The present results are in general agreement with the results of Carbajal et al [75], who have obtained a relationship between hardness and DAS for a 0.6 % Fe alloy. This increase in hardness is due to the formation of the hard and brittle  $\beta$ -phase, whose microhardness value is reported to be 580 HV [76].

#### **4.5.3 : FLUIDITY :**

The effect of melt temperature on fluidity of both 0.15 and 1.0 % iron alloys was studied using a Ragone vacuum fluidity tester and is shown in Fig. 4.17. Although, as expected, fluidity of the melt increases with melt temperature, it does not show any appreciable difference between 0.15 and 1.0 % Fe alloys.

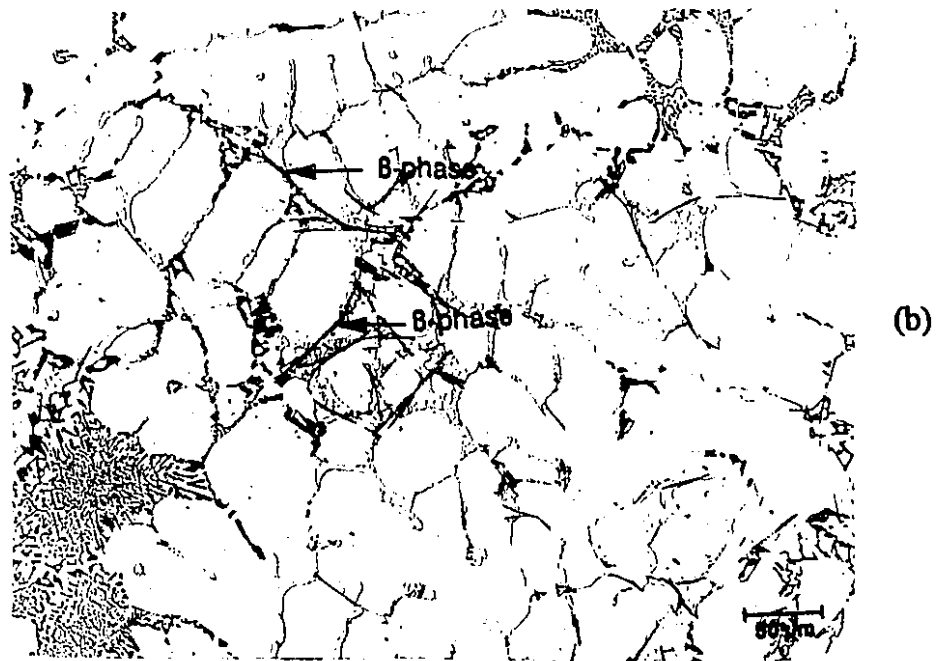
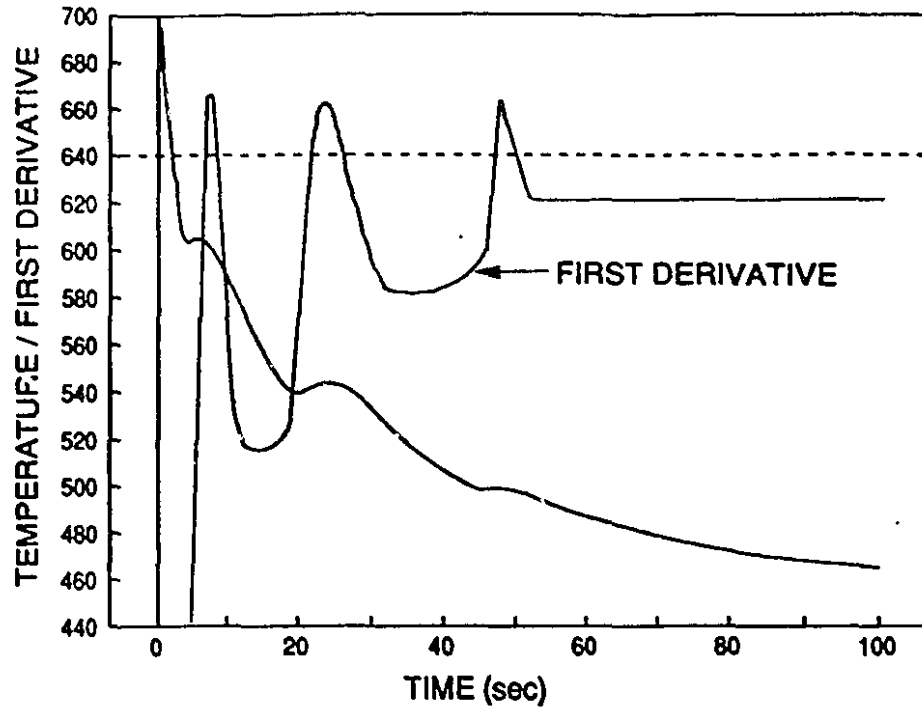


Fig. 4.14 : Thermal analysis and differentiated thermal analysis curves of 0.15 % iron alloy ; (b) micrograph. (Cooling rate = 5 °C/s).

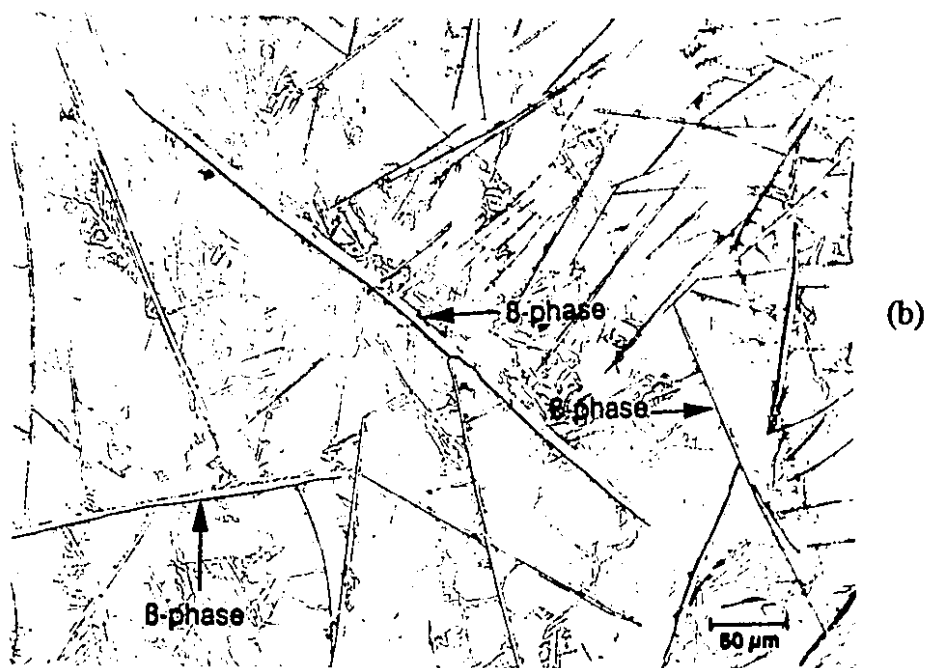
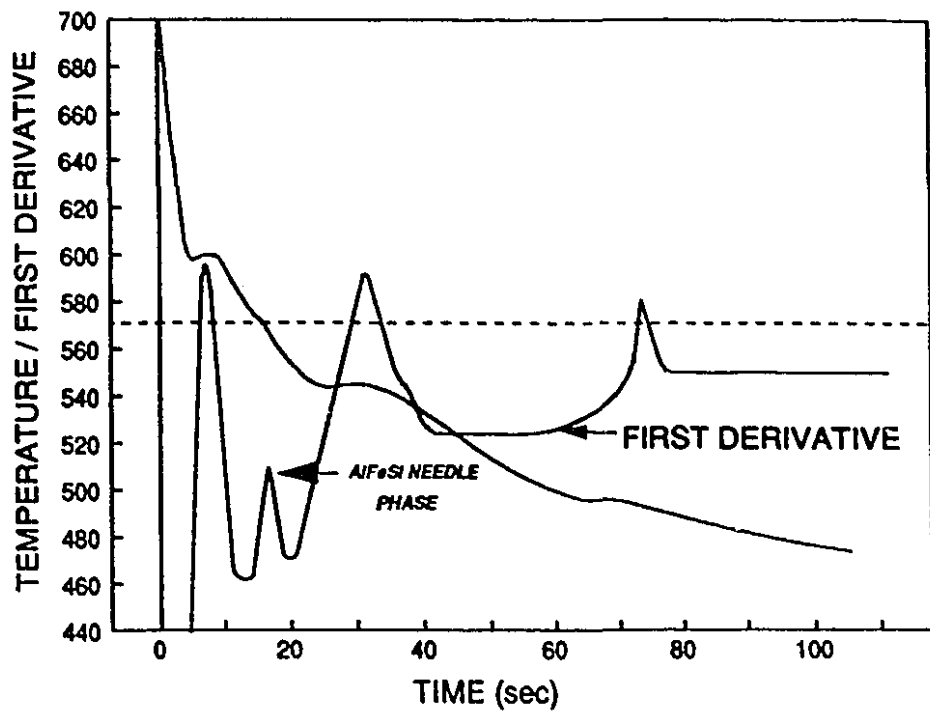


Fig. 4.15 : Thermal analysis and differentiated thermal analysis curves of 1.0 % iron alloy ; (b) micrograph. (Cooling rate = 5 °C/s).

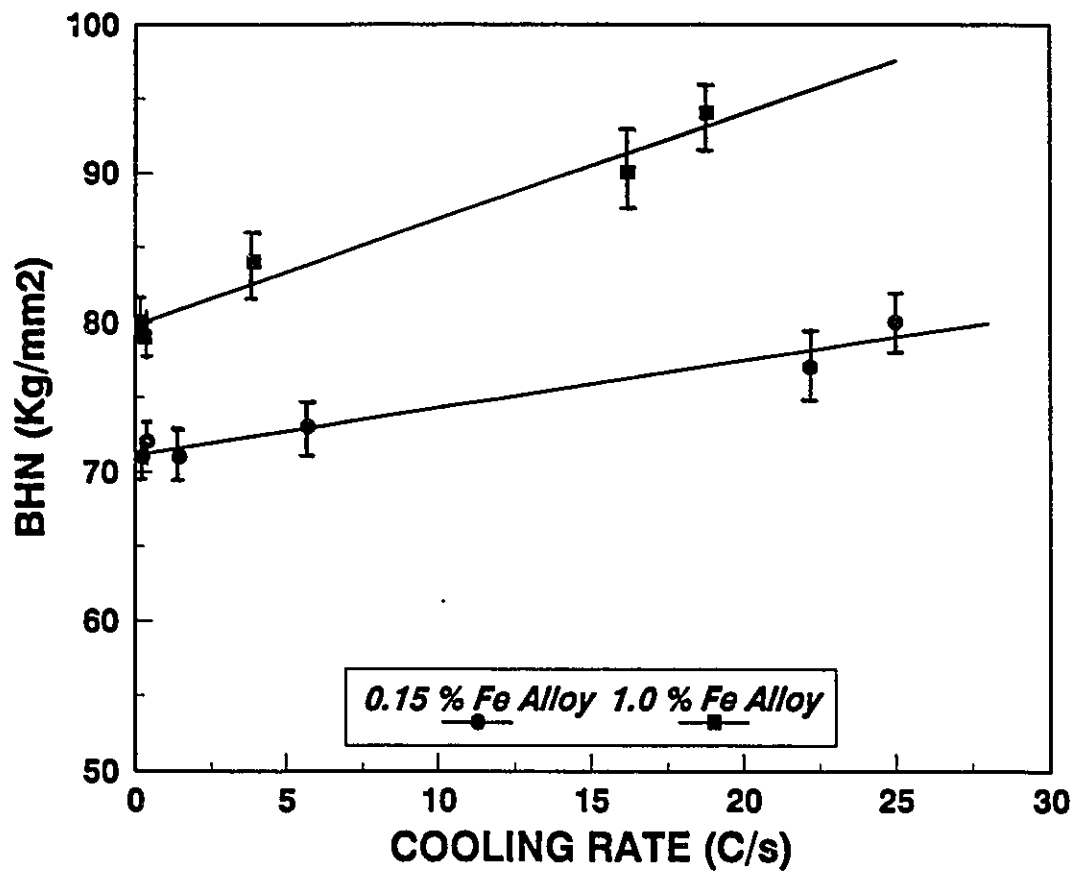


Fig. 4.16 : Plot of hardness versus cooling rate.

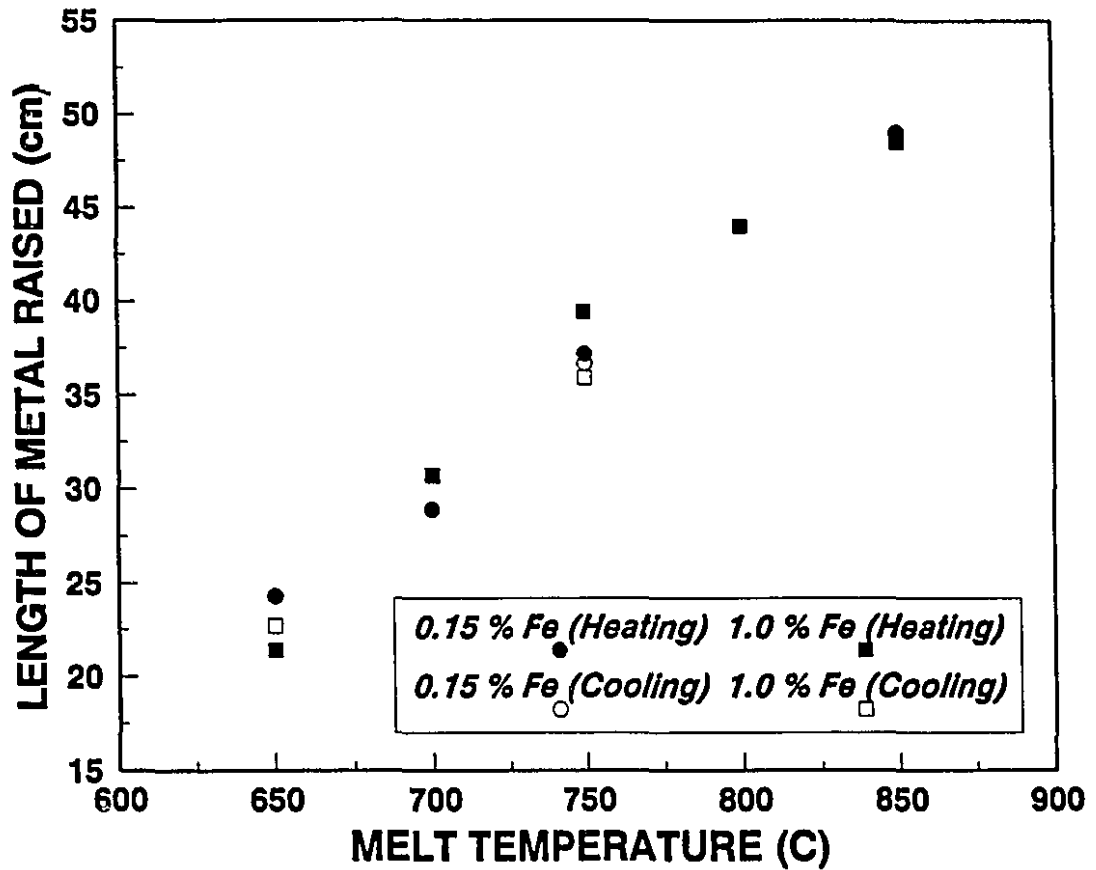


Fig. 4.17 : Effect of melt temperature and iron content on the fluidity.

Due to manual operation of this tester, 2-4 cm error is observed in the length measurements for any single experiments. However, Grand [36] mentions that slow cooling increases the size of the Al-Fe-Si particles and such particles may develop to the point where they will reduce feeding and thus soundness of the casting. Iwahori et al [30], in their work on AC2B aluminum alloy (Al-7Si-3Cu) report that the high iron alloys are uncomensatory for shrinkage in the early stage of solidification because crystallization of primary  $\beta$ -phase needles partly blocks the feeding of the liquid metal. The reason for the discrepancy between these reports and the results of the present study may be related to the inadequacies involved in measuring feedability using fluidity testing. Moreover, fluidity values can vary, greatly from one testing method to another, depending on the cooling conditions involved. For example, in the sand mold - spiral ring fluidity tester, due to the low cooling rates found in this type of mold, iron intermetallics may grow to large needles and affect feedability and thus fluidity of the melt. In the case of the Ragone vacuum fluidity tester, the high cooling conditions which exist due to solidification in a thin pyrex tube, cause iron intermetallics to crystallize as fine needles which have a minimal effect on fluidity.

#### **4.5.4 : POROSITY :**

No quantitative measurements of porosity were made during this study ; however, it was observed that the  $\beta$ -phase needles appear to be active nucleation sites for pores. This is shown in Fig. 4.18 where the relation between the needles and the pores is very clear.

#### **4.5.5 : MANGANESE :**

With the addition of 0.5 % Mn, the iron intermetallics crystallize in the Chinese script morphology, called  $\alpha$ -phase, rather than the needle-like  $\beta$ -form.



Fig. 4.18 : Nucleation of micro-pores on the  $\beta$ -AlFeSi platelets.

This particular morphology can be seen in Fig. 2.2. The size and arm length (distance between any two dendrite-like plates), increases with decreasing cooling rate. The cooling curve does not show any arrest corresponding to the crystallization of the  $\alpha$ -phase iron intermetallics. Several published reports on 319 and similar alloys [77] have also failed to detect this phase by cooling curves.

The  $\alpha$ -phase is reported [76] to be harder and more brittle than the  $\beta$ -phase, whose microhardness is 580 HV as against 700 HV for the  $\alpha$ -phase. However, owing to the complex morphology of the  $\alpha$ -phase, it is considered more crack-propagation resistant than the  $\beta$ -phase. It is also worth noting that microporosity was never observed to be associated with the Chinese script  $\alpha$ -phase. This behaviour is distinctly different from that found with  $\beta$ -phase as shown in Fig. 4.18.

#### 4.6 : SUMMARY :

The effect of cooling rate on the microstructural features of grain size, DAS, eutectic silicon structure and iron intermetallics were studied and compared with thermal analysis characteristic parameters. The effect of the addition of iron, grain refiner and modifier on the microstructural features and thermal analysis parameters were also investigated. The results are summarized as follows :

(i) The addition of iron coarsens the grain size, and this effect is more pronounced at low cooling rates. Possible reasons for this grain coarsening are decreased nucleation potential and/or growth enhancement on addition of iron.

(ii) The addition of iron decreases DAS due to the action of the primary  $\beta$ -AlFeSi platelets acting as nucleation sites for silicon growth, and thus minimizing the isothermal dendrite arm coarsening at the eutectic temperature.

(iii) Iron also affects eutectic silicon particle size both in modified and

unmodified alloys, but to a lesser extent in the former. This phenomenon is attributed to the nucleation and growth of silicon crystals on the  $\beta$ -AlFeSi platelets.

(iv) The volume fraction and size of the iron intermetallics increases with increase in iron content and decrease in cooling rate.

# CHAPTER 5

## CRYSTALLIZATION BEHAVIOUR OF IRON INTERMETALLICS

### 5.1 : INTRODUCTION

Iron in aluminum-silicon alloys leads to crystallization of brittle intermetallic compounds during solidification. Under normal melting and casting conditions, the iron compound is found to crystallize in thin platelets ( $\beta$ -phase). However, as described earlier, the iron compound crystallizes in Chinese script morphology ( $\alpha$ -phase) when the melt is treated with manganese [26], superheated to high temperature [47], or solidified at very high cooling rates [25]. Over the past several years, much of the study on this topic has focussed on the crystallographic details and chemical composition of the iron intermetallics and on the variables affecting their crystallization. Very little information is available in the literature on the actual crystallization mechanisms of these iron intermetallic compounds. A more fundamental study is of utmost importance for a better understanding of the crystallization behaviour of these brittle intermetallic compounds during solidification and would help to formulate efficient techniques to control the detrimental effect of iron.

In the present work, the crystallization behaviour of iron intermetallic compounds in industrial grade 319 aluminum alloy (containing 1.0 % Fe) was studied as a function of cooling rate, by means of thermal analysis and metallography. The role of alloying elements such as iron, manganese and magnesium, and the casting parameters of cooling rate and melt superheating temperature on the crystallization of iron compounds was investigated, and the reasons for their influence on the crystallization behaviour of the iron compounds

was explained.

To date, no completely satisfactory explanation of the nucleation and growth conditions of these phases has been advanced. Iglessis et al [37] have reasonably explained the growth process of  $\alpha$  and  $\beta$  phases in the ternary Al-Si-Fe system, but their mechanism does not explain why the  $\alpha$ -phase should crystallize in preference to the  $\beta$ -phase when the melt is superheated to a high temperature. The effects of manganese, and the reasons why the length of the  $\beta$ -phase platelets decrease with increasing cooling rate and/or increasing melt superheating temperature are also not resolved. An improved mechanism is proposed in the present work, in which both the nucleation undercooling ( $\Delta T_N$ ) and growth undercooling ( $\Delta T_G$ ) are taken into account. Thus, a more complete explanation of the crystallization behaviour of the iron compounds is advanced.

## 5.2 : EFFECT OF COOLING RATE :

According to the Al-Fe-Si phase diagram, the  $\beta$ -phase is a stable phase under equilibrium cooling conditions. However, when castings are manufactured under very high cooling rates [25] and/or when the melt is superheated to high temperatures prior to casting [47], the iron compound crystallizes in the  $\alpha$ -phase (Chinese script morphology), in meta-stable form. In the presence of manganese, the iron compound crystallizes as either  $\alpha$ -phase or a mixture of  $\alpha$ - and  $\beta$ -phases depending on the cooling rate and manganese content. In this case, based on the Al-Si-Fe-Mn phase diagram, the  $\alpha$ -phase is a stable phase under equilibrium cooling conditions (very low cooling rates). Therefore, the crystallization behaviour of the  $\alpha$ -phase cannot be compared between alloys with and without manganese, because the  $\alpha$ -phase is stable in the former and meta-stable in the latter case.

### 5.2.1 : IN ABSENCE OF MANGANESE :

Iron forms a ternary intermetallic phase with the main components of Al-Si alloys and, in the absence of manganese, crystallizes only in needle-like form ( $\beta$ -phase) for silicon and iron contents of 6.0 % and 1.0 %, respectively. Crystallization of the iron compound in the Chinese script form ( $\alpha$ -phase) was not observed even at cooling rates of 20 °C/s.

According to the phase diagram [78], the liquidus and eutectic temperatures for the Al-6.5%Si-1%Fe alloy and the eutectic temperature for the Al-3%Cu alloy are as follows :

(i) the liquidus at 615 °C

(ii) Al,  $\beta$ , Si ternary eutectic reaction at 577 - 578 °C

and (iii) Al-Cu binary eutectic reaction at 548 °C.

In the commercial 319 alloy used here, due to the presence of 0.3 % Mg and other minor alloying / impurity elements, the following changes in the liquidus and eutectic reactions were observed in the cooling curve at a cooling rate of 2.5 °C/s (Fig. 5.1) :

(i) the liquidus decreases to 600 °C

(ii) the silicon eutectic temperature decreases to 542 °C

(iii) Al-Cu binary eutectic reaction depresses to 495 °C.

In addition to these above mentioned shifts in some of the reaction arrest temperatures, one more additional reaction arrest plateau, between the liquidus and silicon eutectic temperature (572 °C at cooling rate of 2.5 °C/s) was observed in the cooling curve (Fig. 5.1). This reaction plateau corresponds to the primary  $\beta$ -phase crystallization start temperature (ie., the temperature at which the first crystals of the  $\beta$ -phase nucleate and grow in primary form which will be termed the  $\beta$ -phase start temperature). With decreasing temperature (or increasing solidification time), the  $\beta$ -phase continues to crystallize until the end of the Si-

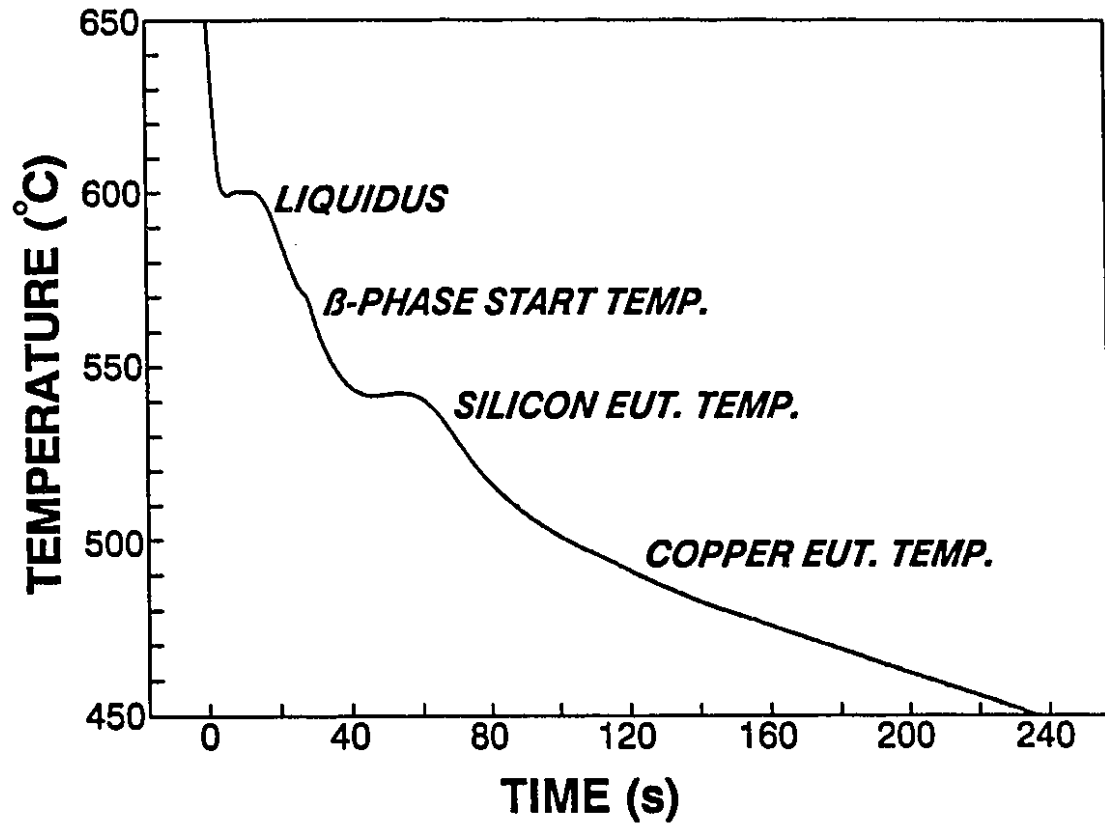


Fig. 5.1 : The cooling curve of 319 alloy (0.3 % Mg). Cooling rate = 2.5 °C/s.

eutectic reaction. One interesting aspect of this reaction temperature is that, unlike the silicon and copper eutectic temperature which is only marginally affected (less than 7 °C) by variations in cooling rate, the  $\beta$ -phase start temperature decreases with decreasing iron content [30], increasing cooling rate and increasing melt superheat temperature until it eventually merges with silicon eutectic temperature.

The average length of the  $\beta$ -phase needles decreases with decreasing iron content, increasing cooling rate, and decreasing magnesium content. The plots of both the average maximum length of  $\beta$ -phase platelets and  $\beta$ -phase start temperature versus cooling rate, exhibit a decrease with increasing cooling rate, as shown in Fig. 5.2.

### 5.2.2 : IN PRESENCE OF MANGANESE :

In the presence of manganese, the iron compound crystallizes in three distinctly different morphologies : (i) needle-like ( $\beta$ -phase), (ii) Chinese script morphology ( $\alpha$ -phase), and (iii) star-like or polyhedral morphology (primary  $\alpha$ -phase), depending on the Fe/Mn ratio and cooling rate. The chemical compositions of these intermetallic phases which are given in Table 5.1 agree well with reported results for 319 aluminum alloy [79]. The chemical composition of the primary  $\alpha$ -phase is almost the same as that of Chinese script  $\alpha$ -phase and the chemical formula for this phase can be represented approximately by  $Al_{15}(Fe,Mn)_3Si_2$ . The  $\alpha$ -phase, especially in primary crystal form, may dissolve a significant amount of copper, chromium, nickel, etc., if these elements are present in the alloy. Such elements replace some of the iron and aluminum atoms. Unlike the  $\alpha$ -phase, the  $\beta$ -phase does not dissolve other alloying elements.

In order to obtain the crystallization of the iron compound in the Chinese script form and to avoid the needle-like and polyhedral crystal morphology, a certain critical ratio of Fe:Mn is required and this ratio depends on the cooling

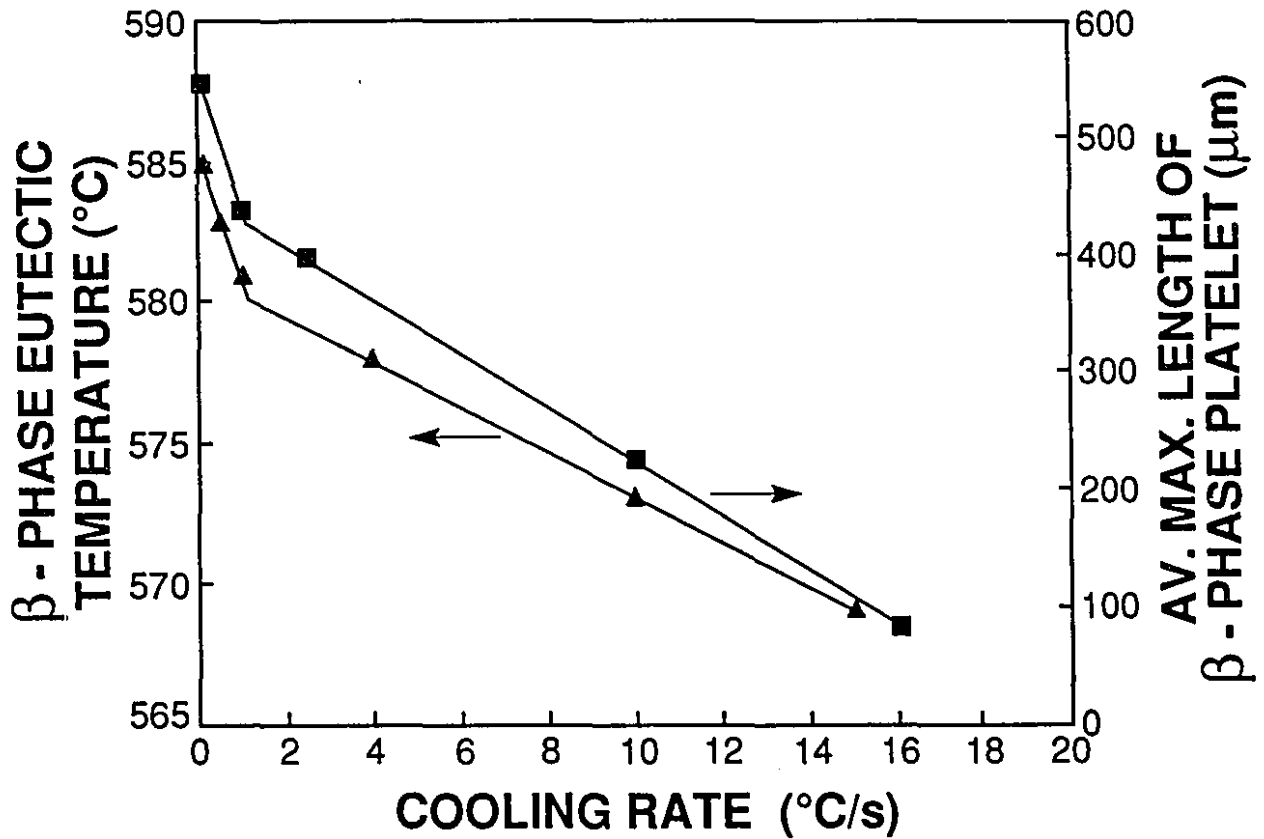


Fig. 5.2 : Plots of average maximum length of  $\beta$ -phase platelets and  $\beta$ -phase eutectic temperature versus cooling rate.

Table 5.1 : EPMA results (wt%) of iron compounds in Al-Si-Fe-Mn alloys.

Reference	Phase	Al	Si	Fe	Mn	Cu
Present	$\beta$	46.5	27.0	20.8	4.2	1.1
Apelian et al [79]	$\beta$	48.5	16.0	29.3	6.1	-
Present	$\alpha$	59.6	8.9	18.49	9.0	3.71
Apelian et al [79] <sub>a</sub>	$\alpha$	48.8	9.4	29.7	12.1	-
Present	pri- $\alpha$	60.9	8.2	15.6	13.5	1.5

rate. With a Fe:Mn ratio of 1.5, at very low cooling rates (0.1 °C/s), the  $\alpha$ -phase begins to develop just above the liquidus and crystallizes as primary- $\alpha$  crystals, as shown in Fig. 5.3 (a). At high cooling rates (10 °C/s), the growth kinetics favour the development of aluminum dendrites and the  $\alpha$ -phase is constrained to interdendritic areas leading to crystallization in the Chinese script morphology, Fig. 5.3 (b). At very high cooling rates (20 °C/s), almost 50 % of the iron compound crystallizes in the  $\beta$ -phase, Fig. 5.3 (c). This behaviour is the reverse of that observed in the absence of manganese due to the fact that, unlike the manganese-free  $\alpha$ -phase (meta-stable) which crystallizes only after the Si-eutectic reaction is over, the manganese containing  $\alpha$ -phase ( $\text{Al}_{15}(\text{Fe},\text{Mn})_3\text{Si}_2$ ) crystallizes below the liquidus but above the silicon eutectic.

The segregation effect displayed by Fe and Mn during solidification has been well explained by Backerud et al [77]. The solidification process starts with the formation of  $\alpha$ -aluminum dendrites (line 1 in Fig. 5.4), with the interdendritic liquid becoming successively enriched in iron and silicon. On further solidification, the segregation line penetrates the  $\text{Al}_{15}(\text{Mn},\text{Fe})_3\text{Si}_2$  surface and the crystallization

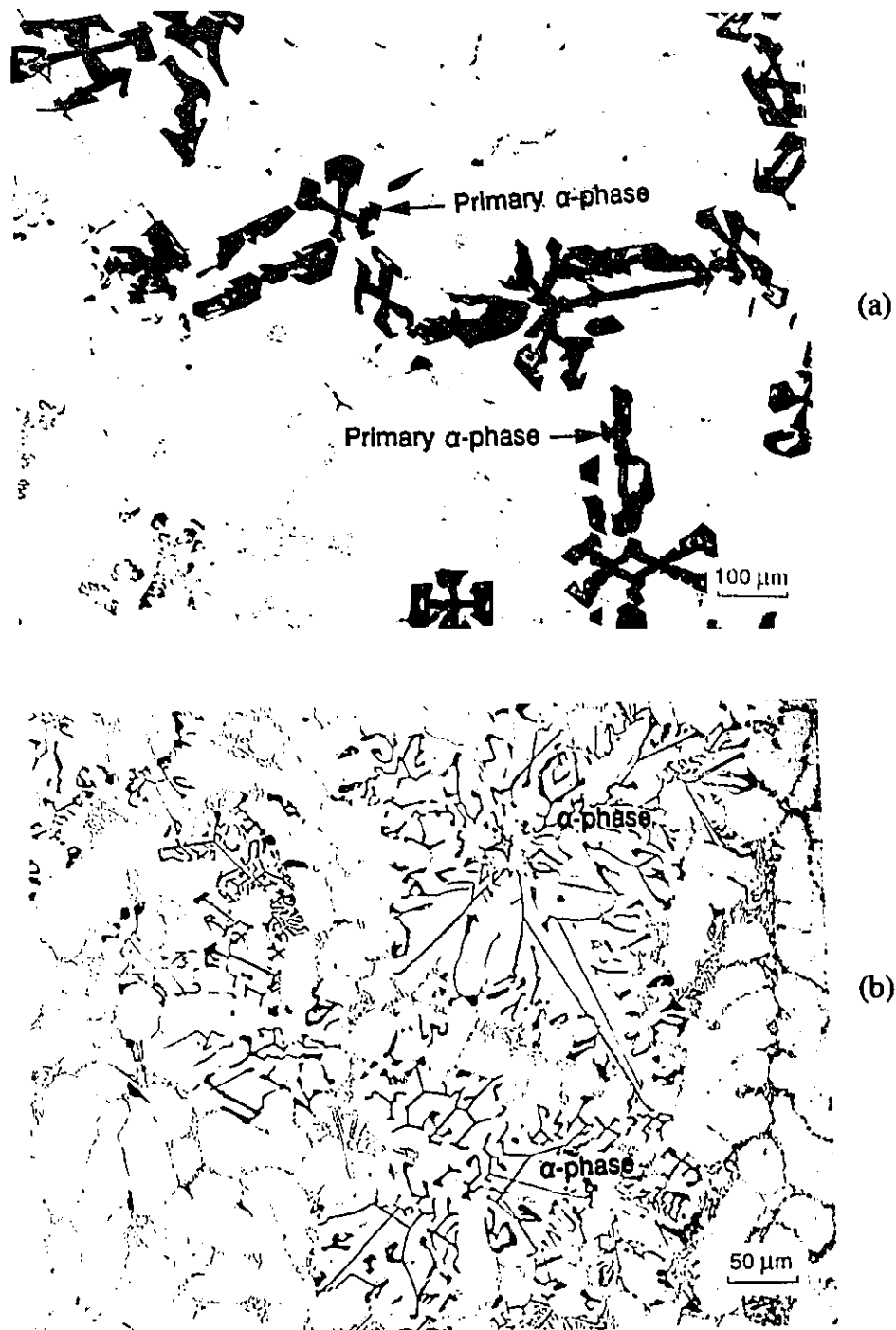
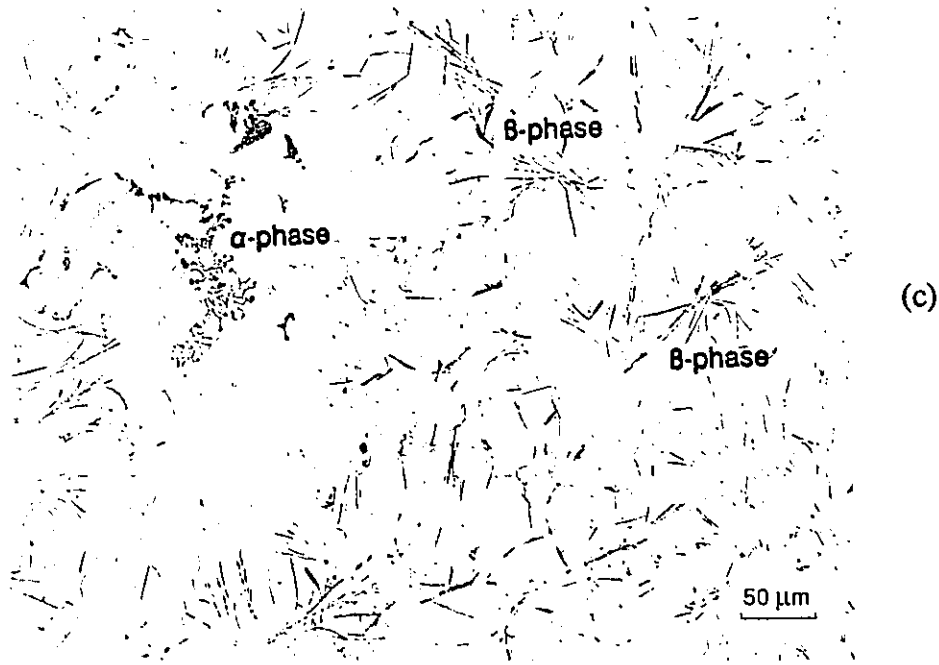


Fig. 5.3 : Micrograph showing crystallization of the iron compounds under different cooling rates : (a) 0.1 °C/s, (b) 10 °C/s and (c) 20 °C/s in high magnesium alloy having an Fe:Mn ratio of 1.5.



of the  $\alpha$ -phase begins (line 2 in Fig. 5.4). The  $\alpha$ -phase continues to crystallize along with aluminum until the trough between  $\text{Al}_{15}(\text{Mn,Fe})_3\text{Si}_2$  and  $\text{Al}_5\text{FeSi}$  is reached, whereupon both the  $\alpha$  and  $\beta$  phases crystallize together (line 3 in Fig. 5.4). When the ternary eutectic valley is obtained Al, Si and  $\beta$ -phase crystallize together in the main eutectic reaction.

The volume fraction of the  $\alpha$  and  $\beta$  phases depends on the cooling rate. At low cooling rates, almost all of the Fe is utilized in crystallization of the  $\alpha$ -phase before reaching line 3 in Fig. 5.4. At high cooling rates, however, not all the Fe is consumed during line 2 due to the short time interval. The remaining Fe is available to form a mixture of the  $\alpha$ - and  $\beta$ -phases, through line 3 in Fig. 5.4 and through the Al-Fe-Si ternary eutectic reaction.

With increasing addition of manganese (decreasing Fe/Mn ratio), the silicon eutectic temperature increases in high magnesium alloys as shown in Table 5.2. A decrease in the Mg level from 0.3 % to 0.003 % itself increases the silicon eutectic temperature by almost 30 degrees, and further addition of manganese has only a small effect on the eutectic temperature. The addition of manganese also depresses the  $\beta$ -phase start temperature (by 6-8 °C for the addition of 0.35 % Mn), thereby reducing the primary  $\beta$ -phase growth time. In Table 5.3, the *average maximum length of  $\beta$ -phase platelets* in low and high magnesium alloys for two

Table 5.2 : The silicon eutectic temperatures of low and high magnesium alloys for different Fe/Mn ratios.

Cooling Rate = 10 °C/s		Fe/Mn=40	Fe/Mn=3.0	Fe/Mn=1.5
Silicon Eutectic Temperature (°C)	High Mg	527	530	545
	Low Mg	555	559	559

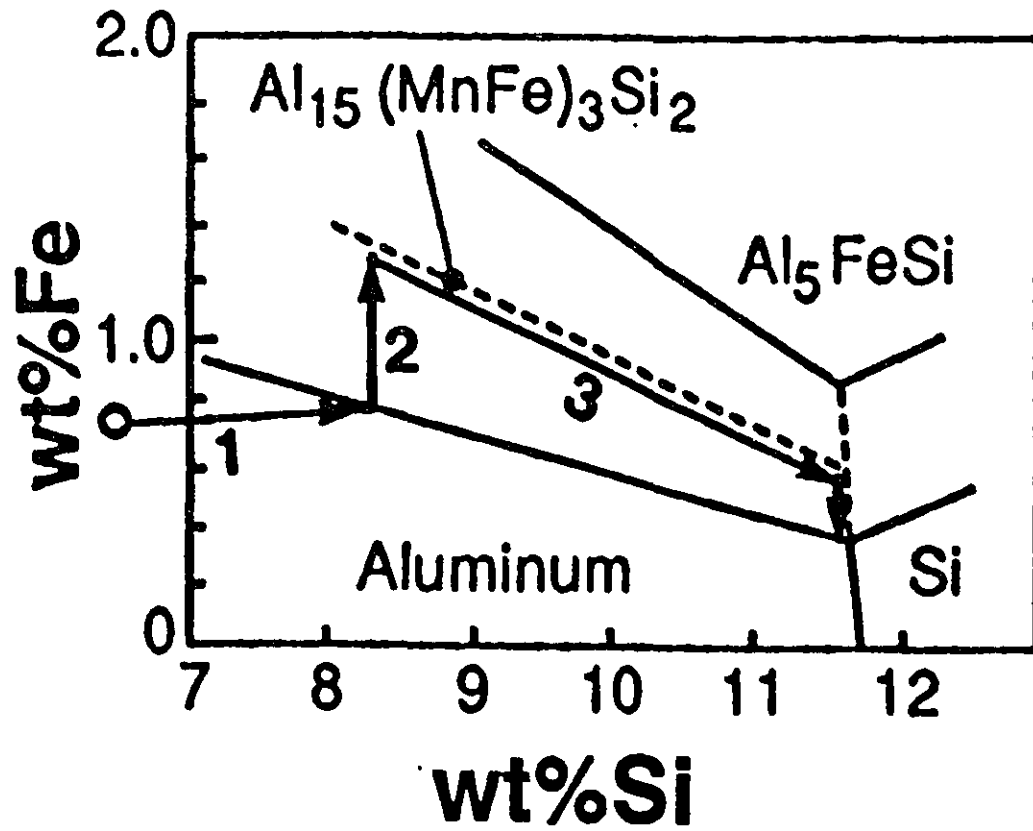


Fig. 5.4 : The segregation effect displayed by Fe and Mn during solidification.

Table 5.3 : Average maximum length of  $\beta$ -phase platelets for low and high magnesium alloys at two different Mn levels.

Alloy Type	Av. Max. Length of $\beta$ -Phase ( $\mu\text{m}$ )	
	C.R = 10 $^{\circ}\text{C/s}$	C.R = 20 $^{\circ}\text{C/s}$
0.3 % Mg - 0.7 % Mn	40 $\pm$ 3	25 $\pm$ 2
0.003 % Mg - 0.7 % Mn	28 $\pm$ 3	18 $\pm$ 2
0.3 % Mg - 0.35 % Mn	150 $\pm$ 6	60 $\pm$ 3
0.003 % Mg - 0.35 % Mn	85 $\pm$ 4	45 $\pm$ 3

different Mn levels is presented. With increases of the manganese level from 0.35 to 0.7 %, the plate length of the  $\beta$ -phase decreases markedly at all cooling rates.

Although the morphology of the iron compound on manganese addition resembles that of the Chinese script form obtained by melt superheating, the  $\alpha$ -phase obtained by melt superheating is much finer in size compared to the former, under the same solidification conditions. This is shown by the photomicrographs presented in Fig. 5.5.

### 5.3 : EFFECT OF MELT SUPERHEAT :

As stated earlier, the crystallization of the iron compound in the Chinese script form on melt superheating depends on the cooling rate, the melt superheat temperature, and the amount of alloying elements -- iron, silicon and magnesium. While the iron and magnesium effects have been studied here, the influence of

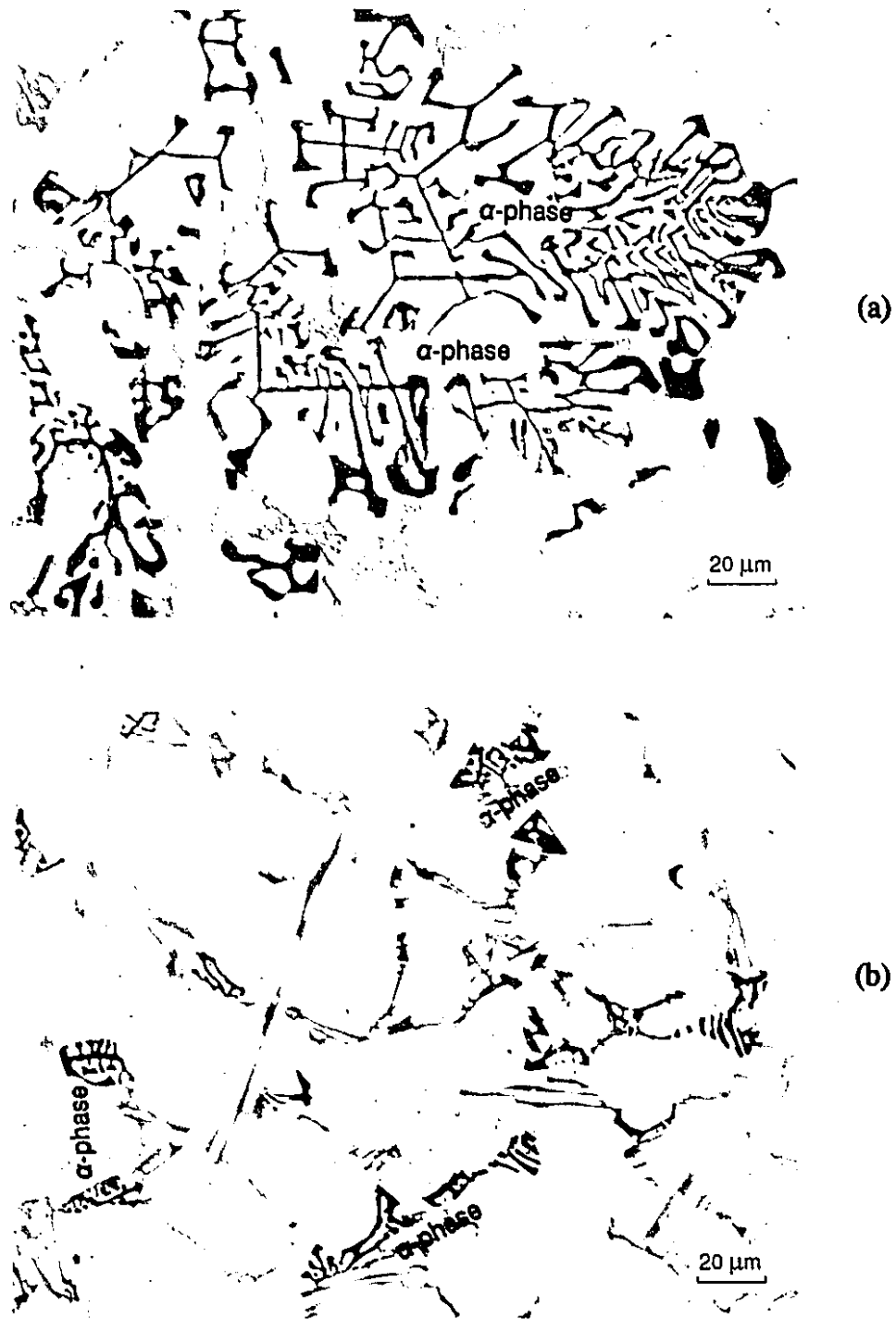


Fig. 5.5 : Microstructure of  $\alpha$ -phase obtained by (a) adding manganese and (b) superheating the melt to 850  $^{\circ}\text{C}$ .

silicon has not.

At a low melt superheating temperature of 750 °C (150 degrees above the liquidus), the iron compound crystallizes in the needle-like form ( $\beta$ -phase) at all cooling rates, whereas at high melt superheating temperatures of 850 or 900 °C (250 or 300 degrees above the liquidus), crystallization occurs in both the Chinese script ( $\alpha$ -phase) and the needle-like forms at high cooling rates. The relative volume fraction of the  $\alpha$ - and  $\beta$ -phase crystallized depends on the iron content, magnesium content and cooling rate.

In the case of high magnesium alloys (0.3 % Mg), the  $\alpha$ -phase does not crystallize even at a high melt superheating temperature of 900 °C and a high cooling rate of 25 °C/s. In the case of low magnesium containing alloys (0.003 % Mg), complete crystallization of the iron compound in the  $\alpha$ -phase is achieved at a superheating temperature of 850 °C or above, and cooling rates of 20 °C/s or greater. Fig. 5.6 shows photomicrographs of an alloy containing 0.003 % Mg superheated to 750 °C and 850 °C prior to casting.

The transition from crystallization in entirely  $\beta$ -phase to entirely  $\alpha$ -phase with increasing melt superheat temperature does not occur at a sharp temperature. It rather occurs over a range of temperatures, and within this temperature range both the  $\alpha$ - and  $\beta$ -phases may crystallize together. Above this range the iron compounds crystallize entirely as the  $\alpha$ -phase. For crystallization of the  $\alpha$ -phase without any manganese addition, both a high melt superheat temperature and a high cooling rate are necessary. Of these two the cooling rate is the more influential.

The chemical compositions of both  $\alpha$  and  $\beta$  phases are presented in Table 5.4 and agree very well with the literature [47], except for the solubility of copper noticed in the present work. The chemical formulae for the  $\beta$ - and  $\alpha$ -phases can be represented approximately by  $\text{Al}_5\text{FeSi}$  and  $\text{Al}_{12}\text{Fe}_3\text{Si}$  respectively.

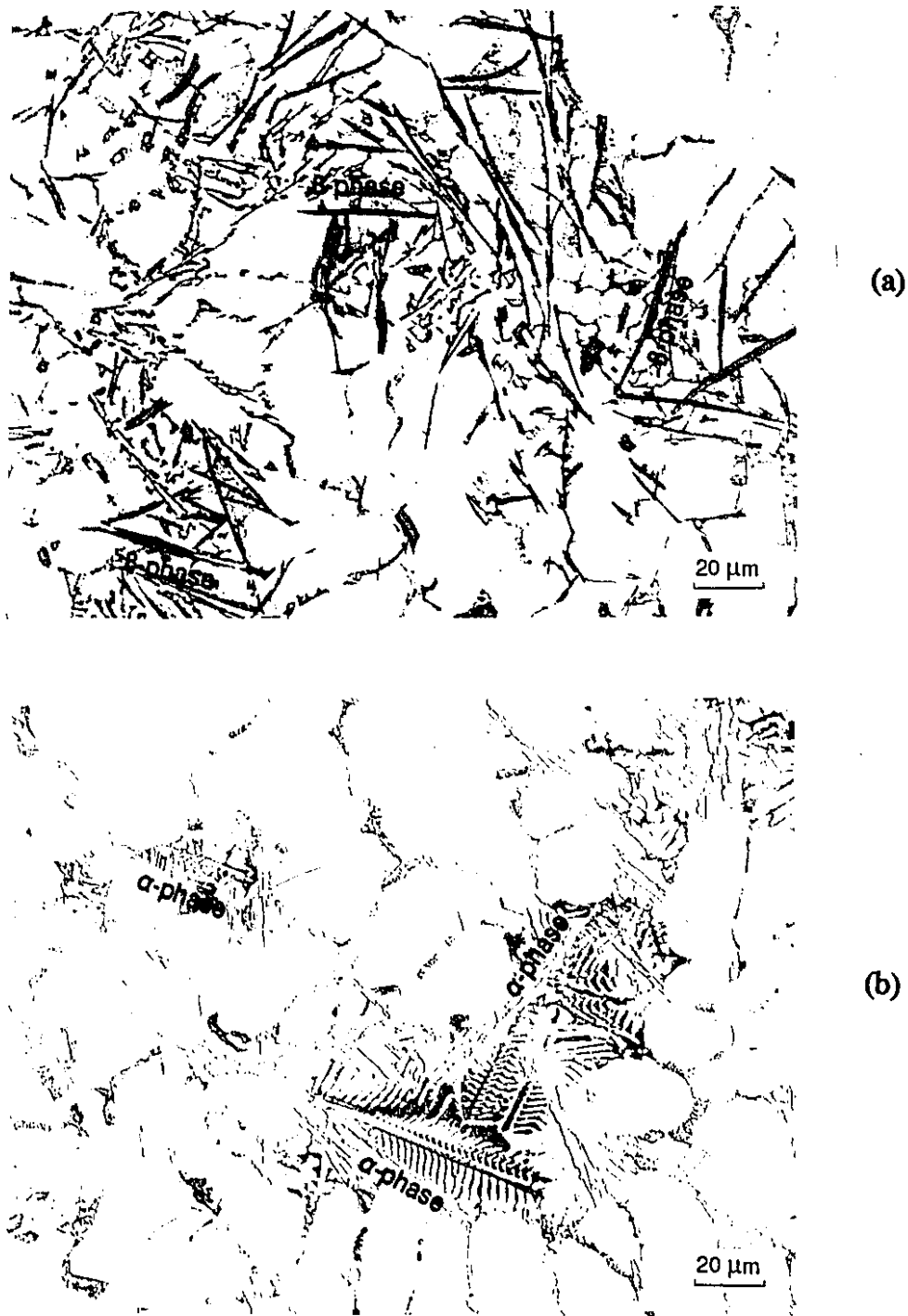


Fig. 5.6 : Micrographs of the alloy containing 1.0 % Fe and 0.003 % Mg : (a) superheated to 750 °C and (b) superheated to 850 °C prior to casting (Cooling rate = 10 °C/s).

Table 5.4 : EPMA results (wt%) of iron containing compounds in Al-Si-Fe alloys superheated to high temperature.

Reference	Phase	Al	Si	Fe	Mn	Cu
Present	$\beta$	58.1	14.9	25.4	0.41	0.93
Awano et al [47]	$\beta$	58.5	15.3	24.0	-	-
Present	$\alpha$	60.6	7.6	23.7	0.52	7.5
Awano et al [47]	$\alpha$	61.5	10.5	28.2	-	-

### 5.3.1 : UNDERCOOLING :

The growth process of the  $\beta$ -phase and the meta-stable  $\alpha$ -phase in the ternary Al-Si-Fe system is well explained by Iglessis et al [37]. They propose that for low values of undercooling, the lateral growth mechanism is aided by the formation of twin planes in the  $\beta$ -phase. The twin planes constituting the solid-liquid interface form a step couple with a fixed angle on which each step acts as a nucleus for atomic plane formation on the opposite face. The growth along the twin plane direction is not limited by nucleation as long as the undercooling is less than a certain critical value,  $\Delta T_C$ . On the other hand, for high undercoolings ( $\Delta T > \Delta T_C$ ), the rigid growth of the  $\beta$ -phase is replaced by the less rigid growth of the  $\alpha$ -phase which has no preferential growth direction.

This mechanism proposed by Iglessis et al considers only the growth processes of these compounds, but in reality, for the crystallization of any compound, consideration of both the nucleation and the growth processes is essential. Therefore, if the total undercooling, i.e., the sum of the nucleation undercooling ( $\Delta T_N$ ) and the growth undercooling ( $\Delta T_G$ ), is greater than a certain

critical value ( $\Delta T_C$ ), the  $\alpha$ -phase will crystallize. The reverse is also true with the  $\beta$ -phase forming below the critical total undercooling.

The importance of the nucleation undercooling ( $\Delta T_N$ ) can be realized from the cooling curves as shown in Figs. 5.7 and 5.8, for high and low magnesium alloys respectively. With increasing melt superheating temperature, the  $\beta$ -phase start temperature decreases until it merges with the silicon eutectic temperature in low Mg alloys. As shown in Fig. 5.2, the  $\beta$ -phase start temperature drops from 583 °C to 571 °C with a change in cooling rate from 0.3 to 10 °C/s. Likewise, for an increase in melt superheating temperature from 750 °C to 900 °C, the  $\beta$ -phase start temperature drops by 4 and 21 degrees for cooling rates of 0.3 and 10 °C/s, respectively. The influence of melt superheating temperature on the silicon eutectic and  $\beta$ -phase start temperatures is presented in Table 5.5. The use of differentiated thermal analysis (first derivative on the cooling curves) in predicting the formation of the primary  $\beta$ -phase and in estimating its exact crystallization start temperature is highlighted in Fig. 5.9.

### 5.3.2 : LENGTH OF THE $\beta$ -PHASE PLATELETS :

The average length and volume fraction of the  $\beta$ -phase platelets decreases with increasing melt superheat temperature. This can be clearly seen in Fig. 5.10, where photomicrographs are presented of the high magnesium alloy sample taken from the top and bottom sections of the casting (indicated A and B in Fig. 3.3) after the melt is superheated to either 750 °C or 850 °C. The dependence of *average maximum  $\beta$ -phase platelet length* on melt superheat temperature and cooling rate for the high (0.3 % Mg) and low (0.003 % Mg) magnesium alloys is summarized in Figs. 5.11 and 5.12, respectively. The decrease in level of magnesium from 0.3 % to 0.003 % results in a shorter length of the  $\beta$ -phase platelets, especially at low cooling rates.

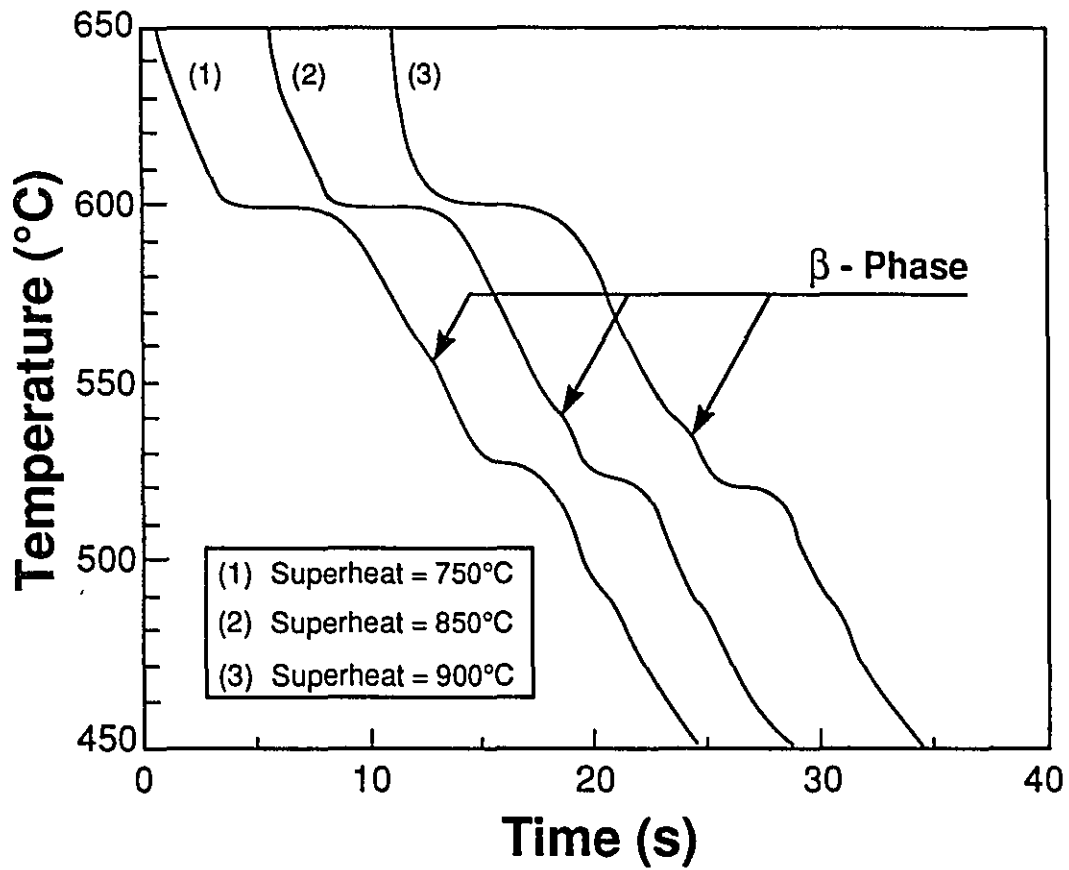


Fig. 5.7 : Cooling curves of high magnesium alloy (0.3 % Mg) superheated to 750, 850 and 900 °C prior to casting. (Cooling rate = 10 °C/s).

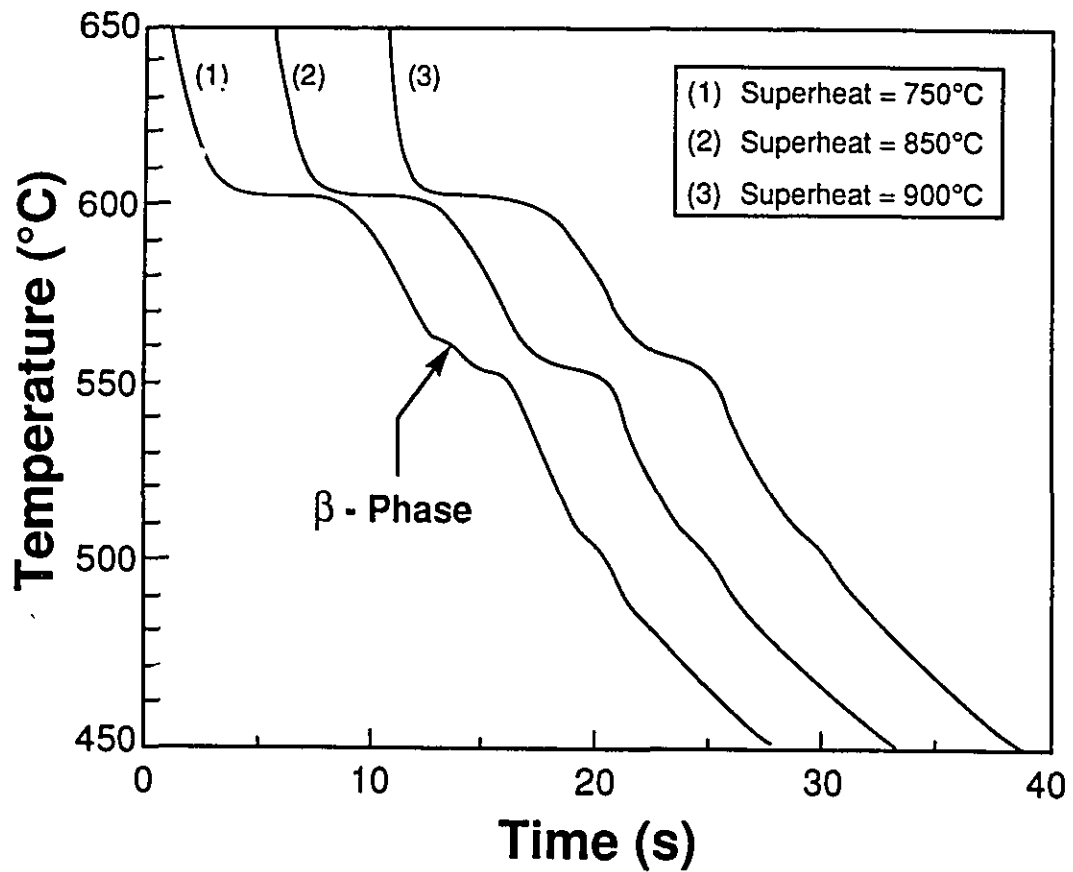
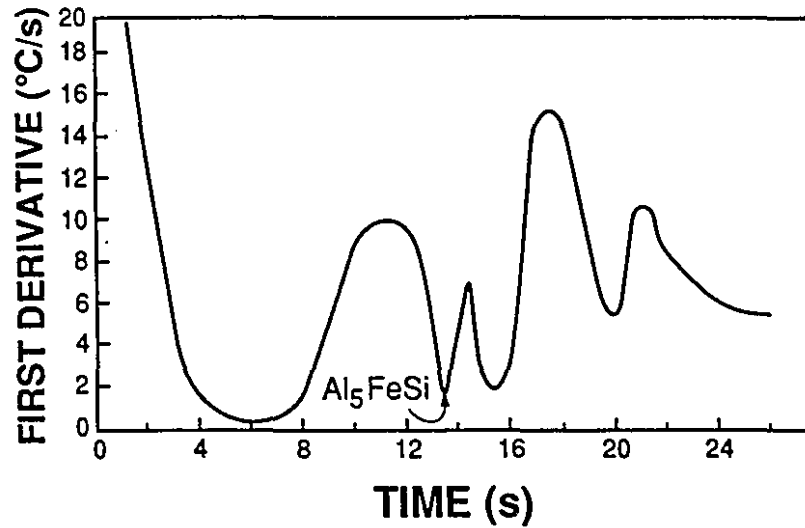
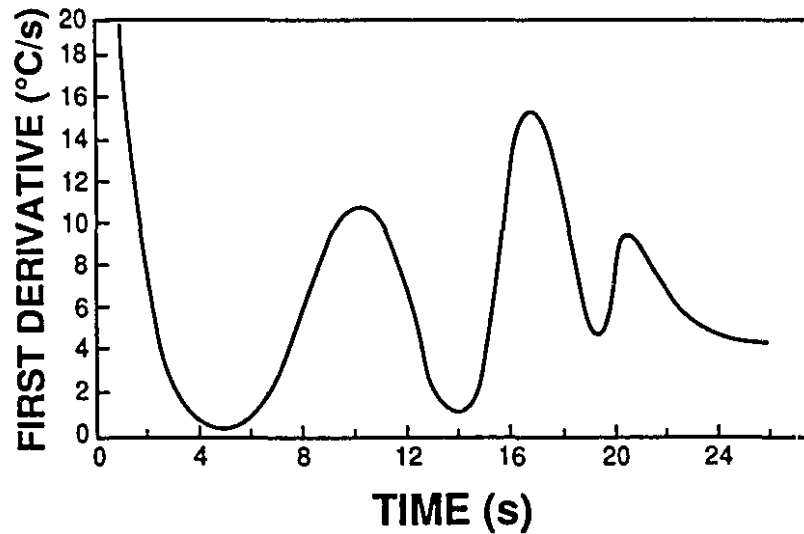


Fig. 5.8 : Cooling curves of low magnesium alloy (0.003 % Mg) superheated to 750, 850 and 900 °C prior to casting. (Cooling rate = 10 °C/s).



(a)



(b)

Fig. 5.9 : The first derivative on the cooling curves of low Mg alloy, superheated to (a) 750 °C and (b) 850 °C. Note that the Al<sub>5</sub>FeSi peak disappears if the melt is superheated to 850 °C.

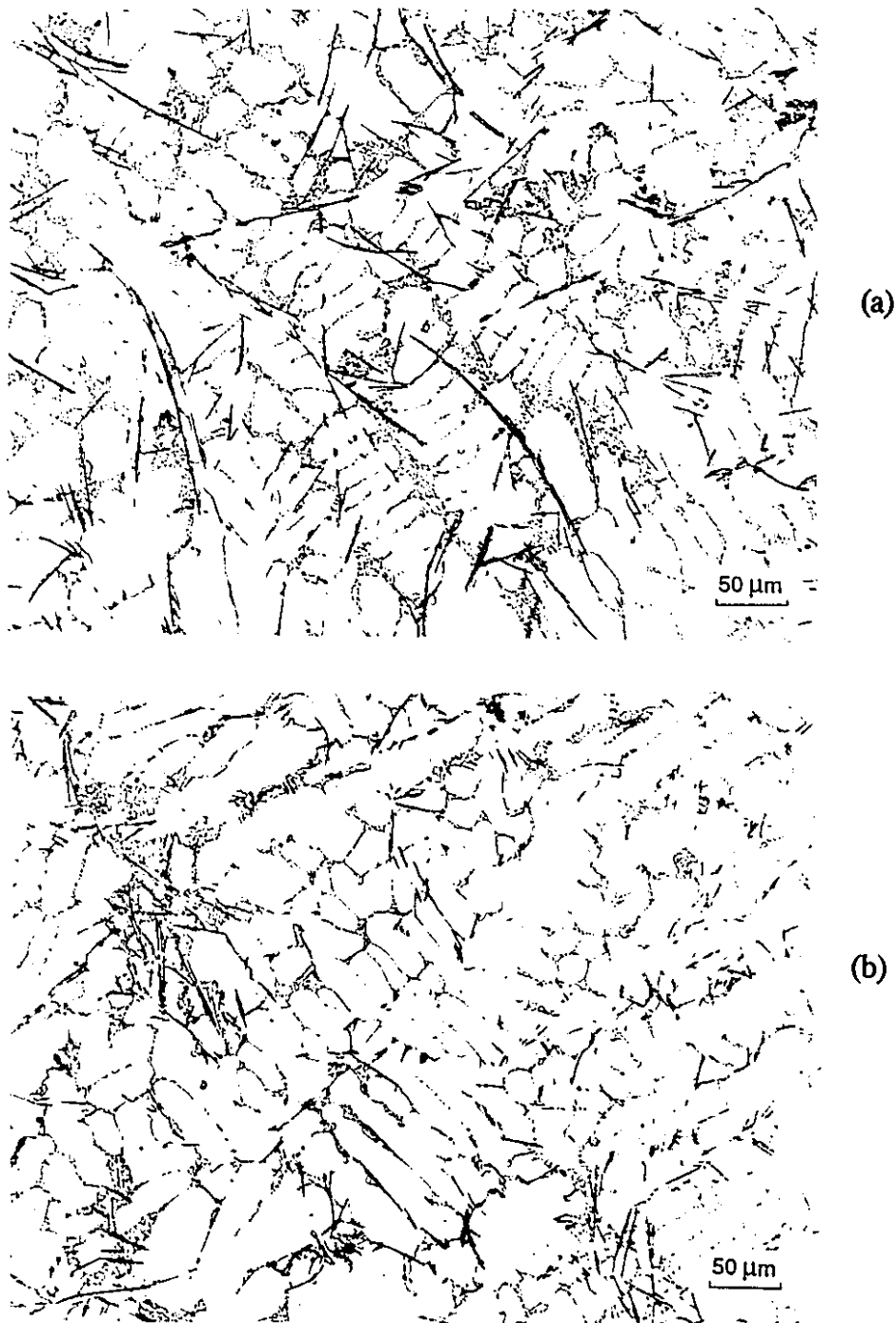
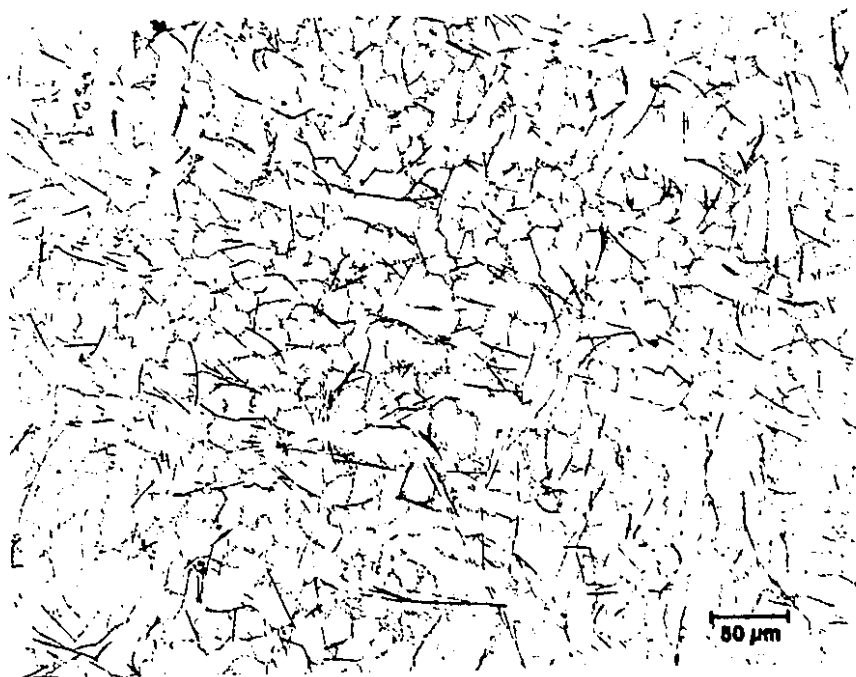
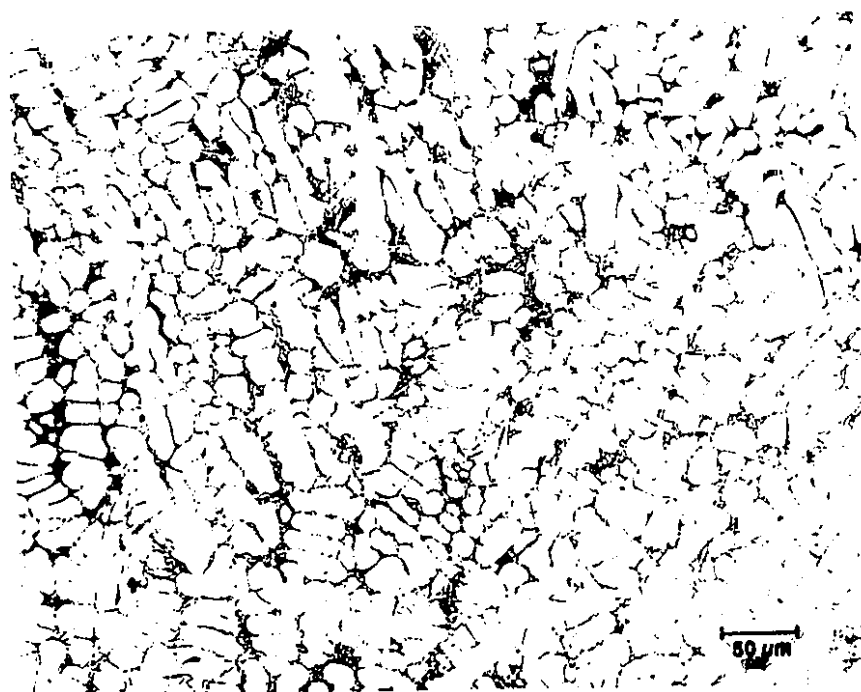


Fig. 5.10 : Photomicrographs of the high magnesium alloy sample showing : top section of the casting (marked A in Fig. 3.3), melt superheated to (a) 750 °C and (b) 850 °C ; and bottom section of the casting (marked B in Fig. 3.3), melt superheated to (c) 750 °C and (d) 850 °C.



(c)



(d)

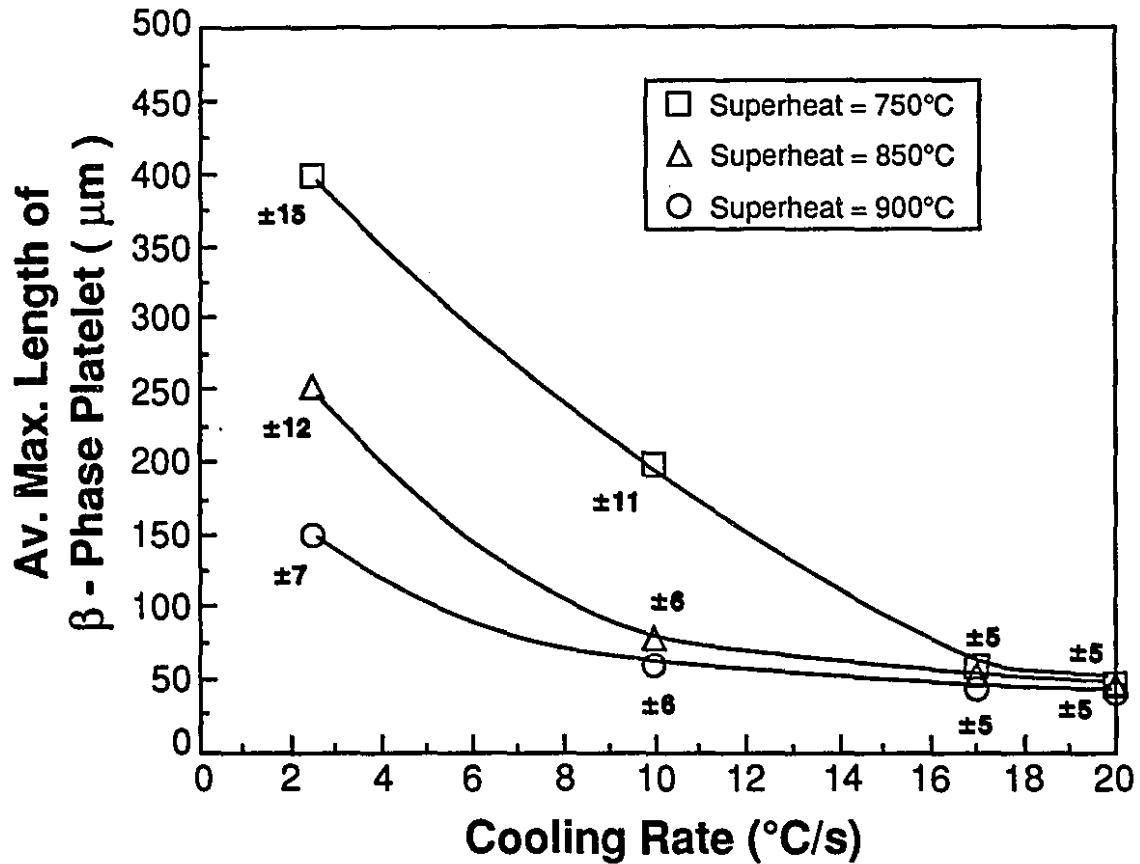


Fig. 5.11 : Plot of average maximum length of  $\beta$ -phase platelets versus cooling rate for the high magnesium alloys superheated to different temperatures.

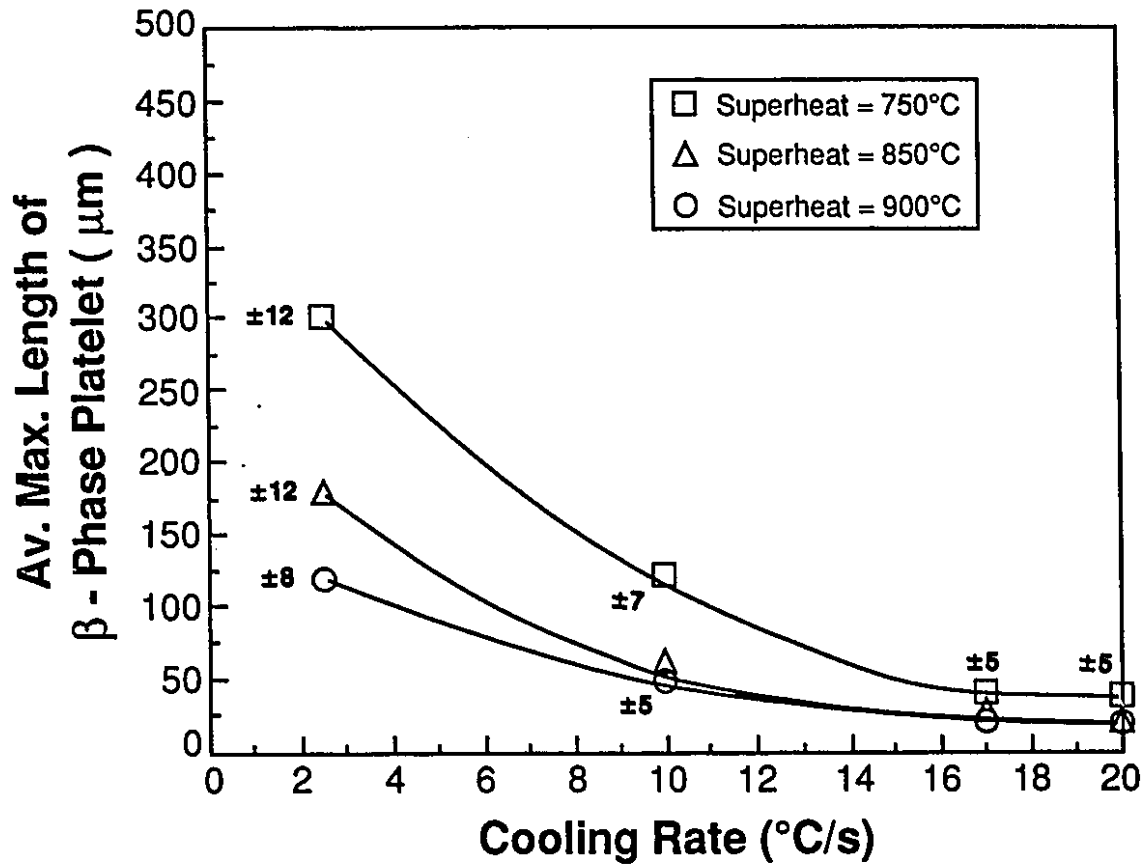


Fig. 5.12 : Plot of average maximum length of  $\beta$ -phase platelets versus cooling rate for the low magnesium alloys superheated to different temperatures.

Table 5.5 : The silicon eutectic and  $\beta$ -phase start temperature as a function of melt superheating temperature.

Alloy Type and Cooling Rate ( $^{\circ}\text{C/s}$ )	$\beta$ -Phase Eutectic Temp. ( $^{\circ}\text{C}$ )			Silicon Eutectic Temp. ( $^{\circ}\text{C}$ )
	Melt Superheating Temperature			
	750 $^{\circ}\text{C}$	850 $^{\circ}\text{C}$	900 $^{\circ}\text{C}$	
High Mg (0.3 %) High C.R (10 $^{\circ}\text{C/s}$ )	561	544	540	527
Low Mg (0.003 %) High C.R (10 $^{\circ}\text{C/s}$ )	561	-	-	555
High Mg (0.3 %) Low C.R (2.5 $^{\circ}\text{C/s}$ )	571	569	567	542
Low Mg (0.003 %) Low C.R (2.5 $^{\circ}\text{C/s}$ )	569	566	568	560

Although the  $\beta$ -phase continues to crystallize until the end of the silicon eutectic reaction, the length of the primary  $\beta$ -phase needles greatly depends on the time interval between the  $\beta$ -phase start temperature and the silicon eutectic temperature, i.e.,  $\beta$ -phase growth time. For this reason, the average length of the  $\beta$ -phase needles decreases with decreasing iron content, decreasing magnesium content, increasing cooling rate, and increasing melt superheat temperature, since all of these parameters decrease the  $\beta$ -phase growth time.

With decreasing  $\beta$ -phase start temperature, the  $\beta$ -phase growth time and therefore the length and volume fraction of this phase decrease until the  $\beta$ -phase

start temperature merges with the silicon eutectic temperature. At the end of the silicon eutectic temperature, the remaining liquid, depleted in silicon, favours the crystallization of the  $\alpha$ -phase.

### 5.3.3 : EFFECT OF MAGNESIUM :

An increasing addition of magnesium depresses the silicon eutectic temperature, and this is one of the reasons why it is more difficult to crystallize the  $\alpha$ -phase in high magnesium alloys even at a high melt superheat temperature of 900 °C. From Table 5.5, it can be seen that the silicon eutectic temperature drops by 28 and 18 degrees for an increase in Mg content from 0.003 % to 0.3 %, for cooling rates of 10 °C/s and 2.5 °C/s, respectively. Thus, it is harder to force the  $\beta$ -phase start temperature to below the silicon eutectic temperature in high magnesium alloys, either by using a high melt superheating temperature, a high cooling rate, or both. In addition, the plate length and volume fraction of the  $\beta$ -phase increase with magnesium content (Figs. 5.11 and 5.12), due to the increase in the primary  $\beta$ -phase growth time.

### 5.3.4 : TGA AND XRD ANALYSIS :

In order to explore the nature of possible nuclei for the crystallization of the  $\beta$ -phase and to investigate how these nuclei disappear on melt superheating, thermogravimetric analysis (TGA) was carried out on the low magnesium alloy samples containing 0.15 %, 0.6 % and 1.0 % Fe, by heating to 750 and 1000 °C under air and argon atmospheres. The results of this analysis on samples containing 0.6 % and 1.0 % Fe heated to 1000 °C, under atmospheric air conditions are presented in Figs. 5.13 (a-d).

Curves for samples heated to 750 °C (ie., normal pouring temperature) are

not shown due to space considerations, but they indicate only two major endothermic peaks corresponding to the silicon eutectic and liquidus temperatures, and a small endothermic peak corresponding to  $\text{Al}_2\text{Cu}$  formation temperature. Since the starting sample is in powder form (ground from the actual alloy), the small endothermic peak corresponding to the formation of  $\text{Al}_2\text{Cu}$  compound is not clear during the first cycle of heating due to poor thermal contact with the thermocouple. In the case of the high iron alloy (1.0 % Fe), the  $\beta$ -phase start temperature can be seen as a small change in the slope of the curve between the silicon eutectic and liquidus temperature peaks, while no peak corresponding to the  $\alpha$ -phase is observed. The same type of peaks is observed during cooling cycles, but they are exothermic in nature.

When the sample is heated to 1000 °C, besides the above mentioned peaks, a diffuse exothermic peak is observed at 900-1000 °C (see Fig. 5.13). This peak is not seen during the cooling cycles. The plot of percent mass change versus temperature shows a sharp slope change at around the same temperature. The exact temperature at which this exothermic peak occurs depends on the iron content and number of heating cycles. The extrapolated onset temperature (O) and peak temperature (P) corresponding to this exothermic reaction, during the first and second cycle of heating for different levels of iron are presented in Table 5.6.

Results from the TGA runs made under argon atmosphere for 1.0 % iron alloys are shown in Figs. 5.14 (a & b). Under the inert atmosphere, the heat flow curve shows exactly the same type of peaks as observed in an air atmosphere except for the absence of the high temperature reaction peak at around 950 °C. These observations suggest that the appearance of this exothermic peak corresponds to the transformation of  $\gamma$ -aluminum oxide to  $\alpha$ -aluminum oxide. X-ray diffraction (XRD) analysis of the oxides collected from the surface of the melt in the present work confirms the presence of  $\gamma$ -alumina and  $\alpha$ -alumina, at low (<

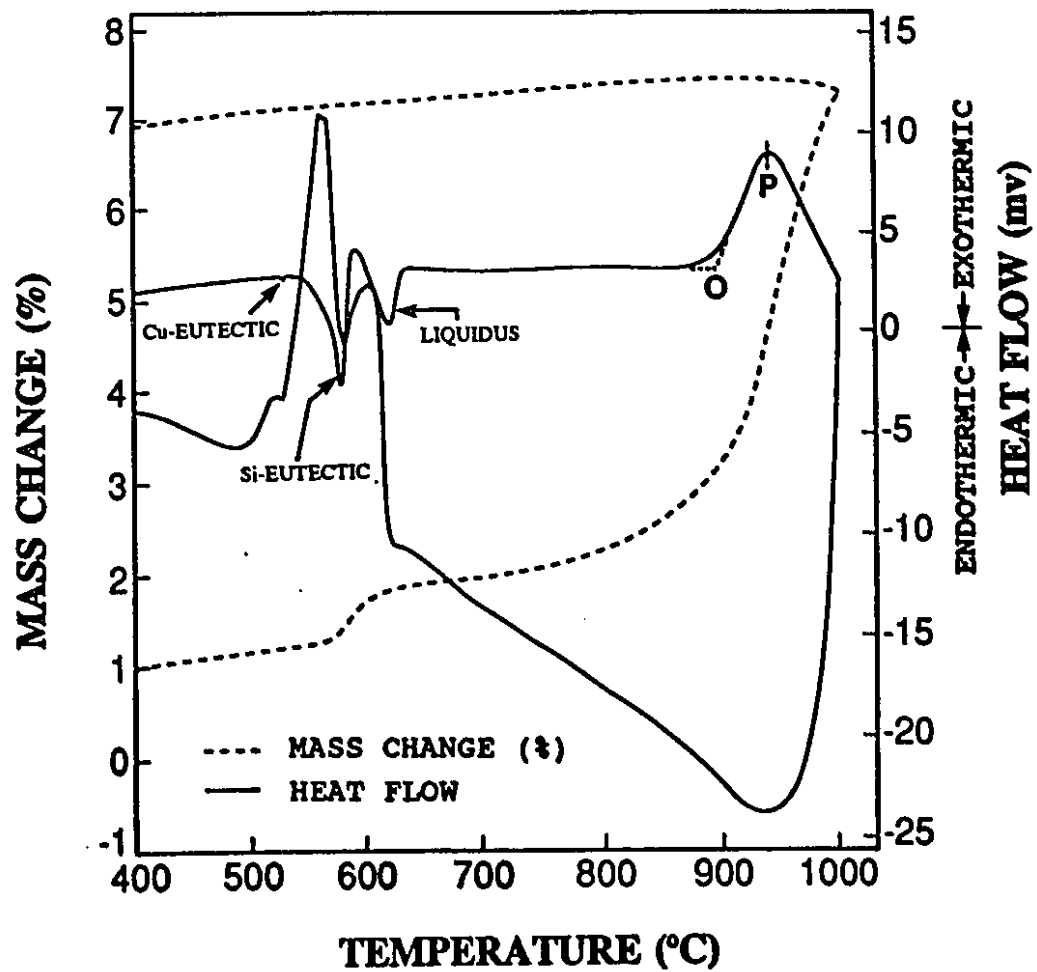


Fig. 5.13(a) : TGA curve of low magnesium alloy containing 0.6 % Fe, heated up to 1000 °C in air, for the first cycle of heating and cooling. (heating rate : 5 °C/min and cooling rate : 25 °C/min).

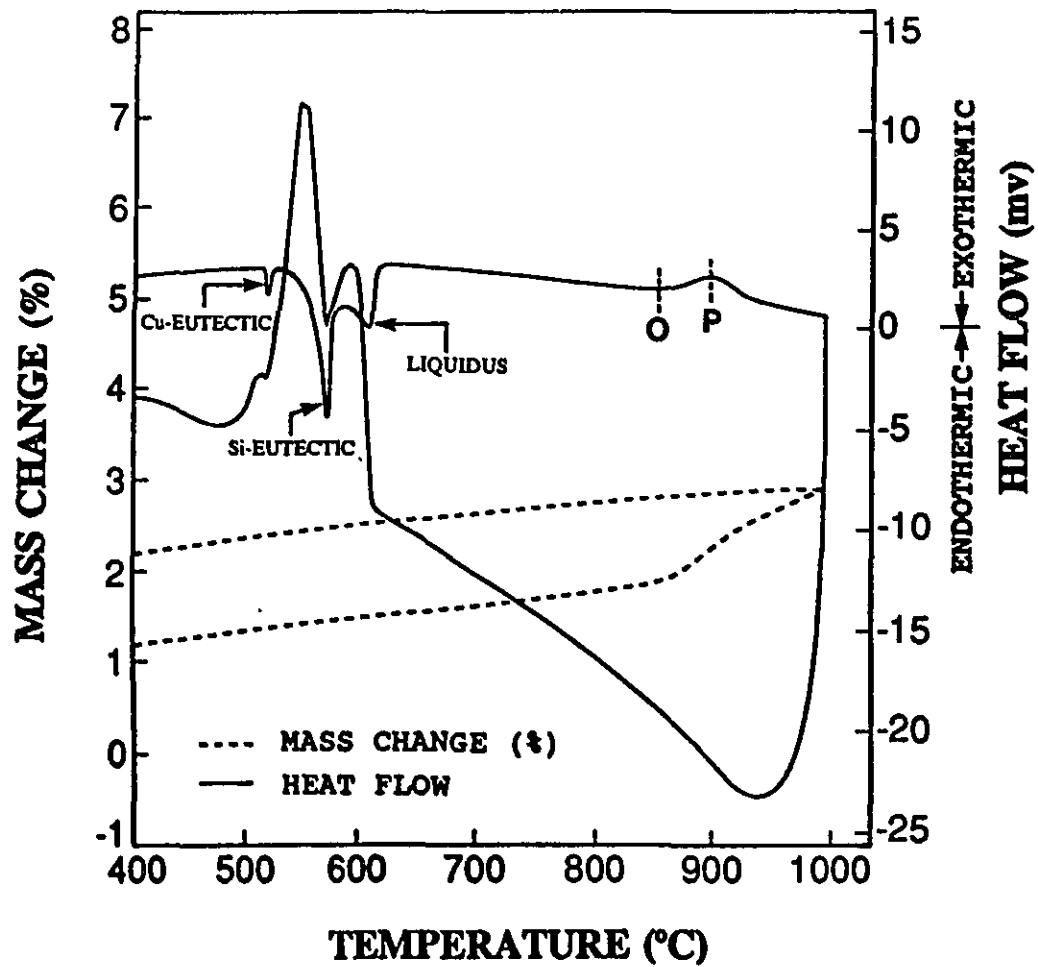


Fig. 5.13(b) : TGA curve of low magnesium alloy containing 0.6 % Fe, heated up to 1000 °C in air, for the second cycle of heating and cooling. (heating rate : 5 °C/min and cooling rate : 25 °C/min).

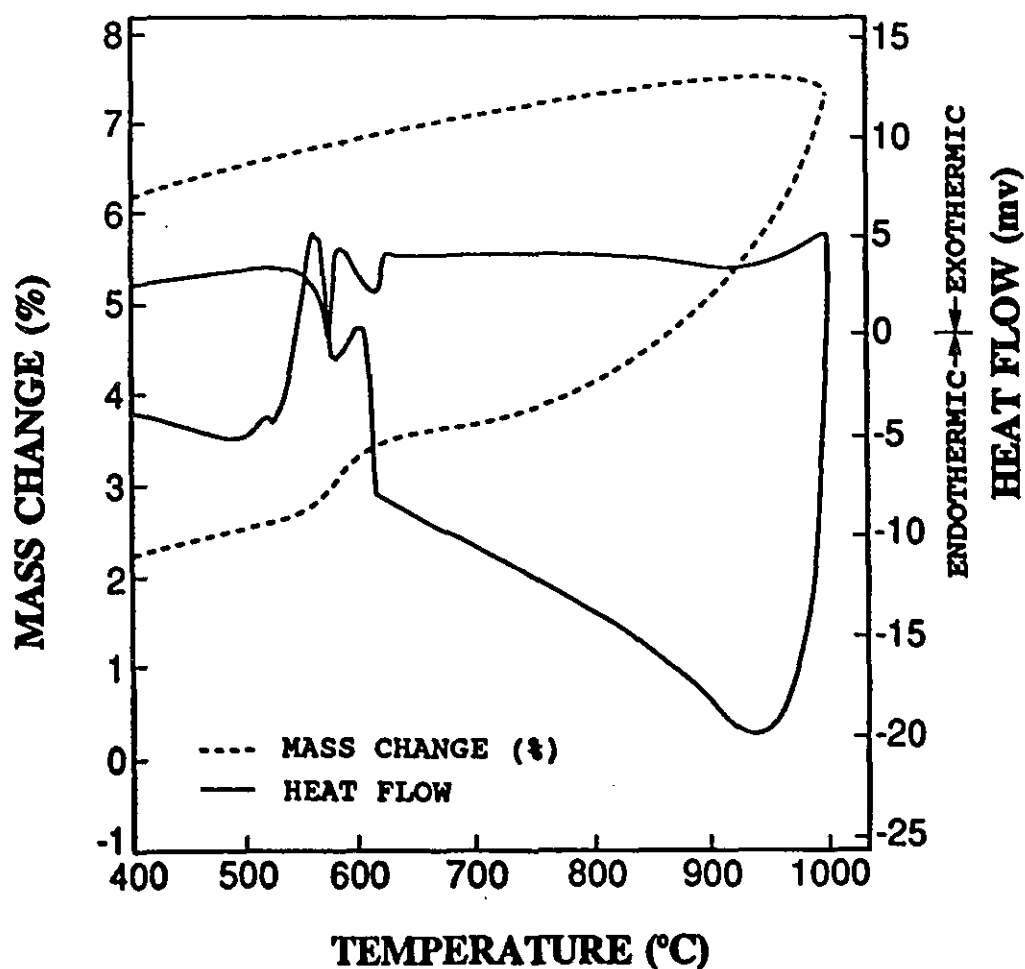


Fig. 5.13(c) : TGA curve of low magnesium alloy containing 1.0 % Fe, heated up to 1000 °C in air, for the first cycle of heating and cooling. (heating rate : 5 °C/min and cooling rate : 25 °C/min).

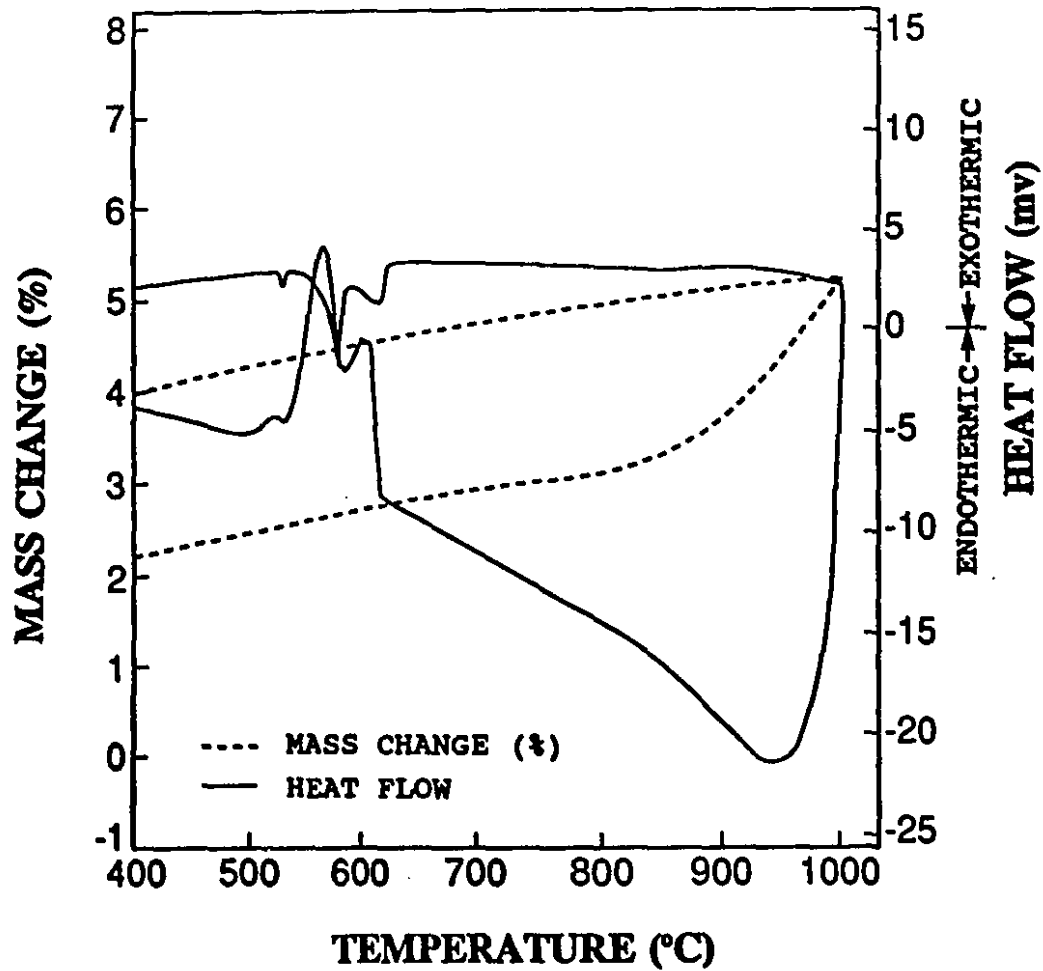


Fig. 5.13(d) : TGA curve of low magnesium alloy containing 1.0 % Fe, heated up to 1000 °C in air, for the second cycle of heating and cooling. (heating rate : 5 °C/min and cooling rate : 25 °C/min).

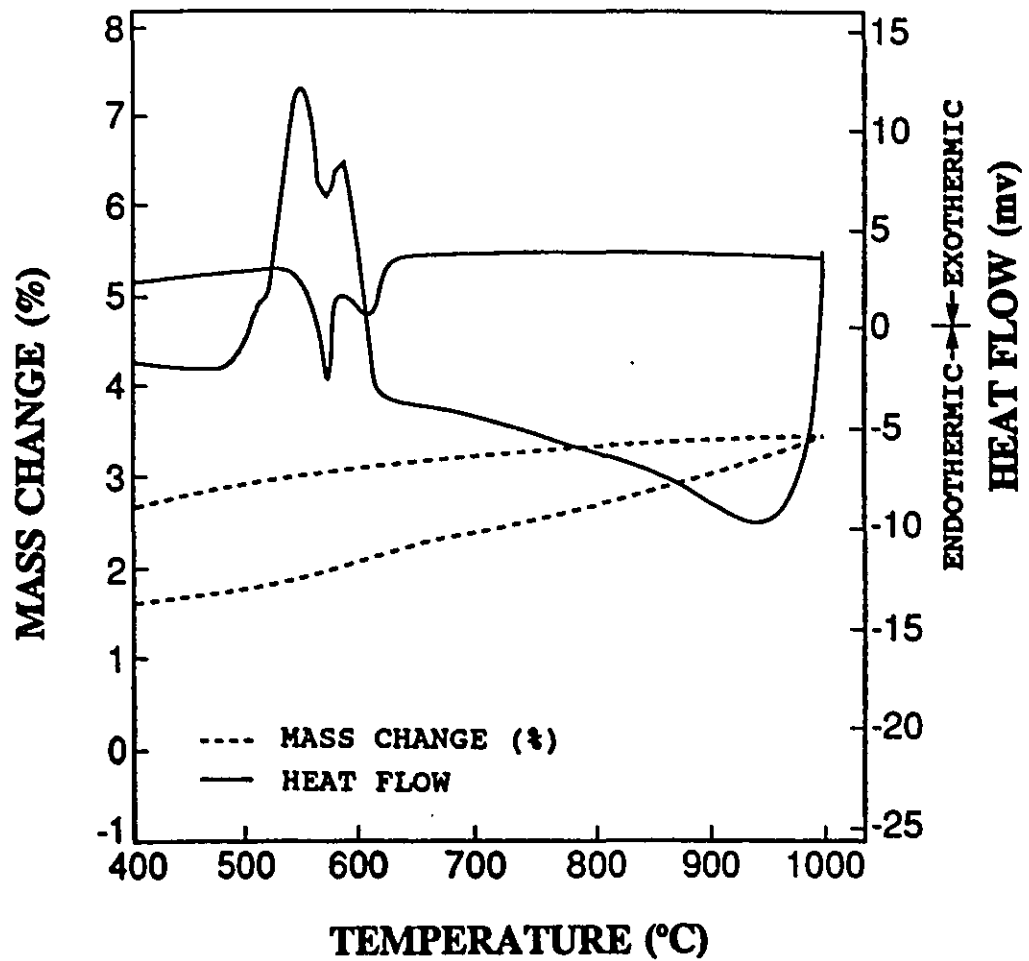


Fig. 5.14(a) : TGA curve of low magnesium alloy containing 1.0 % Fe, heated up to 1000 °C under argon atmosphere condition, for the first cycle of heating and cooling. (heating rate : 5 °C/min and cooling rate : 25 °C/min).

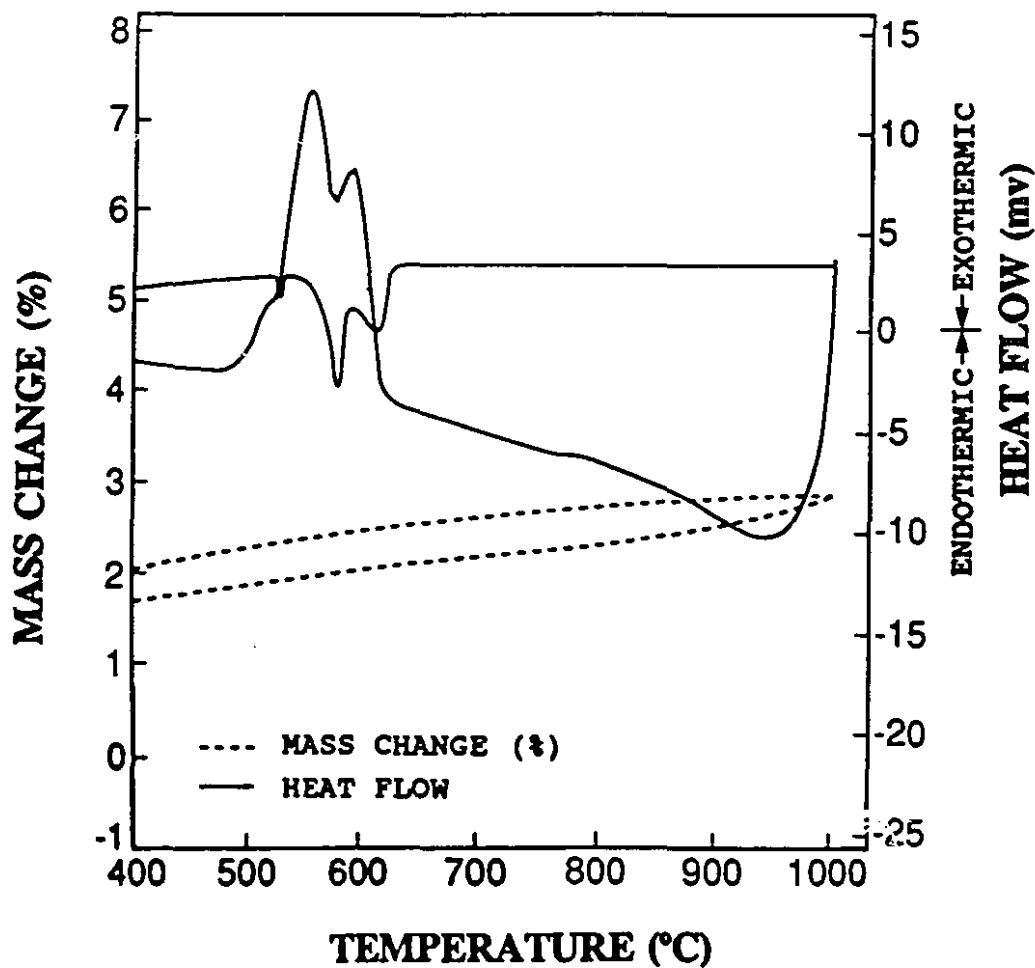


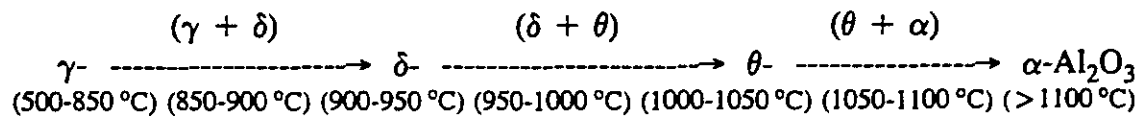
Fig. 5.14(b) : TGA curve of low magnesium alloy containing 1.0 % Fe, heated up to 1000 °C under argon atmosphere condition, for the second cycle of heating and cooling. (heating rate : 5 °C/min and cooling rate : 25 °C/min).

Table 5.6 : The reaction onset and peak temperatures obtained from TGA charts.

Sample		Extrapolated Onset Temp. (°C)	Peak Temp. (°C)
0.15 % Fe	I Cycle	905	945
	II Cycle	860	910
0.6 % Fe	I Cycle	905	940
	II Cycle	860	900
1.0 % Fe	I Cycle	945	> 1000
	II Cycle	860	910

750 °C) and high (950 °C) melt superheat temperatures respectively. Interestingly, this transformation temperature (905 °C) coincides with the critical melt superheat temperature above which the iron compounds crystallize in the  $\alpha$ -phase rather than the stable  $\beta$ -phase form. Therefore, the change in crystallization behaviour of iron compounds on melt superheating can be related to  $\gamma$ -  $\rightarrow$   $\alpha$ -aluminum oxide transformation.

With increasing melt superheat temperature, the transformation from the metastable  $\gamma$ -aluminum oxide does not immediately result in the formation of the thermodynamically stable form of aluminum oxide,  $\alpha$ -alumina (corundum). Rather a series of metastable, highly porous oxide phases is formed, before final conversion to  $\alpha$ -alumina [80] according to the following sequence.



The temperature values quoted are only approximate, with the exact transformation temperatures depending on a variety of factors such as impurity content [81], melt holding time [82], and stirring. The transformation,  $\gamma \rightarrow \alpha\text{-Al}_2\text{O}_3$  is reported to be quite sluggish in nature [82], and this leads to the appearance of a mixture of meta-stable oxides at intermediate temperatures.

According to Plummer [81], a pure  $\gamma$ -alumina sample made in the laboratory by calcining aluminum chloride converts to corundum ( $\alpha$ -alumina) far more readily than does commercial purity  $\gamma$ -alumina. The addition of small amounts of gallium, lithium, manganese, silicon and copper are reported to have a profound effect on the oxidation behaviour of aluminum [83]. This phenomenon could be easily related to the experimental findings of Awano and Shimizu [47]. They have reported that the required superheating temperature to achieve complete crystallization of iron compound in the  $\alpha$ -phase form increases sharply to more than 1200 °C once the iron content exceeds 0.6 % in Al-6%Si alloy of commercial or high purity. In the present case, however, crystallization of the  $\alpha$ -phase is achieved even at temperatures of 850 °C, for iron contents of 1.0 %, due to the presence of a higher content of impurity elements in the industrial grade 319 aluminum alloy used here. These impurity elements strongly affect the  $\gamma$ - to  $\alpha$ -alumina transformation temperature. This is one of the reasons why the exothermic peak observed for the transformation from  $\gamma$ - to  $\alpha$ -alumina occurs at a much lower temperature (at least 100 degrees) than that reported by Misra [84].

The presence of certain alloying elements such as magnesium strongly stabilizes  $\gamma$ -aluminum oxide, since  $\gamma$ -alumina is isomorphous with spinel,  $\text{MgAl}_2\text{O}_4$  [83] and thus increases the  $\gamma \rightarrow \alpha$ -alumina transformation temperature. High iron levels also seem to stabilize  $\gamma$ -aluminum oxide and thus increase the  $\gamma \rightarrow \alpha$ -alumina transformation temperature. As observed in Table 5.6, the on-set and

peak temperatures increase sharply for iron levels greater than 0.6 % during the first heating cycle. With the second cycle, these transformation temperatures are not affected by iron content due to the catalyzation by residual  $\alpha$ -alumina which is generated during the first cycle. This phenomenon explains why it is difficult to crystallize the iron compound in the  $\alpha$ -phase form even at high melt superheats, in high magnesium and iron alloys.

The major difference between the TGA charts obtained by Misra and the present work, is that the percent weight change plot does not show any change in slope at the temperature corresponding to transformation from  $\gamma$ - to  $\alpha$ -alumina. This is due to the rupturing of surface oxide films (volumetric shrinkage due to density changes in  $\gamma \rightarrow \alpha$  transformation) caused by ordering and growth of  $\alpha$ - $\text{Al}_2\text{O}_3$  which leads to creation of channels to the base melt surface and acceleration of the oxidation process [84].

Also observed is an 85 degree decrease in the transformation onset temperature in the 1.0 % Fe alloy (see Table 5.6), when the sample is reheated during the second cycle. The  $\alpha$ -alumina generated during the previous cycle can catalyze the third stage of the transformation, i.e.,  $\theta \rightarrow \alpha$ -alumina, leading to a decrease in the transformation start temperature. According to Plummer [81], the temperature at which the final peak occurs in the differential thermal analysis of  $\gamma$ -alumina can be lowered 31 degrees by the addition of 10 % of  $\alpha$ -alumina.

### 5.3.5 :NUCLEATION EFFECTS :

Although the TGA and XRD analyses show that the transformation of  $\gamma$ - to  $\alpha$ -alumina does occur in the melt when superheated to high temperatures, further clear experimental support is necessary to show the nucleation ability of  $\gamma$ -aluminum oxide for the  $\beta$ -AlFeSi particles. Since the data for the space group or atomic position locations of the  $\beta$ -AlFeSi phase and wettability of  $\beta$ -AlFeSi on

$\gamma$ -alumina are not available, it is difficult to theoretically estimate whether the  $\gamma$ -alumina particles can act as nuclei for the  $\beta$ -AlFeSi phase. Therefore, the following experiments were carried out to study the nucleation behaviour of the iron compounds on the aluminum oxides.

(i) **X-ray Mapping** : To study the nucleation behaviour of the iron compounds on the aluminum oxides, a large amount of surface oxide film was generated by induction melting and mixing a melt by turbulent agitation. The structure of a sample taken from this melt clearly shows the nucleation of  $\beta$ -AlFeSi compound on some of the oxide compounds (Fig. 5.15). Since both the aluminum oxide and porosity have the same darkness (grey) levels and are very often associated, it is difficult to distinguish between them. X-ray mapping carried out on areas such as those shown in Fig. 5.15 indicates the presence of oxygen rich areas adjacent to  $\beta$ -AlFeSi compound and confirms the proposition that oxides are likely nucleation sites for  $\beta$ -AlFeSi particles (Fig. 5.16). As expected, no  $\alpha$ -AlFeSi compound was found to associate with the oxide compound.

(ii) **Alumina Particle Injection** : The nucleation behaviour of the iron compounds on externally added alumina particles was studied by adding both  $\gamma$ - and  $\alpha$ -alumina particles to the melt. A photomicrograph showing the nucleation of  $\beta$ -AlFeSi platelets on a spherical  $\gamma$ -alumina particle is presented in Fig. 5.17. In no case were  $\alpha$ -alumina particles found to nucleate iron compounds.

Two interesting aspects were observed in the nucleation and growth of  $\beta$ -AlFeSi particles on  $\gamma$ -alumina. The (310) plane of the  $\beta$ -AlFeSi platelets nucleated on  $\gamma$ -alumina grows along the twin plane direction [010], at an angle of  $70^\circ$  (approx.) to the tangent of intersection with the  $\gamma$ -alumina particle. Some  $\beta$ -AlFeSi phase was found to not be associated with  $\gamma$ -alumina. This may be due to the activation of sub-microscopic  $\gamma$ -alumina or other secondary nuclei.

Based on the total thermal and metallographic analysis reported here, the

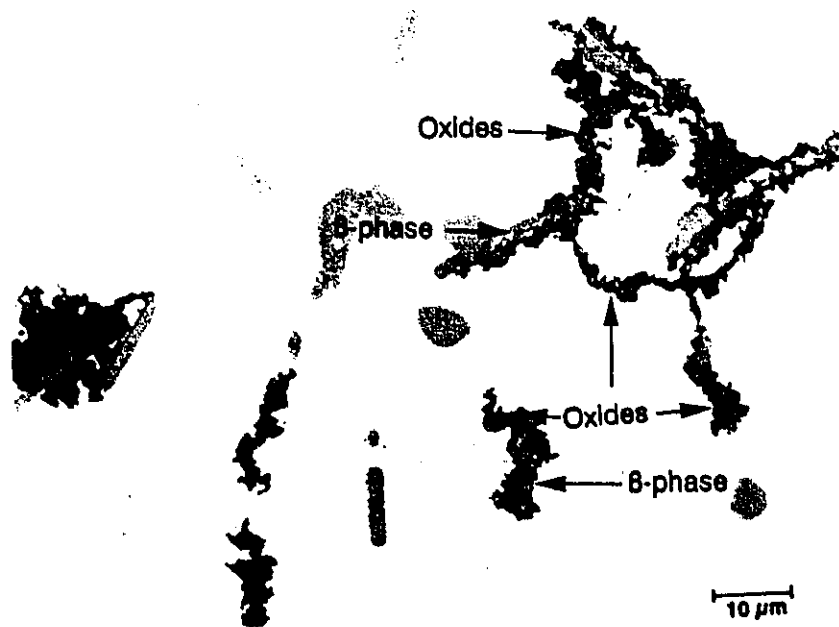


Fig. 5.15 : Photomicrograph showing nucleation of the  $\beta$ -AlFeSi platelets on the oxide stringers (dark chains).

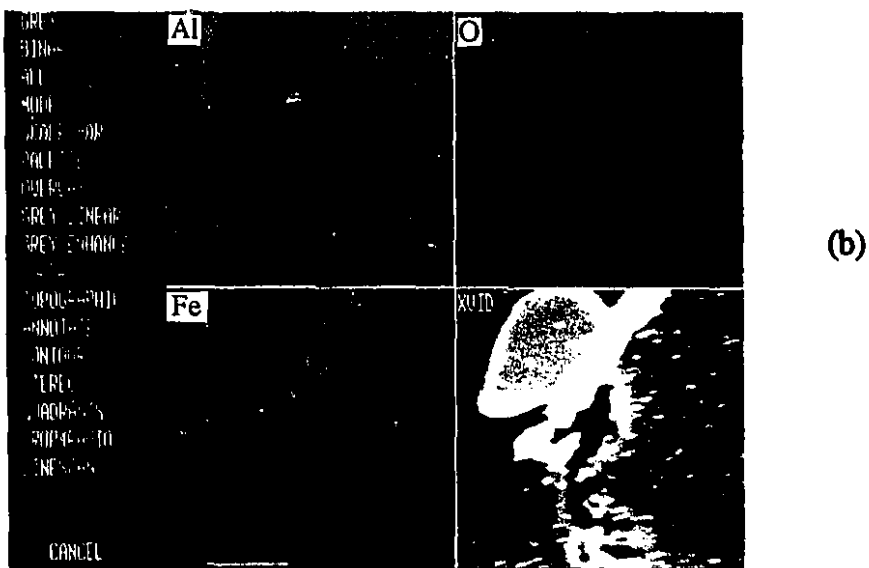
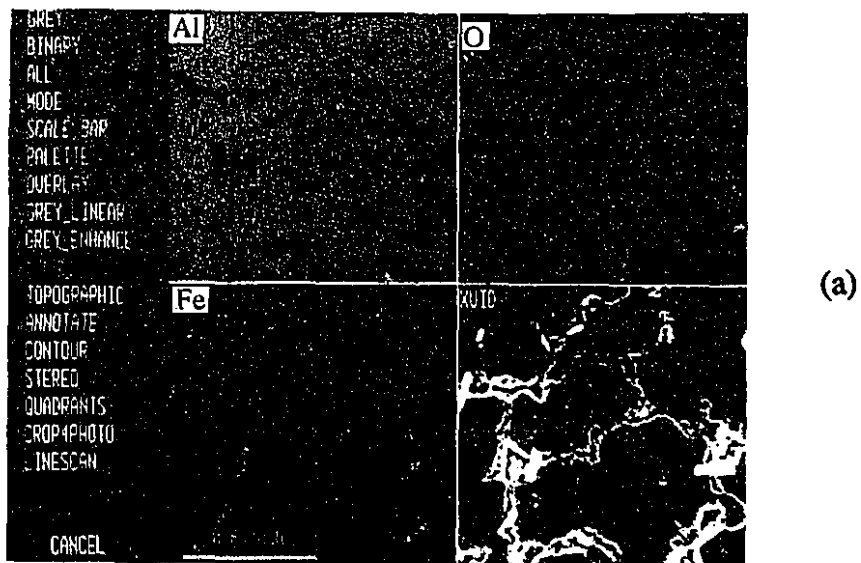


Fig. 5.16 : X-ray mapping of Al, O, and Fe regions. (b) corresponds to enlarged view at the region indicated by box and arrow in (a).

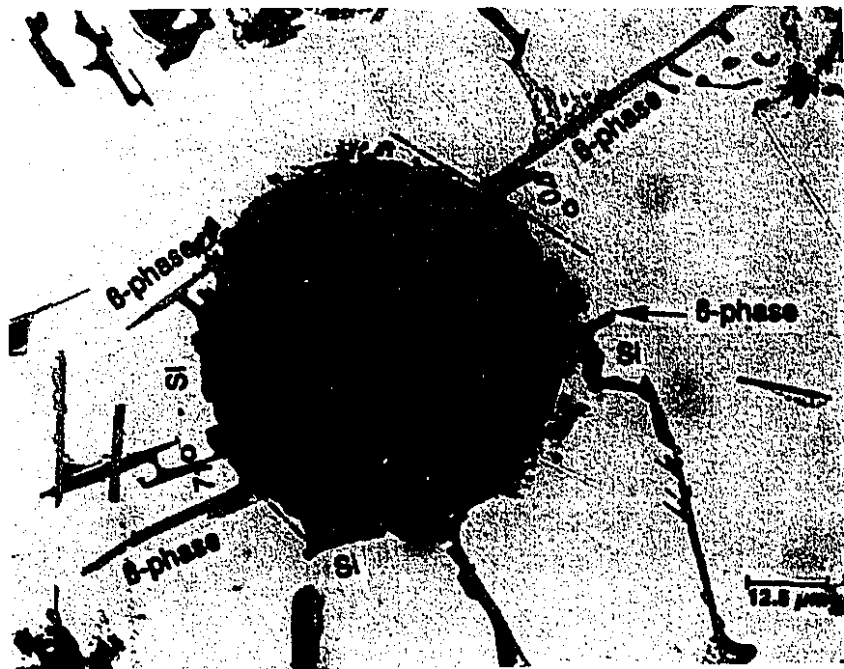


Fig. 5.17 : Nucleation of the  $\beta$ -AlFeSi needles on the  $\gamma$ -Alumina (light grey spherical particle), at an angle of  $70^\circ$  (approx.) to the tangent of intersection with the particle.

following mechanism for the change in crystallization from  $\beta$ -AlFeSi to  $\alpha$ -AlFeSi phase on melt superheating is proposed.

### 5.3.6 : MECHANISM :

At low melt superheat temperatures ( $< 750$  °C),  $\gamma$ -aluminum oxide forms on the surface of the melt, and some of this is incorporated within the main body of the melt as particles ranging in size from submicron to visually observable stringers. During solidification, these solid  $\gamma$ -aluminum oxide particles act as nucleation sites for the  $\beta$ -AlFeSi intermetallic compounds leading to the ready crystallization of primary  $\beta$ -phase compounds.

When the melt is superheated to high temperatures, the  $\gamma$ -aluminum oxide present in the melt transforms to  $\alpha$ -aluminum oxide which is not a good nucleus for the  $\beta$ -AlFeSi compound. This leads to a decrease in the nucleation potential for the  $\beta$ -AlFeSi phase, observed as a drop in the  $\beta$ -phase start temperature in the cooling curves with increasing melt superheat. When the  $\beta$ -phase start temperature is finally forced below the silicon eutectic temperature, the  $\alpha$ -AlFeSi phase crystallizes in meta-stable form. At low cooling rates (0.1 °C/s), this drop in  $\beta$ -phase start temperature is only marginal (less than 4 degrees) even at high melt superheats, and the iron compound can crystallize only as the  $\beta$ -phase. This is probably due to the activation of nuclei other than  $\gamma$ -aluminum oxide for the  $\beta$ -AlFeSi compound.

### 5.4 : SUMMARY :

The crystallization behaviour of iron containing intermetallic compounds in industrial grade 319 aluminum alloy containing 1.0 % Fe was studied by means of thermal analysis and metallography. The influence of iron, magnesium,

manganese, cooling rate and melt superheating temperature were investigated. The results obtained and the conclusions drawn may be summarized as follows :

(i) In the absence of manganese, the iron compound crystallizes only in the  $\beta$ -phase, which is a stable phase, at cooling rates less than 20 °C/s. When the melt is superheated to a high temperature and solidified under high cooling rates, the iron compound crystallizes in the  $\alpha$ -phase, in meta-stable form.

(ii) With increasing cooling rate and increasing melt superheating temperature, the  $\beta$ -phase start temperature decreases until it merges with the silicon eutectic temperature. At this point the chemical composition of the remaining liquid favours the crystallization of the  $\alpha$ -phase.

(iii) The primary  $\beta$ -phase growth time (time between the silicon eutectic and  $\beta$ -phase start temperatures) decreases with increasing melt superheating temperature due to the depression in the  $\beta$ -phase start temperature, thereby decreasing the average length of the  $\beta$ -phase platelets. An increasing magnesium content, however, has an opposite influence due to the decrease in silicon eutectic temperature. It is more difficult for the iron compounds to crystallize in the  $\alpha$ -phase in high magnesium alloys even at high melt superheating temperatures.

(iv) In presence of manganese, at low cooling rates, the iron compounds crystallize in the  $\alpha$ -form while at high cooling rates, both  $\alpha$  and  $\beta$  phases crystallize.

(v) The change in crystallization behaviour of the iron compound on melt superheating is due to the  $\gamma \rightarrow \alpha$  aluminum oxide transformation since  $\gamma$ -alumina is a preferred nucleus for  $\beta$ -AlFeSi.

# **CHAPTER 6**

## **DISSOLUTION BEHAVIOUR OF IRON INTERMETALLICS**

### **6.1 : INTRODUCTION :**

The main objective of the solution heat treatment is to homogenize the castings, and to allow soluble hardening elements of the alloy to dissolve into solid solution to prepare for subsequent aging. Because both solubility and diffusion rate increase with temperature, it is desirable to use the highest possible temperature which will neither decrease mechanical properties nor lead to shape distortion of the castings. The secondary objective of the solution heat treatment is to dissolve and/or modify the morphology of second phase particles. To date, research work on morphology changes associated with heat treatment has been limited only to studies of spheroidization and coarsening of the silicon particles.

As described in the previous chapters, the presence of brittle iron intermetallics in Al-Si alloys has a detrimental effect on the mechanical properties. Even after the adoption of various neutralization techniques such as manganese addition [26] and melt superheating [47], these alloys do not completely attain the mechanical properties of equivalent iron-free alloys. This is due to the inherent deficiency associated with all the neutralization techniques, which change only the morphology of iron intermetallics from the more detrimental needle-like shape to the less detrimental Chinese-script morphology. Considering the hardness values of these intermetallics [76], the latter phase seems to be harder and more brittle compared to the former. In order to further improve the mechanical properties of Al-Si alloys, it is essential to discover new ways of partly/entirely dissolving the harmful iron intermetallics in the matrix through thermal treatment.

## 6.2 : NON-EQUILIBRIUM HEAT TREATMENT :

Many heat treatment specifications, including AA standards [12], generally restrict solution temperatures to below the final solidification point, i.e., 498 °C, for Al-Si alloys containing copper (equilibrium heat treatment). These temperature standards are developed with the assumption that the formation of small amounts of liquid phase during solution treatment at a temperature slightly higher than the specified limits (non-equilibrium heat treatment), is detrimental to mechanical properties. That is to say, grain boundary melting and other localized melting are undesirable and should be avoided by all means during heat treatment. This has been the philosophy to date in choosing the solution temperature ; however, recent research work of Shimizu et al [85] utilized a higher solution temperature than the previous maximum, and opened a new avenue for the heat treatment of AlCuMgSi alloys such as 319.

Non-equilibrium heat treatment was suggested by Shimizu et al [85] for the AC2B aluminum alloy (Al-7Si-3Cu alloy). Their treatment involves a regular T6 temper heat treatment but with a solution temperature higher than the final solidification temperature, i.e., the copper eutectic temperature. Under equilibrium heat treatment conditions, it is not possible to take the full amount of copper intermetallics into solid solution, and even at long solution treatment times, the majority of the Cu-rich phases remain undissolved. However, by means of non-equilibrium heat treatment, copper intermetallics readily dissolve, and it is possible to obtain up to 100 percent dissolution.

Shimizu et al [85] studied the impact strength as a function of different solution temperatures ranging from 485 to 535 °C. According to their results, impact properties increase with increasing solution temperature to reach a maximum at 520 - 525 °C. Above this temperature range, properties are reported to decrease due to partial grain boundary melting. Since their alloy contained only

very little iron (0.15 % Fe), they did not study the dissolution kinetics of the iron intermetallics. Their results are, however, encouraging, and suggest that non-equilibrium heat treatment could be extended to the iron intermetallics, and may result in significant improvement in mechanical properties.

In the present study, a similar non-equilibrium heat treatment to that proposed by Shimizu et al [85] was carried out on the 319 alloy samples containing 1.0 % iron to study the dissolution behaviour of iron intermetallics. In order to study the influence of shape and size of the iron intermetallics on the dissolution kinetics, heat treatment was carried out on alloys with and without Mn and solidified under two different cooling rates.

### **6.3 : MICROSTRUCTURE :**

#### **6.3.1 : EFFECT OF SOLUTION TEMPERATURE :**

To determine the effect of solution temperature on the dissolution behaviour of the iron intermetallics, samples were solution treated at temperatures from 485 °C to 535 °C, in steps of 10 degrees, for 8 hours. Following the solution treatment, all the samples were subjected to artificial aging treatment at 150 °C for 5 hours. Since the present work is aimed at studying dissolution of iron intermetallics, the aging treatment conditions which have no influence on this were not varied. As described in the experimental procedure, cooling curves were obtained for each specific set of alloy/casting conditions. The measured cooling rate and copper eutectic temperature (final solidification temperature) from the thermal analysis curve were found to be 10 °C/s and 498 °C. Fig. 6.1 shows the solution temperature ranges used for the equilibrium and non-equilibrium heat treatments, indicated on a cooling curve for 319 alloy.

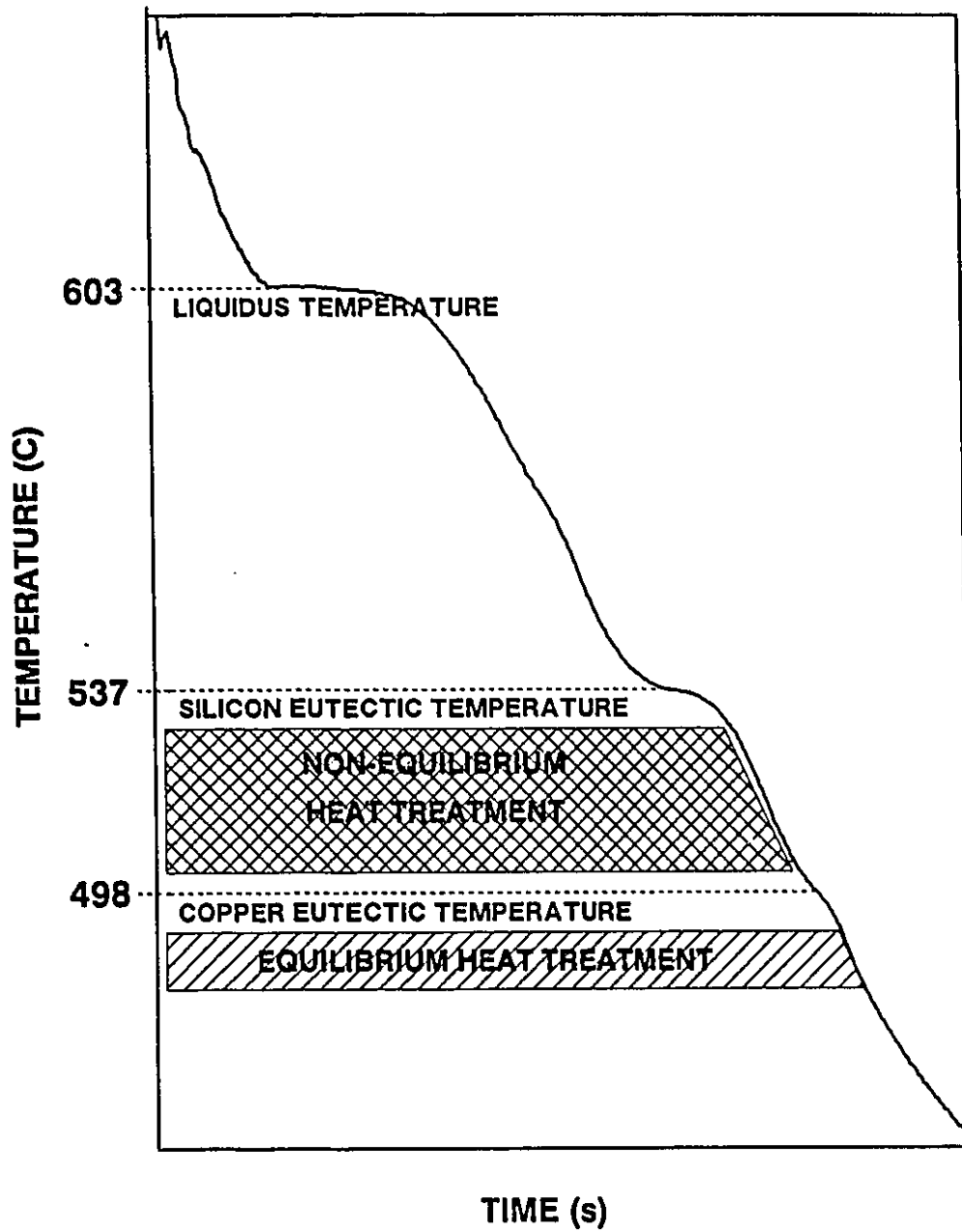


Fig. 6.1 : Solution temperature ranges used for the equilibrium and non-equilibrium heat treatment.

The results given by Shimizu et al [85] suggest that the non-equilibrium heat treatment improves mechanical properties as long as a critical solution temperature is not exceeded. Above this critical temperature, a large amount of grain boundary melting occurs leading to a sudden decrease in mechanical properties. Grain boundary melting and liquid phase formation on heat treatment is very dependent on alloying elements and casting conditions. Therefore, in order to study the dissolution behaviour of iron intermetallics and understand the phenomenon of grain boundary melting on non-equilibrium heat treatment, it is essential to perform microstructural analysis of various phases produced by different alloying and casting conditions.

#### **6.3.1.1 : IN THE ABSENCE OF MANGANESE :**

In the absence of Mn the iron intermetallics crystallize only in needle-like form, i.e.,  $\beta$ -phase, at all cooling rates ranging from 0.1 °C/s to 25 °C/s. According to one literature review [26], the  $\beta$ -phase has a detrimental influence on the mechanical properties due to its long plate-like nature and its inherent brittleness. These thin platelets can increase the stress intensity factor, and owing to the poor bonding between the  $\beta$ -phase and Al-matrix [28], the crack can propagate easily along the interface. Therefore, it is desirable to either completely dissolve, or at least fragment, these  $\beta$ -phase platelets into small pieces through non-equilibrium heat treatment.

#### **6.3.1.1.1 : SILICON PARTICLES :**

Photomicrographs of the sample treated at three different solution temperatures of 485, 515 and 535 °C are presented in Fig. 6.2. As the initial microstructure is modified with Sr, some spheroidization of the Si particles is seen

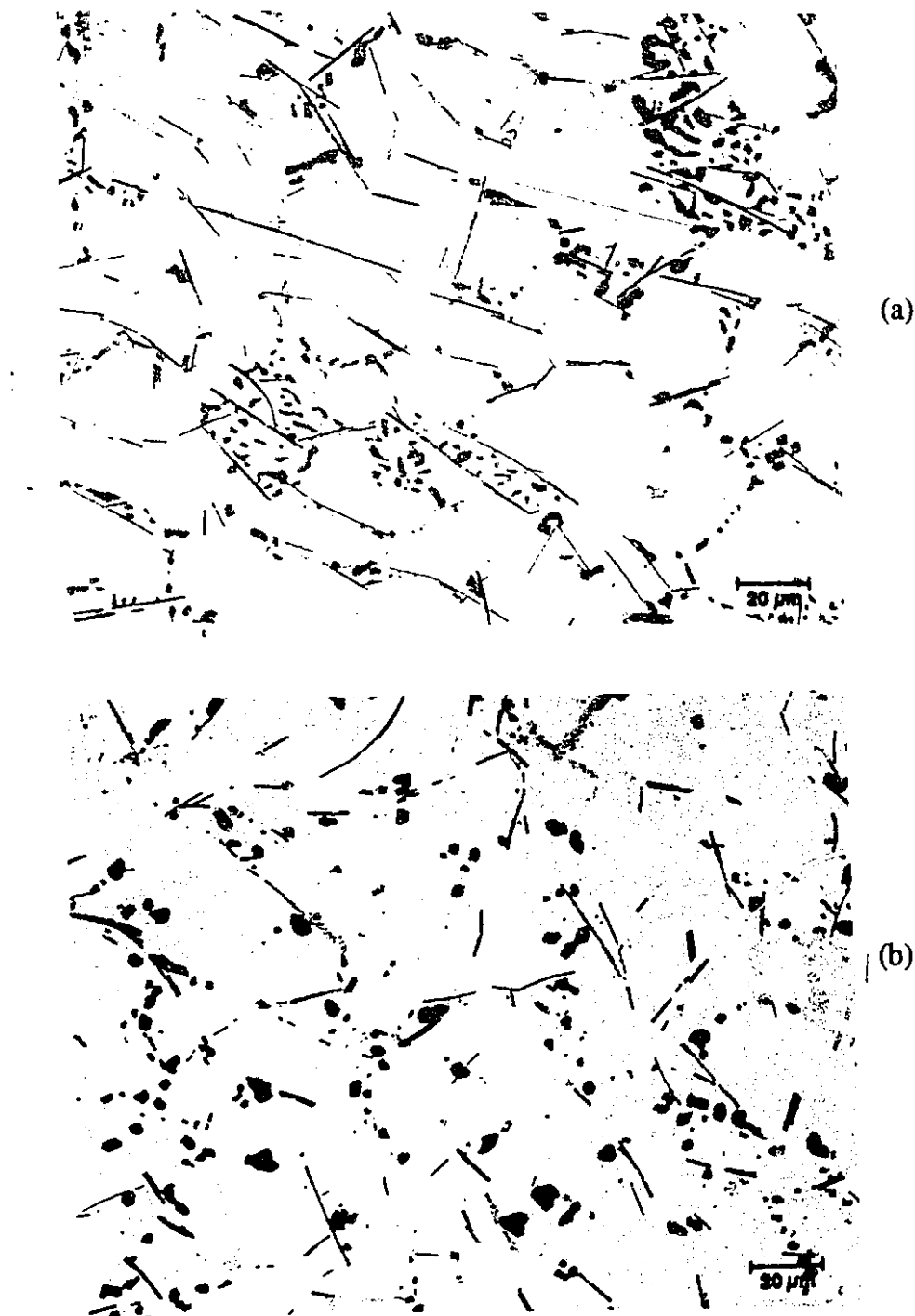
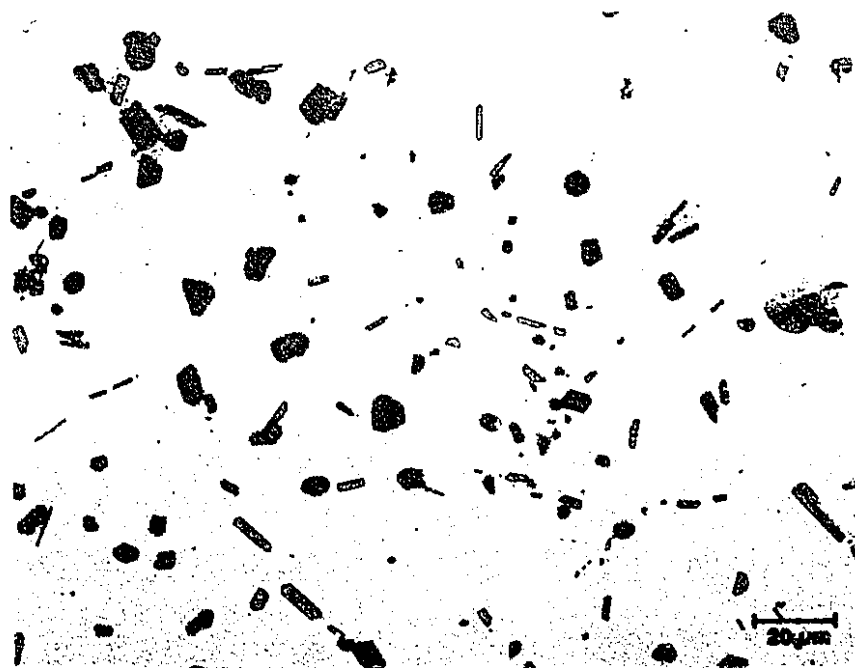


Fig. 6.2 : Photomicrographs of the manganese-free alloy samples at three different solution temperatures of (a) 485 °C, (b) 515 °C and (c) 535 °C. (Cooling rate = 10 °C/s).



(c)

to occur at a solution treatment temperature of 485 °C, as shown in Fig. 6.2(a). Modification is reported to facilitate fragmentation and spheroidization due to its effect on the eutectic silicon to produce a fibrous morphology [56][57]. The coarsening of eutectic Si increases at increasing solution temperatures above 500 °C (see Figs. 6.2(b) & 6.2(c)). The theory of spheroidization and coarsening of silicon particles on heat treatment is well explained by Paray [57].

#### **6.3.1.1.2 : COPPER INTERMETALLICS :**

At solution temperatures of less than 500 °C, a significant amount of copper intermetallics ( $\text{Al}_2\text{Cu}$ ) in block form remains undissolved ; however, those present as a fine eutectic dissolve easily. The copper intermetallics are observed to dissolve quickly once the solution temperature exceeds 500 °C.

#### **6.3.1.1.3 : IRON INTERMETALLICS :**

Microstructural observation of alloys containing no manganese and solution treated at 485 °C (equilibrium heat treatment) shows no change in the size and shape of the  $\beta$ -phase particles. Basically, they remain undissolved. With increasing solution treatment temperature, the  $\beta$ -phase platelets dissolve slowly through concurrent fragmentation across the plate and dissolution at the plate tips, as shown in Fig. 6.2(b). However, at the high solution treatment temperature of 535 °C, the  $\beta$ -phase particles coarsen and spheroidize after the initial fragmentation and dissolution, as shown in Fig. 6.2 (c).

In order to estimate the dissolution rate of iron intermetallics, both volume percent and average length of the  $\beta$ -phase were measured using image analysis. These quantities are plotted in Fig. 6.3. Owing to the same color contrast between various phases, it is very difficult to quantify these phases exactly. Moreover,

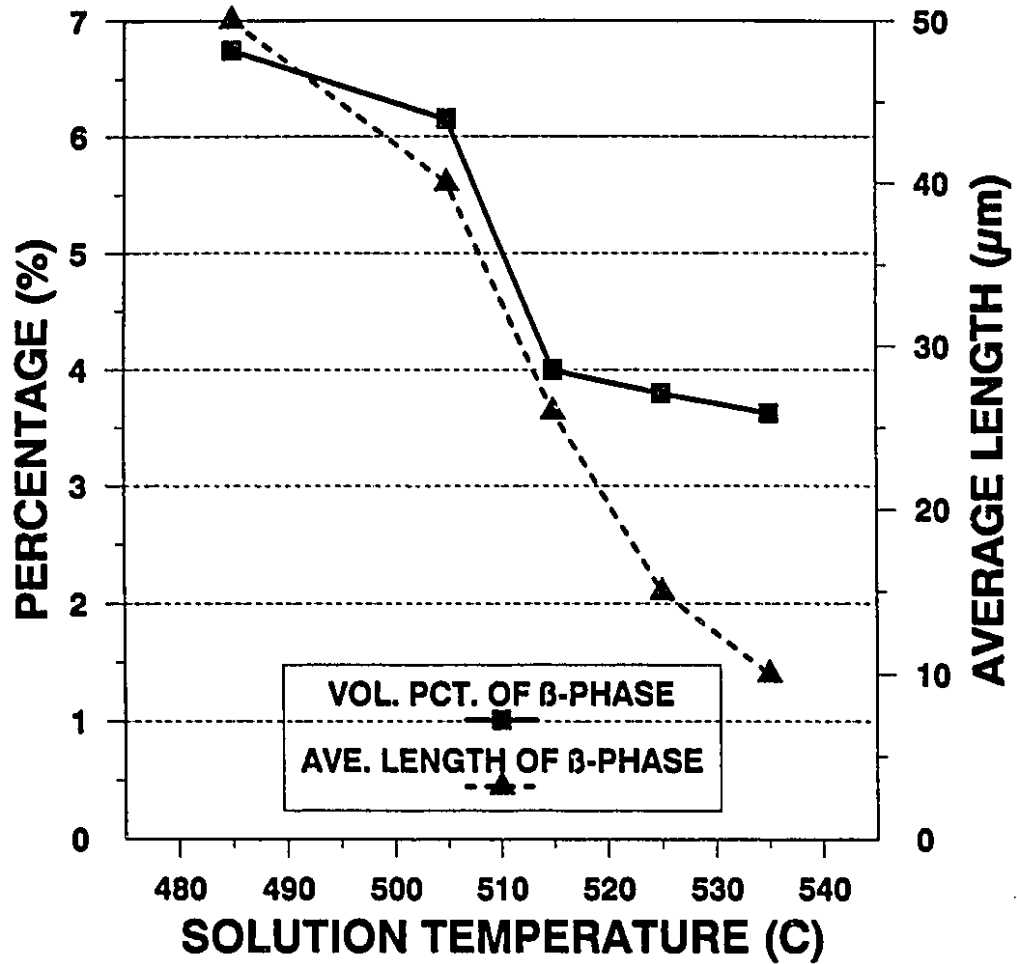


Fig. 6.3 : Image analysis results of manganese-free alloy samples solidified at 10 °C/s.

repeatability of results within close range is greatly affected due to non-uniform distribution (segregation) of various phases in the sample. Nevertheless, the maximum deviation in the measurement of volume percent and average length of the  $\beta$ -phase does not exceed  $\pm 0.15$  percent and  $\pm 15 \mu\text{m}$  respectively. For the increase in solution treatment temperature from  $485^\circ\text{C}$  to  $535^\circ\text{C}$ , the volume fraction of the  $\beta$ -phase decreases by almost 50 percent. It is evident from the plot that the average length of the  $\beta$ -phase platelets drastically decreases to below  $10 \mu$  from an initial  $50 \mu$ .

#### **6.3.1.1.4 : INCIPIENT MELTING :**

The main advantage with non-equilibrium heat treatment is the dissolution of the  $\beta$ -phase platelets with increasing solution temperature. The volume percent and average length of the  $\beta$ -phase decreases to 3.5 % and  $10 \mu$  respectively at a solution temperature of  $535^\circ\text{C}$ . Iron intermetallics dissolve rapidly with increasing solution temperature, but above a certain critical temperature, a large amount of liquid phase forms at grain boundaries and interdendritic regions. The nature and type of incipient melting observed in the present study will be discussed later. Unfortunately, it was not possible to quantify the amount of liquid phase formation at different solution temperatures using image analysis owing to a lack of color contrast between the melted regions and other phases. However, based on visual observation it was seen that the amount of liquid phase formed suddenly increased when the sample was solution treated at  $525$  and  $535^\circ\text{C}$ . Since the relative influence on the mechanical properties of the beneficial dissolution of iron intermetallics in the matrix and the harmful formation of liquid phase cannot be estimated on the basis of microstructural studies alone, the optimum solution treatment temperature is not proposed here. However, it will be dealt with in the following chapter on mechanical properties.

### 6.3.1.2 : IN THE PRESENCE OF MANGANESE :

With the addition of manganese, the iron intermetallics crystallize either in the  $\alpha$ -phase (Chinese script morphology) or as a mixture of  $\alpha$ - and  $\beta$ -phases depending on the Fe/Mn ratio and cooling rate. Since the alloy used in the present study contained only 0.5 % Mn and castings were made at a relatively high cooling rate (10 °C/s), a large proportion of the intermetallics crystallized in the  $\beta$ -phase form with smaller amounts in the form of  $\alpha$ -phase. In order to compare the dissolution behaviour of the iron intermetallics in the presence and absence of manganese, the same solution treatment temperatures were used in both cases.

The addition of manganese is not seen to cause any significant change in the dissolution behaviour of iron intermetallics when solution treated at temperatures below 500 °C (final solidification temperature) with the iron intermetallics remaining essentially undissolved. This is clearly shown in Fig. 6.4(a). However, with increasing solution treatment temperature above 500 °C, the  $\beta$ -phase platelets begin to slowly dissolve non-uniformly along the edges, thus making the platelets appear as serrated needles in polished section. The  $\beta$ -phase platelets do not undergo any fragmentation, and the microstructures of the sample heat treated at 515 and 535 °C, shown in Figs. 6.4 (b) and (c), clearly illustrate this behaviour. One interesting phenomenon observed is that, unlike the  $\beta$ -phase, the  $\alpha$ -phase does not undergo any appreciable dissolution at any of the solution treatment temperatures studied, suggesting that the  $\alpha$ -phase is much more stable compared to the  $\beta$ -phase. Fig. 6.5 shows a photomicrograph of the  $\alpha$ -phase structure in a sample solution treated at the highest temperature used in this study, 535 °C.

Quantitative metallographic results are shown in Figs 6.6 and 6.7. The  $\beta$ -phase decreases by nearly one percent in the microstructure at solution temperatures above the final solidification point, i.e., > 500 °C, but owing to non-uniform dissolution all around its perimeter and its serrated needle-like appearance,

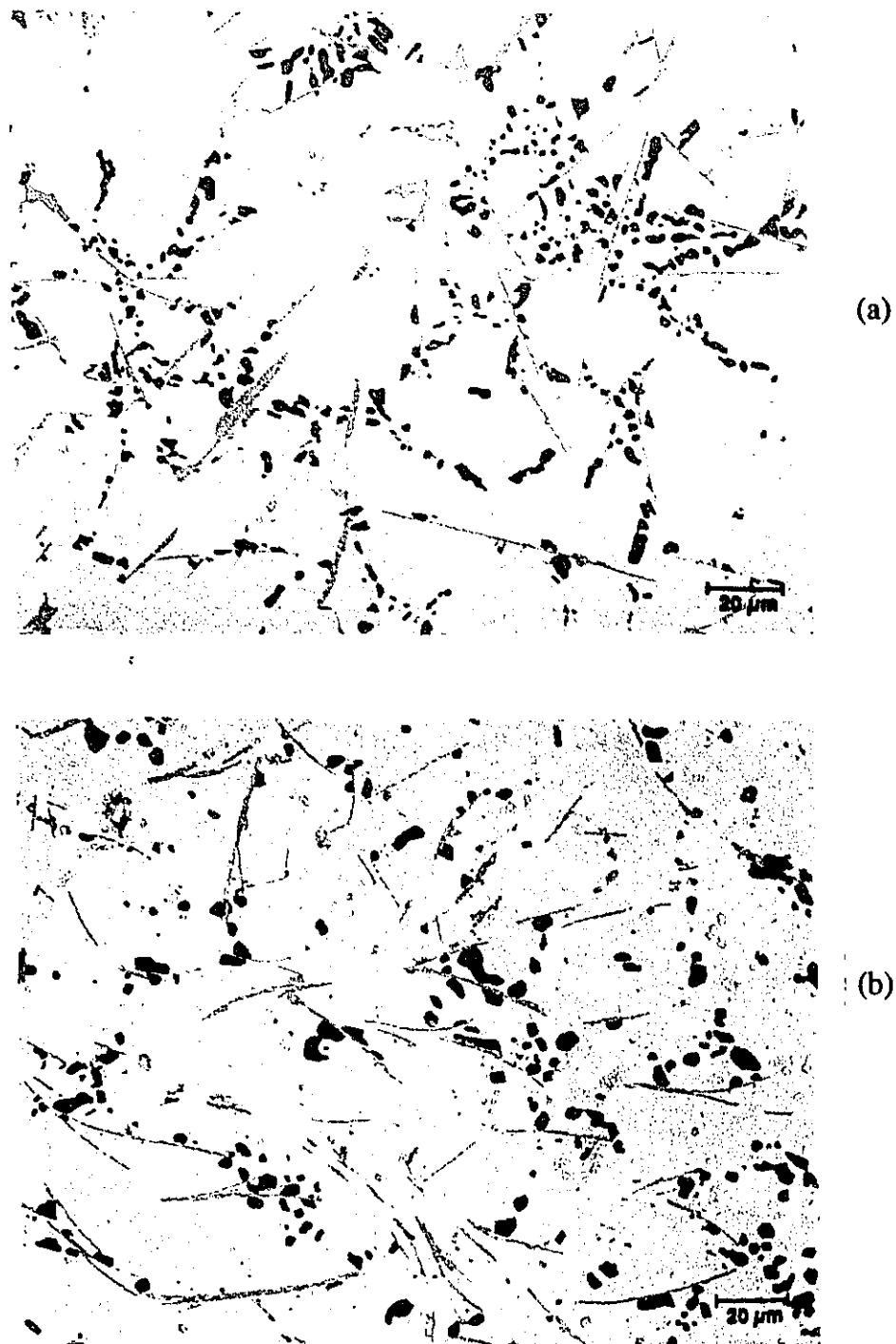
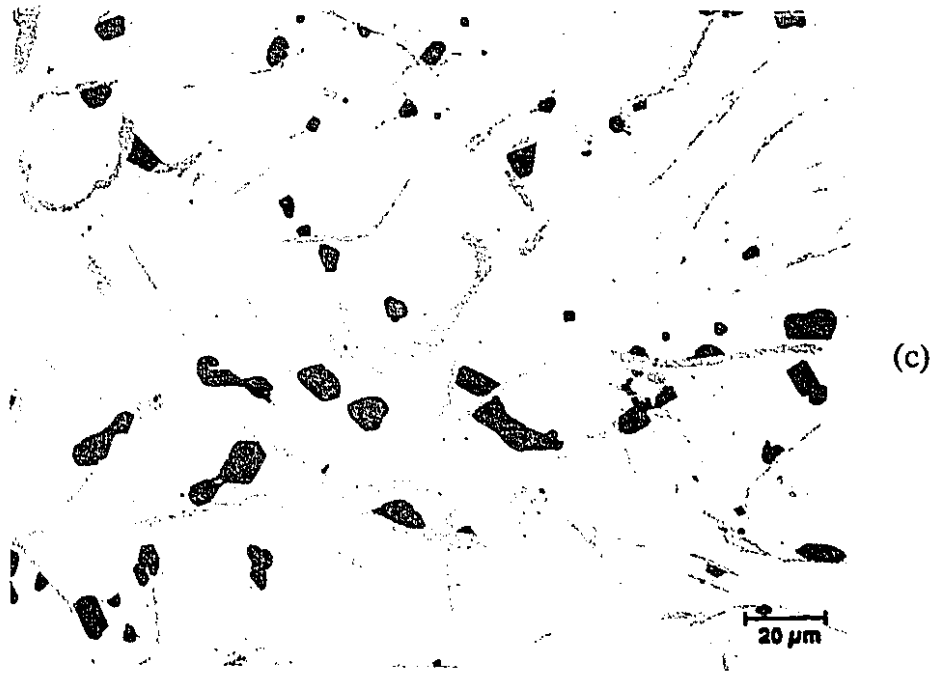


Fig. 6.4 : Photomicrographs of the manganese containing alloy samples at three different solution temperatures of (a) 485 °C , (b) 515 °C and (c) 535 °C (Cooling rate = 10 °C/s).



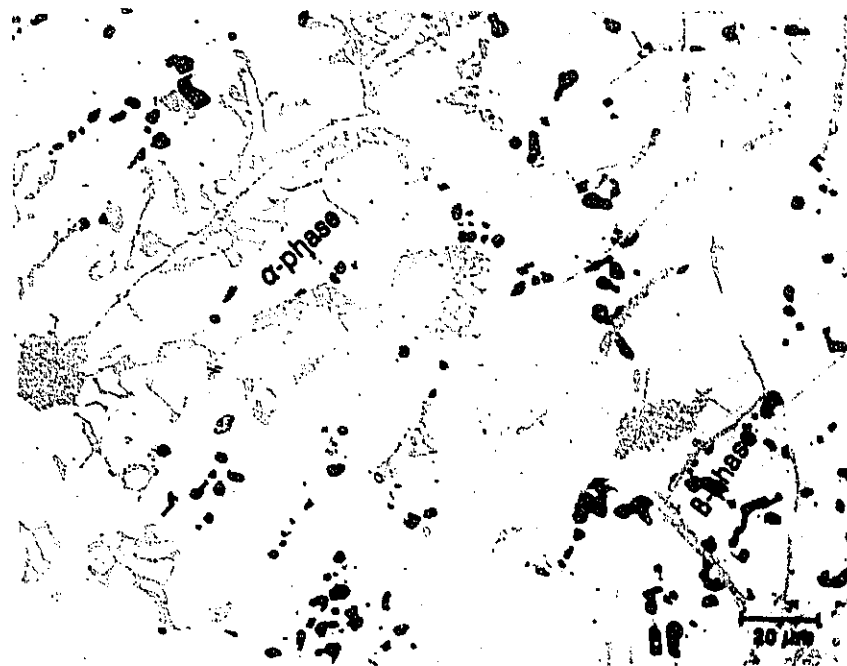


Fig. 6.5 : Photomicrograph of the  $\alpha$ -phase structure in a manganese containing alloy sample solution treated at 535 °C (Cooling rate = 10 °C/s).

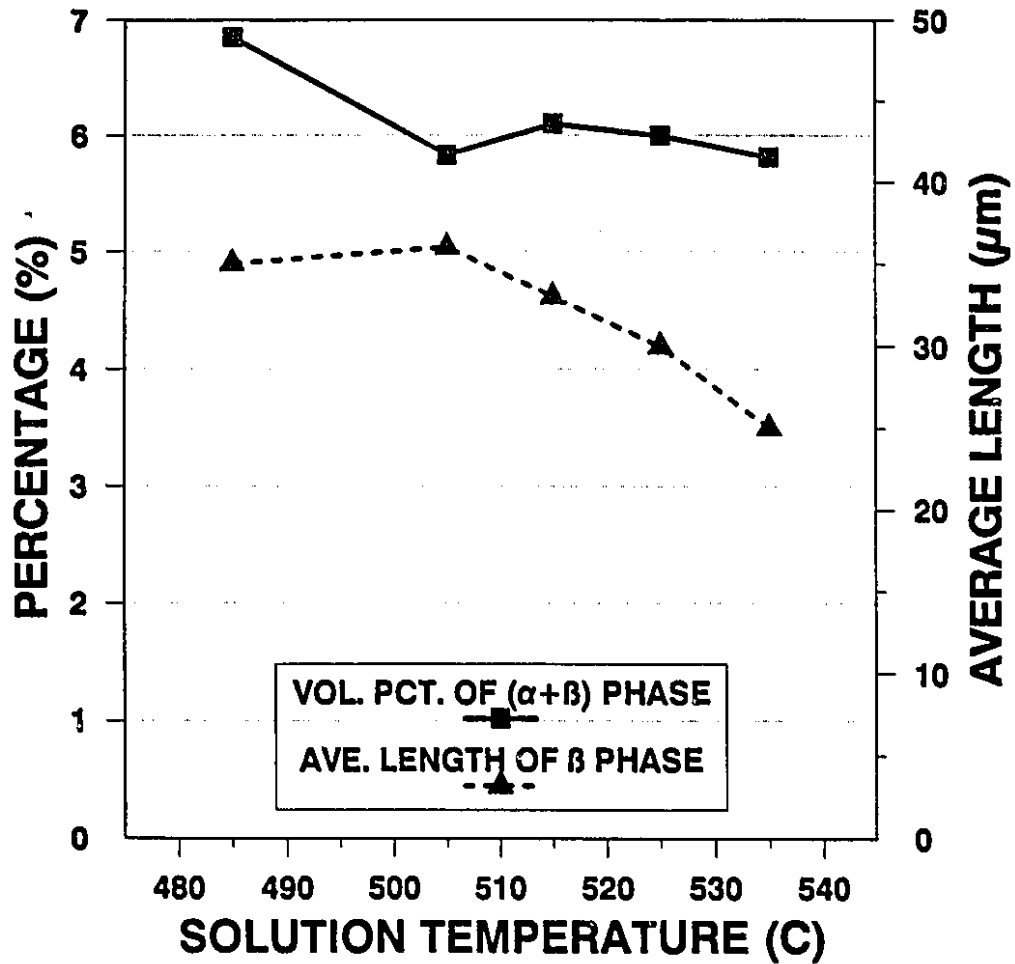


Fig. 6.6 : Image analysis results of manganese containing alloy samples solidified at 10 °C/s.

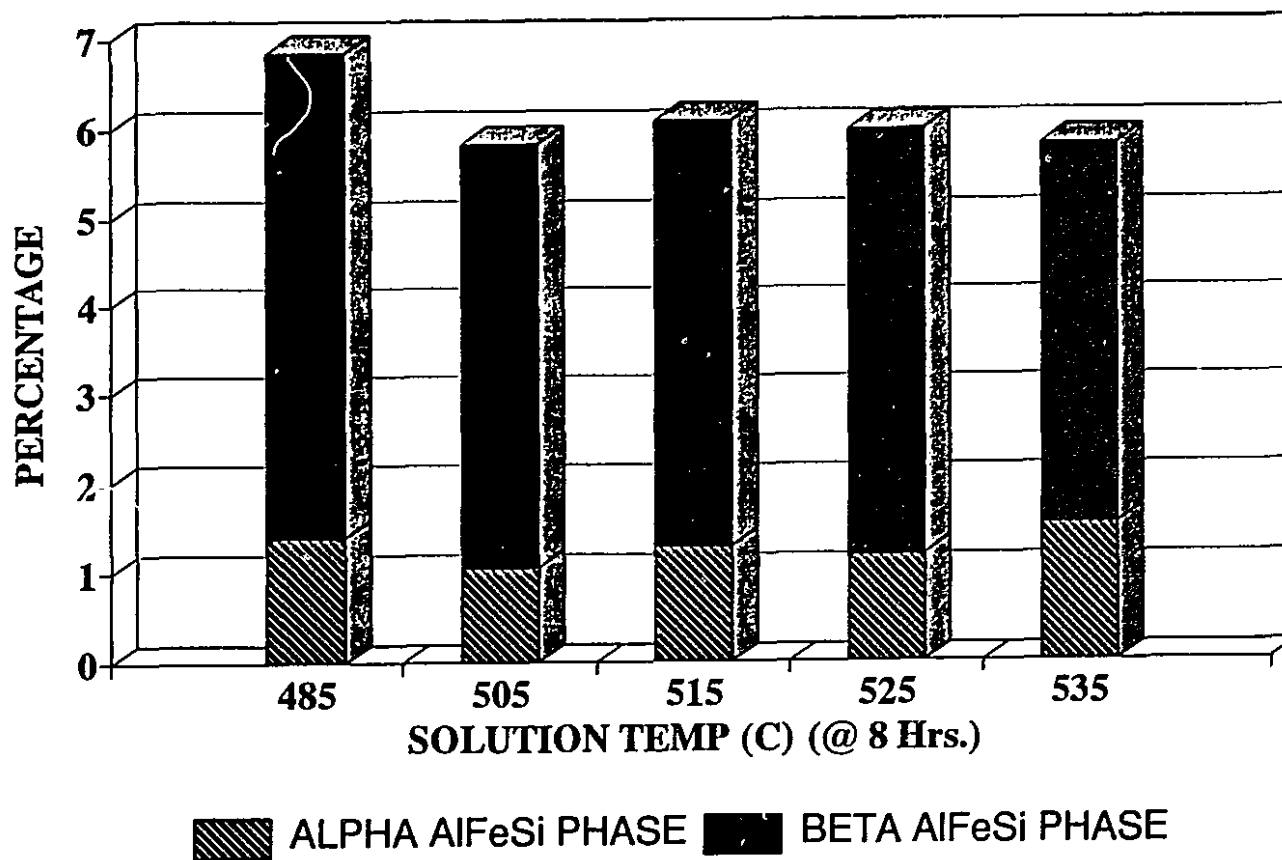


Fig. 6.7 : Bar chart showing the dissolution of iron intermetallics in manganese containing alloys as a function of solution temperature.

image analysis results indicate a lower value compared to the actual one. Unlike the  $\beta$ -phase, the  $\alpha$ -phase remains stable and its volume percent is not seen to be affected by the solution temperature, as shown in Fig. 6.7.

The image analysis results, Fig. 6.6 and 6.7, indicate that the volume percent of total iron intermetallics ( $\alpha + \beta$  phase) decreases only marginally by about one percent, and the average length of the platelets decreases slightly, by about 10 microns. As reported for manganese-free alloys, a large amount of incipient melting occurs once the 520 °C temperature limit is crossed.

### 6.3.2 : EFFECT OF COOLING RATE :

High cooling rates, in general, produce fine microstructures. Therefore, as the cooling rate increases, both the volume fraction and average length and width of the  $\beta$ -phase needles decrease. Since the dissolution of iron intermetallics on heat treatment is a diffusion controlled process, the thinner and shorter are the  $\beta$ -phase platelets, the faster is their fragmentation and/or dissolution. In order to study the effect of size of initial microstructure on the dissolution rate, manganese free and manganese containing alloy samples solidified at a high cooling rate of 15 °C/s were subjected to non-equilibrium heat treatment.

As expected, the dissolution kinetics of the  $\beta$ -phase are much faster in the castings solidified at 15 °C/s compared to those at 10 °C/s. This can be observed by comparing the microstructure of both the alloys heat treated at 515 °C shown in Figs. 6.2(b), 6.4(b) and 6.8.

Image analysis results for the manganese-free alloy samples are presented in Fig. 6.9. Comparing these results with Fig. 6.3, it can be observed that as the cooling rate is increased from 10 to 15 °C/s, the initial volume percent of the  $\beta$ -phase in the as-cast microstructure is less (7 vol. pct. compared to 6). With increasing solution treatment temperatures, the volume percent of the  $\beta$ -phase

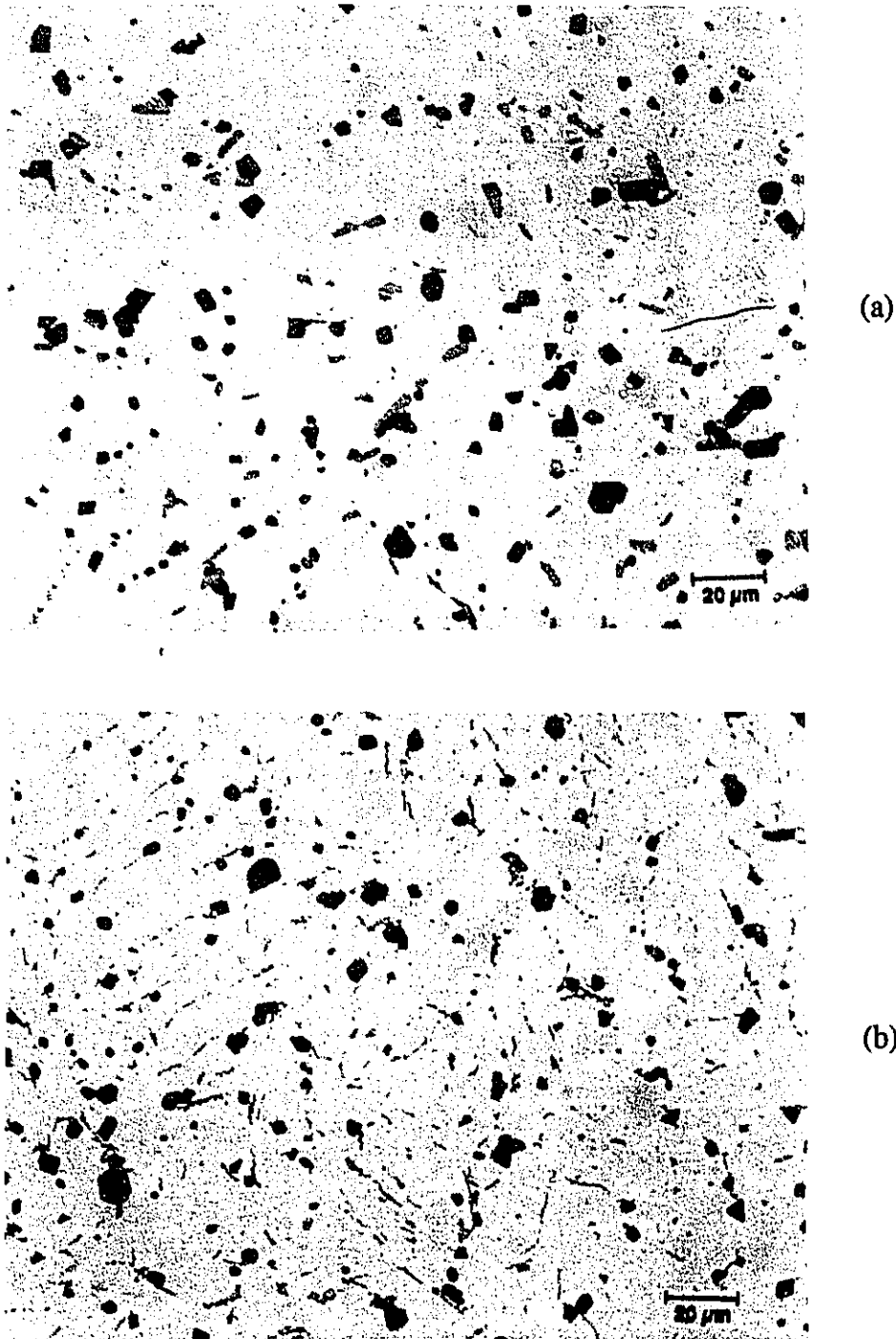


Fig. 6.8 : Photomicrographs showing the dissolution of iron intermetallics in (a) manganese-free and (b) manganese containing alloy samples initially solidified at 15 °C/s and solution treated at 515 °C.

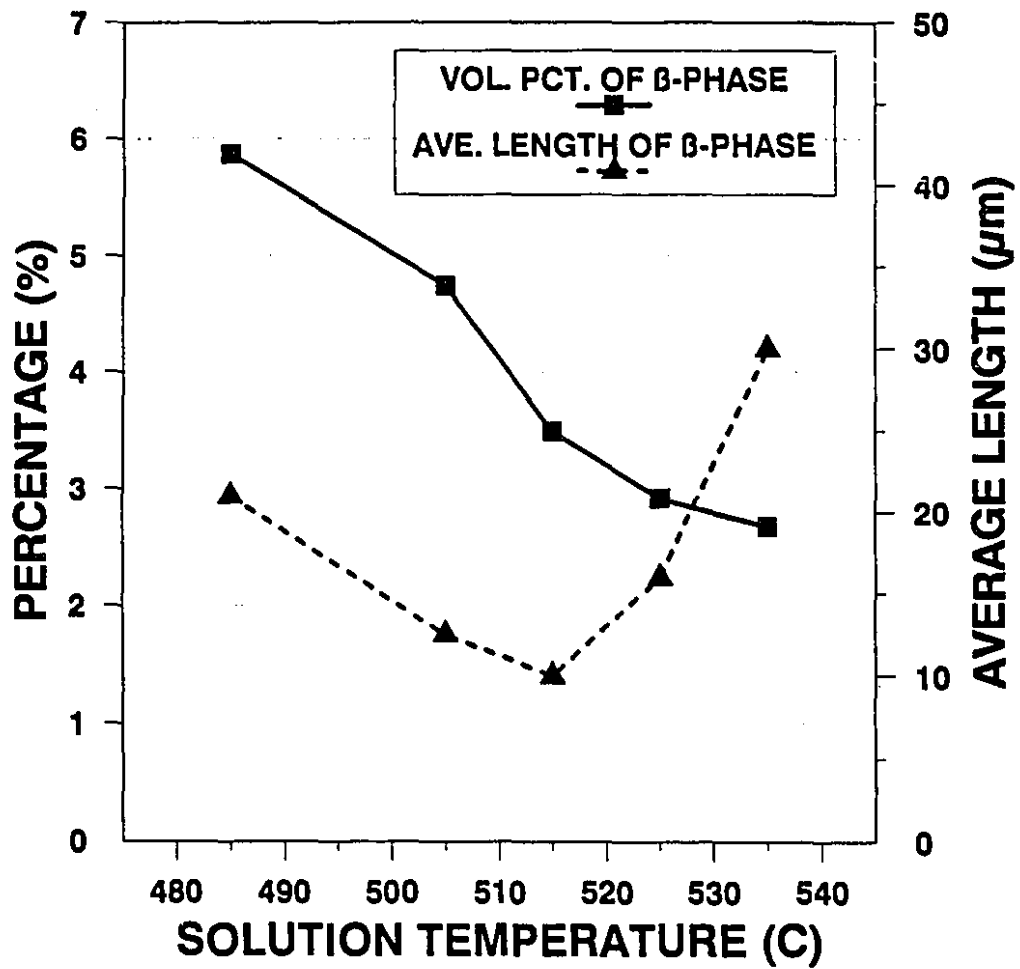


Fig. 6.9 : Image analysis results of manganese-free alloy samples solidified at 15 °C/s.

decreases at a faster rate and it decreases by more than 50 percent for the increase in solution temperature from 485 to 535 °C. The average length of the  $\beta$ -phase platelets decreases with solution temperature until 515 °C, and thereafter it increases. Normally the average length of the  $\beta$ -phase should either decrease, or at least remain unchanged, with increasing solution temperature. The reason for this sudden growth of the iron intermetallics at higher solution temperatures is attributed to the formation of a considerable amount of liquid phase enriched with alloying elements. This liquid phase, on quenching, will lead to re-solidification of silicon and other intermetallics including the  $\beta$ -phase as shown in Fig. 6.10. This particular problem of "partial melting" will be dealt with in section 6.4. Considering the large amount of liquid phase formation and re-precipitation of second phases, it would be advisable to limit solution temperatures to 515 °C or less, for best mechanical properties.

Image analysis results for the manganese containing alloy samples are presented in Fig. 6.11. Once again, the initial volume percent of the iron intermetallics in the as-cast microstructure is lower due to the high cooling rate, as can be seen from Figs. 6.6 and 6.11. Unlike the former case, the volume percent of the iron intermetallics in the manganese containing alloys decreases marginally up to 515 °C and then increases at higher solution temperatures. The plot of average length of the  $\beta$ -phase platelets versus solution temperature follows exactly the same pattern as observed in the manganese-free alloy, with a minimum at 515 °C. At temperatures above 515 °C, both the volume percent and average length of the  $\beta$ -phase increase due to substantial melting along the grain boundaries and subsequent re-precipitation of second phase constituents during quenching. Compared to manganese-free alloys, manganese containing samples show a large amount of re-precipitated iron intermetallics in the melted zone and their shape resembles sludge, as shown in Fig. 6.12. As discussed in earlier chapters,

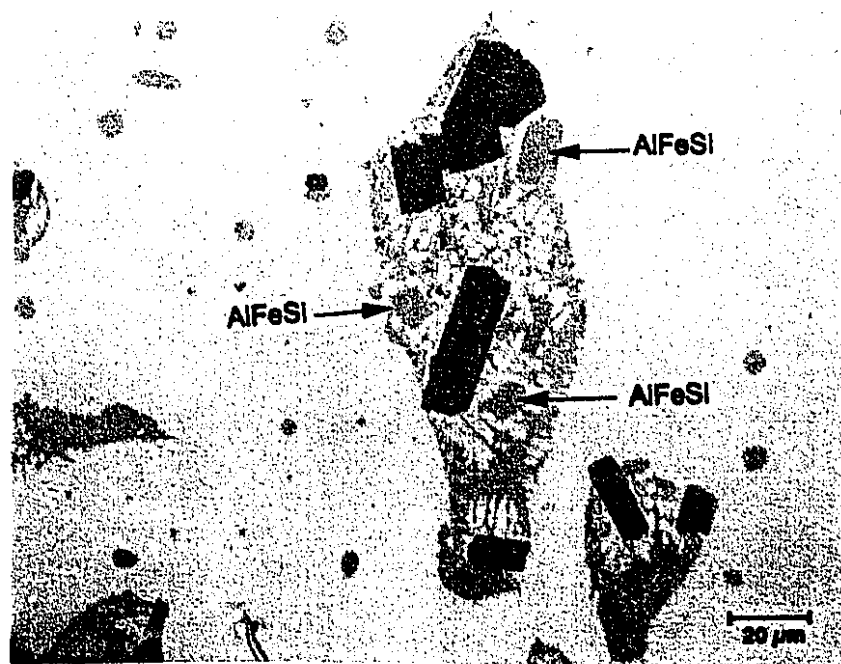


Fig. 6.10 : Re-precipitation of iron intermetallics from melted zone in manganese-free alloys (Cooling rate = 15 °C/s)

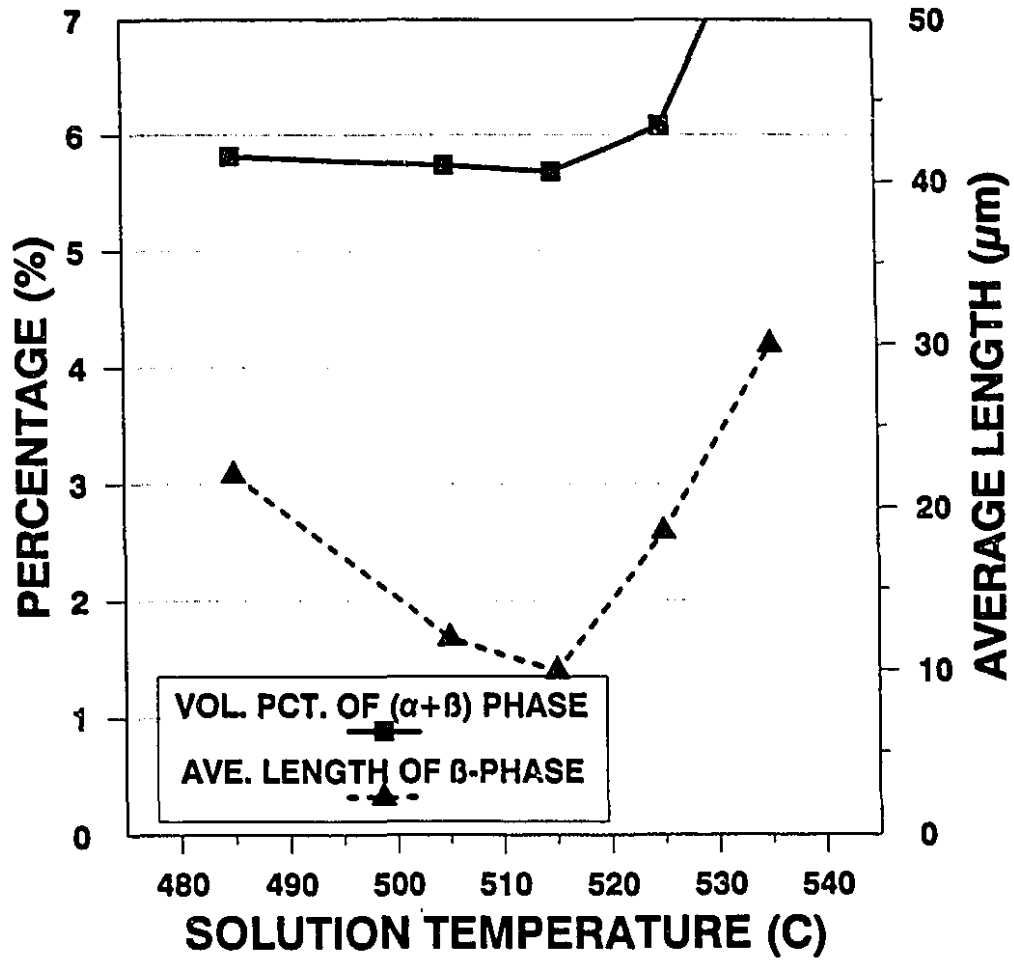


Fig. 6.11 : Image analysis results of manganese containing alloy samples solidified at 15 °C/s.

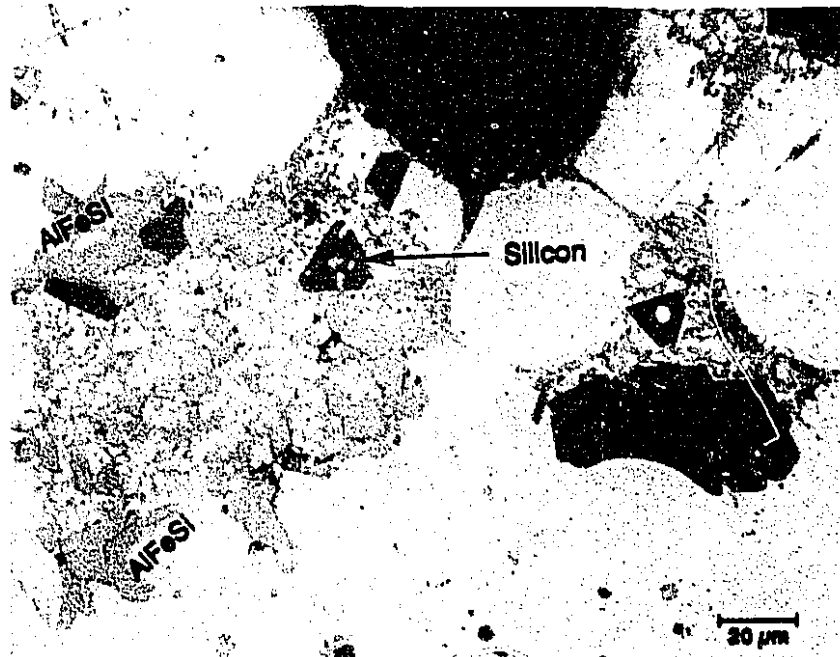


Fig. 6.12 : Re-precipitation of iron intermetallics from melted zone in manganese containing alloys (Cooling rate = 15 °C/s).

manganese has a strong tendency to promote sludge formation when the liquid alloy is held at low temperatures. Under these conditions there is a sharp increase in both volume percent and average length of the iron intermetallics, and once again, the maximum safe temperature for solution treatment without encountering significant liquid phase formation would be 515 °C.

### **6.3.3 : EFFECT OF SOLUTION TIME :**

The dissolution of iron intermetallics during non-equilibrium heat treatment is a diffusion controlled phenomenon which depends on both time and temperature. In the previous sections, the effect of solution temperature on the dissolution kinetics is explained. In order to study the influence of solution time, both manganese-free and manganese containing alloy samples were heat treated at 515 °C for different times ranging from 8 hrs to 168 hrs (one week). This particular temperature, 515 °C, was selected because it results in minimum liquid phase formation, yet yields good dissolution of iron intermetallics in all of the alloys considered.

The image analysis results shown in Fig. 6.13, indicate that the dissolution kinetics of iron intermetallics do not depend on solution time in excess of 8 hours. The volume percent of the iron intermetallics and average length of the  $\beta$ -phase do not show any appreciable variation with times greater than 8 hours. Therefore, it is concluded that solution times of 8 hrs or less are sufficient to achieve maximum dissolution as kinetics depend mainly upon solution temperature.

### **6.4 : PARTIAL MELTING :**

The major problem associated with the non-equilibrium heat treatment is liquid phase formation which increases with temperature. Backerud et al [77]

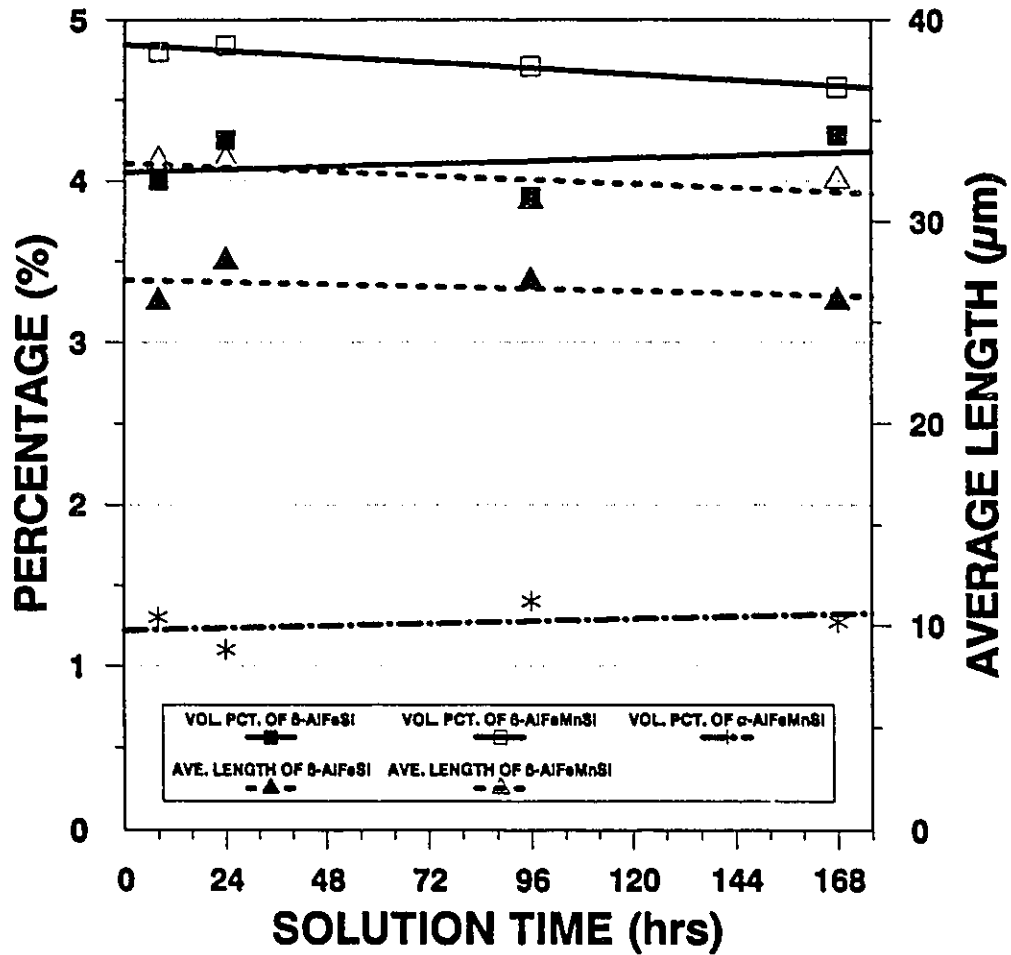


Fig. 6.13 : Image analysis results plotted as a function of solution time for the samples solution treated at 515 °C.

obtained a relationship between fraction of solid ( $f_s$ ) and temperature of solidifying B319.1 alloy as shown in Fig. 6.14 for a cooling rate of 0.6 °C/s. With increasing solution temperature above 490 °C (final solidification point), the amount of liquid phase ( $100-f_s$ ) increases at first marginally and then rapidly near the silicon eutectic reaction. It can be seen from Fig. 6.14 that the fraction of liquid, ( $100-f_s$ ), is about 6 percent at a temperature of 535 °C.

At relatively low solution temperatures, i.e., below 520 °C, melting initially starts at grain boundaries and interdendritic regions. Since grain boundaries often contain fairly high concentrations of alloying elements/impurities, a thin line of liquid first forms. In alloys with a dendritic structure, local melting also occurs at interdendritic regions leading to formation of spherical liquid droplets within the grains. The nature of grain boundary and interdendritic melting is shown in Figs. 6.15 and 6.16 respectively. At high solution temperatures (535 °C), the width of the grain boundary melted zone increases and interdendritic spherical liquid droplets enlarge and coalesce to form a large network of interdendritic liquid. On quenching this liquid, re-precipitation of silicon and other intermetallic particles occurs, and hence the average length and volume fraction of the  $\beta$ -phase platelets increases in samples which are solidified initially at high cooling rates and solution treated above 515 °C. Quenching also leads to a large amount of shrinkage porosity adjacent to melted regions, as shown in Fig. 6.17.

The amount of liquid phase formed on non-equilibrium heat treatment depends greatly on the cooling rate of the castings. Castings solidified at 15 °C/s showed large amounts of grain boundary melting as compared to those solidified at 10 °C/s. The importance of cooling rate during solidification on the amount of liquid phase formation can be understood from Table. 6.1, where,  $f_s$  values are tabulated as a function of temperature at two different cooling rates during freezing [77]. At any given solution temperature, the fraction of liquid phase ( $100-f_s$ ) is

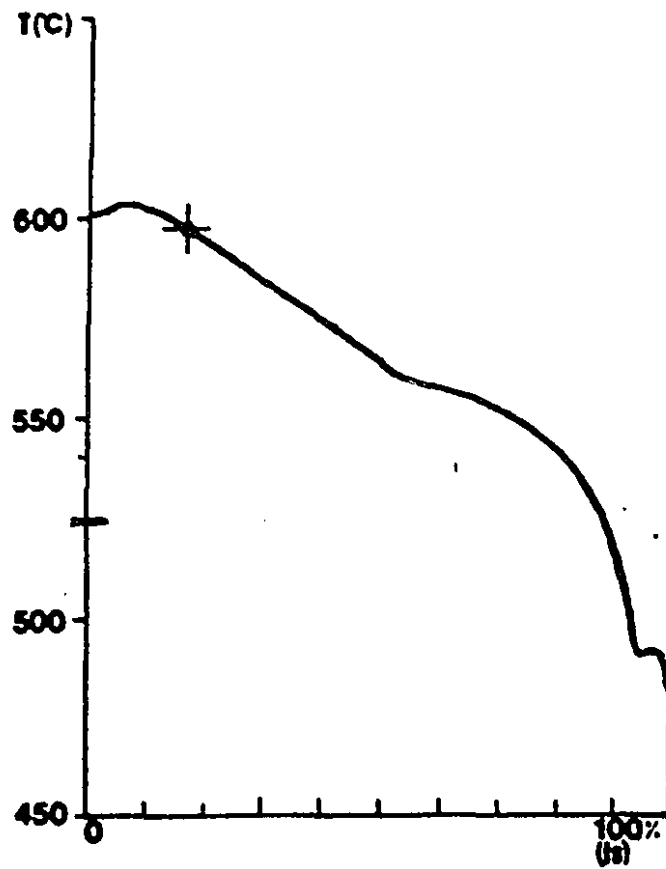


Fig. 6.14 : Fraction solid versus temperature of a B319.1 alloy [77].

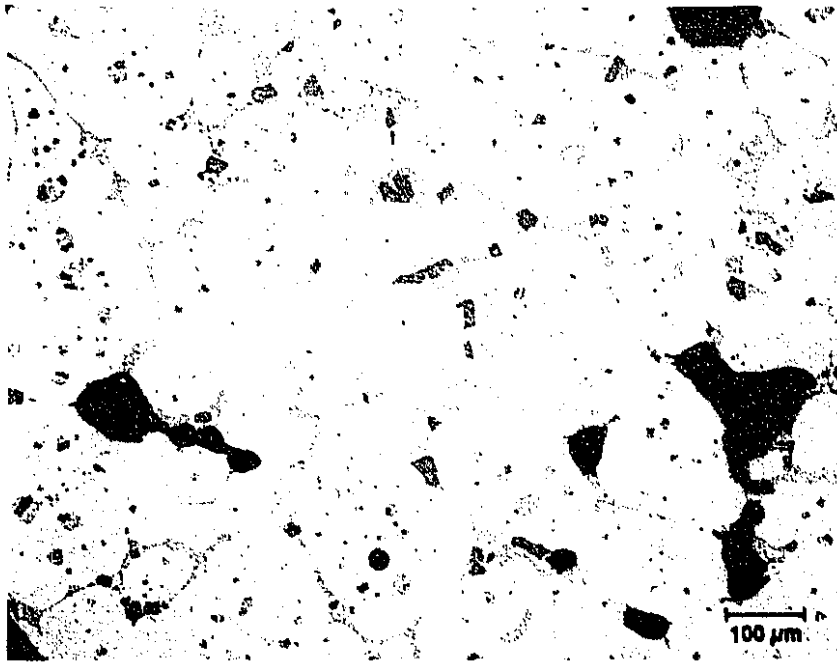


Fig. 6.15 : Grain boundary melting.

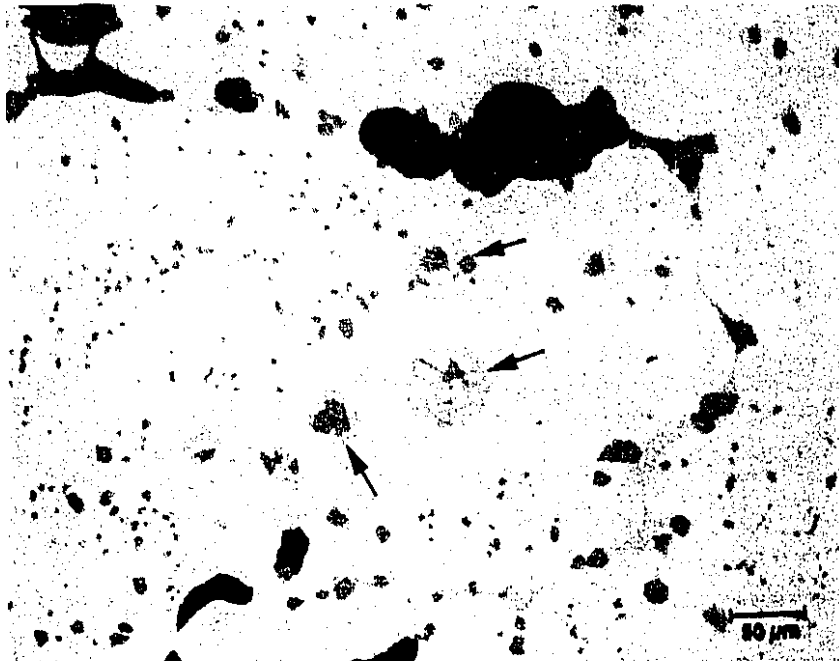
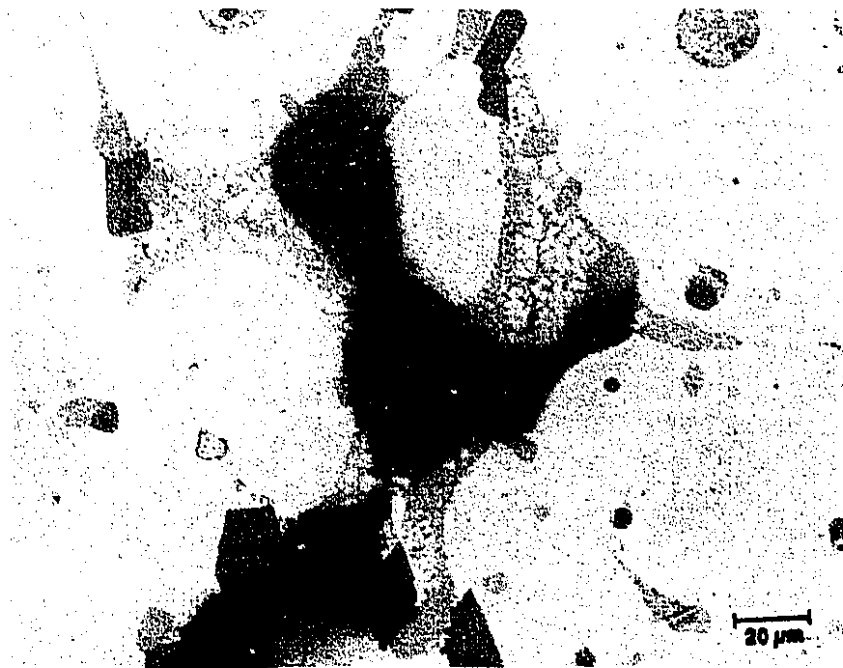


Fig. 6.16 : Interdendritic melting.



**Fig. 6.17 : Shrinkage porosity developed due to sudden quenching of liquid phase.**

higher for the samples initially solidified at 4.4 °C/s, compared to those at 0.3 °C/s. This is due to a higher segregation of solute elements at grain boundaries and interdendritic regions when a sample is initially solidified at higher cooling rates. Samples which are solidified at high cooling rates tend to melt preferentially at interdendritic areas compared to grain boundaries owing to higher segregation there.

The dimensional and density change measurements show no appreciable change for the samples before and after solution treatment at different temperatures ranging from 485 °C to 520 °C. This alleviates the major fear that the non

Table. 6.1 : Fraction solid (fs) as a function of temperature at two different cooling rates [77].

Cooling rate = 0.3 °C/s		Cooling rate = 4.4 °C/s	
Temperature °C	fs (%)	Temperature °C	fs (%)
602-599	9	598-594	32
599-590	26	594-569	47
590-569	47	569-558	60
569-559	53	558-542	74
559-551	71	542-490	91
551-491	94	490-485	94
491-491	98	485-482	98
491-483	100	482-459	100

-equilibrium heat treatment might affect dimensional stability of the castings. However, high solution temperatures of 530 °C and above cause heavy surface oxidation and surface irregularities due to liquid formation. Therefore, care should be exercised to not exceed the 515-520 °C limit.

## **6.5 : DISSOLUTION MECHANISM :**

### **6.5.1 : BASIS OF DISSOLUTION :**

The  $\beta$ -AlFeSi phase is a discontinuous eutectic phase comprising crystals having a thin plate-like morphology. The degree of solubility of the discontinuous phase in the matrix increases with temperature. The dissolution of the  $\beta$ -phase depends on the combined solubility of Fe and Si in aluminum. If the heat treatment temperature is high, the solute atoms and matrix atoms can diffuse cooperatively in the matrix and the dissolution of the  $\beta$ -phase can occur.

### **6.5.2 : NATURE OF DISSOLUTION :**

The  $\beta$ -phase does not dissolve at equilibrium heat treatments, i.e., solution treatment at temperatures below 500 °C, as shown in Fig. 6.2(a) ; however, the phase particles are seen to undergo dissolution through fragmentation and dissolution at tips with non-equilibrium heat treatments. The dissolution rate increases with increasing solution temperature, as shown in Figs. 6.2(b) and 6.2(c). At low solution temperatures, the  $\beta$ -phase platelets undergo necking and separate into segments which retain their original morphology. Due to this fragmentation, the average length of the  $\beta$ -phase particles decreases as shown in Fig. 6.3. The dissolution of the  $\beta$ -phase occurs mainly at the tips of the platelets, and hence, the  $\beta$ -phase platelets shrink lengthwise but do not thin. Therefore, with

increasing solution temperature, the fragmented  $\beta$ -phase platelets shrink more and more and take on the appearance of discrete particles. X-ray mapping of the Fe and Si fields in the microstructure containing two adjacent particles which formed by fragmentation of a single platelet is shown in Fig. 6.18. The absence of Fe and Si at the region between the fragmented needles suggests that these atoms have diffused far into the matrix region.

With increasing solution temperature, fragmentation and dissolution of the  $\beta$ -phase increases. The thinner and smaller the  $\beta$ -phase platelets, as obtained in samples solidified at high cooling rates, the greater the fragmentation and dissolution rate (Fig. 6.8). Once the  $\beta$ -phase plate lengths are decreased to below  $15 \mu$  (approx.), they start thickening along the width, and the platelets become blunt at the tips (Fig. 6.2(c)). The mechanism of  $\beta$ -phase fragmentation and dissolution is illustrated schematically in Fig. 6.19.

### 6.5.3 : DRIVING FORCE :

When a eutectic is subjected to thermal treatments at elevated temperatures, instability of the interface between the phases arises due to an increase in shape perturbations of the discontinuous phase. A common feature of eutectic alloys is a certain degree of solubility of the discontinuous phase in the matrix with increasing solution temperature. However, the solubility of iron and silicon from the  $\beta$ -phase to the matrix is not constant over the entire crystal surface because the  $\beta$ -phase is imperfect and contains minute crevices or lattice mismatches along the plate widths. According to the curvature of the surface, the interfacial energy will vary and dissolution of the  $\beta$ -phase will be affected. For example, the solubility of Fe and Si in the matrix is larger at points such as the crevice locations (A) or the tips (B) than at the flat face of the platelets (Fig. 6.19). During the high temperature treatment, mass transport of solute occurs from areas of high energy.

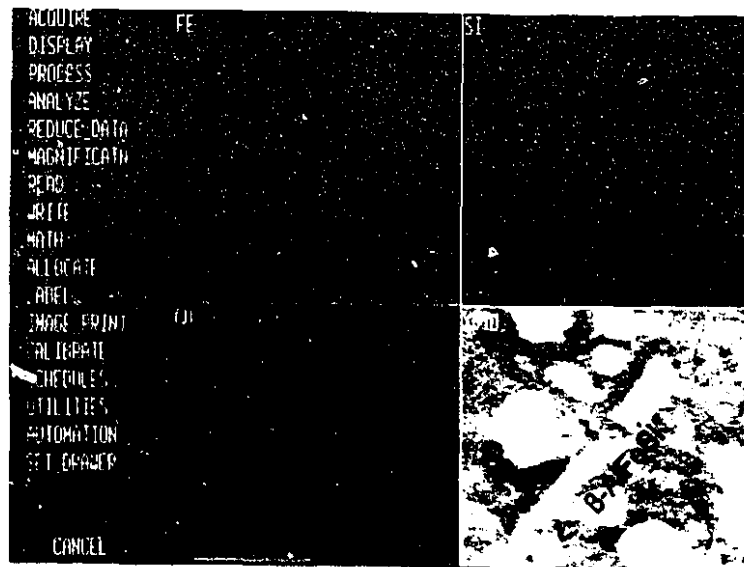


Fig. 6.18 : X-ray mapping of Fe, Si and Cu fields in the microstructure containing fragmented and partly dissolved  $\beta$ -phase particles.

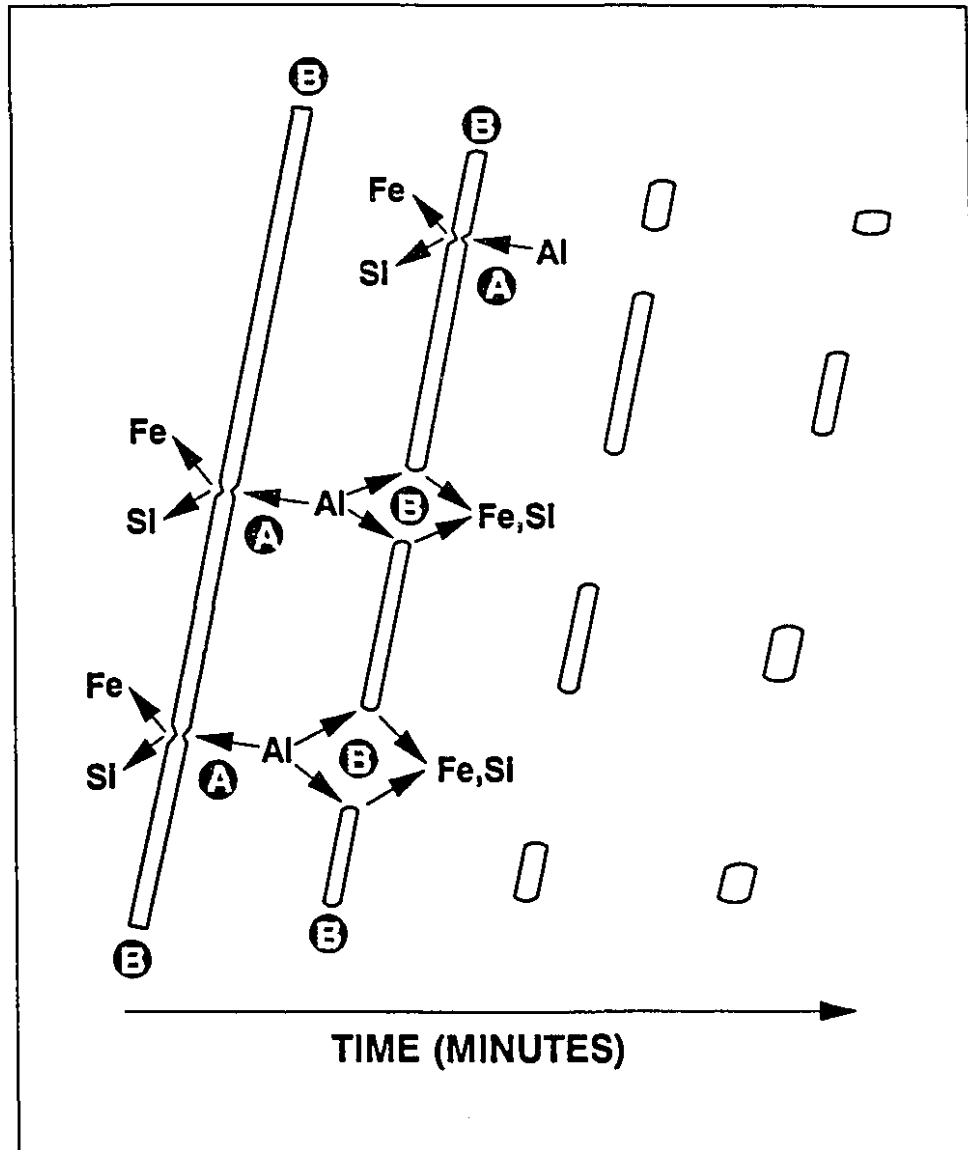


Fig. 6.19 : Schematic illustration of the mechanism of the  $\beta$ -phase fragmentation and dissolution.

The diffusion of solute atoms and matrix atoms at locations A and B will lead to dissolution of the  $\beta$ -phase platelets, causing fragmentation at these points.

Based on the granulation theory of silicon particles suggested by Zhu and Liu [86], the factors affecting the kinetics of the dissolution are proposed to be :

- (i) average length of the  $\beta$ -phase platelets
- (ii) average thickness of the  $\beta$ -phase platelets
- (iii) number of  $\beta$ -phase particles after fragmentation
- (iv) heat treatment temperature
- (v) heat treatment time
- (vi) average energy state of the  $\beta$ -phase platelets

Short, thin and more fragmented platelets, high heat treatment temperature and time, and high average energy state of the  $\beta$ -phase favour easy dissolution.

#### **6.5.4 : IN PRESENCE OF MANGANESE :**

With the addition of a small amount of manganese, iron intermetallics crystallize with a mixture of both  $\beta$ -AlFeMnSi phase (needle-like) and  $\alpha$ -AlFeMnSi phase (Chinese-script) at intermediate and high cooling rates. At all solution temperatures studied, the  $\alpha$ -AlFeMnSi phase is observed to remain stable and to not undergo any dissolution at all. However, the Mn-containing  $\beta$ -phase showed a significant amount of dissolution, but this was sluggish compared to Mn-free  $\beta$ -phase. The major difference observed between the dissolution of  $\beta$ -AlFeSi and  $\beta$ -AlFeMnSi phases is that the former phase dissolves by mass transport only at the plate tips, whereas, the latter dissolves all around its perimeter. This leads to the appearance of serrated needles when a polished section is observed under the microscope (Fig. 6.4(b) and 6.4(c)). The non-uniform dissolution along the plate lengths and appearance of serrated needle-like structure on heat treatment suggests that  $\beta$ -AlFeMnSi is a highly imperfect crystal, and a close examination

under high magnification reveals many interfacial defects and holes in the  $\beta$ -AlFeMnSi platelets.

According to Jonason [76], additions of Mn significantly increase the volume percent of the iron intermetallics for a given iron level, due to the crystallization of the  $\alpha$ -phase ( $\text{Al}_{15}(\text{Fe},\text{Mn})_3\text{Si}_2$ ) rather than the  $\beta$ -phase ( $\text{Al}_5\text{FeSi}$ ). This is also observed in the present work, as shown in Figs. 6.3 and 6.6. Since the  $\alpha$ -AlFeMnSi particles cannot be dissolved during heat treatment, the use of Mn additions may have a negative effect if castings are to be heat treated. The exact reason for the absence of dissolution of the  $\alpha$ -AlFeMnSi particles during non-equilibrium heat treatment is unknown, but it may be speculated that these particles have quite perfect crystals and the dissolution process is hindered by the lack of defects.

## 6.9 : SUMMARY :

A new technique of dissolution of iron intermetallics in Al-Si alloys through non-equilibrium heat treatment has been demonstrated. The influence of shape and size of the iron intermetallics, solution temperature and time, and cooling rate on the dissolution kinetics was studied and is summarized as follows :

(i) With increasing solution temperature, the  $\beta$ -phase platelets dissolve slowly through concurrent fragmentation along plate widths and dissolution at the plate tips.

(ii) Addition of manganese hinders the dissolution kinetics of iron intermetallics. The  $\beta$ -phase undergoes substantial dissolution, whereas, the  $\alpha$ -phase does not undergo any dissolution.

(iii) Solution temperature plays a much more important role in dissolution of iron intermetallics than does solution time.

(iv) The thinner and shorter the  $\beta$ -phase platelets, the faster is the

fragmentation and dissolution process.

(v) The amount of liquid phase formed during heat treatment increases dramatically once a critical temperature is exceeded. This temperature was found to be 520 °C and 515 °C for samples initially solidified at 10 °C/s and 15 °C/s respectively.

# CHAPTER 7

## EFFECT OF IRON INTERMETALLICS ON TENSILE PROPERTIES

### 7.1 : INTRODUCTION :

The mechanical properties of aluminum-silicon alloys are greatly dependent on the alloy structure, especially on the eutectic silicon which may assume an acicular form during solidification of "unmodified" melts, or may be fibrous in nature during solidification of "modified" melts. In alloys such as 319 which contain major alloying elements such as Si, Cu and Mg and impurity elements such as Fe, Mn, Ni and Cr, several brittle intermetallic compounds may form in addition to eutectic silicon particles. Among these brittle compounds, iron intermetallics are considered to be more detrimental to mechanical properties compared to other second phase particles [87]. According to Jonason [76], the eutectic Si phase seems to be the most important crack initiator in AlSi7Cu3Fe0.2 alloy. However, he claims that, for high iron content ( $> 0.6\%$ ), the Fe phases are more fracture initiating than the Si-eutectic.

The iron intermetallic in the plate-like form ( $\beta$ -phase) is considered detrimental due to its stress raising potential at the plate tips [26]. It is common practice to add a small quantity of manganese (Fe:Mn=2:1) to the alloy, which converts crystallization of iron intermetallics in plate-like form ( $\beta$ -phase) to Chinese script form ( $\alpha$ -phase). Owing to its complex morphology, the  $\alpha$ -phase is considered less detrimental to mechanical properties compared to the  $\beta$ -phase. However, addition of Mn significantly increases the volume percent of iron intermetallic for a given iron level [76]. Manganese must, therefore, be considered to be an important Fe phase generator, and thus the total amount of brittle iron-

rich phase increases with additions of manganese. According to Jonason [76], the positive effect of Mn on modifying the morphology of the Fe phase to make the material more resistant to crack-propagation is somewhat offset by the increased brittleness and volume of the phase.

Another possible way to neutralize the detrimental effect of iron intermetallics is by dissolving the harmful  $\beta$ -phase in the matrix through non-equilibrium heat treatment. The usefulness of this particular new technique developed by the author was demonstrated in the previous chapter, with the help of metallography results. Although the non-equilibrium heat treatment proves to be useful in dissolving the harmful  $\beta$ -phase in the matrix, it also leads to formation of grain boundary and interdendritic melting. The metallographic observation suggests that the volume percent of liquid phases increases dramatically once a critical temperature is exceeded, and this temperature is found to be 520 °C and 515 °C for samples solidified at 10 °C/s and 15 °C/s respectively. Since the combined effect of the beneficial dissolution of iron intermetallics and the harmful formation of liquid phases on the mechanical properties cannot be determined from metallographic studies alone, a detailed mechanical property evaluation at different heat treatment conditions was done. This evaluation will provide valuable insight on the usefulness of this new technique of dissolving the harmful iron intermetallics and in understanding the role of these intermetallics in decreasing the mechanical properties.

Tensile properties were evaluated on the as-cast and T6 heat treated alloy samples containing 1.0 % Fe and 1.0 % Fe + 0.5 % Mn. Heat treatment ranges were extended to include both equilibrium and non-equilibrium heat treatment conditions. The improvement of mechanical properties due to dissolution of iron intermetallics was studied by comparing non-equilibrium heat treated high iron alloys (1.0 % Fe) with equilibrium heat treated low iron alloys (0.15 % Fe) which

contained a minimal amount of iron intermetallics. In order to study the influence of size of the iron intermetallics and their subsequent dissolution during non-equilibrium heat treatment, test bars cast at two different cooling rates of 10 °C/s and 15 °C/s were used.

## 7.2 : TENSILE PROPERTIES :

### 7.2.1 : AS-CAST :

The effect of iron and manganese on the tensile properties was studied by pulling the test bars of alloy samples containing 0.15 % Fe, 1.0 % Fe and 1.0 % Fe + 0.5 % Mn in the as-cast condition. Table. 7.1 gives the average tensile properties of these three alloys in the as-cast condition at two different cooling rates of 10 and 15 °C/s. Increasing iron from 0.15 % to 1.0 % decreases yield strength, tensile strength and elongation at both the cooling rates studied, but the effect is more pronounced with samples solidified at the lower rate. Since all the

Table. 7.1 : As-cast tensile properties of alloy samples solidified at two different cooling rates of 10 and 15 °C/s.

ALLOY	YS (MPa)		UTS (MPa)		% ELONGATION	
	10 °C/s	15 °C/s	10 °C/s	15 °C/s	10 °C/s	15 °C/s
0.15 % Fe	167±5	136±4	217±6	233±4	1.4±0.3	1.3±0.2
1.0 % Fe	148±3	134±3	178±7	208±8	0.6±0.1	1.0±0.3
1.0 % Fe + 0.5 % Mn	179±6	143±3	212±5	231±5	0.5±0.1	1.5±0.3

alloys used in the present study were modified with strontium, the microstructure of each sample was fully modified. The decrease in mechanical properties due to addition of iron is attributed mainly to the presence of brittle iron intermetallics in needle-like form ( $\beta$ -phase) whose average length and volume percent increases with decreasing cooling rate. With the addition of 0.5 % Mn, the tensile strength of the material improves to an extent matching that of low iron alloys (0.15 % Fe). This improvement is essentially due to the crystallization of the less harmful  $\alpha$ -phase, and the absence of primary  $\beta$ -phase. Manganese also increases yield strength, but the percent elongation remains unchanged with respect to Mn-free alloys.

### **7.2.2 : EQUILIBRIUM HEAT TREATMENT :**

Among the many variables that affect the mechanical properties of Al-Si-Cu-Mg alloys, heat treatment is a major parameter. Heat treatment affects the microstructure by causing the spheroidization and coarsening of the eutectic silicon on solution treatment, and precipitation of numerous sub-microscopic particles such as  $\text{Al}_2\text{Cu}$  and  $\text{Mg}_2\text{Si}$  during aging. The effect of heat treatment on the 319 alloy was studied by subjecting the test bars to T6-heat treatments recommended by the AA standards [12], i.e., solution treatment at 485 °C for 8 hours, quenched in water at 60 °C and artificially aged at 150 °C for 5 hours.

Tensile properties of 0.15 % Fe, 1.0 % Fe and 1.0 % Fe + 0.5 % Mn alloys under equilibrium heat treated conditions are given in Table. 7.2. Heat treatment in general improves the tensile properties of all the alloys studied. Among these, the 0.15 % Fe alloy exhibits highest tensile strength and % elongation. Although the tensile properties of samples solidified at a high cooling rate (15 °C/s) are superior to those at low cooling rate (10 °C/s), the differences are minimized after heat treatment. Mn containing alloys (1.0 % Fe + 0.5 % Mn)

exhibited the highest yield strength both in the as-cast and the heat treated condition. The summary of as-cast and heat treated tensile property results (Tables. 7.1 & 7.2) reveals that, although the addition of Mn to high iron alloys substantially improves tensile properties, the highest tensile strength and elongation were always exhibited by the alloy with the lowest iron level, ie., 0.15 % Fe.

**Table. 7.2 : Tensile properties of equilibrium heat treated alloy samples initially solidified at two different cooling rates of 10 and 15 °C/s.**

ALLOY	YS (MPa)		UTS (MPa)		% ELONGATION	
	10 °C/s	15 °C/s	10 °C/s	15 °C/s	10 °C/s	15 °C/s
0.15 % Fe	177±3	150±5	269±7	278±6	3.4±0.1	3.0±0.3
1.0 % Fe	176±4	162±7	228±5	239±5	0.95±0.1	1.5±0.1
1.0 % Fe + 0.5 % Mn	186±2	182±2	252±6	263±5	1.6±0.4	1.4±0.3

**7.2.3 : NON-EQUILIBRIUM HEAT TREATMENT :**

As we have seen from the previous sections the high iron alloys (1.0 % Fe) have inferior mechanical properties to the low iron alloys (0.15 % Fe) in the as-cast condition. Manganese additions and/or equilibrium heat treatment do not make the mechanical properties of high iron alloys match those of low iron alloys under similar casting and heat treatment conditions due to the presence of brittle iron intermetallics which do not undergo any morphological changes under equilibrium heat treatment, as shown in Figs. 6.2(a) and 6.4(a).

The only way to reduce the stress raising potential of the  $\beta$ -phase platelets, and thereby improve mechanical properties of high iron (1.0 % Fe) alloys, is by resorting to alternate ways of eliminating or minimizing the amount of harmful  $\beta$ -

phase platelets. In the previous chapter, the process of concurrent fragmentation and dissolution of the  $\beta$ -phase platelets through non-equilibrium heat treatment was demonstrated. In the present section, the usefulness of non-equilibrium heat treatment in recovering the mechanical properties of high iron (1.0 % Fe) alloys will be discussed. Tensile test results of 1.0 % Fe and 1.0 % Fe + 0.5 % Mn alloy samples which were heat treated at different solution temperatures are shown in Figs. 7.1-7.3.

As discussed earlier, since extensive metallographic studies were carried out on the dissolution kinetics of iron intermetallics through non-equilibrium heat treatment, only a limited number of test bars was available for tensile property evaluation. The metallographic studies indicate that the dissolution kinetics of iron intermetallics increases with solution temperature, the amount of liquid phase dramatically increasing once a critical solution temperature of 515 - 520 °C is exceeded. Therefore, for the tensile property evaluation, one batch of samples was solution treated at 515 or 520 °C, another at a temperature above this range i.e., 535 °C, and one or two batches solution treated at a temperature above the equilibrium heat treatment range, i.e., 485 °C, but below that of the critical solution temperature of 515-520 °C.

The tensile strength of all the alloys increases with solution temperature and reaches a maximum value at the optimum solution temperature range of 515 - 520 °C. As expected, the alloys cast at 15 °C/s show higher tensile strength compared to those cast at 10 °C/s, at all solution temperatures, due to the presence of finer  $\beta$ -phase platelets which undergo easy fragmentation and dissolution under non-equilibrium heat treatment. At the solution temperature of 535 °C, just 15 °C above the optimum range, the test specimens failed at very low stresses, typically 60-130 MPa. This behaviour is attributed to the generation of a high volume of liquid phases at grain boundaries and interdendritic regions, which on quenching

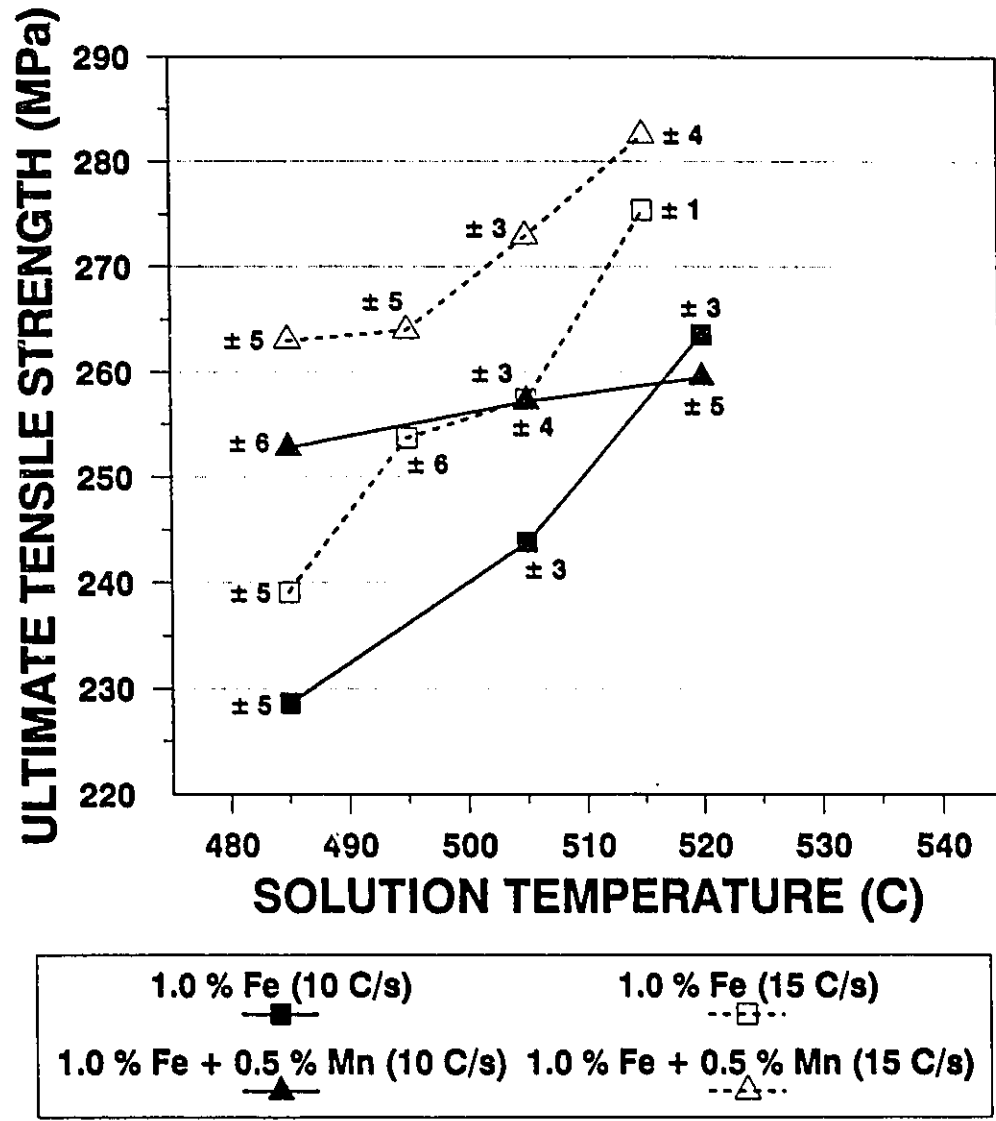


Fig. 7.1 : Effect of non-equilibrium heat treatment on tensile strength of the alloy.

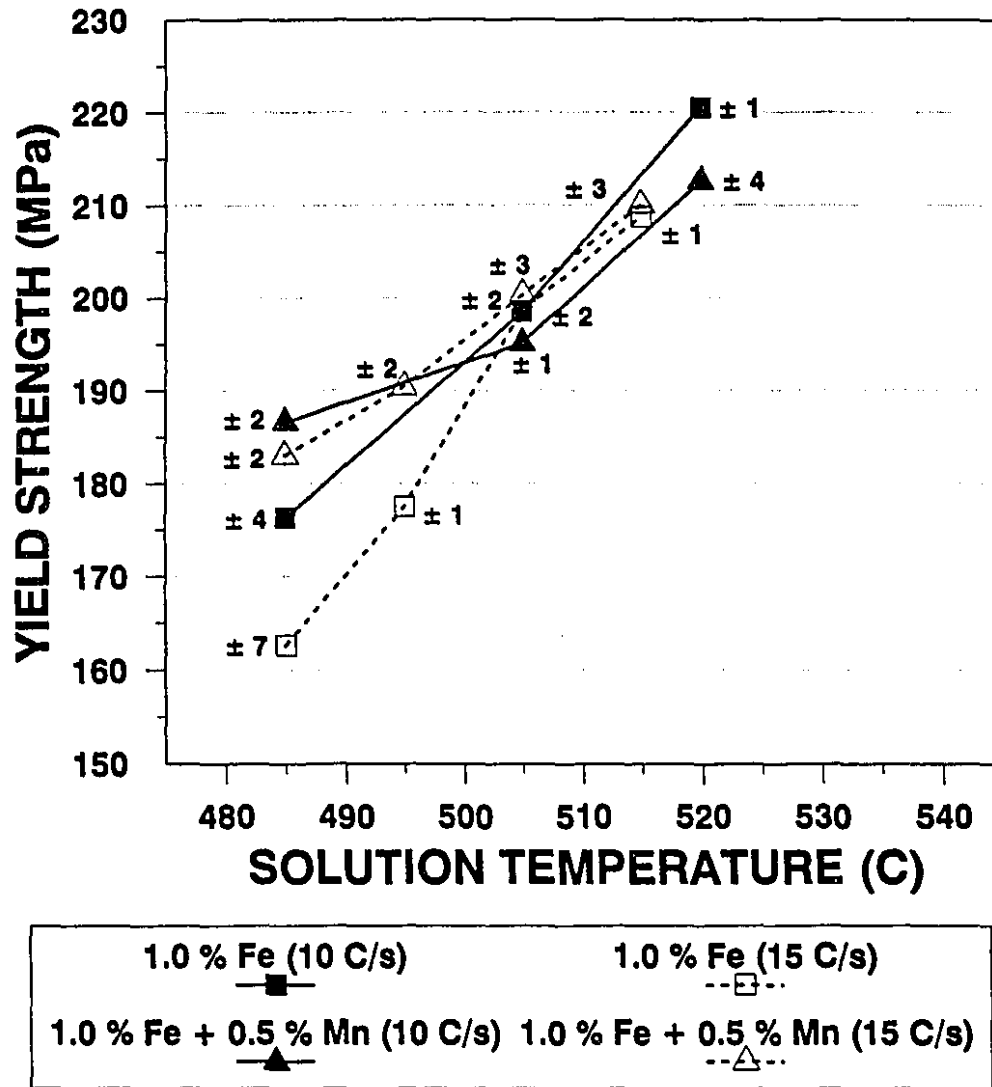


Fig. 7.2 : Effect of non-equilibrium heat treatment on yield strength of the alloy.

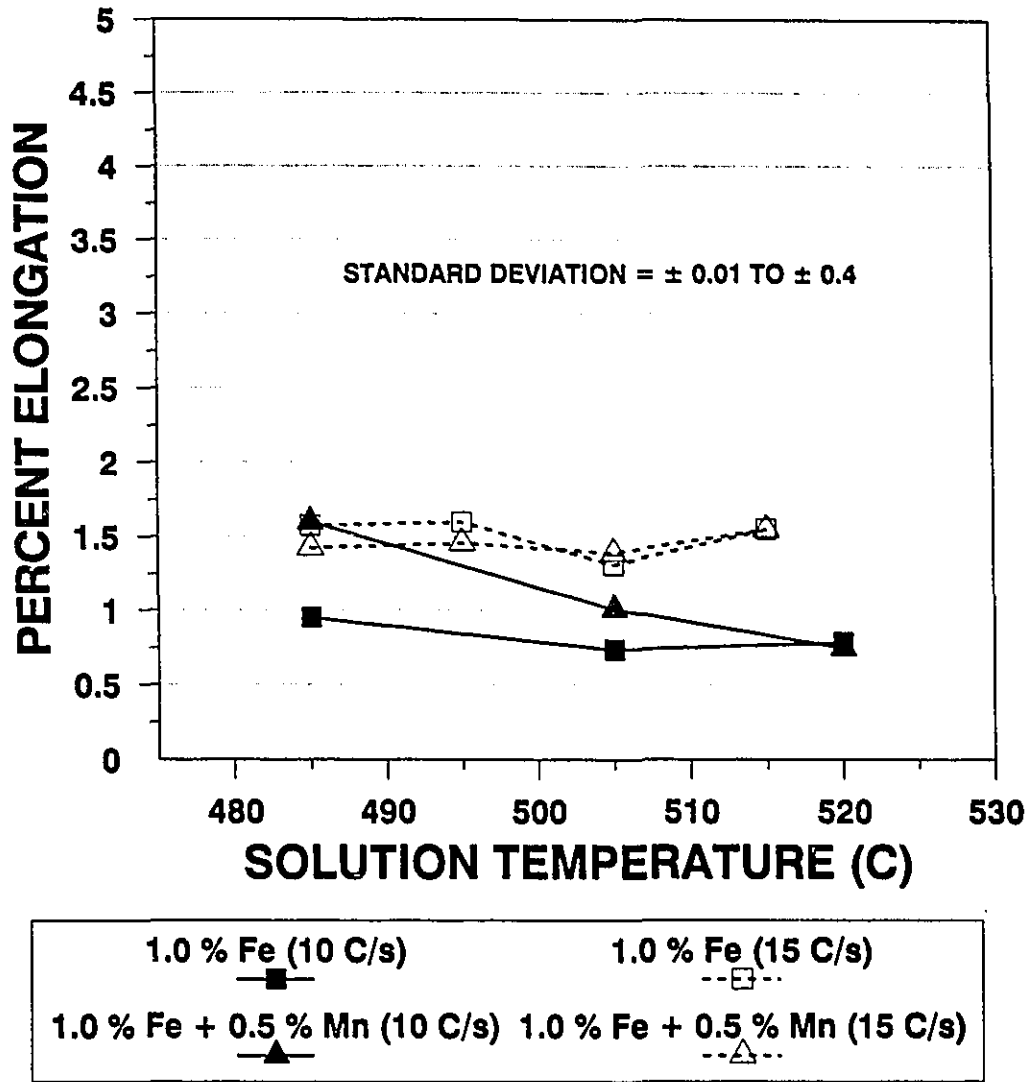


Fig. 7.3 : Effect of non-equilibrium heat treatment on percent elongation of the alloy.

leads to reprecipitation of brittle intermetallic compounds. Although a wide difference in tensile strength values exists between 1.0 % Fe and 1.0 % Fe + 0.5 % Mn alloy under equilibrium heat treatment conditions, the difference decreases to a minimum, or practically nil, at solution temperatures of 515 - 520 °C, and manganese additions lead to no additional strengthening of non-equilibrium heat treated 1.0 % Fe alloys. Based on a comparison with microstructural results, Figs. 6.2, 6.3, 6.4 and 6.6, and tensile property results, Fig. 7.1, it is suggested that the average length of the fragmented  $\beta$ -phase plays a more important role on the mechanical properties than the volume percent of dissolved  $\beta$ -phase.

The yield strength of all alloys increases with solution temperature as shown in Fig. 7.2. Although an appreciable difference in yield strength value (20 MPa approx.) exists between 1.0 % Fe and 1.0 % Fe + 0.5 % Mn alloys at low solution temperature, the difference narrows with increasing solution temperature. This suggests that yield strength of this material is not greatly affected by alloying elements or casting conditions, when solution treated under non-equilibrium heat treatment conditions. Since the samples failed prematurely at the solution temperature of 535 °C, these yield strength values could not be calculated.

319 alloys contain high levels of magnesium (0.3 %) and copper (> 3 %), which decrease the percent elongation to less than 2 percent. The percentage elongation of low iron (0.15 % Fe) alloy samples increases from 1.4 to 3.4 (see Table. 7.2) under equilibrium heat treatment ; however, high iron alloys do not show much variation with solution temperature, see Fig. 7.3, and non-equilibrium heat treatment has no effect on improving the elongation of high iron (1.0 % Fe) alloys. This is possibly due to an increase in the amount of grain boundary and interdendritic melting, and an increase in the amount of secondary precipitates such as  $Mg_2Si$  and  $Al_2Cu$  on artificial aging, with increasing solution temperature.

### **7.3 : FURTHER SCOPE OF NON-EQUILIBRIUM HEAT TREATMENT:**

The present results show that non-equilibrium heat treatment confers a dramatic improvement in mechanical properties of 319 type of alloys. A summary of tensile properties of three different alloy samples (0.15 % Fe, 1.0 % Fe and 1.0 % Fe + 0.5 % Mn) at two different cooling rates (10 °C/s and 15 °C/s) is given in Table. 7.3. The tensile strength and elongation of high iron alloys (1.0 % Fe and 1.0 % Fe + 0.5 % Mn) are inferior to low iron alloy (0.15 % Fe) under similar equilibrium heat treatment conditions. However, under non-equilibrium heat treatment condition, ie., just 30 degrees above the equilibrium solution temperature, the strength properties of high iron alloys exceeds or at least equals that of equilibrium heat treated low iron alloy. This suggests that the negative effects of the presence of iron in Al-Si alloys can be off-set by non-equilibrium heat treatment without resorting to conventional neutralization techniques such as manganese addition and melt superheating. All of these conventional techniques basically convert harmful  $\beta$ -phase needles to less harmful  $\alpha$ -phase Chinese script morphology, but do not restore or improve the mechanical properties. In addition the  $\alpha$ -phase structure has the disadvantage that it cannot be dissolved by non-equilibrium heat treatment.

As shown in Fig. 6.1, the solution temperature range for the non-equilibrium heat treatment is limited by the silicon eutectic temperature, which is 537 °C as determined from the thermal analysis curve. It is well known that certain alloying elements alter the eutectic temperature and any element which increases the silicon eutectic temperature would provide a greater degree of dissolution of iron intermetallics through non-equilibrium heat treatment without the introduction of a high amount of liquid phase.

Table. 7.3 : Summary of tensile properties of as-cast, equilibrium and non-equilibrium heat treated samples.

(a) Cooling rate = 10 °C/s

ALLOY	YS (Mpa)			UTS (Mpa)			% ELONGATION		
	AS-CAST	EQU 485 °C	NON-EQU 520 °C	AS-CAST	EQU 485 °C	NONEQU 520 °C	AS-CAST	EQU 485 °C	NON-EQU 520 °C
0.15 % Fe	167±5	177±3	-	217±6	269±7	-	1.4±0.3	3.4±0.1	-
1.0 % Fe	148±3	176±4	220±2	178±7	228±5	263±3	0.6±0.1	0.95 ± 0.01	0.78 ± 0.03
1.0 % Fe + 0.5 % Mn	179±6	186±2	212±5	212±5	252±6	260±5	0.5±0.1	1.6±0.4	0.75±0.1

(b) Cooling rate = 15 °C/s

ALLOY	YS (Mpa)			UTS (Mpa)			% ELONGATION		
	AS-CAST	EQU 485 °C	NON-EQU 515 °C	AS-CAST	EQU 485 °C	NON-EQU 515 °C	AS-CAST	EQU 485 °C	NON-EQU 515 °C
0.15 % Fe	136±4	150±5	-	233±4	278±6	-	1.3±0.2	3.0±0.3	-
1.0 % Fe	134±3	162±7	208±1	208±8	239±5	275±1	1.0±0.3	1.5±0.1	1.6±0.07
1.0 % Fe + 0.5 % Mn	143±3	182±2	210±3	231±5	263±5	282±3	1.5±0.1	1.4±0.3	1.6±0.2

As discussed in the previous chapters, removal of 0.1 % Mg increases the silicon eutectic temperature by 10 degrees C. Therefore 319 alloy with 0.003 % Mg has a silicon eutectic temperature 30 degrees C above that of 0.3 % Mg alloys. Moreover, the average length of the  $\beta$ -phase platelets decreases with increasing silicon eutectic temperature. Therefore non-equilibrium heat treatment on 0.003 % Mg alloys containing 1.0 % Fe was studied in order to exploit the inherent advantages possessed by this technique. Figs. 7.4 (a) & (b) show the structure of samples in the as-cast and solution treated at 535 °C (for 8 hrs.) condition. In the as-cast condition, the  $\beta$ -phase needles are thin and short, and silicon particles are fibrous in nature ; however, on heat treatment, silicon particles spheroidize and coarsen, and the  $\beta$ -phase needles undergo fragmentation and spheroidization. The final microstructure, Fig. 7.4(b), shows a uniform distribution of spheroidized silicon and iron intermetallic particles. Such a structure should exhibit superior mechanical properties.

Encouraged by the superior results from the present study a similar project on the same alloy (319) but containing low magnesium (0.001 % Mg) and iron (0.15 % Fe) was initiated by Gauthier et al [88]. Their results shown in Figs. 7.5-7.7, also confirm the observation of increased tensile properties with increasing solution temperature. Although these authors suggest an optimum solution temperature of 515 °C, their paper does not indicate clearly how they arrive at the optimum temperature value of 515 °C. At any rate, their results indicate that a value of 535 °C or higher is possible. The work of Gauthier et al also supports the present conclusion that the solution temperatures play a more important role in improving the tensile properties than does solution time, once a minimum solution time of 8 hrs. is exceeded.

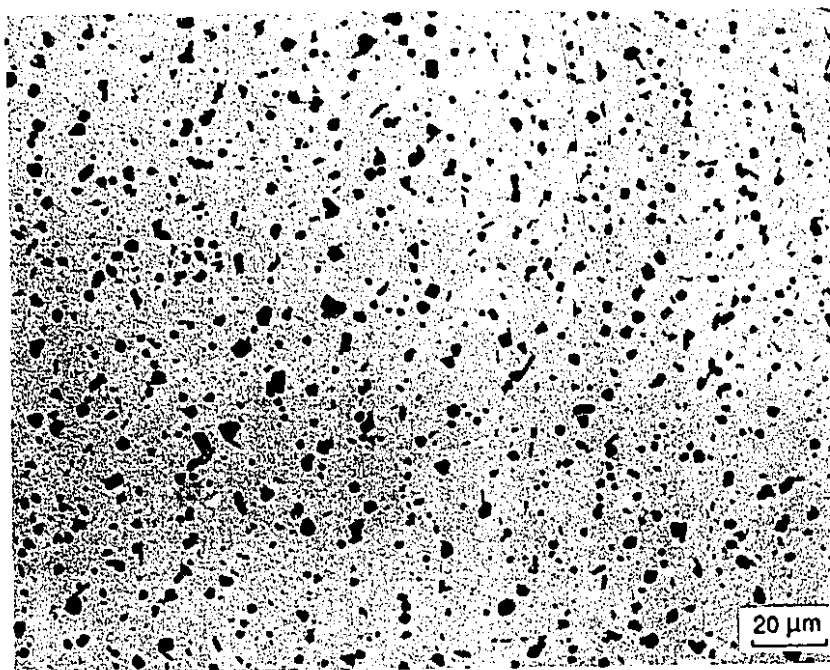
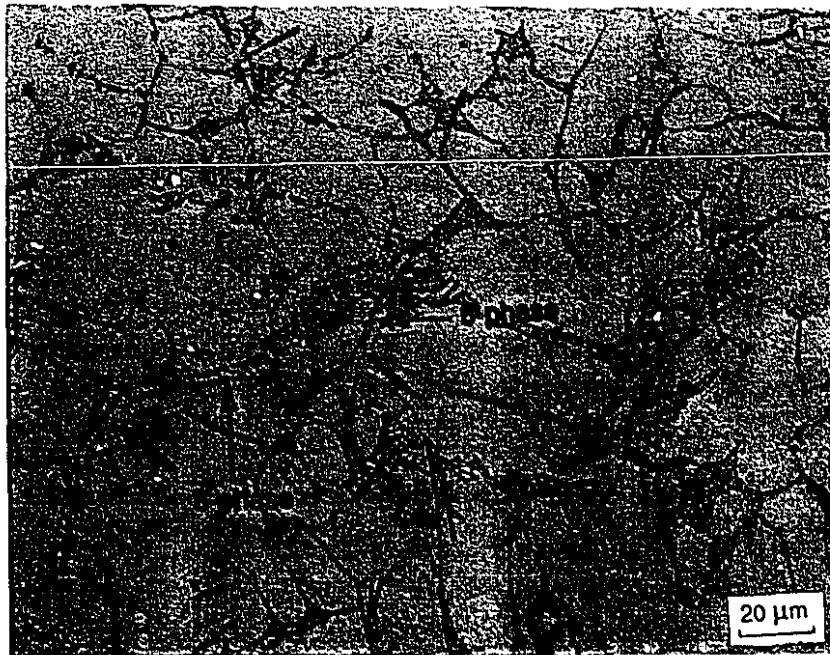


Fig. 7.4 : (a) As-cast and (b) solution treated at 535 °C, microstructure of low magnesium alloys (0.003 % Mg) (Cooling rate = 20 °C/s).

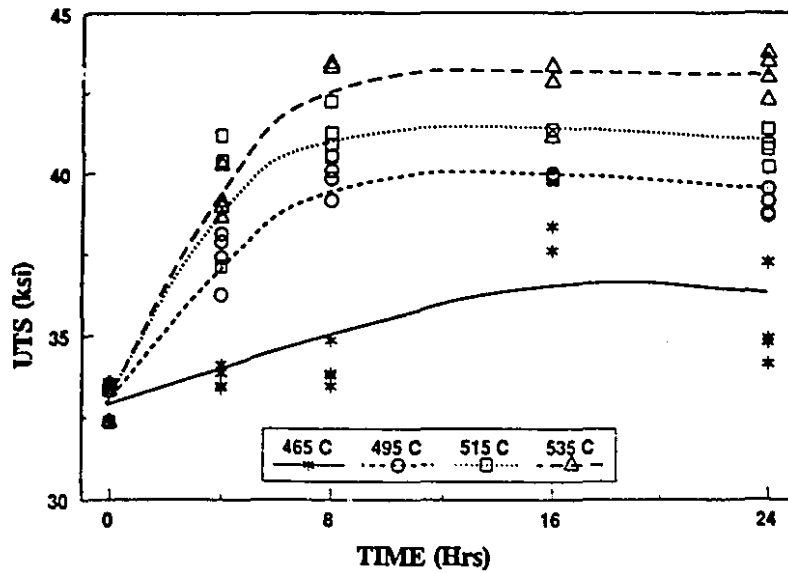


Fig. 7.5 : Plot of tensile strength vs. solution time, as a function of solution temperature, for low magnesium (0.001 %) alloys [88].

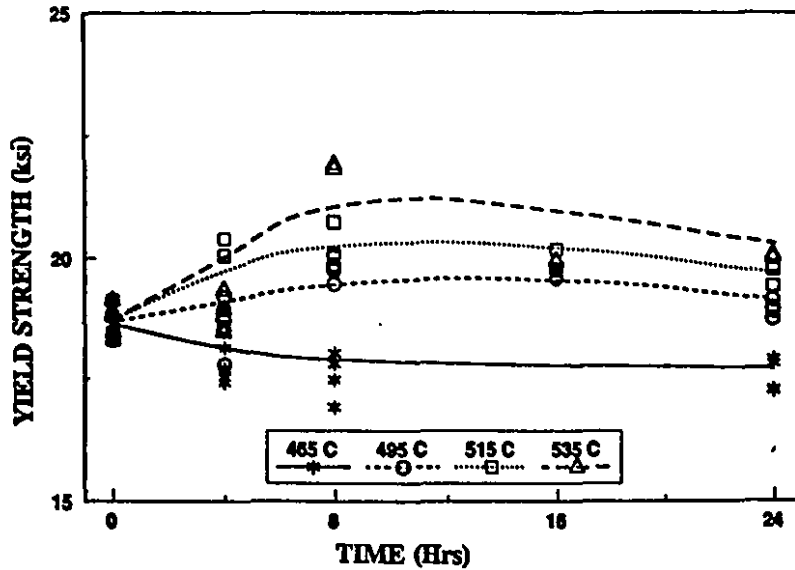


Fig. 7.6 : Plot of yield strength vs. solution time, as a function of solution temperature, for low magnesium (0.001 %) alloys [88].

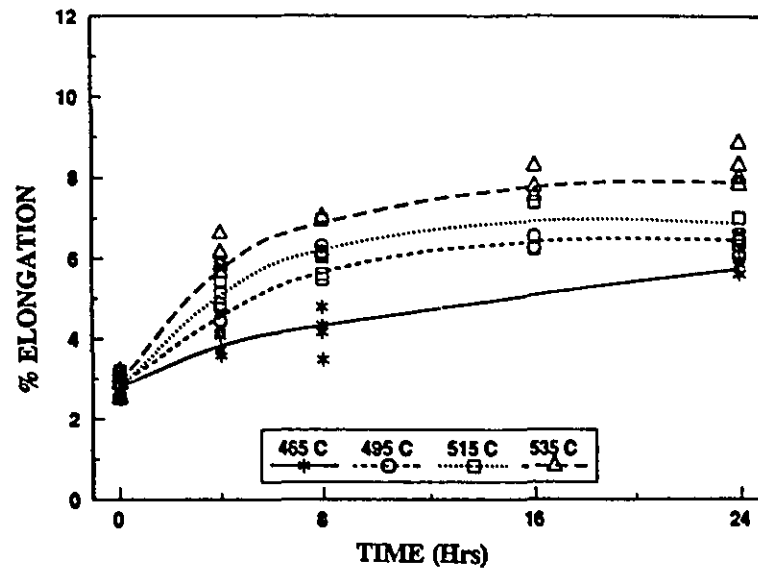


Fig. 7.7 : Plot of percent elongation vs. solution time, as a function of solution temperature, for low magnesium (0.001 %) alloys [88].

#### **7.4 : FRACTURE MECHANISMS :**

In order to investigate crack propagation through iron intermetallics, SEM fractography analysis was carried out and some typical results are shown in Figs. 7.8 and 7.9. From Fig. 7.8, it can be seen that the crack propagates along the boundary between the  $\beta$ -phase platelets and the aluminum matrix suggesting poor interphase boundary cohesion. This is clearly shown by arrows in Fig. 7.8. Mondolfo [28] has also reported that the  $\beta$ -phase is very hard and brittle and has a relatively low bond strength with the matrix. According to Jonaston et al [76], not all the  $\beta$ -phase platelets in the vicinity of the fracture zone contribute to crack propagation, but only those aligned parallel to the fracture direction favour crack propagation. In the case of the  $\alpha$ -phase, the crack propagates through the iron compound, as shown in Fig. 7.9. This probably is the reason for the better strength properties associated with the  $\alpha$ -phase. These observations were confirmed by optical microscope studies on polished samples which were cut in the transverse direction (as described in chapter 3), the results of which are shown in Figs. 7.10 and 7.11.

In heat treated samples, cracks propagate mainly through silicon particles, leading to interdendritic fracture. At the higher solution temperatures of 535 °C, owing to grain boundary melting, fracture occurs along the grain boundaries and fracture surface appears bright and grainy.

#### **7.5 : SUMMARY :**

Tensile properties were evaluated on the as-cast, equilibrium heat treated and non-equilibrium heat treated alloy samples containing 1.0 % Fe and 1.0 % Fe + 0.5 % Mn. The influence of initial solidification rate of test bars on the tensile properties was also studied and is summarized as follows :



Fig. 7.8 : SEM picture showing crack propagation along the boundary between the  $\beta$ -phase platelets and aluminum matrix.



Fig. 7.9 : SEM picture showing crack propagation through the  $\alpha$ -phase.

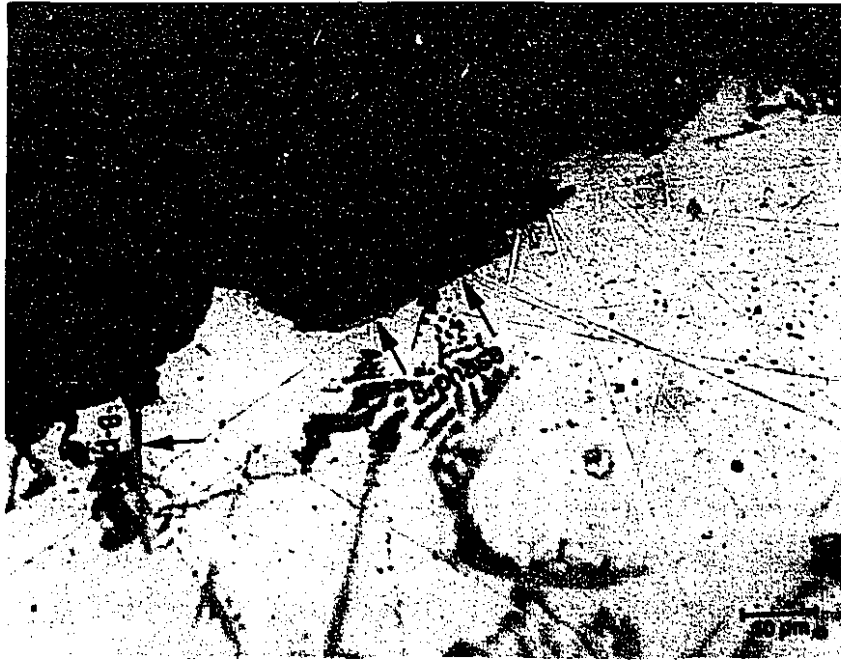


Fig. 7.10 : Optical photograph showing fracture along the boundary between the  $\beta$ -phase and aluminum matrix.



Fig. 7.11 : Optical photograph showing fracture through the  $\alpha$ -phase colony.

- (i) Addition of iron decreases yield strength, tensile strength and elongation at all cooling rates studied ; however, neutralization of these high iron alloys with manganese improves tensile and yield strengths.
- (ii) Equilibrium heat treatment improves properties of all alloys studied ; however, low iron alloys exhibit the highest improvement.
- (iii) Non-equilibrium heat treatment increases the strength properties of high iron alloys matching that of low iron alloys. The optimum solution treatment temperature was found to be 515-520 °C.
- (iv) Fractography results indicate that the  $\alpha$ -phase is more fracture resistant compared to the  $\beta$ -phase.

# CHAPTER 8

## CONCLUSIONS AND FUTURE WORK

### 8.1 : CONCLUSIONS :

In this research work, the crystallization behaviour during solidification and the dissolution behaviour during heat treatment of iron intermetallics in a 319 alloy have been thoroughly investigated by microstructure and mechanical property studies. Microstructural studies were aided by metallography and thermal analysis, while, mechanical properties were evaluated by tensile tests. The main conclusions that can be drawn from the present study are as follows :

#### 8.1.1 : FROM THE CRYSTALLIZATION STUDIES :

- 1 In the absence of manganese, the iron compound crystallizes only in the stable  $\beta$ -phase, at cooling rates up to 20 °C/s. The volume fraction and size of the  $\beta$ -phase platelets increases with increase in iron content and decreasing cooling rate.
- 2 The addition of iron decreases DAS and affects eutectic silicon particle size as nucleation and growth of silicon crystals takes place on the  $\beta$ -AlFeSi platelets, thus minimizing isothermal dendrite arm coarsening at the eutectic temperature.
- 3 In the presence of manganese, at low cooling rates, the iron intermetallics crystallize in the  $\alpha$ -phase form, while at high cooling rates, both  $\alpha$  and  $\beta$  phases crystallize. This behaviour is the reverse of that observed in the absence of manganese. This is due to the fact that, unlike the manganese-

free  $\alpha$ -phase (metastable) which crystallizes only after completion of the Si-eutectic reaction, the manganese containing  $\alpha$ -phase ( $\text{Al}_{15}(\text{Fe},\text{Mn})_3\text{Si}_2$ ) crystallizes below the liquidus but above the silicon eutectic.

- 4 Increasing addition of manganese decreases the average length of the  $\beta$ -phase platelets due to the reduction in primary  $\beta$ -phase growth time.
- 5 When the melt is superheated to a high temperature and solidified under high cooling rates, the iron compound crystallizes in the  $\alpha$ -phase, in metastable form.
- 6 The average length of the  $\beta$ -phase needles decreases with decreasing iron content, decreasing magnesium content, increasing cooling rate, and increasing melt superheat temperature, since all of these parameters decrease the  $\beta$ -phase growth time.
- 7 With increasing cooling rate and increasing melt superheating temperature, the  $\beta$ -phase start temperature decreases until it merges with the silicon eutectic temperature. At this point the chemical composition of the remaining liquid favours the crystallization of the  $\alpha$ -phase.
- 8 Addition of magnesium (from 0.003 to 0.3 %) depresses the silicon eutectic temperature. This is one of the reasons why it is more difficult to crystallize the  $\alpha$ -phase in high magnesium alloys even at a high melt superheat temperature of 900 °C. Also, the plate length and volume percent of the  $\beta$ -phase increase with magnesium content, due to the increase in the primary  $\beta$ -phase growth time.

- 9 The change in crystallization behaviour of the iron compound on melt superheating is attributed to the  $\gamma \rightarrow \alpha$  aluminum oxide transformation since  $\gamma$ -alumina is a preferred nucleation site for the  $\beta$ -phase.

### 8.1.2 : FROM DISSOLUTION STUDIES :

- 1 With increasing solution temperature above the equilibrium solution temperature, the  $\beta$ -phase platelets dissolve slowly through concurrent fragmentation and dissolution. Solution temperature plays a more important role in dissolution of iron intermetallics than does the solution time.
- 2 Addition of manganese hinders the dissolution kinetics of iron intermetallics. The  $\beta$ -phase undergoes substantial dissolution, whereas, the  $\alpha$ -phase does not dissolve during heat treatment.
- 3 The thinner and the shorter the  $\beta$ -phase platelets, the faster is the fragmentation and dissolution. Therefore, iron intermetallics in low iron and magnesium containing castings solidified at high cooling rates undergo rapid dissolution.
- 4 The amount of liquid phase formed during heat treatment increases dramatically once a critical temperature is exceeded. This critical temperature was found to be 520 and 515 °C for samples initially solidified at 10 and 15 °C/s respectively. Quenching this liquid phase leads to re-precipitation of silicon and iron intermetallics in the melted zone.
- 5 The dissolution of the manganese-free  $\beta$ -phase occurs mainly at the tips of the platelets, and hence, the  $\beta$ -phase platelets shrink lengthwise but do not

thin. Manganese-containing  $\beta$ -phase dissolves around its perimeter at crevices or surface irregularities giving the appearance of serrated needles.

### **8.1.3 : FROM MECHANICAL PROPERTY STUDIES :**

- 1** Increasing iron from 0.15 % to 1.0 % decreases yield strength, tensile strength and elongation of the as-cast alloys. This is attributed mainly to the presence of brittle iron intermetallics in long needle-like form ( $\beta$ -phase).
- 2** The addition of a small amount of manganese improves the tensile strength of the material to that obtainable in low iron alloys (0.15 % Fe). This improvement is due to the crystallization of the less harmful  $\alpha$ -phase and the absence of primary  $\beta$ -phase.
- 3** Although equilibrium heat treatment improves the tensile properties of all the alloys studied, the 0.15 % Fe alloy exhibits the highest tensile strength and percent elongation compared to 1.0 % Fe and 1.0 % Fe + 0.5 % Mn alloys.
- 4** Under non-equilibrium heat treatment conditions, i.e., 30 degrees above the T4 equilibrium solution temperature, the strength properties of high iron alloys exceed, or at least equal, that of equilibrium heat treated low iron alloy. The yield strength of the material also increases with non-equilibrium heat treatment.
- 5** Fractography analysis shows that cracks propagate along the boundary between the  $\beta$ -phase platelets and the aluminum matrix suggesting poor interphase boundary cohesion. In the case of the  $\alpha$ -phase, the crack

propagates through the iron compound.

## **8.2 : SUGGESTIONS FOR FUTURE WORK :**

The following areas for further work are suggested in order to extend the present scientific studies to industrial applications.

- 1 Although the effect of iron content, grain refiner, eutectic modifier and cooling rate on the microstructural and thermal analysis parameters of 319 alloy were studied independently and compared with each other, they were not correlated. For this, a large number of trials is necessary under closely controlled melting and casting conditions. Exact correlation of the interactive effects of these parameters as a function of cooling rate would be helpful in industrial applications where microstructure can be predicted based on thermal analysis parameters.
- 2 It was determined that  $\gamma$ -aluminum oxide present in the melt acts as a potential nucleus for the crystallization of the  $\beta$ -phase. Other secondary nuclei for the  $\beta$ -phase or nuclei for the  $\alpha$ -phase are unknown. Further investigation of these nucleation mechanisms would help to identify different nuclei for these intermetallics and to preferentially enhance or suppress the crystallization of certain types of intermetallics.
- 3 Non-equilibrium heat treatment was studied only on 1.0 % iron containing alloys. This high level of iron is seldom utilized in most of the permanent mold casting alloys. It is expected that iron intermetallics would dissolve rather easier when the iron content is below 0.7 percent. Detailed studies should be carried out on the dissolution mechanisms of iron intermetallics

as a function of iron content.

- 4 Although the tensile test is a standard testing procedure to evaluate the mechanical properties of the castings, it yields only properties in simple tension. It is suggested that a more extensive series of mechanical tests be performed such as hardness, impact and fatigue testing

# STATEMENT OF ORIGINALITY

The specific original contributions made in this work may be summarized as follows :

- 1 For the first time, the effect of iron on the microstructural features such as grain size, DAS, silicon structure and iron intermetallics has been investigated as a function of cooling rate in 319 alloys.
- 2 Dendrite arm coarsening exhibited by low iron alloys has been explained using quenching experiments.
- 3 The crystallization start temperature of the primary  $\beta$ -phase platelets has been determined using thermal analysis. The temperature is observed to decrease with cooling rate.
- 4 The effect of addition of manganese on the crystallization of iron intermetallics as a function of cooling rate, and the complete crystallization behaviour has been explained for the first time.
- 5 Complete crystallization of the  $\alpha$ -phase rather than the  $\beta$ -phase on melt superheating in 1.0 % Fe containing alloys has been successfully demonstrated for the first time.
- 6 The importance of nucleation undercooling in addition to growth undercooling for the crystallization of the  $\beta$ -phase platelets has been illustrated using thermal analysis curves.

- 7** The hitherto unexplained influence of magnesium on the crystallization behaviour of iron intermetallics on melt superheating has been explained for the first time.
- 8** A mechanism for the change in crystallization behaviour of the iron compound on melt superheating is proposed for the first time.
- 9** The concept of dissolution of iron intermetallics through non-equilibrium heat treatment is newly developed.
- 10** The effect of low magnesium alloy in enhancing the critical solution temperature and thereby improving the mechanical properties has been demonstrated.
- 11** The effect of non-equilibrium heat treatment in restoring the mechanical properties of high iron alloys without resorting to conventional neutralization techniques has been established through tensile test results.

## REFERENCES

- (1) G.L. Armstrong, Alloy Selections for Automotive Aluminum Castings, SAE, no.780249, 1978.
- (2) T.B. Massalski, Binary Alloy Phase Diagrams, ASM, Metals Park, Ohio, 1986.
- (3) W. Bonsack, ASTM Bulletin, p.41, Oct 1943.
- (4) R.S. Archer and L.W. Kempf, Technical Publication No. 352, Am. Inst. Mining and Metallurgical Engrs., p.1, 1930.
- (5) C. Gurtler, Aluminium, vol.19, no.2, p.66, 1937.
- (6) Aluminum Alloy Data Book, Wabash Alloys, U.S.A.
- (7) W.H. Glaisher, Metallurgia, p.127, 1951.
- (8) J.K. Resch and E.W. Miguelucci, AFS Trans., vol.94, p.17, 1986.
- (9) E.L. Rooy, AFS Trans., vol.93, p.935, 1985.
- (10) G.K. Sigworth, AFS Trans., vol.91, p.7, 1983.
- (11) G.K. Sigworth and M.M. Gozowski, AFS Trans., vol.93, p.907, 1985.
- (12) Aluminum 319.0, Data on World Wide Metals and Alloys, Alloy Digest, May 1985.
- (13) D. Munson, J. Inst. Metals, vol.95, p.217, 1967.
- (14) W.B. Pearson, A Handbook of Lattice Spacings and Structures of Metals and Alloys, Pergamon Press, New York, 1964.
- (15) G. Phragmén, J. Inst. Metals, vol.77, p.489, 1950.
- (16) L.F. Moldolfo, Aluminum Alloys : Structure and Properties, Butterworths, London, 1976.
- (17) A.L. Dons, Z. Metallkunde, vol.76, p.609, 1985.
- (18) Y. Langsrud, Key Engineering Materials, vol.44&45, p.95, 1990.
- (19) I. Miki, H. Kosuge and K. Nagahama, J. Jap. Inst. Light Metals, vol.32, p.1, 1975.
- (20) E.H. Hollingsworth, G.R. Frank and R.E. Willett, Trans. Met. Soc. AIME, vol.224, p.188, 1962.
- (21) H. Westengen, Z. Metallkunde, vol.73, p.360, 1982.

- (22) C.Y. Sun and L.F. Mondolfo, *J. Inst. Metals*, vol.95, p.384, 1967.
- (23) C.J. Simensen and R. Vellasamy, *Z. Metallkunde*, vol.68, p.428, 1977.
- (24) A.L. Dons, *Z. Metallkunde*, vol.75, p.170, 1984.
- (25) J. Igléssis, C. Frantz and M. Gantois, *Memoires Scientifiques Revue Metallurgie*, p.237, 1977.
- (26) A. Couture, *AFS Int. Cast Metals Journal*, p.9, Dec 1981.
- (27) G.M. Vorobev, R.M. Golshtein and I.I Maurits, *Metallurgical Abstracts*, vol.32, p.960, 1964.
- (28) L.F. Mondolfo, *Manganese in Aluminium Alloys*, The Manganese Centre, France, 1990.
- (29) A. Franek, J. Pazdernik and A.K. Hanna, *World Aluminum Abstracts*, vol.7, no.53-0036X, 1974.
- (30) H. Iwahori, H. Takamiya, K. Yonekura, Y. Yamamoto and M. Nakamura, *Casting (Japanese)*, vol.60, p.590, 1988.
- (31) G. Gustafsson, T. Thorvaldsson and G.L. Dunlop, *Met. Trans.*, vol.17A, p.45, 1986.
- (32) W. Bonsack, *ASTM Bulletin*, vol.117, p.45, 1942.
- (33) S. Hajas, *Chemical Abstracts*, vol.73, no.133571, 1970.
- (34) V. Bischofberger, G. Neite and H.E. Exner, *Key Engineering Materials*, vol.44&45, p.333, 1990.
- (35) C. Mascré, *Fonderie*, vol.108, p.4330, 1955.
- (36) L. Grand, *Fonderie*, vol.217, p.95, 1964.
- (37) J. Igléssis, C. Frantz and M. Gantois, *Memoires Scientifiques Revue Metallurgie*, vol.75, no.2, p.93, 1978.
- (38) *Properties of Cast Aluminum Alloys*, *Metals Handbook*, ASM, vol.2, p.152, 1991.
- (39) D.L. Colwell and R.J. Kissling, *AFS Trans.*, vol.69, p.610, 1961.
- (40) G. Gurtler and E. Schulz, *Metallurgical Abstracts*, vol.7, p.9, 1940.

- (41) S. Yaneva, N. Stoichev, Z. Kamenova and S. Budurov, *Z. Metallkunde*, vol.75, p.395, 1984.
- (42) J.D. Evensen and T.B. Pedersen, *Proc. 7 th Light Metals Congress, Leoben/Vienna*, p.77, 1981.
- (43) M. Tagami and K. Hashiura, *J. Inst. Light Metals*, vol. 31, p.479, 1981.
- (44) Y. Komiyama, K. Uchida and M. Gunshi, *J. Inst. Light Metals*, vol.26, 1976.
- (45) H.W.L. Phillips and D.C. Varley, *J. Inst. Met.*, vol.69, p.317, 1943.
- (46) J.G. Barlock and L.F. Mondolfo, *Z. Metallkunde*, vol.65, p.605, 1975.
- (47) Y. Awano and Y. Shimizu, *AFS Trans.*, vol.98, p.889, 1990.
- (48) L.R. Morris and F.B. Miners, U.S. Patent no. 392 6690, 1975.
- (49) M.H. Mulazimoglu, B. Closset and J.E. Gruzleski, *Aluminum*, vol.6, p.162, 1992.
- (50) J.E. Hatch, *Aluminum Properties and Physical Metallurgy*, ASM, p.165, 1984.
- (51) *Heat Treating of Aluminum Alloys*, *Metals Hand Book*, ASM, vol.4, p.841, 1991.
- (52) J.T. Staley, *Industrial Heating XLIV*, Oct 1977.
- (53) D.E. Talbot and D.A. Granger, *J. Inst. Met.*, vol.92, p.290, 1963.
- (54) P.Y. Zhu and Q.Y. Liu, *Mat. Sci. Technol.*, vol.2, p.500, 1986.
- (55) C.M. Adam and D.C. Jenkinson, *Proc. of the 27 th Annual Conf. of the Australian Institute of Metals, Christchurch, New Zealand*, p.58, 1974.
- (56) S. Shivkumar, S. Ricci, B. Steenhoff and G. Sigworth, *AFS Trans.*, vol.97, p.791, 1989.
- (57) F. Paray, *Heat Treatment and Mechanical Properties of Al-Si Modified Alloys*, Ph.D. Thesis, McGill University, Dec 1992.
- (58) A. Griger, V. Stefaniay, A. Lendval and T. Turmezey, *Aluminum*, vol.10, p.1049, 1989.
- (59) R. DasGupta, C.C. Brown and S. Marek, *Proc. of 2 nd International Conf. on Molten Aluminum Processing*, *AFS Trans.*, p.3, 1989.
- (60) A.L. Purvis and R.D. Pehlke, *AFS Trans.*, vol.96, p.539, 1988.

- (61) B.L. Tuttle, *Modern Castings*, p.39, Nov 1985.
- (62) M.R. Ghomashchi, *Z. Metallkunde*, vol.78, p.784, 1987.
- (63) P.S. Mohanty, F.H. Samuel and J.E. Gruzleski, *Met. Trans.*, 1993 (under communication).
- (64) H. Beumler, A. Hammerstad, B. Wieting and R. DasGupta, *AFS Trans.*, vol.96, p.1, 1988.
- (65) O. Vorren, J.E. Evensen and T.B. Pedersen, *AFS Trans.*, vol.96, p.1, 1988.
- (66) J. Charbonnier, *Int. Conf. on Liquid Metal Processing*, p.21, Sept 1986.
- (67) S. Nishi, T. Shinoda and E. Kato, *J. Inst. Light Metals (Japanese)*, vol.18, no.12, p.627, 1968.
- (68) M.C. Flemings, *Solidification Processing*, McGraw-Hill Book Company, p.150, 1974.
- (69) P.C. Dann, L.M. Hogan and J.A. Eady, *Metals Forum*, vol.12, no.4, p.212, 1979.
- (70) J. Kaneko, *J. of Mat. Science*, vol.12, p.53, 1966.
- (71) P.B. Crosley and L.F. Mondolfo, *AFS Trans.*, vol.74, p.53, 1966.
- (72) D.C. Jenkinson and L.M. Hogan, *J. of Crystal Growth*, vol.28, p.171, 1975.
- (73) D. Apelian, G.K. Sigworth and K.R. Whaler, *AFS Trans.*, vol.92, p.297, 1984.
- (74) D. Apelian and J.J. Cheng, *AFS Trans.*, vol.94, p.797, 1986.
- (75) J.L. Carbajal, C. Casado, J. Mojica and S. Valtierra, *3 rd Int. Conf. Molten Metal Processing*, *AFS Trans.*, p.141, 1992.
- (76) P. Jonason, *AFS Trans.*, vol.100, p.601, 1992.
- (77) L. Backerud, *Solidification Characteristics of Aluminum Alloys*, *AFS/SkanAluminium*, Oslo, vol.2, p.143, 1990.
- (78) H.W.L. Phillips, *Annotated Equilibrium Diagrams of Some Aluminum Systems*, *Inst. of Metals*, London, 1959.
- (79) Apelian et al, *Annual Workshop - 1991*, *Aluminum Casting Research Laboratory*, Dept. of Mech. Eng., WPI, Worcester, USA.

- 
- (80) K. Wefers and G.M. Bell, Technical paper no. 19, Alcoa, Pittsburgh, Pa, p.1, 1972.
- (81) M. Plummer, J. Appl. Chem. (London), vol.8, p.35, 1958.
- (82) S.J. Wilson and J.D.C. McConnell, J. Solid State Chem., vol.34, p.315, 1980.
- (83) M.J. Dignam, J. Elec. Chem. Soc., vol.109, p.184, 1962.
- (84) C. Misra, Industrial Alumina Chemicals, Alcoa Technical Centre, 1986.
- (85) Y. Shimizu, Y. Awano and M. Nakamura, 96 th Casting Cong., AFS no.92-135, Milwaukee, Wisconsin, 1992.
- (86) P.Y. Zhu and Q.Y. Liu, Mat. Sci. and Tech., vol.2, p.500, 1986.
- (87) V.S. Zolotarevsky, A.A. Axenov and N.A. Belov, Key Eng. Mat., vols. 44&45, p.347, 1990.
- (88) J. Gauthier, H. Liu and F.H. Samuel, CIM Conf., Quebec, 1993.
- (89) U.S. Patent no. 2,908,566, Oct 13, 1959.